Synthesis and Characterization of Nonstoichiometric Ternary and Quaternary Compounds of Bismuth Metallates, Alkali Metal Tungsten Oxides and Tungsten Metaphosphates

The dissertation submitted to the Department of Chemistry, Faculty of Science, University of Dhaka, Bangladesh in partial fulfillment of the requirements for the degree of **Doctor of Philosophy (PhD).**
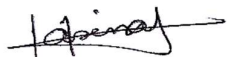
SUBMITTED BY

Hasina Akhter Simol

Reg. No.: 09/2015-2016 and 63/2019-2020 (Re-Reg.)

Department of Chemistry
Faculty of Science
University of Dhaka, Bangladesh

September 2022

DECLARATION

I hereby declare that the dissertation entitled **"Synthesis and Characterization of Nonstoichiometric Ternary and Quaternary Compounds of Bismuth Metallates, Alkali Metal Tungsten Oxides and Tungsten Metaphosphates"** is my own research work carried out during PhD period under the supervision of Professor Dr. Pradip Kumar Bakshi, Department of Chemistry, Dr. Tapas Debnath, Associate Professor, Department of Theoretical and Computational Chemistry, and Dr. Rumana Akther Jahan, Principal Scientist, Centre for Advanced Research in sciences (CARS), University of Dhaka, Dhaka-1000, Bangladesh. I also declare that the matter embodied in this dissertation has nor been submitted either in part or full or in any other form to any other University or Institution for any Degree or any other purpose.

(Hasina Akhter Simol)

PhD Student

Department of Chemistry

Faculty of Science

University of Dhaka

Dhaka-1000

Bangladesh

Date and Place

September, 2022

University of Dhaka

SUPERVISORS' CERTIFICATE

This is to certify that Hasina Akhter Simol has worked under our supervision and guidance for her PhD thesis entitled "Synthesis and Characterization of Nonstoichiometric Ternary and Quaternary Compounds of Bismuth Metallates, Alkali Metal Tungsten Oxides and Tungsten Metaphosphates". The work is original and that has been carried out in the Department of Chemistry, Faculty of Science, and Centre for Advanced Research in Sciences (CARS), University of Dhaka, Dhaka-1000, Bangladesh. We also certify that no part of this thesis has previously been submitted to any University/Institute for any degree or diploma or other similar title. Hasina Akhter Simol has also fulfilled all terms and conditions of the PhD course including presentation of the results of her study in seminars held in the Department of Chemistry, Faculty of Science, University of Dhaka and also in different scientific sessions of conferences. We have gone through the final draft of the thesis and recommended its submission for the degree of Doctor of Philosophy (PhD) in Chemistry.

Professor Dr. Pradip Kumar Bakshi

Department of Chemistry,

University of Dhaka, Dhaka-1000

Dr. Tapas Debnath

Associate Professor, Department of Theoretical and Computational Chemistry,

University of Dhaka, Dhaka-1000

Dr. Rumana Akther Jahan

Principal Scientist, Centre for Advanced Research in Sciences (CARS)

University of Dhaka, Dhaka-1000

Dedicated to

My

Family

ACKNOWLEDGEMENTS

ABSTRACT

Attempts were taken to prepare ternary and quaternary compounds of bismuth metallates, alkali metal tungsten oxides, and tungsten metaphosphates. All these compounds except reduce nonstoichiometric solid solution of alkali metal tungsten oxides were synthesized by the solution combustion synthesis (SCS) method. Conventional solid state method was used to prepare the reduce solid solution of alkali metal tungsten oxides.

Bismuth metallates with the composition $Bi_2M_4O_9$ (M = Al^{3+}, Fe^{3+}, Ga^{3+} etc.) exist in the system Bi_2O_3-M_2O_3 and belong to the mullite-type structure family. Series of polycrystalline materials, $Bi_2Cr_xGa_{4-x}O_9$ has been synthesized by SCS method using a mixture of corresponding metal nitrates and glycerin followed by calcination at 800°C in air. The samples were characterized using XRD, FT-IR, Raman spectroscopy and SEM/EDX methods. Rietveld refinement of the X-ray diffraction powder data shows that the lattice parameter *a* remains nearly constant with increasing nominal Cr content. The *b* cell parameters decrease upto a nominal composition of x=1.0 and then remains constant for further increasing chromium content. The cell parameter *c* increases up to a nominal composition of 0.6, after which it remains constant. These changes in cell parameters indicate the successful doping of chromium in mullite type bismuth gallate $Bi_2Ga_4O_9$. The calculated site occupancy factors obtained from Rietveld refinement indicate that Cr prefer to occupy the octahedral site of $Bi_2Ga_4O_9$, which is similar to Cr doped $Bi_2Al_4O_9$ reported in the literature. The partial replacement of only octahedrally coordinated Ga by Cr in $Bi_2Ga_4O_9$ is also supported from the FTIR absorption spectra of these compounds. The absence of any splitting of characteristic IR absorption peak centered at 850 cm^{-1} and systemic splitting and shifting of other low wavenumber peaks related to stretching and bending modes of GaO_6 octahedra in $Bi_2Cr_xGa_{4-x}O_9$ solid solution series support the preferential distribution of Cr in octahedral coordination. The systematic shifting of Raman peaks and their broadening may also indicate successful partial substitution of gallium by chromium in $Bi_2Cr_xGa_{4-x}O_9$ compounds. Three other bismuth metallates series with the nominal composition $Bi_2Fe_2(Cr_xAl_{1-x})_2O_9$ (x = 0.0, 0.1, 0.2, 0.4, 0.5, 0.6), $Bi_2Fe_3(Cr_xAl_{1-x})O_9$ (x = 0.0, 0.1, 0.2, 0.4, 0.5, 0.6) and $Bi_2Fe(Cr_xAl_{1-x})_3O_9$ (x = 0.0, 0.1, 0.2, 0.4, 0.5, 0.6) have been synthesized by the same method as used for $Bi_2Cr_xGa_{4-x}O_9$ compounds. In this case the calcination temperatures were varied from 700°C to 900°C. Crystal structure, phase formation, and crystallite size were confirmed

with XRD, FT-IR, and SEM data. The X-diffraction patterns their Rietveld refinements results reveal that the compounds of the $Bi_2Fe_3(Cr_xAl_{1-x})O_9$ series, with all studied compositions, show an orthorhombic mullite-type phase at 900°C. The FT-IR spectra also comply with the XRD pattern. The color of the compounds systematically changes with the substitution of Al by Cr in this series. Similar XRD patterns are observed for both $Bi_2Fe_2(Cr_xAl_{1-x})_2O_9$ and $Bi_2Fe_3(Cr_xAl_{1-x})O_9$ series. At 900°C, all members of the $Bi_2Fe_2(Cr_xAl_{1-x})_2O_9$ series in all studied compositions show orthorhombic mullite-type phase except x = 0.6 sample.

Three series of nonstioiometric solid solution of alkali metal tungsten oxides with nominal compositions $Rb_xV_yW_{1-y}O_3$ (x = 0.25, 0.30, and $0.0 \leq y \leq x$), $Cs_xV_xW_{1-x}O_3$ (x = 0.15, 0.20, 0.25, and 0.30) and $K_xV_xW_{1-x}O_3$ (x = 0.15, 0.20, 0.25, and 0.30) are also synthesized in the present work. The reduced solid solution series $Rb_xV_yW_{1-y}O_3$ were synthesized by the conventional solid-state method in evacuated SiO_2 glass ampoules and SCS method were used to prepare other two series. Powder X-ray diffraction data for the $Rb_xV_yW_{1-y}O_3$ (x = 0.25, 0.30 and $0.0 \leq y \leq x$) showed the formation of single-phase hexagonal tungsten bronze (HTB). Samples with $y \geq 0.20$ showed the presence of other phases along with HTB. An overall decreasing trend in the calculated unit cell volume was observed with increasing vanadium content. The FT-IR absorption spectrum of the sample at y = 0.0 shows a featureless increase in intensity with increasing wavenumber due to phonon screening by the polaron. This effect gradually disappears with the successive replacement of W^{5+} ions by V^{5+} and they develop a phonon absorption feature as a function of y. The incorporation of vanadium in the $Rb_xW_{1-y}V_yO_3$ system was also verified by SEM/EDX analysis. The of calcination temperatures (300°C to 800°C with 100°C intervals) on the crystallite sizes of $Cs_xV_xW_{1-x}O_3$ and $K_xV_xW_{1-x}O_3$ series are also studied. The broadening of XRD peaks reaveals that nanocrystalline HTB phase formation can be reported at temperature 400°C and 500°C. The SEM images as well as the calculated crystallite size using Scherrer equation in XRD patterns of these compounds support the nanocrystallinity. The XRD pattern of the prepared samples confirms that HTB forms at all studied temperatures. The nominal composition x = 0.15 and 0.20 shows the appearance of an unknown second phase together with the HTB phase at higher temperatures. The XRD patterns also show the peak positions of the diffraction lines shift systematically as the V content of the sample increases. SEM images show rod-like nanoparticles for $K_xV_xW_{1-x}O_3$ and flex-like for $Cs_xV_xW_{1-x}O_3$, which increase in size with

increasing temperatures. Both the observed K and V or Cs and V levels are in good agreement well with nominal compositions found in EDX analysis of $K_xV_xW_{1-x}O_3$ and $Cs_xV_xW_{1-x}O_3$.

In the present work, attempts were also made to prepare three new series of monophosphate tungsten bronze (MPTBs) type compounds, $A_{4/3-x}T_xW_{20/3})O_{24}(PO_2)_4$, where A/T = Cr, Fe, Al, and $0.00 \leq x \leq 4/3$ by SCS method. For all compositions of solid solution series $(Cr_{4/3-x}Fe_xW_{20/3})O_{24}(PO_2)_4$ at 500°C-750°C, XRD patterns were found cubic except x = 4/3 which shows cubic phase up to 700°C. At 850°C and 900°C, the X-ray pattern could be perfectly indexed as an orthorhombic structure. Cell parameters for cubic phase at 600°C and 650°C decrease up to the nominal composition x = 1, then increase. For the orthorhombic phase, cell parameters, *a and b* increases, but *c* remains constant. Similar results were observed for the other two series $(Cr_{4/3-x}Al_xW_{20/3})O_{24}(PO_2)_4$ and $(Fe_{4/3-x}Al_xW_{20/3})O_{24}(PO_2)_4$ when the samples were prepared at 700°C. At 800°C, the XRD pattern of nominal composition x = 0, 1/3, 2/3, and 1 of $Cr_{4/3-x}Al_xW_{20/3}O_{24}(PO_2)_4$ series shows a mixture of cubic and orthorhombic phases. At 850°C and 900°C the XRD pattern could be perfectly indexed as the orthorhombic phase. But at the nominal composition x = 4/3 of $Cr_{4/3-x}Al_xW_{20/3}O_{24}(PO_2)_4$ series $(Al_{4/3}W_{20/3}O_{24}(PO_2)_4)$ at 800°C is cubic with some new lines which do not relate to the orthorhombic phase. Further heating, the product may be decomposed into separate phases. The cell parameters at 600°C and 650°C for the cubic phase of $Cr_{4/3-x}Al_xW_{20/3}O_{24}(PO_2)_4$ show that the cell parameters slightly increase up to the nominal composition x = 1/3, then remain almost constant. For the third series $Al_{4/3-x}Fe_xW_{20/3}O_{24}(PO_2)_4$, only nominal composition x = 4/3 shows orthorhombic phase at 850°C and 900°C. The cell parameters at 600°C and 650°C for the cubic phase of $Al_{4/3-x}Fe_xW_{20/3}O_{24}(PO_2)_4$, cell parameters slightly increase up to nominal composition x = 2/3, then decrease. Therefore, Cr and Fe can form a complete solid solution series $(A_{4/3-x}T_xW_{20/3})O_{24}(PO_2)_4$ having an MPTBs type structure. On the other hand, other two series $(Cr_{4/3-x}Al_xW_{20/3})O_{24}(PO_2)_4$ and $(Al_{4/3-x}Fe_xW_{20/3})O_{24}(PO_2)_4$ show composition-dependent structural variation. The broadening of XRD peaks for all cubic phases reveals the nanocrystallinity of the compounds, which was further confirmed by SEM images.

Contents

List of Tables

List of Figures

Chapter One

General Introduction

1.1 Non-stoichiometric compounds and solid solution

Non-stoichiometric compounds (NS) are chemical compounds with non-integral coefficients or variable atom ratios. It occurs in compounds when a fraction of the atoms of one type is absent or in excess of the regular structure or replaced by atoms of another type. Their basic structure cannot be defined by integers, so they deny the law of fixed proportions [1]. Usually, these compounds have characteristics such as variable composition, bright colors, metallic or semiconductors, and differences in chemical reactions from the stoichiometric compounds from which they are derived. Non-stoichiometric compounds have a continuous flaw structure which makes them different from stoichiometric compounds in which they possess a definite structure. $A_{m-x}B_{n+x}$ is the simplest approach to formulate a non-stoichiometric compound, where x is a positive quantity of elements A and B significantly less than 1. Non-stoichiometry is common in transition metal oxide, but it also occurs in fluoride, hydride, carbide, nitride, sulphide, and boride.

Non-stoichiometric compounds are usually associated with the creation of vacancies or defects to accommodate incoming and outgoing atoms/ions, commonly referred to as a point defect. An interstitial defect is formed when a foreign atom is found in the crystal structure which is usually unoccupied. Since the interstitial atom is smaller than the bulk atom and larger than the site it occupies, the surrounding crystal structure is distorted shown in Fig. 1.1 (b). Hence the ratio between the number of atoms in a cell and the number of sites is not equal [2] in nonstoichiometric compounds.

(a)   (b)
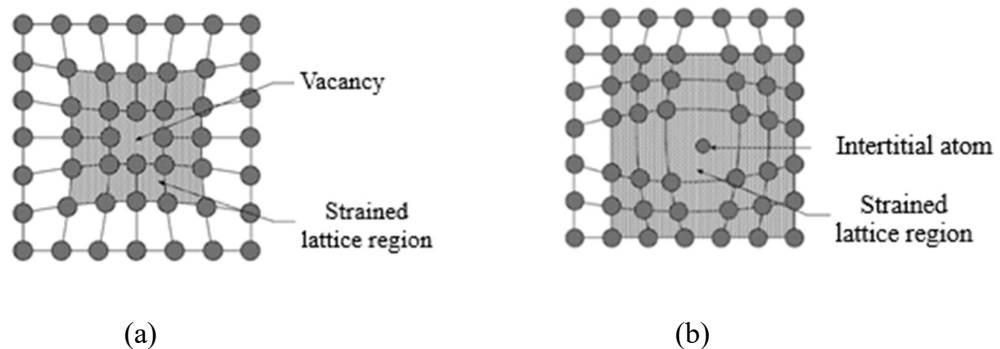
Fig. 1.1. (a) Point defect vacancy and (b) Interstitial defect in a crystal structure.

The unique properties of nonstoichiometric compounds are determined by their crystal defect structure, solid phase composition and thermodynamic properties.

Nonstoichiometric compounds represent a uniform physical state in which the parameters of a single cell continuously change with its structure [1]. The microscopic and macroscopic structural thermodynamic properties of nonstoichiometric compounds vary in their phases and unit cell parameters [3-5] Note that stoichiometric crystalline compounds or mixtures of stoichiometric compounds each have their own XRD pattern and unit cell parameters.

A solid solution is a combination of crystalline solids or mixtures to form a new crystalline solid. There are two forms of solid solution: substitutional and interstitial. Substitutional solid solution occurs when the atoms of one initial crystal replace the other while interstitial solid solution forms when atoms occupy positions in the lattice that are normally empty. Several crystalline compound especially oxides, sulphides, selenides, etc., of the transition metals form solid solutions whose composition can vary widely without modifying the crystal structure. For example, solid solutions of these compounds show deviations from stoichiometry toward nonstoichiometry, where composition becomes an important factor. A range of composition of a single phase compound can be interpreted as a solid solution when one or more atoms are added or lost and the resulting compounds possess nonstoichiometry. Usually, such compounds are formed when the addition of a dopant does not produce a new phase, but one continuous phase over a certain compositional range. Non-stoichiometry by doping can lead to compounds in which the ratio of metal to non-metal varies and the structure remains unchanged over the ranges of the metal to non-metallic atoms. But when the total value of the metal-to-non-metal ratio remains unchanged, solid solutions are usually formed [6].

In general, non-stoichiometric compounds can be referred to as heteroionic solid solutions, in which the cations of the parent structure are replaced by controlled and predetermined cationic values of another object in a different valence state. The effect of this change depends on the valence of the host and its replacement [2]. Such changes can be represented as follows:

Table 1.1. The valence properties of host and substituent during the formation of non-stoichiometric compounds due to cationic substitution.

Host species	Substituent	Effect
Variable Valency	Fixed Valency	Controlled valence of host cations
Fixed Valency	Variable Valency	Induced valence of substituent cations
Fixed Valency	Fixed Valency	Controlled structural defects

1.2 Properties of the nonstoichiometric compound and solid solution

Nonstoichiometric compounds have a variety of features, including magnetism, conductivity, catalytic activity, and other unusual solid-state properties, many of which have vital practical applications. Non-stoichiometry may control the properties and reactivity of oxide-based materials for both catalytic and non-catalytic applications. Due to their unique physical and chemical features, nonstoichiometric oxides, metal nitrides, and semiconductors are extensively used in electronics and nanotechnology [7]. Low levels of non-stoichiometry in functional oxides can lead to significant functional property changes due to unintentional material loss/gain during intended material doping or processing or raw material impurities [8-10]. The nonstoichiometric mixed metal oxide of the Perovskite family ($A_{n+1}B_nO_{3n+1}$: n = 1, 2, 3 - - - ∞; A = alkaline earth/rare earth metal; B = transition metal) has attracted much attention for many catalytic application [11]. Moreover, these oxides offer a wide compositional space which offers the possibility of synthetically adjusting their chemical and physical properties.

Due to their improved ionic and electrically conductive properties, nonstoichiometric mixed metal oxides provide high temperature oxygen electrolysis in solid oxide fuel cells (SOFCs) and solid oxide electrolysis cells (SOECs) [12]. Nonstoichiometric mixed metal oxides such as perovskite, double perovskite with mixed ionic and electrically conductive properties were used as oxygen electrodes for catalyzing the oxygen reduction and evolution reaction (ORR and OER) at high and low temperature due to the versatility of the surface composition and characteristics of rapid oxygen conduction [12] and [8]. Low cost metal based electro-catalysts for oxygen reduction and evolution can be made from nonstoichiometric mixed metal oxides [8].

Non-stoichiometric metal oxides e.g., WO_{3-x}, MoO_{3-x}, are suitable for a variety of applications due to their strong photo-absorption properties over a wide wavelength range of NIR regions, especially, tungsten-oxide based materials have been used effectively in the NIR region. It is observed that WO_3 has no NIR absorption; but when converted into non-stoichiometric oxides by doping Cs ($CsWO_3$) or reduction of WO_3 to $WO_{2.72}$ and WO_3 nanoparticles, it has a strong NIR absorption capacity [13, 14]. The different forms of WO_{3-x} such as $WO_{2.9}$, $WO_{2.83}$ and $WO_{2.72}$, showed better electrical conductivity than WO_3 [14]. In the case of pollutant degradation, the activity of $WO_{2.72}$ is higher than that of WO_3 and the most active species for pollutant mineralization is O_2 [14, 15].

Nonstoichiometric metal oxides containing ternary and quaternary bismuth have a wide range of potential applications such as sensors, oxidation catalysts, pigments, superconductors, scintillators, photocatalysts, high-temperature electrolytes and next-generation data storage materials [16]. An area of growing importance for basic and applied research projects is focused on bismuth alloy metal oxide components that exhibit a wide-range of electronic, magnetic and optical properties. These multi-metallic bismuth oxides have applications as high Tc superconductors (high temperature superconductors), nonlinear optical materials, and green lubricating materials [17-18].

1.3 Objective of this research

Extensive studies on non-stoichiometric compounds show that Sr, Ca, and also Cr substituted Bi-aluminate and Bi-ferrite are reported [19-21], but there is no report about Cr-doped Bi-metallate containing both Fe and Al. In addition, it was also found that the Cr substituted in the Bi-gallate system was not studied. For this reason, this study has been done to redefine and confirm some known crystal structures of Bi-metallates, in particular structures of $Bi_2Ga_4O_9$, $Bi_2Al_4O_9$, $Bi_2Fe_4O_9$, and also Cr-doped Bi-gallate and Bi-metallate system (where both Al as well as Fe present) studied. Under the above circumstances, attempts were made in this study to prepare the flowing series of Bi-metallates.

i. Synthesis and characterization of Cr-doped Bi-gallates ($Bi_2Cr_xGa_{4-x}O_9$), solid solution series with nominal compositions, x = 0.0, 0.2, 0.4, 0.6, 0.8, 1.0, 1.2, 1.4, 1.6, 1.8 and 2.0.

ii. Reproduce Bi-ferrite and Bi-aluminate ($Bi_2Fe_xAl_{4-x}O_9$) with nominal compositions, x = 0.0, 0.2, 0.4, 0.5 and 0.6.

iii.   Synthesis and characterization of Cr-doped bismuth mixed metallate solid solution series

   a) $Bi_2Fe(Cr_xAl_{1-x})_3O_9$ with x = 0.0, 0.2, 0.4, 0.5 and 0.6.

   b) $Bi_2Fe_2(Cr_xAl_{1-x})_2O_9$ with x = 0.0, 0.2, 0.4, 0.5 and 0.6.

   c) $Bi_2Fe_3(Cr_xAl_{1-x})O_9$ with x = 0.0, 0.2, 0.4, 0.5 and 0.6.

Another interesting subject for this present work is the study of the alkali metal tungsten oxide i.e., tungsten bronzes/bronzoid system. Reported research on alkali metal tungsten oxide, such as partially or fully oxidized bronzes or bronzoid systems, has described a Tetragonal Tungsten Bronze (TTB) type phase in the KT_aWO_3-WO_3 system [22], niobium substituted hexagonal tungsten bronzes (K- and Rb-HTB) [23]. There are also reports on Inter Growth Tungsten Bronzoids (IITB) with Nb and Ta in the K- and Cs- systems [24, 25] and perovskite-type structure, $Na_{0.5}NbO_{2.75}$ in the system of sodium tungsten bronze doped with niobium, $Na_{0.8}Nb_yW_{1-y}O_3$ [26].

But almost no reports have been found on the substitution of tungsten by vanadium atoms in the potassium, cesium and rubidium tungsten bronzes in any phase. Therefore, an attempt was made to thoroughly study the synthesis of alkali metal tungsten oxide type compounds in which tungsten is partially replaced by pentavalent cations of different ionic radii (vanadium) in this system with their structure-property relationship. In this study, the following alkali metal tungsten oxide series has been prepared:

   i.   Synthesis and characterization of vanadium doped alkali metal tungsten oxides, $A_xV_xW_{1-x}O_3$ (A = K, Cs and x = 0.15, 0.20, 0.25 and 0.30) at relatively lower temperature by a new simple approach known as solution combustion synthesis (SCS) where particle size could be controlled.

   ii. Synthesis and characterization of vanadium doped alkali metal tungsten oxides, $Rb_xV_yW_{1-y}O_3$ with x = 0.25, 0.30 and y < x.

Raveau *et al.* synthesized $A_xP_yM_zO_w$ (M = Ti, V, Nb, Mo, W) where some WO_6 octahedra have been substituted in an ordered fashion by monophosphate (PO_4) or diphosphate (P_2O_7) groups [27, 28]. As tungsten phosphates show the great adaptability of WO_6 octahedra to PO_4 tetrahedra, and also show the different oxidation states, especially at low and intermediate valence state. Very few reports are available on the substitution of W(V) in these mixed-valent W(V, VI) phosphates with other transition metals. Therefore, mixed transition metal phosphate containing hexavalent

tungsten in addition to the trivalent cation can show promising results. Considering the entire phenomenon, this study was initiated to prepare for the first time a new series of Mono Phosphate Tungsten Bronze (MPTBs) compounds and the study of their structure-property relationship is an additional area of interest in this ongoing work. Therefore, an attempt was made to

➢ Synthesis and characterization of mixed-metal monophosphate tungsten bronze, $A_{4/3-x}T_xW_{20/3}O_{24}(PO_2)_4$ with nominal compositions x = 0, 1/3, 2/3, 3/3, 4/3, where A and T are the trivalent cations such as Cr, Al and Fe.

1.4 Sample preparations

The method of preparation of the compounds plays an important role in its characteristics. The choice of methods for synthesizing nonstoichiometric chemicals is influenced by a number of important criteria, such as temperature, instrumental facilities, and time availability. A series of samples of bismuth metallates, alkali metal tungsten oxides, and mixed metal monophosphate tungsten bronze were prepared using the solution combustion synthesis (SCS) method. The solid states synthesis method was also used for the synthesis of some selected samples, vanadium doped alkali metal tungsten oxides, $Rb_xV_yW_{1-y}O_3$. There are also several methods for preparing these types of nonstoichiometric chemical samples. Here is a brief summary of some of these methods.

1.4.1 Solution combustion synthesis (SCS)

Solution combustion synthesis (SCS) is an excellent synthesis method due to its simplicity, cost-efficiency and product powder quality. SCS is based on a rapid and self-sustaining redox reaction between a fuel and an oxidant in the presence of metallic cations [29]. Oxidants are usually a precursor to the metal itself, where nitric acid or ammonium nitrate or metallic nitrate are used as oxidizers and high soluble energy components containing C, N, H are used as oils, such as citric acid, glycine, urea, glycerin, etc. capable of forming complexes with metallic ion interest. In solution combustion synthesis, the combustion of dry weight or gel obtained from homogeneous solutions of precursors, oils and oxidizers occurs. Gas molecules, CO_2, H_2O, N_2, and NO_x are released during the combustion process. Combustion synthesis is also referred to as fire synthesis or self-propagating high-temperature synthesis (SHS). In a combination of fire or combustion, the necessary ingredients for fuel and oxidizer are used [30]. Proper temperature is important when choosing a combustion reaction. The reaction between fuel and oxidizer is a redox reaction

releasing large amounts of energy and gaseous reaction products. The combustion process begins with the evaporation of the remaining water molecules from a slightly dry or gelatinous mass before melting and decomposing. Later, the ignition begins with a hot spot. The redox mixture burns and the reaction spread with the continuous inflammation of the reaction mixture and the release of a large amount of gaseous material. A red hot spot is observed during combustion, indicating that the temperature is around $800^{\circ}C$, which lasts for a very short time. The final products obtained with the SCS method include superior surface with superior powder properties, narrow particle size distribution, optimal aggregate and excellent phase purity with better centering properties [29]. The combustion process has been widely used for synthesis as both soluble and insoluble [29] precursors can be used. The SCS method was used to prepare mixed metal oxide phosphates $Ti^{iv}_{6/3}W^{vi}_{6/3}O_{12}(PO_2)_4$, $M^{III}_{4/3}W^{vi}_{8/3}O_{12}(PO_2)_4$ and $M^{III}_{4/3}W_{20/3}O_{24}(PO_2)_4$ by heating of reaction intermediates [31]. $Bi_2Cr_xAl_{4-x}O_3$ was prepared by a modified SCS method using metal nitrate and glycerin [32]. Voll *et al*. also used this method for the preparation of $Bi_2Al_{4-x}Fe_xO_9$ [33]. A few salient features of SCS methods are [34]:

- Oxides and their composites can be prepared at low temperatures as $< 400^{\circ}C$.
- The products are homogeneous, crystalline, soft and delicate with high surfaces due to their fuel-rich condition.
- The prepared materials are of high purity (99.99%).
- The particles show less coagulation and can be used as a direct coating.
- Large quantities can be prepared relatively cheaply. The short reaction time and the evolution of large amounts of gas favor the formation of small particle-sized components.

1.4.2 Solid-state synthesis method

The conventional solid-state synthesis method involves heating two or more non-volatile solids which react to form the required product. Mixed metal oxides, sulfides, nitrides, aluminosilicates, and other compounds can be prepared using solid-state synthesis processes. Because much energy is required to overcome the lattice energy and disperse a cation or anion to a new site, high temperature (500-2000°C) is usually required. The probability and rate of a solid state reaction depends on the reaction state, the structural properties of the reactants, the surface area of the solid, their reactivity, and the thermodynamic free energy changes associated with the reaction. It is necessary to select an appropriate container material that is chemically inert to reactants under high heating

conditions, and platinum and gold are generally used. For low-temperature reactions (below 600-700°C) nickel can be used. The slow reaction rate of solid reactions due to the slow diffusion rate of the reactants can be overcome by high temperatures annealing. Certain minerals (such as Cl_2) can erode the silica tube and dissolve SiO_2 into the system from the ampoule wall. By reducing the diffusion path length, the reaction rate can be increased, which can be achieved by making a pellet of the reactive mixture at high pressure. The pellet has less contact with the silica ampoule surface and reduces the reaction between the sample and the silica wall. The finely ground powder is reduced at high temperature in evacuated silica, gold, or platinum tubes. Abdullah *et al.* prepared vanadium substituted potassium hexagonal tungsten bronze by reducing a mixture of K_2CO_3, V_2O_5 and WO_3 with WO_2 in the absence of air [35]. $K_xTa_yW_{1-y}O_3$ was prepared by Shakil *et al.* using K_2WO_4, Ta_2O_5, WO_3 and WO_2 by a conventional solid-state synthesis method [36]. Dey *et al.* also used conventional solid-state synthesis method for the preparation of $Cs_xNb_yW_{1-y}O_3$ using Cs_2WO_4, Nb_2O_5, WO_3 and WO_2 [37]. $Ga_{2-x}Fe_xO_3$ was prepared by Roy *et al.* and Lu *et al.* by solid-state synthesis method using Ga_2O_3 and Fe_2O_3 [38, 39]. Microcrystalline, dark brown $WOPO_4$ was synthesized from m-$(W_2O_3)(PO_4)_2$, WO_3 and red phosphorus at 100^oC in a sealed tubes by a solid state reaction [31]. In general, solid-state reactions may have the following advantages over solution-phase reactions:

(i)   Solid-state reactions are economical and produce only limited side products.

(ii)   The reaction does not require a solvent, therefore there are no waste disposal issues associated with the solvent to consider, and extensive product refining does not require the removal of solvent and impurities.

Solid-state reactions also have a number of disadvantages:

(i)   If the ideal process produces a homogenous or uniform substance, this process tends to produce inhomogeneous end-products.

(ii)   Due to the enormous number of starting reactants in the combination, the formation of less reactive intermediate phases can occur.

1.4.3 Chemical vapor transport

The chemical vapor transport reaction is an effective method for the synthesis of various inorganic compounds and intermetallic phases and for crystal growth. A solid usually evaporates in the presence of a gaseous reagent (transport agent) and accumulates elsewhere in the form of crystals. A carrier gas transports the primary materials to the substrate after heating to form volatile vapors. They are then assembled at the appropriate temperature and transferred to the surface with steam. Common starting materials include hydrides, halides, and organometallic compounds because they tend to be volatile. The various parameters that need to be optimized for successful CVT are increased temperance, direction of transport, rate of mass transport, choice of transport agent, and free energy of the reaction.

The main drawback is that the transport experiments are usually performed in evacuated, melted quartz glass ampoules and require a transport agent to dissolution of the solids in the gas phase. The equilibrium position of the CVT reaction must be at the bottom, so that by slightly modifying the experimental conditions it is possible to dissolve the gas phase and re-condense the solid. Li_xWO_3 crystals (nominal compositions, x = 0.1, 0.25, 0.3, 0.4 and 0.45) were prepared by the chemical vapor transport method using $HgCl_2$ as the transport agent [40].

1.4.4 Hydrothermal method

The hydrothermal synthesis method is a heterogeneous reaction to the synthesis of inorganic substances in aqueous media at ambient temperature and pressure [41]. This synthetic method is simple, gentle, clean, inexpensive and has template-free. This method involves the use of high pressure and temperature to move water to its critical point and therefore the rapid hydrolysis and dehydration of the metal salts in solution to achieve the desired one. In such cases, water density and the dielectric constant regularly indicate a decrease and promote increased hydrolyzing area [42]. In this case, an aqueous mixture of precursors is heated in a sealed stainless steel autoclave to a temperature of 125°C to 200°C, and subsequently, the pressure in the reaction autoclave rises significantly above atmospheric pressure.

It is a one-step process to produce highly crystalline materials without any post-annealing treatment. The nature of the precursors, solvents, stabilizers and reaction temperatures, the

pH of the reaction medium and the reaction time have a significant impact on the crystalline structure of the constructed phase. This method provides an opportunity for the synthesis of mixed metal oxides that require the metal to be in a state of poor oxidation. Since the reaction takes place in a closed system, it is possible to control oxidation or reduction the air inside the autoclave [42]. However, the product has a relatively low yield in the hydrothermal method compared to other methods. Chongshen Gao *et al*. prepared one dimensional nanostructure potassium tungsten oxide under hydrothermal reaction condition using K_2WO_4 and K_2SO_4 [43]. Reducing potassium tungsten oxide converted into potassium tungsten bronze in an atmosphere of H_2 (5 vol %)/N_2 for one hour at a temperature range 400-600°C. Ammonium tungsten bronze nanoplatelets were synthesized by Lu *et al.* using sodium tungstate dehydrate and thiourea in a Teflon sealed autoclave at 220, 240 and 260°C [39].

1.4.5 Sol-gel method

The sol-gel method is a highly advanced and established solution based on the synthesis of mixed metal oxides, metal oxide glasses and ceramics that form hydrolyzed chemical precursors or a mixture of precursors that pass through the solution and gel state [42]. A glass or ceramic is dehydrated. This procedure is performed using raw metal alkoxides and involves calcination at the end. These metallic alkaloids interact with van der Waals force or H-bonding to act as precursors to the formation of oxide particles, which are dispersed in a "sol" that is "gel" by solvent evaporation or other chemical reaction. This method promotes the formation of extremely homogeneous iron ion precursor networks which help to produce pure oxide phases at much lower temperatures calculated than the required solid state formation. The high uniformity of the precursor complex in solution helps in the successful synthesis of complex oxides (high and quaternary). This process involves the formation of a suspension network from solute ions in a solute metal, which is later converted into a waterless 3D network called a gel. This technology is used to make fibers, microspheres, thin films, fine powders and monoliths. Sol-gel technology is also used for the synthesis of protective coatings, catalysts, piezoelectric devices, waveguides, lenses, high-strength ceramics, superconductors, nanoparticles and insulating materials. There are a number of critical variables, some of which are discussed, that need to be controlled in a hydrothermal synthesis method for reproducibility [44]. The preparation of metallic oxide using sol gel methods, partially hydrolysis of metal alkoxides occurs to form active monomers and condensing of these monomers forms colloid-like oligomers (sol

formation). Additional hydrolysis occurs to promote polymerization and bonding, forming a three-dimensional matrix (gel structure).

The advantages of using sol-gel processing instead of high temperature processing methods with low synthesis temperatures, high purity, new materials and low cost. There are also some disadvantages of this method. The compression that occurs during processing often leads to fractures due to the large capillary pressure and makes it difficult to obtain large monolithic fragments. Due to the residual hydroxyl and/or carbon groups, preferential precipitation of a certain oxide occurs during sol formation (in multicomponent glass) due to different reactions of the alkoxide precursors. In sol-gel method long processing time required, residual porosity and OH groups are difficult to avoid. Organic solutions are used in this method, which may be toxic.

1.5. Characterization techniques

1.5.1 X-ray powder diffraction (XRD)

XRD technique is one of the most important characterization techniques for crystalline solids. Powder analysis of sample phase identification, sample purity, crystallite size, crystal structure, unit cell parameter, and in some situations morphology is all provided by XRD. A crystal's fingerprints are X-rays. Since solid atoms or molecules are identical, they give different information via X-ray diffraction. This is because the scattering factor of different atoms is different. By means of X-ray powder diffraction, X-rays are produced inside a closed tube. When current energy is used, electrons are released from a filament of tungsten (cathode). High power consumption speeds up these electrons and strikes the target, usually made of copper (anode). The electron energy of the incident is able to ionize copper 9K shell electrons. The electron is an external orbital rapidly (2p or 3p) descending to the level of 1s empty and the energy released from the transition appears as X-ray radiation. X-ray diffraction is the technique that radiates an element with incoming X-rays and measures the intensity and scattering angles of the X-rays coming out of the substance. X-rays can be thought of as electromagnetic waves, in which crystals are a regular series of atoms. Part of the X-ray beam is transmitted, part is absorbed by the sample, part is refracted and scattered, and part is scattered when it meets these atomic planes. The scatters in a regular pattern creates a regular arrangement of spherical waves. These waves

are destructive interventions, for the most part, rejecting each other, but they also constructively connect in a few selected directions, as indicated by Bragg's law:

$$2d\sin\theta = n\lambda$$

where n is the scattering order, λ is the wavelength of incoming X-ray, d is the distance (d-pause) between consecutive atomic planes, and θ is the X-ray beam angle beam. The diffracted x-rays found, processed, and counted are then analyzed. Due to the random orientation of the powder material, scanning the sample at 2θ angles should reveal all possible directions for lattice dispersion. X-radiation is detected by a detector, which is then processed by a microprocessor or electronically to convert a signal into a count rate. Because each mineral has a separate space separator (d-spacing) known as "fingerprints", it allows the material to be detected by converting the peaks of scattering into d-spacing. This allows the "fingerprint" element to be identified by comparison with conventional reference patterns and measurements.

Experimental conditions for sample analysis with XRD

X-ray diffraction patterns (XRD) of all synthesized powder samples were recorded using a Rigaku (Ultima IV) diffractometer equipped with CuK_α (= 1.540598 Å) radiation at 40 kV and 30 mA. XRD patterns were taken at a scan speed of 2° per minute in a continuous scan mode in the 2θ range of 5–80°. X-rays were exposed for 40 min of each sample. For some selected samples, Bruker D8 diffractometer (CuK_α radiation) was used to collect X-ray powder diffraction data. The measurement was carried out at room temperature in a range between 10° and 120° 2θ with a step size of 0.02° and a data collection time 25 s/step. The Rietveld program 'Diffrac Plus Topas-4.2′ (Bruker AXS, Karlsruhe, Germany) was used to refine the structures. Some samples were refined using Rietveld program profex [45].

1. 5.2 FT-IR and Far-IR spectroscopy

FTIR spectroscopic technique was employed to expose the feature of bonding in the prepared samples. IR spectroscopy can be divided into three regions: the near infrared (NIR, 4000-25000 cm^{-1}), the mid-infrared (400-4000 cm^{-1}) and the far infrared (10-400 cm^{-1}). With the development of FTIR (Fourier-transform) spectrometers, sophisticated instruments cover full areas by interchange of source, beam splitter, detector and sample cell. Mid-IR radiation can be produced by heating an inert solid e.g., silicon carbide at a temperature of 1,000 - 1,800°C. In the Far-IR region, a mercury arc lamp used

as a source. The energy supplied in the sample is processed by an interferometer in FT-IR. An interferometer comprises a beam splitter and two mirrors (a stationary mirror and a moving mirror). The beam splitter of mid-IR, which is a semi-reflective device, is formed by depositing a skinny film of germanium on a flat potassium bromide (KBr) substrate, which allows incoming radiation to pass through it but divides it into two perpendicular rays, one unchanged, the opposite 90° angles. The beam is located at 90°, goes to a fixed or stationary mirror and returns to the beam splitter again. The unreflected beam returns to the beam splitter through a moving mirror. The difference in optical paths between the two beams causes constructive and destructive interference when they are reconnected after being reflected from two mirrors. The optical path difference is made by changing the position relative to the moving mirror and stationary mirror. The combination of these interventions is called interferogram, which contains all the radiation emanating from the source. Generally, the beam splitters of Far-IR based on polymer films which cover a limited wavelength range. Synthesized IR rays pass through the sample and at the same time absorb the entire wavelength (frequency) commonly found in its infrared spectrum. The converted interferogram signal that reaches the detector contains information about the amount of energy absorbed by each wavelength (frequency). To create a comparison level, the computer compares the updated interferogram to the reference laser beam. The final interferogram contains all the information on a one-time domain signal (intensity vs. time) for the entire IR region. The interferogram is converted to a common domain spectrum (intensity vs. frequency) using Fourier transform [46], a mathematical process to extract isolated frequencies which absorbed and to recreate and plot a simple infrared spectrum.

Experimental conditions for sample analysis with FT-IR

KBr pellets were prepared using a weight ratio of ~ 0.01 for sample to KBr and FT-IR spectra were recorded in the mid-IR region (4000-400 cm^{-1}) by Shimadzu spectrophotometer (IR Prestige-21). Bruker Vertex 80v FT-IR spectrometer under vacuum was also used for some selected samples. Avoid the presence moisture both powdered samples and KBr were heated in an oven before preparing the pellets. The background was done with a pure KBr pellet to avoid the contribution of infrared-activated atmospheric gas, carbon dioxide and water vapor to the sample spectrum. Background and sample spectra were obtained from 30 scans with a nominal resolution of 1 cm^{-1}. The spectra were recorded in the absorption unit, (log (I/I_o), where I_o and I are the intensities transmitted by

the reference and the reference with the sample, respectively. Absorption spectra below 400 cm^{-1} (Far-IR range), polyethylene was used instead of KBr as a reference material, and both the spectra were merged using overlapping range.

1.5.3 Scanning electron microscopy and energy dispersive X-ray spectroscopy, SEM/EDX

The scanning electron microscope (SEM) is basically a high magnification microscope that uses a focused scanned electron beam to create a sample image, both top-down and cross-section depending on the sample preparation required. SEM uses an electron beam to image samples through a resolution down to the nanometer scale. In the electron source, electrons are emitted from a filament and collimated into a beam. A set of lenses in the electron column then focuses the beam on the sample surface. The advantage of SEM over a traditional optical microscope is that it has higher field depth and resolution, making it possible to focus on fine particles and to study closely spaced features. External morphology (texture), crystal formation, and adaptation of the elements that make up the pattern is one of the signals that provides information about the pattern. In conventional SEM techniques, spatial resolution of 50 to 100 nm is used for amplification of 20 to 30,000 times. SEM is usually applicable for conductive and semi-conductive materials.

SEM consists of an electron gun, electronically controlled lens and apertures, X-ray detector and a sample chamber. The sample is placed on the sample stage inside the sample chamber, which is vacuumed before applying the electron beam. The electron gun located at the top of the column generates a beam of electrons, which is guided down the column using gun alignment control. The beam is condensed by a pair of condensing lenses and focused on the sample using an objective lens. A magnetic field is created by energizing the scan coils to deflect the electron beam back and forth in a controlled pattern. Once the beam touches the surface of the sample, it produces secondary electrons. These induced secondary electrons are collected by an appropriate detector and converted into a voltage signal. The different voltages produced by the scan coil that make up the pattern on the surface of the sample and the voltage signal detected from the sample are applied to the cathode ray tube (CRT), which creates the image on the screen. The quality of the image depends on the number of secondary electrons generated, which depends on the strength of the electron beam generated by the gun. The voltage and current parameters of the gun are adjusted to get a good resolution image.

EDX was used for qualitative analysis of the chemical composition of some selected samples, and it is a non-destructive analytical technique. The basic and sample treatment conditions of this characterization technique are described in the following sections. It depends on some sources of X-ray excitation and the investigation of the interaction of a sample. When the high-energy ray of charged particles is focused on the studied sample, it can excite an inner shell electron of the sample, ejecting it out of the shell formed a hole, where the electron was.

An electron from the high energy level fills the hole, and the energy difference between the two levels is expressed in the form of X-rays. The number and energy of X-rays emitted from the sample can be measured by an energy scattering spectrometer. Since the X-ray energy emitted differs in the energy between the two shells and the properties of the atomic structure of the material from which they are emitted, this allows the composition of the sample material to be measured.

Experimental conditions for sample analysis with SEM/EDX

SEM micrographs were recorded using JEOL analytical scanning electron microscope (model JSM-6490LA). The acceleration voltage of the electron gun was 20 kV with probe current 1.0 nA. The samples were placed in a carbon stab and platinum sputtering was done before recording the micrographs in each case to create a thin conducting film on the non-conducting surface of the sample.

The stoichiometry of some calcined samples was examined in the range of 0 – 20 KeV with a JOEL JSM 6490 LA scanning electron microscopy equipped with an EDX detector (EDS, S-NP5194001070107, JEOL, Japan). The acceleration voltage of the electron gun was 20 KV. An Energy Dispersive X-ray Spectrometer (EDAX Team, EDAX, USA) was used to calculate the elemental composition of some selected prepared samples.

1.5.4 Raman spectroscopy

Raman spectroscopy is a molecular spectroscopic technique that uses light to relate to matter in order to understand the structure and features of matter. Raman spectroscopy describes intra- and inter-molecular vibration, although rotational and other low-frequency modes may also be observed. Raman spectroscopy provides a structural fingerprint with the detection of Raman scattered in a sample, where molecules can be identified. When light interacts with molecules in electricity, liquids or solids, most photons disperse with the same wavelength. This is known as Rayleigh scattering. A few of these photons,

approximately 1 in 10 million photons, will be dispersed at a different wavelength than the incident photon. This is an inelastic scattering process with a transfer of energy between the molecule and scattered photon. This scattering phenomenon is known as Raman effect, named after Sir C.V. Raman discovered this in 1930. Raman gives the information to compile a vibrating signature of a molecule, providing insight into how it is assembled, and how it interacts with other molecules around it. The sample is irradiated with a laser and some scattered light is analyzed with a spectrograph (FT technology), then the Raman spectrum obtained with the characteristics signals or bands of the material being investigated.

The standard Raman instrument comprises three main parts. The instrument must have an illumination system, which is usually built with one or more laser. The main limitation of the illumination system is that the incident light frequency must not be absorbed by the sample or solvent. The next component is the sample illuminating system, to determine the phase of material to be investigated. The last main part is Raman system spectrometer. This is usually set at 90° away from the incident light and may include a series of filters or monochromator. The macro-Raman spectrometer has spatial resolution from 100 micrometers to one millimeter, while micro-Raman spectrometer uses a microscope to increase its spatial resolution.

Experiment conditions for the sample analysis with Raman

Micro-Raman spectra were recorded at the Institute of Mineralogy, Leibniz University of Hanover, Germany using a SENERRA Raman spectrometer fitted with a microscope in the range of 200-700 cm^{-1}. The spectra were collected using a compressed pellet with a diameter of 5 mm. Laser radiation (λ = 532 nm) was used as a source of excitation at 5 mW. The spectrum was recorded for 10 seconds of integration time and 10 accumulations using a 50× magnification objective and a 125 pinhole.

Chapter Two

Bismuth Metallates

2.1 Introduction

Bismuth(III) oxide, Bi_2O_3, is the most technologically important compound of bismuth. It is found that both the preparative method and experimental conditions strongly influence the crystallinity and the structure of Bi_2O_3. Specifically, four crystalline phases of bismuth oxide with an additional three distinct nonstoichiometric phases are known. The crystalline phases are monoclinic α-Bi_2O_3, tetragonal β-Bi_2O_3, body centered cubic γ-Bi_2O_3, face centered cubic δ-Bi_2O_3 [47, 48] Bismuth oxide, with many other metal oxides, forms solid solutions. The structures and properties of these doped systems depend on the type of dopant, the dopant concentration, and the thermal history of the sample. Due to the presence of variable oxidation states, high coordination ability, polarizability and the stereochemical nature of the lone pair of bismuth, these compounds have versatile applications. Bismuth oxide based materials have many distinctive properties, like energy band gap, refractive index, dielectric permittivity, and photoconductivity. Due to these properties, these compounds are of vital importance for modern solid-state technology such as optical coatings, photovoltaic cells, micro-wave integrated circuits, etc. [47].

Bismuth metallates, $Bi_2M_4O_9$ (M = Al^{3+}, Ga^{3+}, Fe^{3+}) attracts researchers for many potential applications, like oxygen-ion conductors or mixed ionic-electronic conductors. The possibility of these bismuth metallates as strong candidates for use as electrolytes of solid fuel cells has been discussed in the literature due to their favorable oxygen conductivity at high temperatures with good mechanical strength [33, 49]. The compound's composition can be defined as $Bi_2Al_4O_9$, $Bi_2Ga_4O_9$, and $Bi_2Fe_4O_9$ in the systems Bi_2O_3-Al_2O_3, Bi_2O_3-Ga_2O_3, and Bi_2O_3-Fe_2O_3 [32, 50, 51].

2.1.1 Crystal structure of bismuth metallate, $Bi_2M_4O_9$

Bi-metallates with compositions $Bi_2M_4O_9$ (M = Al, Fe, Ga, etc.) are known as members of the family of mullite type structure [52, 53]. Mullite is a mineral, with the general composition $Al_2(Al_{2+x}Si_{2-2x})O_{10-x}$ [52]. The end member of the system is SiO_2-rich sillimanite with x = 0. The backbone of the structure of sillimanite (space group *Pbam*) and mullite (space group *Pbam*) are edge-shared AlO_6 octahedra (M sites) formed into chains which are parallel to the crystallographic c-axis. In sillimanite, the octahedral chains are joined by tetrahedral T_2O_5 dicluster groups (T = Al^{3+}, Si^{4+}) to form double chains with an ordered distribution of Al and Si atoms (Figs. 2.1. (a) and (b)) and in mullite, the Si^{4+} part is substituted by Al^{3+} (Figs. 2.1. (c) and (d)). Due to the replacement of Si^{4+} with Al^{3+},

excess negative charge is produced in mullite, which is compensated by the removal of oxygen atoms, bridging two adjacent tetrahedral. As a result, the two tetrahedral cations that were initially linked to the O(C) site are displaced to a new position, and O(C) becomes threefold coordinated, forming T_3O groups (triclusters) and that are preferably occupied by Al [52, 54 and 55].

Along with true mullites, structurally correlated mullite-type materials exist [56]. Mullite-type materials are categorized in a subgroup of having space group *P4/mbm* and should have characteristic orthogonal edge-shared MO_6 octahedra. The isostructural $Bi_2M_4O_9$ (M = Al^{3+}, Ga^{3+} and Fe^{3+}) belong to mullite-type crystal structure family with orthorhombic phases and the space group is *Pbam* [57]. The crystal structure is built by typical edge-shared MO_6 octahedral chains along the c-axis which are linked by corner-shared M_2O_7 double tetrahedral units [57-59]. The octahedral chains are also connected with BiO_6 polyhedra, which are highly asymmetric. Half of the octahedral chains are rotated clockwise along [110] and the other half counter-clockwise. The M_2O_7 double tetrahedral units are organized in *ab* planes and alternate with BiO_6 planes along the *c*-axis. Bi-atoms are situated in channels between the polyhedra and show stereochemical activity of the nonbonding valence electrons pair, Bi $6s^2$ lone electron pair, pointing to the vacant 0,0,0 site [60]. Due to this orientation, the central oxygen atoms of the M_2O_7 dimers alternate with vacant sites [57]. For $Bi_2Ga_4O_9$, $Bi_2Fe_4O_9$ and $Bi_2Al_4O_9$, the oxygen lone electron pairs, denotes as O_4, linked by the di-ortho groups, exhibit a large and extremely anisotropic atomic displacement ellipsoid. This can be described by the static or dynamic disorder of these oxygen positions [57, 60-62] $Bi_2M_4O_9$ exhibits structural stability for the Bi^{3+} lone electron pair. Strong anharmonicity is due to Bi^{3+} cations forming polar covalent bonds by sharing oxygen p-electrons and their s-electrons shells deformed by lattice vibration [63].

a)

b)

c)

d)

e)

f)
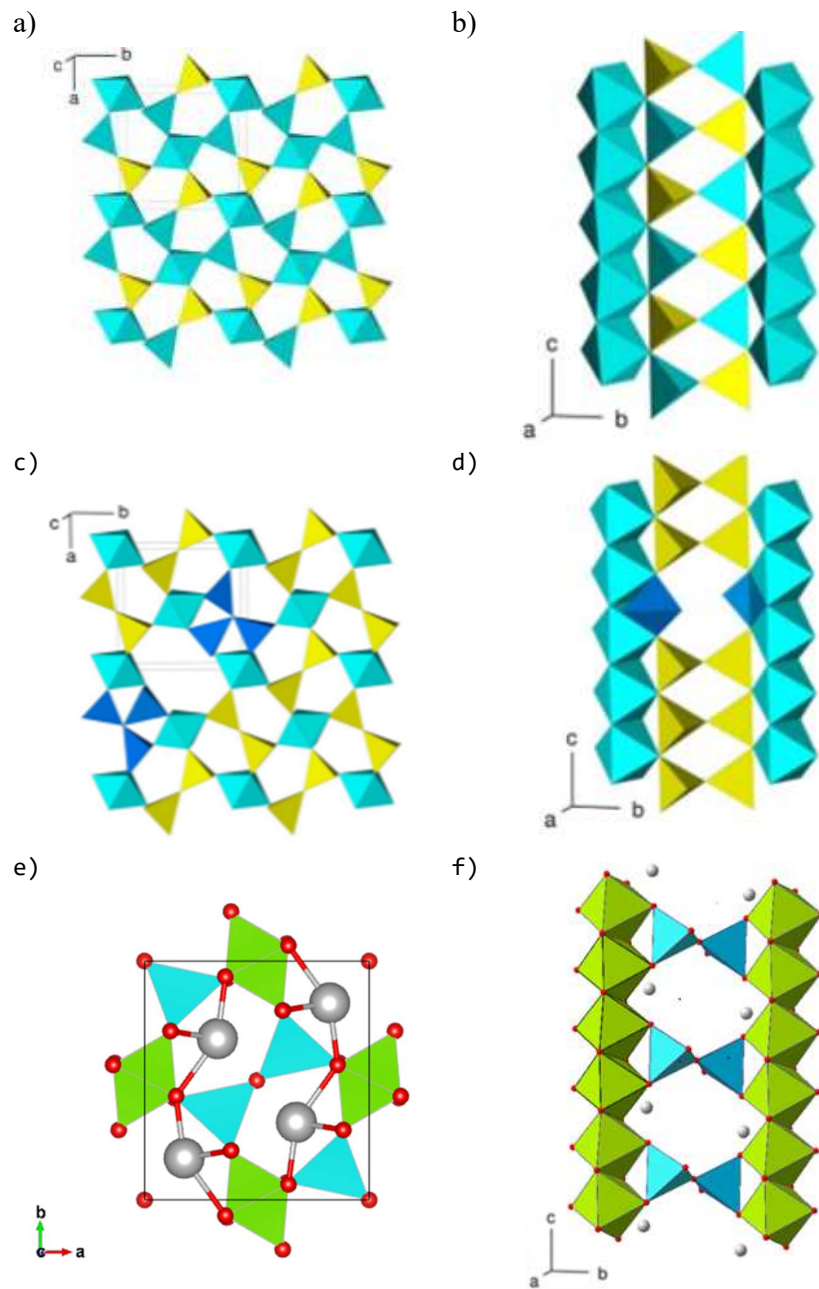
Fig. 2.1 Crystal structure of sillimanite (a, b), mullite (c, d) and $Bi_2M_4O_9$ Projection to the c-axis (a, c, e) and parallel to the a-axis (b, d, f) are shown.

2.1.2 Properties of bismuth metallates and mixed metal bismuth metallates

In bismuth based mullite-type metal oxides, two non-equivalent sites of M^{3+} ions (Al^{3+}, Fe^{3+}, Ga^{3+}) can receive transition and main group metal ions and many material properties depend on the distribution of different M^{3+} ions [64]. A number of these materials show significant ionic conductivity, which is used as oxygen sensors [19]. Some of these materials show high remissibility in the infrared region and can be used as high energy scintillator materials [64, 65]. Lone electron pair of Bi^{3+} in respect to structure also control many properties.

The mechanical properties of $Bi_2M_4O_9$ are directly controlled by its crystal structure. Strongly bonded octahedral chains running parallel to the crystallographic c-axis are responsible for the stiffness of the phases. Little anisotropy is observed for perpendicular octahedral chains [66]. The octahedral chains of $Bi_2M_4O_9$ are cross-linked by tetrahedral dimers and Bi-O polyhedral. The softer character of $Bi_2M_4O_9$ in comparison to mullite, sillimanite and alusite can be explained by moderately weak inter-octahedral bonding. The electrical conductivities of the mullite type phases $Bi_2M_4O_9$ ($M = Al^{3+}$, Ga^{3+}, Fe^{3+}) and their derivatives are medium (for $Bi_2Al_4O_9$, $\sigma \approx 1$ Sm^{-1} at 873°C) [66]. Substitution of Bi^{3+} by M^{3+} cations disturb the electrical neutrality and therefore additional oxygen vacancies are formed, which increases ion conductivity. It has been observed that by doping divalent cations (e.g. Ca^{2+}, Sr^{2+}), conductivity improves [20, 66 and 67] and is successfully used for traditional superconductor $Bi_2Sr_2CaCu_2O_8$ as membrane materials for oxygen separation. This is possible due to its mixed electronic and ionic conductivity, which originates from its unique crystal structure by two separate conducting routes. Because of their high emission in the red color region at 27°C, $Bi_2Al_4O_9$ and $Bi_2Ga_4O_9$ are suitable for scintillation detectors, particularly for high energy electron beams described the electrochemical and photocatalytic performances of $Bi_2Ga_4O_9$ nanoplates [66, 68]. Brixner *et al.* [69-72] observed green-yellow and red emission bands in $Bi_2Al_4O_9$ and $Bi_2Ga_4O_9$.

Luminescence at room temperature is rare in Bi-compunds. At room temperature, $Bi_2Al_4O_9$ exhibits efficient green luminescence with a broad emission band at 490 nm and a broad excitation band at 285 nm [72, 73]. The Cr^{3+} ion has an effect on the luminescence behaviour of $Bi_2Al_4O_9$ [65]. $Bi_2Ga_4O_9$ shows similar luminescence behaviour as $Bi_2Al_4O_9$ and an emmission band ranging from 450 to 750 nm. The red luminescence in $Bi_2Al_4O_9$ and $Bi_2Ga_4O_9$ is due to the structutal deffect [74].

Doping of various transition metal ions in mullite system can be performed to tailor the physical properties of the parent compound. Several attempts have been made to improve the electrical and magnetic properties of $Bi_2M_4O_9$ by incorporation of Sr^{2+}, Ca^{2+}, and Cr^{3+} into $Bi_2Al_4O_9$ (M = Al and Fe) and $Bi_2Fe_4O_9$ [66]. Zha *et al.* and Daneshmand *et al.* prepared $Bi_{2-2x}Sr_xAl_4O_{9-\delta}$ and $Bi_{2-2x}Sr_xFe_4O_9$ respectively with improved electrical properties [20, 75]. Gesting *et al.* also synthesized partially Sr^{2+} substituted $Bi_2Al_4O_9$ [76]. Daneshmand *et al.* synthesized $Bi_2Cr_xAl_{4-x}O_9$ and observed a limitting value for Cr droping in the range of $1.2 \leq x \leq 1.4$. Qiu *et al.* reported on the synthessis of $Bi_2Fe_{4(1-x)}Cr_{4x}O_9$ and observed enhanced magnetic and ferroelectric properties due to Cr doping [77]. These cations mostly occupy the octahedral site, substituting Al^{3+}/Fe^{3+}, though a small amount enters the tetrahedral site. The incorporation of these cations depends on the oxidation states and ionic radii of these cations that best fit with Al^{3+} and Fe^{3+}. But there is no research on the Cr in the Bi-gallate system. There have been a few reports of Cr in $Bi_2Al_4O_9$ and $Bi_2Fe_4O_9$, but no reports of Cr doped $Bi_2M_4O_9$ systems with both Al and Fe. So an attemp was made to synthesize two new series of solid solutions of Cr doped Bi-gallate and Cr doped Bi-mixed metallate where both Al and Fe are present. Other known crystalline structures of Bi-metallates, such as $Bi_2Ga_4O_9$, $Bi_2Al_4O_9$, $Bi_2Fe_4O_9$, and Cr doped $Bi_2M_4O_9$ (M = Al, Fe), were redefined and confirmed.

2.2 Experimental of bismuth metallates

2.2.1 Synthesis of bismuth metallates series

Attempts were taken to synthesize following solid solution series of bismuth metallates in the present work listed in Table 2.1.

Table 2.1 Prepared bismuth metallates series in present work.

No.	Solid solution series	Nominal gross composition	Status
i.	$Bi_2Cr_xGa_{4-x}O_9$	x = 0.0, 0.2, 0.4, 0.6, 0.8, 1.0, 1.2, 1.4, 1.6, 1.8 and 2.0	newly reported
ii.	$Bi_2Fe_xAl_{4-x}O_9$	x = 0.0, 1.0, 2.0, 3.0 and 4.0	Reproduce [33, 66]
iii.	$Bi_2Fe_3(Cr_xAl_{1-x})O_9$	x = 0.0, 0.2, 0.4, 0.5 and 0.6	newly reported
iv.	$Bi_2Fe_2(Cr_xAl_{1-x})_2O_9$	x = 0.0, 0.2, 0.4, 0.5 and 0.6	newly reported
v.	$Bi_2Fe(Cr_xAl_{1-x})_3O_9$	x = 0.0, 0.2, 0.4, 0.5 and 0.6	newly reported

The series of materials were prepared using the gel combustion method, which is a modified solid solution combustion method and is used for the preparation of high quality crystalline mixed metal oxides.

This method of synthesis consists of two steps; the first step is gelation, and the second step is combustion. Appropriate amount of hydrated metal nitrates (below equations under series: i-v were used) and glycerin were used for the synthesis of bismuth metallates solid solution series.

The mixture was stirred thoroughly to achieve complete homogeneity (homogeneous situation/dissolution) of all the solid reagents. The synthesized mixture was then heated to about 100°C on a hot plate to form a gel. The gel was then heated in a burner until the release of the brown gases (NO_x), which confirms the decomposition of the metal nitrate. The release of the brown gases led to the formation of the fluffy mass. Later, the fluffy mass was calcined at temperature varying from 700 to 900°C for 24 hours.

Stoichiometry of the metal nitrates (oxidant) and fuel can be measured considering the total oxidizing and reducing valency of the oxidant and fuel, which is a numerical coefficient of stoichiometric balance. Then the equivalent ratio is equal to unity and the energy release is minimum.

The following scheme represents the reaction process for forming solid solution series.

i. series: $Bi_2Cr_xGa_{(4-x)}O_9$

$$2Bi(NO_3)_3.5H_2O + xCr(NO_3)_3.9H_2O + (4-x)Ga(NO_3)_3.9H_2O = Bi_2Cr_xGa_{(4-x)}O_9$$

ii. series: $Bi_2Fe_xAl_{4-x}O_9$
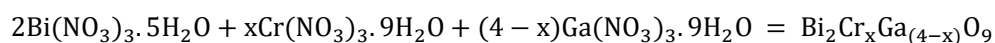
$$2Bi(NO_3)_3.5H_2O + xFe(NO_3)_3.9H_2O + (4-x)Al(NO_3)_3.9H_2O = Bi_2Fe_xAl_{(4-x)}O_9$$

iii. series: $Bi_2Fe(Cr_xAl_{(1-x)})_3O_9$
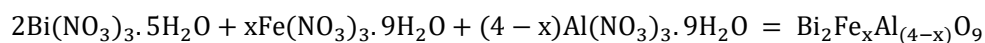
$$2Bi(NO_3)_3.5H_2O + Fe(NO_3)_3.9H_2O + 3(1-x)Al(NO_3)_3.9H_2O + 3xCr(NO_3)_3.9H_2O$$
$$= Bi_2Fe(Cr_xAl_{(1-x)})_3O_9$$
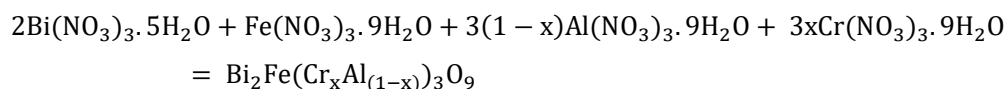
iv. series: $Bi_2Fe_2(Cr_xAl_{(1-x)})_2O_9$

$$2Bi(NO_3)_3.5H_2O + 2Fe(NO_3)_3.9H_2O + 2(1-x)Al(NO_3)_3.9H_2O + 2xCr(NO_3)_3.9H_2O$$
$$= Bi_2Fe_2(Cr_xAl_{(1-x)})_2O_9$$

v. series: $Bi_2Fe_3Cr_xAl_{(1-x)}O_9$
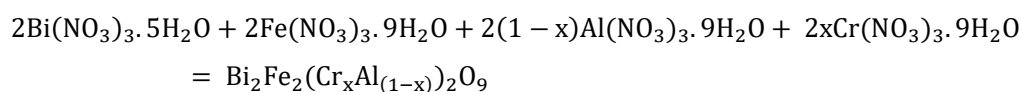
$$2Bi(NO_3)_3.5H_2O + 3Fe(NO_3)_3.9H_2O + (1-x)Al(NO_3)_3.9H_2O + xCr(NO_3)_3.9H_2O$$
$$= Bi_2Fe_3Cr_xAl_{(1-x)}O_9$$
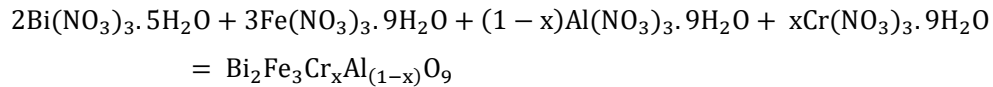
The sample preparation process is schematically shown in the following flow chart –

| Mixture of metal suitable nitrates with appropriate amounts |

⇩ Glycerin + heat at 100°C

| Gel |

⇩ Heat at 300°C

| Dry mass |

⇩ Calcined at 700-900°C

| Bismuth Metallates |
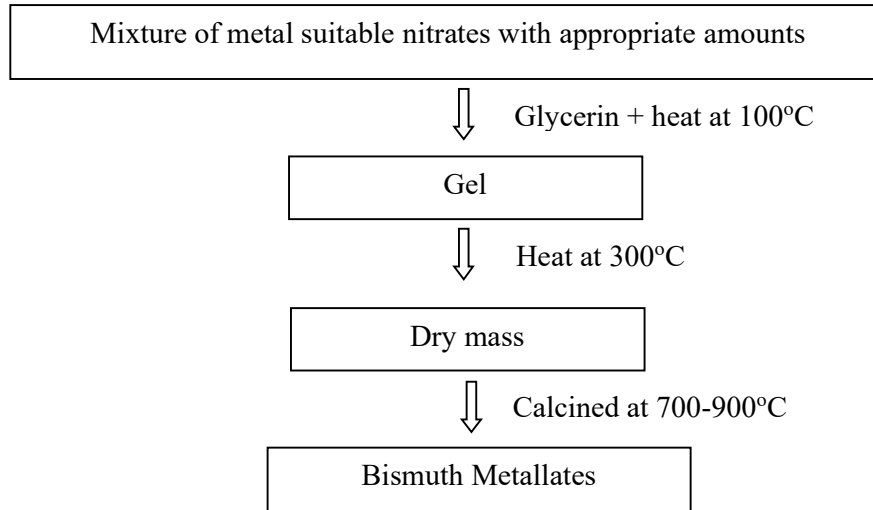
Fig. 2.2. Flowchart for preparation of bismuth metallates.

2.2.2 Characterization of bismuth metallates

The crystlline structure of the prepared sample was determind with an X-ray powder diffractmeter (Model- Rigaku Ultima IV, Japan) eqipped with CuK$_\alpha$ radiation. The 2θ range for collecting XRD patterns was 5 to 80° in a continuous scan mode. Scanning Electron Microscope (SEM) (Model JEOL JSM-6490LA, Japan) with an electron voltage of 20 KV was used to examine the morphology and size distribution of the prepared samples. In this method, sample were riding on a curved-shaped stage which is made of aluminum and the maintaining work distance is 10 mm. An Energy Dispersive X-ray Spectrometer (EDAX Team, EDAX, USA) was used to calculate the elemental composition of the prepared samples. A Fourirer Transform Infrared (FT-IR) spectometer (Moldel IR Prestige-21, Shimadju, Japan) was used for the molecular characterization of the prepared samples. Bruker Vertex 80v FTIR spectrometer under vacuum was also used for characterization $Bi_2Cr_xGa_{4-x}O_9$ solid solution series. In this method, the ground powdered samples were mixed with KBr (2 mg sample and 198 mg KBr) and pressed to prepare pelletes. Absorption spectra below 400 cm^{-1}, polyethylene was used instead of KBr as a reference material, and both the spectra were merged uging overlapping range.

Micro-Raman measurements were performed at the Institute of Mineraligy, Leibniz University of Hannover, Germany using a SENERRA Raman spectrometer fitted with a microscope in the range of 200-700 cm^{-1}. Laser radiation (λ = 532 nm) was used as a source of excitation at 5 mW. The spectrum was recorded for 10 seconds of integration time and 10 accumulations using a 50x magnification objective and a 125 pinhole.

2.3 Results and discussion of bismuth metallates

2.3.1 Results and discussion of Bi$_2$Cr$_x$Ga$_{4-x}$O$_9$ series

2.3.1.a X-ray diffraction and Rietveld refinement of Bi$_2$CrxGa$_{4-x}$O$_9$

The X-ray powder diffraction patterns of samples with a nominal composition of Bi$_2$Cr$_x$Ga$_{4-x}$O$_9$ (x = 0.0 - 2.0) are given in Fig. 2.3 and Fig. 2.4. The samples having nominal composition x = 0.0, 0.2, 0.4 and 0.6 are pure single phases and could be indexed as mullite type orthorhombic phase. The samples with nominal chromium content x = 0.8 - 2.0 show mainly mullite type phases and very low intense peaks of an additional phase (Fig. 2.5), which could not be indexed as a mullite type phase. The mullite type phase structure parameters were refined by the Rietveld refinement method. The Rietveld refinement was performed using the space group *Pbam* and the same initial setting of positional parameters given by Niizeki and Wachi [78].

There is excellent agreement between the XRD patterns calculated and measured as shown for the three samples (Bi$_2$Cr$_{0.4}$Ga$_{3.6}$O$_9$, Bi$_2$Cr$_{0.8}$Ga$_{3.2}$O$_9$, and Bi$_2$Cr$_{1.0}$Ga$_{3.0}$O$_9$) in Fig. 2.6. For nominal gross compositions x = 0.8 - 2.0, additional phase(s) were observed. However, Rietveld refinement can be done by considering only the mullite type phase, too. During refinement, chromium atoms are placed in the same crystallographic space as the gallium atom, considering their displacement parameters are the same. The occupancy of chromium in an octahedral coordinated position was measured as one minus gallium occupancy (occ(Cr) = 1 - occ(Ga)). It may be noted that the final refinements of the Rietveld were performed with a fixed occupation factor of Ga = 1.0 in the tetrahedral region. Opportunities to provide free Cr work in the octahedral and tetrahedral regions are also considered, but no improvement was observed. The structural parameters found from Rietveld refinement are listed in Table 2.2 and Table 2.3. The cell parameters are plotted as a function of nominal composition and compared with a similar system reported in the literature (Fig. 2.7) [32]. Debnath *et al.* reported that in the Cr doped Bi$_2$Al$_4$O$_9$ system, all cell parameters (*a*, *b* and *c*) increase according to the Cr content up to x = 1.2 and do not

continue to change significantly to increase further to x, which indicates the limiting value of Cr doping in the $Bi_2Al_4O_9$ system.

In the present work for Cr doped $Bi_2Ga_4O_9$, the lattice parameter *a* remains almost constant with increasing nominal Cr content. But in the case of *b* cell parameter, it decreases up to nominal composition 1.0 and then remain almost constant. Cell parameter *c* increases slightly up to nominal composition 0.6 and then it remains almost constant. Unit cell volume is found by multiplying *a*, *b*, *c* cell parameters and it remains almost constant. Therefore, a significant lattice distortion occurs at the bc plane (Figs. 2.7-2.9). Cr^{3+} has a crystal radius of 75.5 pm (0.755 Å) in six fold coordination, which is very close to the crystal radius of Ga^{3+} (0.76 Å) in six fold coordination. So, the doping did not have much effect on the unit cell volume.

The cation occupancy factors obtained from Rietveld refinement are shown (Fig. 2.8) as a function of nominal composition and compared with a similar system ($Bi_2Cr_xGa_{4-x}O_9$) reported earlier [32]. It has been reported that Ga equally replaces octahedral and tetrahedral in the crystal structure of $Bi_2Ga_4O_9$ [78] and ions such as Al^{3+} and Fe^{3+} do the same and form a strong solution like $Bi_2Al_xGa_{4-x}O_9$ [79], $Bi_2Fe_xGa_{4-x}O_9$ [80] and $Bi_2Al_xFe_{4-x}O_9$ [81]. However, Debnath *et al.* reported that Cr dopants prefer occupying the octahedral site of Ga^{3+} in this solid solution series, $Bi_2Cr_xGa_{4-x}O_9$. This fact is supported by the occupation factor found regarding Cr/Ga on octahedral sites (Fig. 2.8). In the solid solution $Bi_2Ga_xAl_{4-x}O_9$, some preferred Ga occupation in the octahedral site also found compared to the tetrahedral site.[79]. Here it is obtained that Cr can replace Ga only in octahedral sites, which was also reported for Cr-doped pure mullite ($3Al_2O_3.2SiO_2$) [82] and Cr-doped $Bi_2Al_4O_9$ systems. The occupancy in the octahedral position systematically increases for Cr up to x = 1.6 and remains almost constant for a further increase in x. Cr dopants favor occupying the octahedral site of Ga^{3+} in this solid solution series because of the appropriate crystal radii and strong ligand-free stabilization energy of Cr in six-fold coordination. Considering final formation x = 1.6, i.e., $Bi_2Cr_{1.6}Ga_{2.4}O_9$, approximately 13 wt% Cr_2O_3 can be incorporated into the mullite type bismuth gallate, very similar to the maximum amount of Cr doping in pure mullite ($3Al_2O_3.2SiO_2$), where approximately 12 wt % of Cr_2O_3 was reported [82].
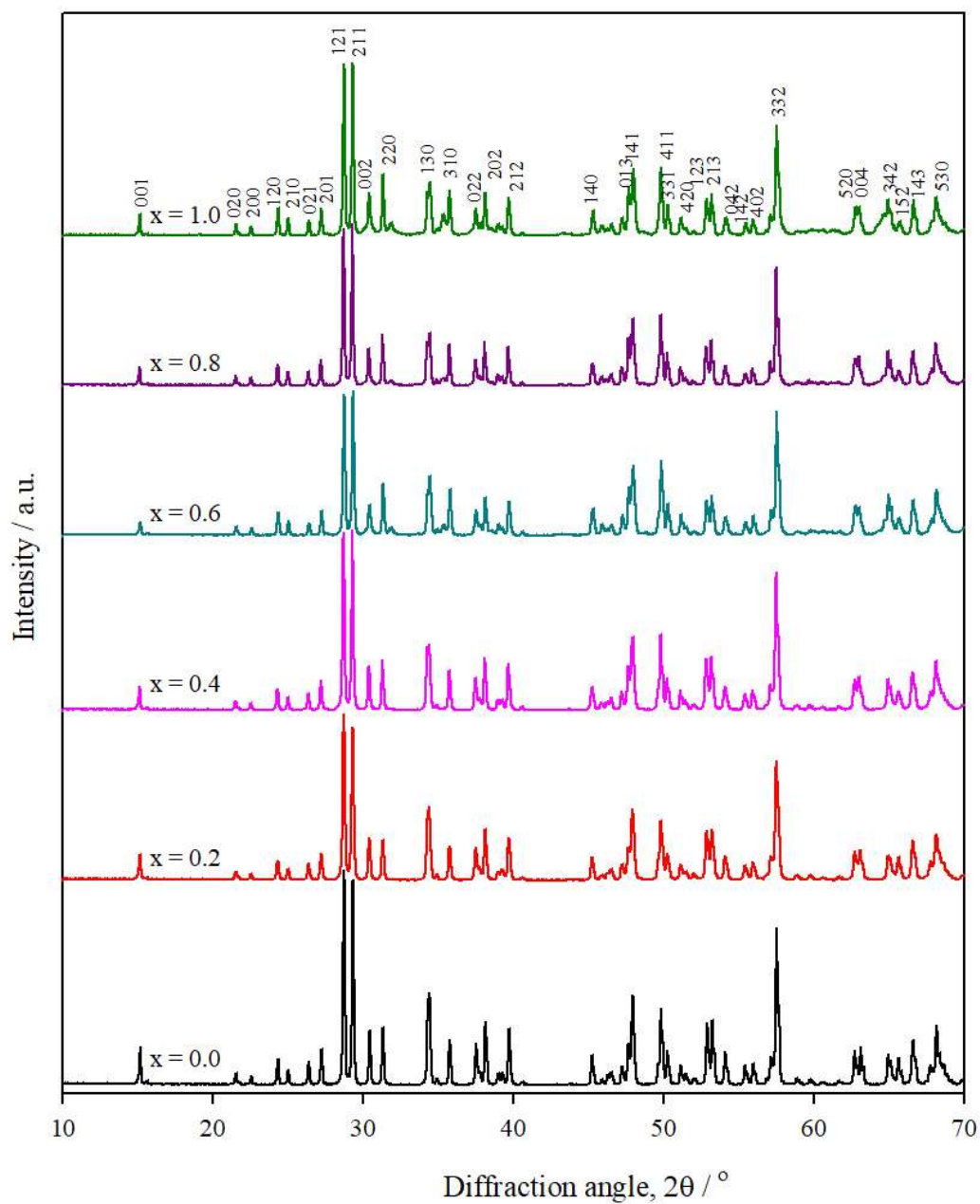
Fig. 2.3. The XRD pattern of $Bi_2Cr_xGa_{4-x}O_9$ at different nominal compositions (x = 0.0 - 1.0) at 800ºC. For clarity the diffraction patterns are plotted vertically. The figure shows the patterns forming the orthorhombic phase for all compositions.
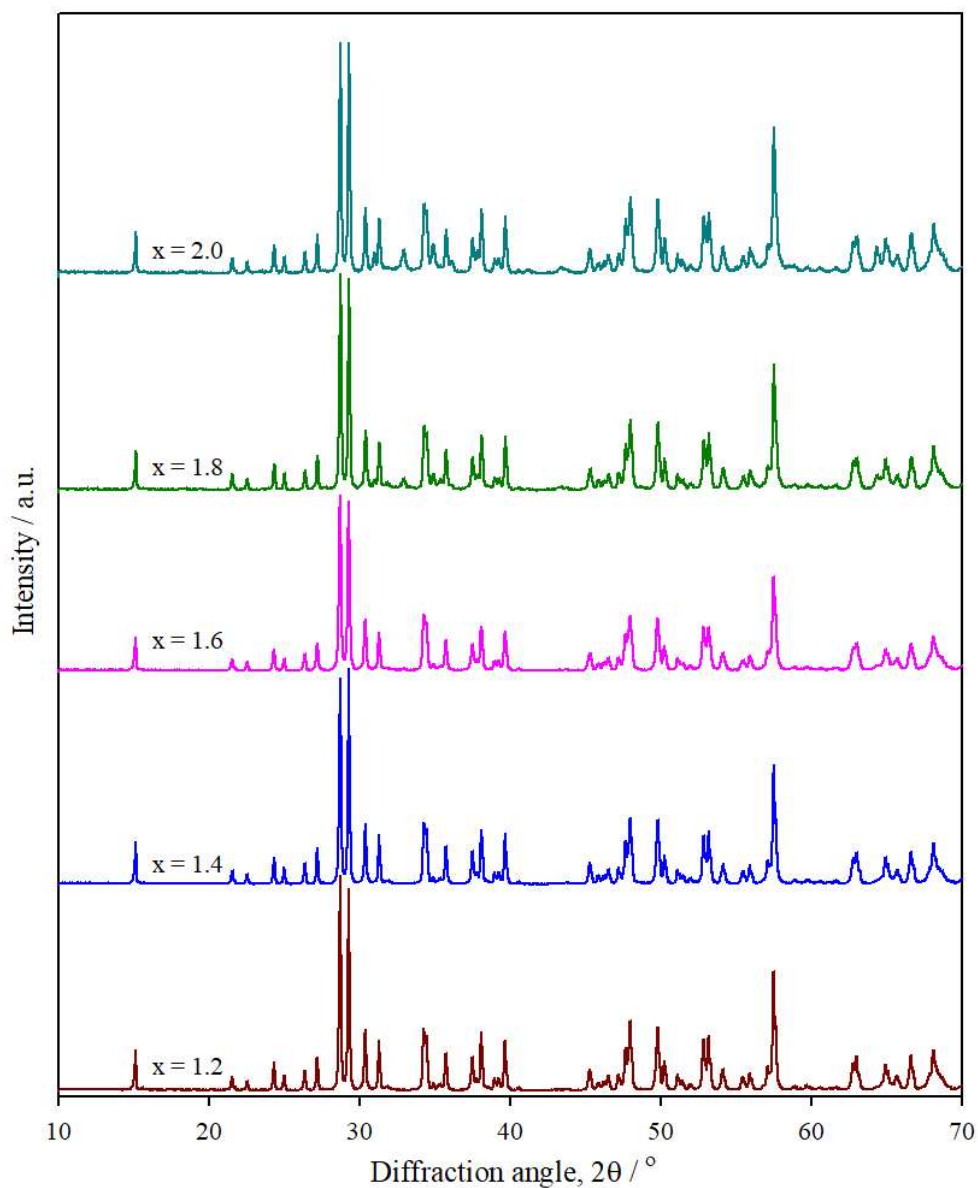
Fig. 2.4. The XRD pattern of $Bi_2Cr_xGa_{4-x}O_9$ at different nominal compositions (x = 1.2 - 2.0) at 800°C. For clarity the diffraction patterns are plotted vertically. The figure shows the patterns forming the orthorhombic phase for all compositions.
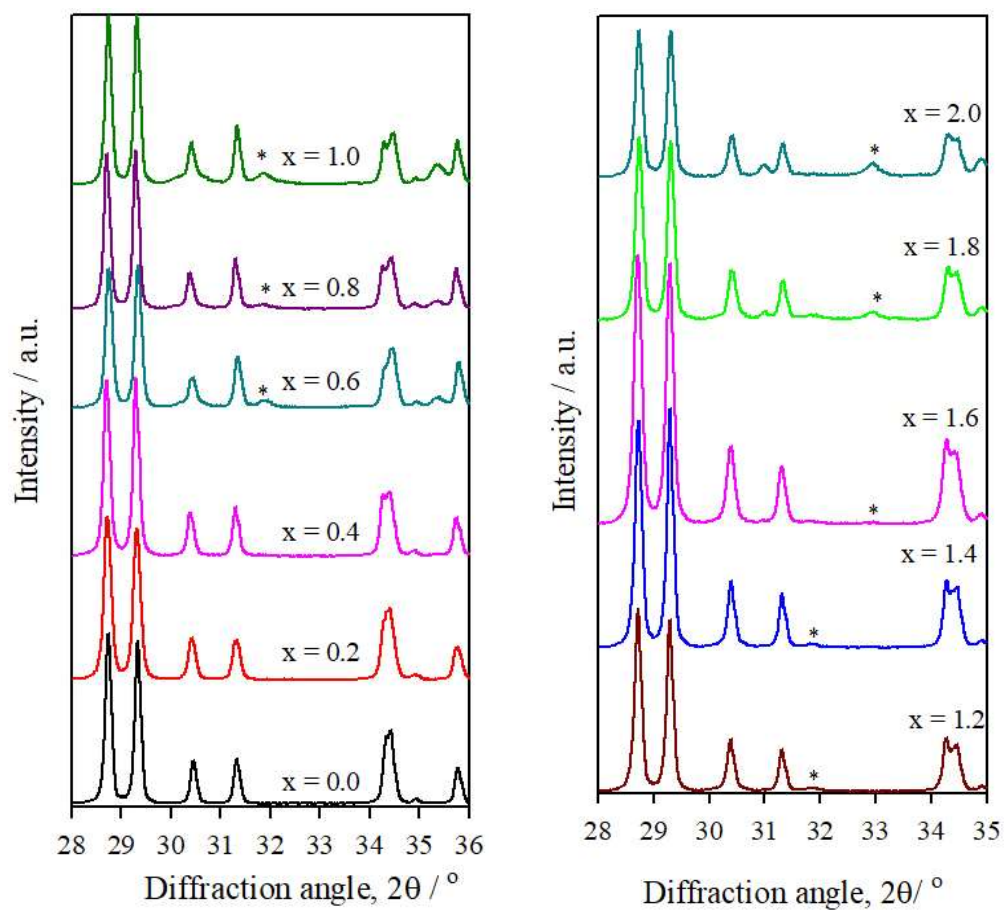
Fig. 2.5. The XRD pattern of $Bi_2Cr_xGa_{4-x}O_9$ (magnified) at different nominal compositions (a) x = 0.0 - 1.0 and (b) x = 1.2 - 2.0 at 800°C. At nominal composition x = 0.6, a small additional peak (*) was observed to shift to the higher angle region with increasing chromium concentration and all the diffraction peaks slightly shifted to the low angle region with chromium doping.
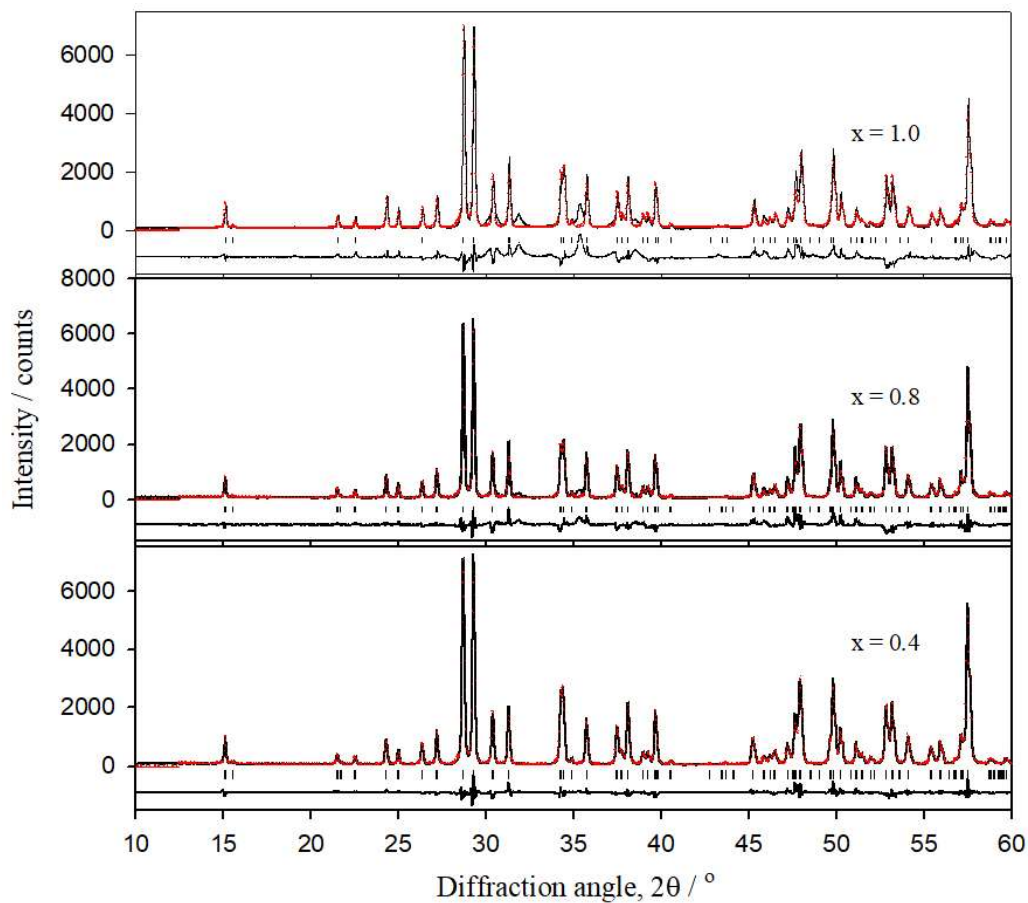
Fig. 2.6. Rietveld refinements fit three selected samples of the $Bi_2Cr_xGa_{4-x}O_9$ series. The black spectrum represents observed/measured spectrum, and the red spectrum represents calculated data. The black bars below the patterns are the expected reflections according to the symmetry of *Pbam*, and the curve below the bars represents the difference spectrum.

Table 2.2 Cell parameters of $Bi_2Cr_xGa_{4-x}O_9$ with different nominal compositions at 800°C.

Composition (x)	Cell parameters / pm			Cell volume (Å³)	Occupancy		Rwp	GOF
	a	*b*	*c*		Ga/Cr (oct)	Ga (tet)		
0.0	792.7470(73)	830.2909(74)	589.5259(49)	388.0323(59)	0.960(25)	0.040(25)	8.29	1.55
0.2	792.6948(83)	830.0640(85)	589.7521(61)	388.0495(70)	0.884(23)	0.116(23)	7.01	1.29
0.4	792.657(11)	829.957(11)	590.0705(77)	388.1906(88)	0.742(31)	0,258(31)	9.08	1.71
0.6	792.5650(28)	829.8970(28)	590.2490(18)	388.234(22)	0.839(86)	0.161(86)	21.34	3.96
0.8	792.7000(20)	829.4610(20)	590.1990(14)	388.0634(17)	0.611(66)	0.389(66)	17.68	3.14
1.0	792.7970(34)	829.0870(34)	590.088(24)	387.863(28)	0.530(97)	0.470(97)	24.38	4.63
1.2	792.8640(15)	829.0670(15)	590.0860(11)	387.886(13)	0.403(41)	0.597(41)	12.39	2.31
1.4	792.9060(15)	829.0220(16)	590.0210(12)	387.842(13)	0.375(40)	0.625(40)	11.96	2.25
1.6	792.9020(17)	829.144(18)	590.0410(13)	387.911(14)	0.270(37)	0.730(37)	10.67	1.97
1.8	792.9150(26)	828.9580(27)	589.8840(20)	387.726(22)	0.293(64)	0.707(64)	16.31	2.83
2.0	792.7620(33)	829.0380(34)	589.9230(25)	387.715(28)	0.299(79)	0.701(79)	18.66	3.12

Table 2.3 Details of the positional parameters of different atoms of the $Bi_2Cr_xGa_{4-x}O_9$ solid solution series were obtained from the Rietveld refinements X-ray data.

Atomic site	Coordinate	Nominal composition, $Bi_2Cr_xGa_{4-x}O_9$						
		0.0	0.2	0.4	0.6	0.8	1.0	1.2
Bi	X	0.3258	0.3260	0.3265(1)	0.3272(2)	0.3273(2)	0.3277(3)	0.3270(1)
Bi	Y	0.1713	0.1713	0.1709(1)	0.1712(3)	0.1708(2)	0.1708(42)	0.1708(1)
Bi	Z	0.0000	0.0000	0.0000	0.0000	0.0000	0.00000	0.0000
Ga/Cr (oct.)	X	0.5000	0.5000	0.5000	0.5000	0.5000	0.50000	0.5000
Ga/Cr (oct.)	Y	0.5000	0.5000	0.5000	0.5000	0.5000	0.50000	0.5000
Ga/Cr (oct.)	Z	0.2592(3)	0.2591(3)	0.2592(4)	0.2603(12)	0.2596(9)	0.2636(15)	0.2595(7)
Cr (tet.)	X	0.1481(2)	0.1479(2)	0.1479(2)	0.1501(77)	0.1497(6)	0.1512(9)	0.1474(3)
Cr (tet.)	Y	0.3377(3)	0.3376(2)	0.3377(3)	0.3363(9)	0.3360(7)	0.3351(12)	0.3378(5)
Cr (tet.)	Z	0.5000	0.5000	0.5000	0.5000	0.5000	0.5000	0.5000
O1	X	0.3508(14)	0.3508(12)	0.3515(17)	0.3808(47)	0.3625(38)	0.4001(52)	0.3548(25)
O1	Y	0.4296(12)	0.4330(11)	0.4334(15)	0.4398(48)	0.4355(35)	0.4400(58)	0.4328(22)
O1	Z	0.0000	0.0000	0.0000	0.00000	0.0000	0.0000	0.0000
O2	X	0.3685(13)	0.3685(11)	0.3727(15)	0.3950(42)	0.3799(34)	0.3820(56)	0.3634(21)
O2	Y	0.4071(11)	0.4073(9)	0.4081(13)	0.4144(38)	0.4095(30)	0.4092(49)	0.4045(18)
O2	Z	0.5000	0.5000	0.50000	0.5000	0.5000	0.5000	0.5000
O3	X	0.1329(7)	0.1319(6)	01344(9)	0.1442(28)	0.1391(21)	0.1472(37)	0.1319(13)
O3	Y	0.2060(7)	0.2053(7)	0.2044(9)	0.1990(28)	0.2042(21)	0.1987(36)	0.2028(14)
O3	Z	0.2445(11)	0.2428(10)	0.2439(13)	0.2478(33)	0.2473(44)	0.2473(44)	0.2423(19)
O4	X	0.0000	0.0000	0.0000	0.0000	0.0000	0.0000	0.0000
O4	Y	0.5000	0.5000	0.5000	0.5000	0.5000	0.5000	0.5000
O4	Z	0.5000	0.5000	0.5000	0.5000	0.5000	0.5000	0.5000
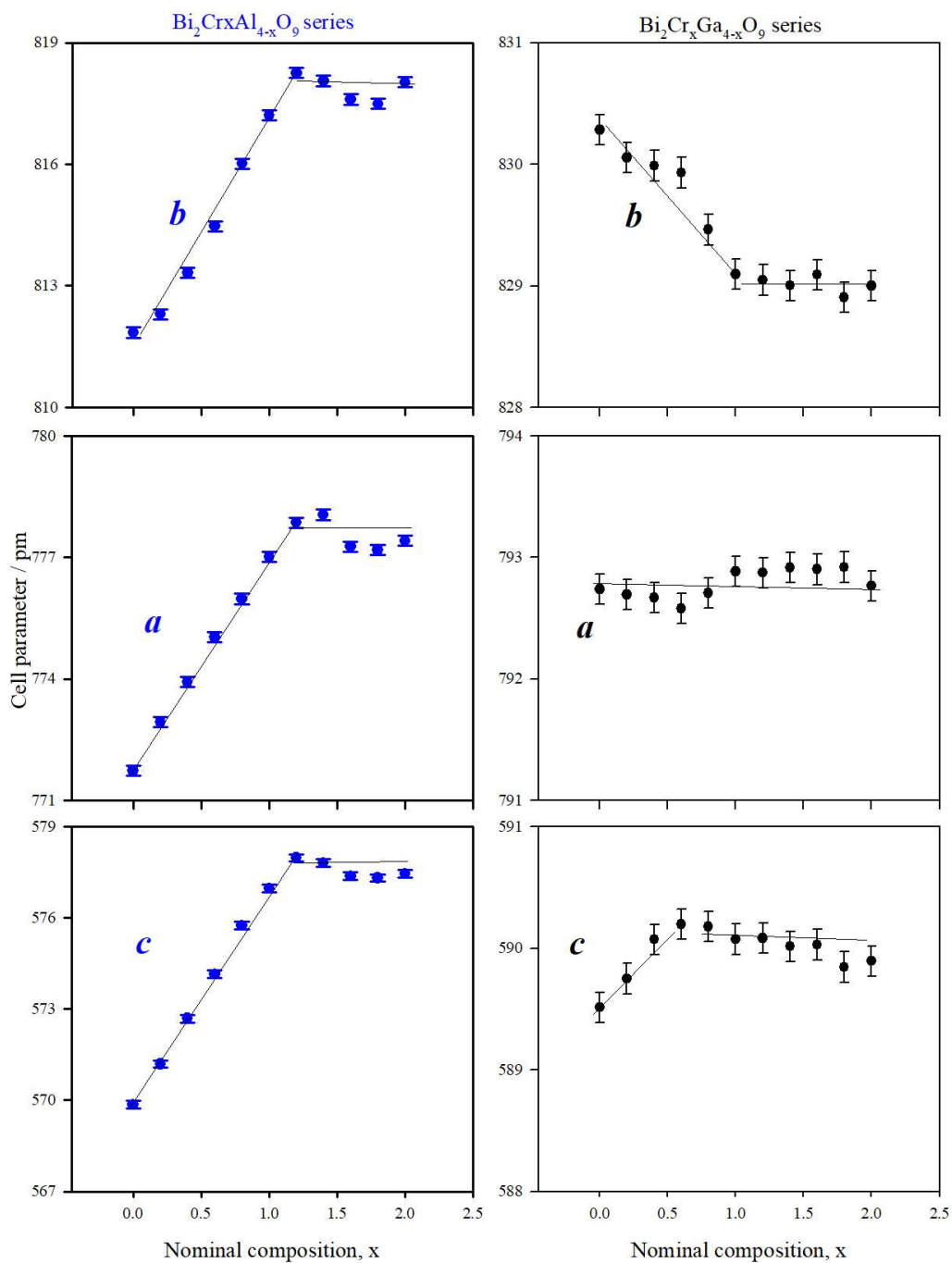
Fig. 2.7. The lattice parameters (*a, b, c*) of $Cr_xGa_{4-x}O_9$ and $Bi_2Cr_xAl_{4-x}O_9$ as a function of nominal composition, x.
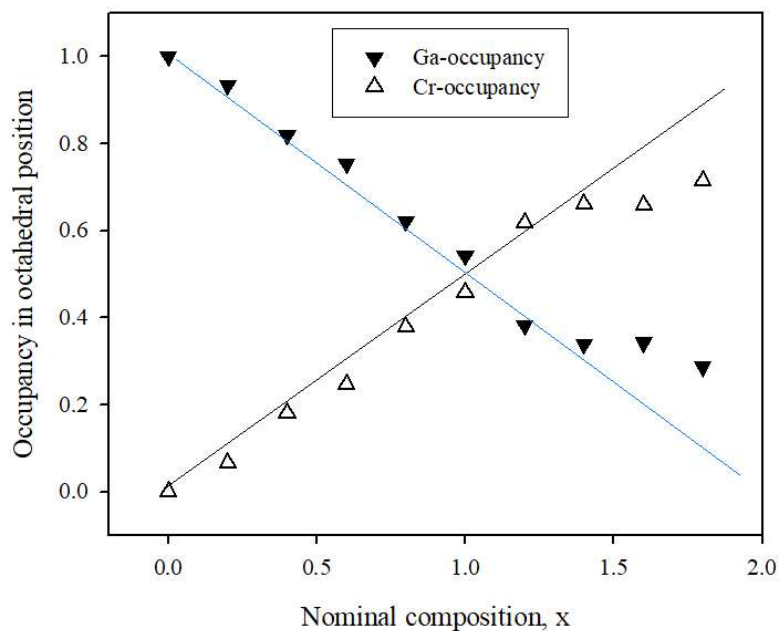
Fig. 2.8. Octahedral occupancies of Ga and Cr in $Bi_2Cr_xGa_{4-x}O_9$ series found from Rietveld refinement fit of XRD data.
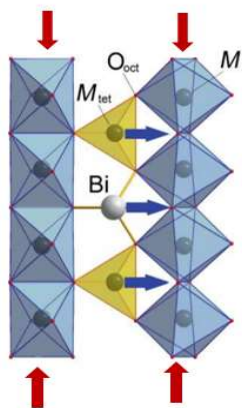
➢ The red verticle arrow indicates shrinkage of the octehedral chain pararllal to the *c*-axis.

➢ The blue horizontal line indicates associated stretching perpendicular to the octehedral chains.

Fig. 2.9. Crosslinking of octahedral chains in a projection parallel to the *c*-axis.

2.3.1.b FT-IR spectroscopic study of $Bi_2Cr_xGa_{4-x}O_9$ series

The FT-IR absorption spectra of the $Bi_2Cr_xGa_{4-x}O_9$ solid solution series are shown in Fig. 2.10 in the region 50-1000 cm^{-1}. Characteristics of four bands for the mullite type orthorhombic phase of $Bi_2M_4O_9$ (M = Al^{3+}, Ga^{3+}, Fe^{3+}) were observed, namely group-A, group-B, group-C, and group-D [32, 33 and 83]. Group A (800-900 cm^{-1}) can be assigned as Ga-O_c-Ga stretch in Ga_2O_7 dimer (O_3Ga-O_c-GaO_3); Group B (800-600 cm^{-1}) for Ga-O stretch, Ga-O-Ga bend at GaO_4 tetrahedra; Group C (600-400 cm^{-1}) O-Ga-O bend for GaO_4 tetrahedra, Ga-O-Ga bend for GaO_6 octahedra and Ga-O stretch at GaO_6 octahedra; Group D (below 400 cm^{-1}) for Bi-O vibration. The absorption peak of group-A due to the M–O_c–M stretching mode of vibration in O_3M–O_c–MO_3 dimer of MO_4 tetrahedra is a characteristic peak for the system $Bi_2M_4O_9$ system. If partial substitution of Cr for Ga in GaO_4 tetrahedra occurs, it will split this band due to the formation of two new bonds, Ga-O-Cr and Cr-O-Cr, as reported in a related system [32]. From Fig. 2.10, it is observed that there is no splitting of IR absorption peak group A, which indicates no tetrahedral substitution of Cr for Ga in GaO_4 tetrahedra occurs. In other words, the absence of any splitting of the absorption peak of band group-A reveals that Cr^{3+} substituted Ga^{3+} in GaO_6 octahedra. Tetrahedrally coordinated Cr^{3+} has two types of electronic configurations: high spin state and low spin state, whereas octahedrally coordinated Cr^{3+} has only one type electronic configuration. Due to weaker crystal field stabilization energy, the low spin state tetrahedrally coordinated Cr^{3+} is unstable at higher temperatures and stable only at low temperatures [32]. Thus, at higher temperatures, tetrahedrally coordinated Cr^{3+} is found in the high spin state, which is unstable. Therefore, the trivalent Cr eventually becomes highly stabilized in octahedral sites at high temperatures due to the strong ligand-free stabilization energy of Cr in six-fold coordination. Therefore, it can be concluded that Cr^{3+} substitutes Ga^{3+} in GaO_6 octahedra.

The shift in peak positions of the lowest energy vibrational mode (Bi–O-Bi) and Ga–O_c–Ga stretching mode are compared with the Cr doped $Bi_2Al_4O_9$ system and shown as a function of nominal compositions x in Fig. 2.11 and Fig. 2.12, respectively. The peak positions of Ga-O_c-Ga shifted slightly to lower vibrational energy up to nominal composition x = 1.0 and then remained constant for a further increase in nominal Cr content. However, it remains almost constant for similar Al-O_c-Al vibrational modes in the $Bi_2Cr_xGa_{4-x}O_9$ series [32]. The peak positions for the Bi-O-Bi bending mode systematically shift to higher wavenumbers up to nominal composition x = 1.0 and remain

constant for further increases in x, which, however, decrease for the Cr doped $Bi_2Al_4O_9$ system. It is also observed that the absorption peak at 470 cm^{-1} for Ga-O stretch at GaO_6 octahedra slightly shifted to higher wavenumber with increasing Cr concentration due to the decrease of octahedral Ga-O and Cr-O distance.
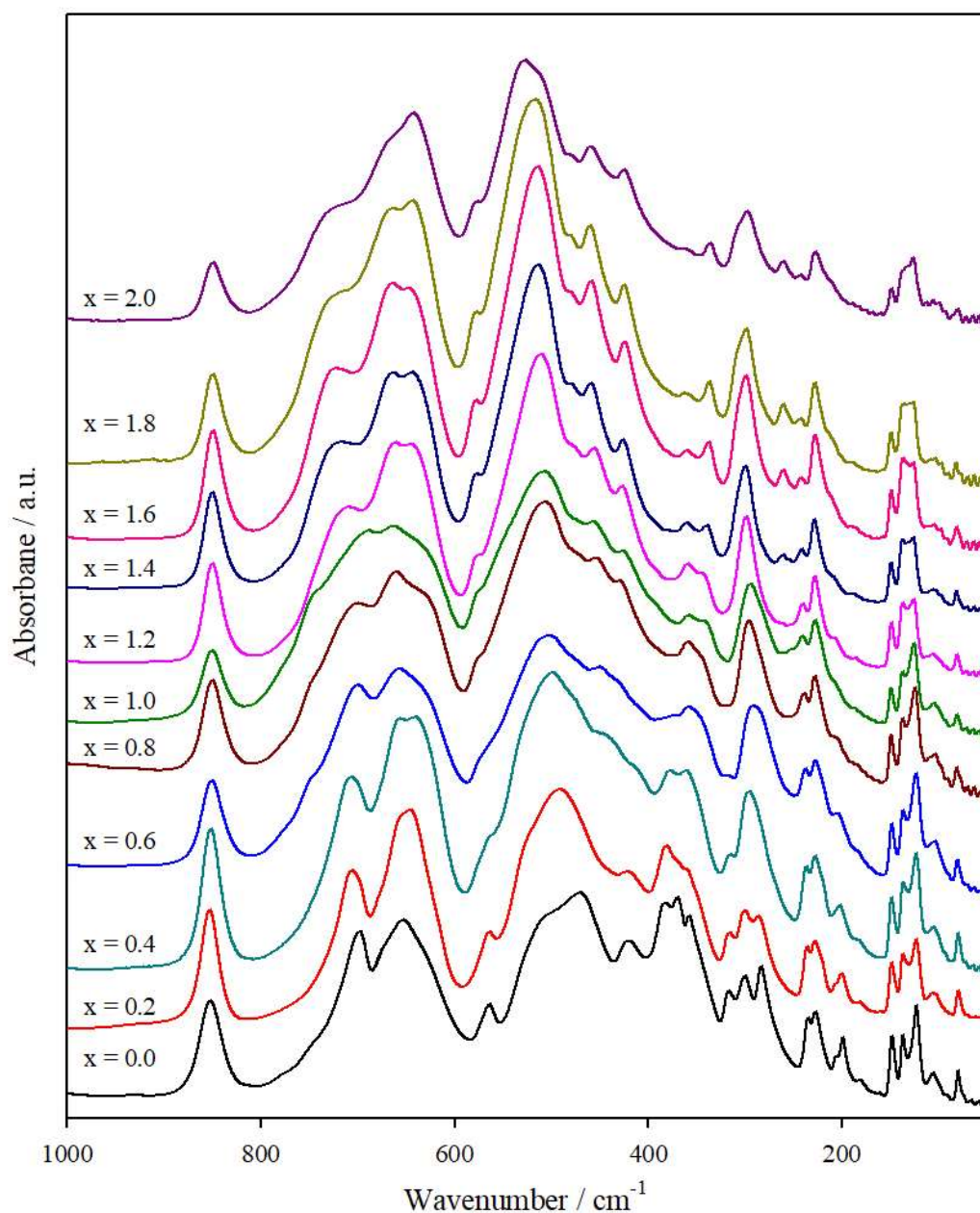
Fig. 2.10. The FT-IR spectrum of $Bi_2Cr_xGa_{4-x}O_9$ at different nominal compositions at 800°C. The spectra reveal that characteristics of four bands for the mullite type orthorhombic phase of $Bi_2M_4O_9$ (M = Al^{3+}, Ga^{3+}, Fe^{3+}) are present.

$Bi_2Cr_xGa_{4-x}O_9$ $Bi_2Cr_xAl_{4-x}O_9$
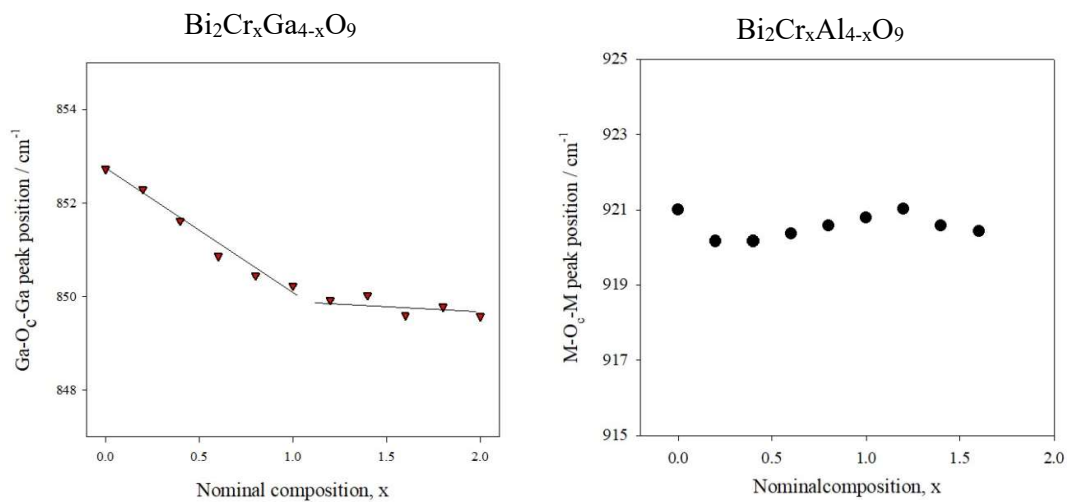
Fig. 2.11. Position of peak maxima of highest frequency Ga-O_c-Ga as a function of nominal composition, x.

$Bi_2Cr_xGa_{4-x}O_9$ $Bi_2Cr_xAl_{4-x}O_9$
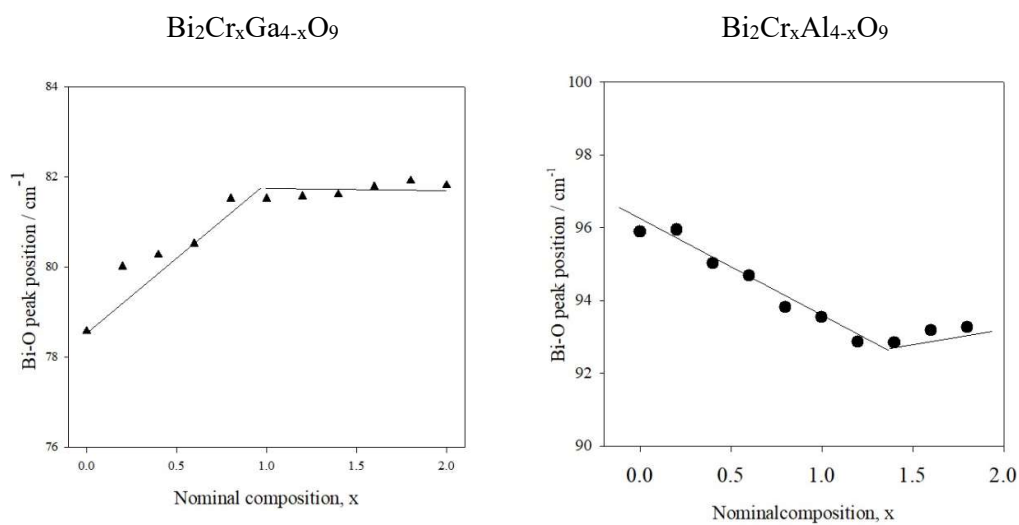
Fig. 2.12. Band mode shifts of Bi-O-Bi vibrational mode as a function of nominal composition, x.

2.3.1.c Raman spectra analysis of Bi$_2$Cr$_x$Ga$_{4-x}$O$_9$ series

Fig. 2.13 shows the room temperature Raman spectra of Cr^{3+} substituted Bi$_2$Ga$_4$O$_9$ depending on the composition (x). Beran *et al.* measured polarized Raman spectra of single crystal B$_2$Ga$_4$O$_9$ and reported strong bands in the z(xx)z′ spectrum at 698.5, 590.5, 442, 349, 322, 297, 239 and 201.5 cm^{-1} [83].

The band centered at 698.5 cm^{-1} in Raman spectra is assigned to stretching vibrations of the GaO$_4$ tetrahedral units, and the 590.5 cm^{-1} is assigned to Ga-O-Ga bending modes. The weak bands present at 541.5 cm^{-1} and at 566 cm^{-1} are due to the O-Ga-O bending modes of the GaO$_4$ units. The band present at 442 cm^{-1} is assigned to the stretching vibrations of the octahedral GaO$_6$ unit. A very high intensity band at 357 cm^{-1} with is also assigned to the stretching vibration of GaO$_6$ but in a different crystallographic plane. The strongest intensity peak at 322 cm^{-1} is assigned to the O-Ga-O bending vibration. The relatively weak Raman band at 297 cm^{-1} is a highly probable candidate for an assignment to the symmetric bending mode of the GaO$_4$ tetrahedra. Raman band presents at 239 cm^{-1} is attributed to the Bi-O stretching vibrational mode.

A Raman spectrum of powder sample Bi$_2$Ga$_4$O$_9$ recorded at room temperature is also included in Fig. 2.13 for direct comparison. The powder sample Bi$_2$Ga$_4$O$_9$ shows Raman peaks at 698, 590, 560, 480, 440, 357, 320, 290, 238 and 215 cm^{-1}, which are comparable with the single crystal data. Some additional vibrational mode found and some vibrational modes are missing than reported by Bearn *et al.* due to polycrystalline present instead of single crystal and stabilization of CrO$_6$ octahedron.

In spite of their different chemical compositions, all the products of this series have similar Raman spectra. In particular, vibrational properties depend on changes in nominal composition; some of the lower wavenumber modes, such as peak at 290 and 215 cm^{-1}, disappear due to overlapping vibration with the change in chemical composition. Significant mode shifts at higher-wavenumbers were observed by substituting Cr for gallium. The figure shows that the peak at 357 cm^{-1} (assigned as stretching vibration of GaO$_6$ octahedra) with extremely high intensity splits into two peaks with increasing Cr content in Bi$_2$Cr$_x$Ga$_{4-x}$O$_9$, indicating the formation of Ga-O-Cr (oct) and Cr-O-Cr (for higher value of x) bonds. Moreover, all the bands are successively becoming broad due to the incorporation of Cr. This indicates that Cr and Ga are statistically distributed in MO$_6$ (M = Ga/Cr) octahedra in the same chemical compound. Such broadness is an indication

of compound peaks formed from all possible stretching vibrations of Ga–O–M (M = Ga/Cr) bonds in MO_6 octahedra.
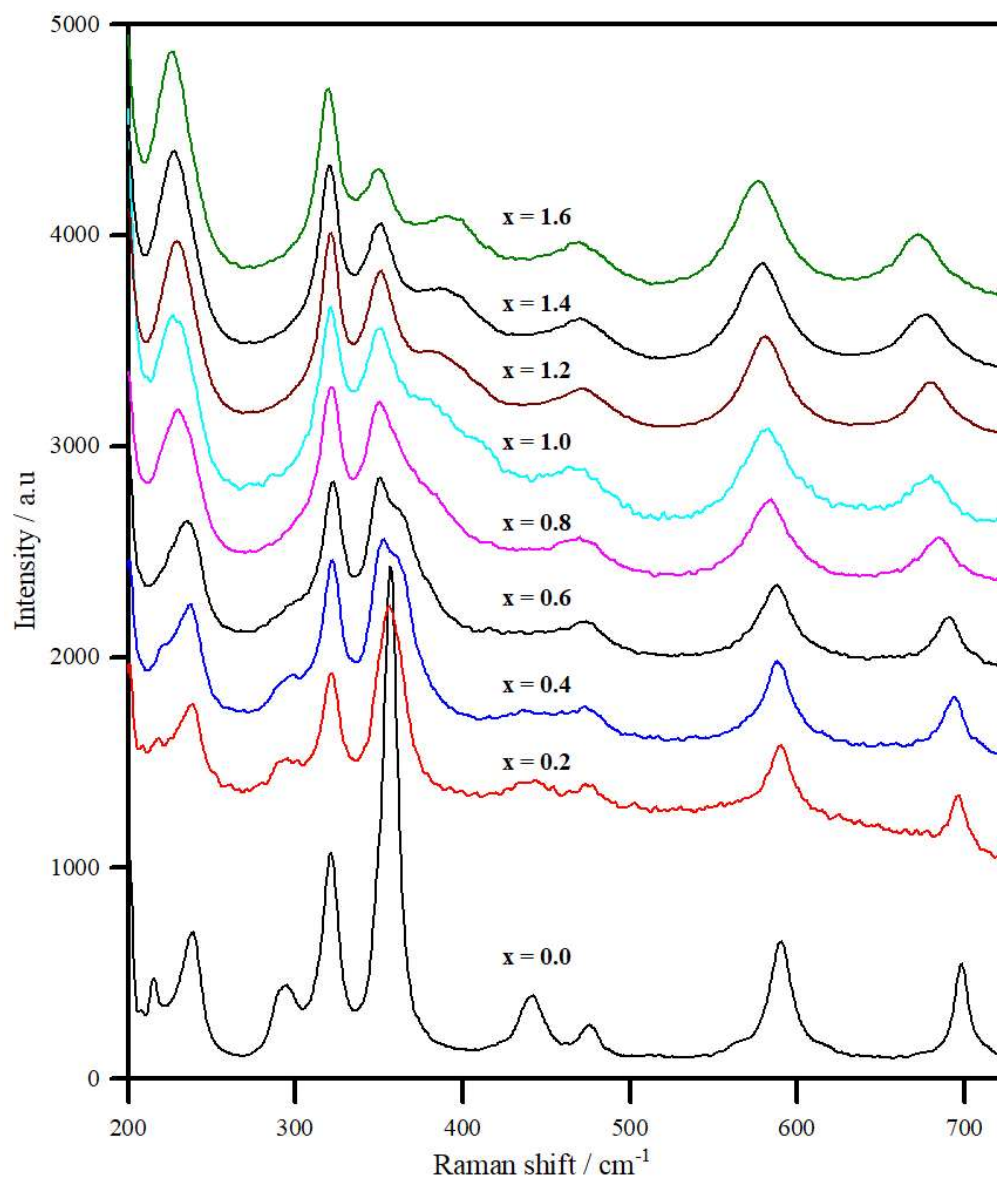
Fig. 2.13. Raman spectrum of $Bi_2Cr_xGa_{4-x}O_9$ at different nominal compositions at 800°C.

2.3.1.d SEM/EDX analysis of $Bi_2Cr_xGa_{4-x}O_9$ series

Fig. 2.14 shows the scanning electron microscope (SEM) images of $Bi_2Cr_xGa_{4-x}O_9$ at different nominal compositions. Here it is observed that all are polycrystalline and have microstructure. The EDX results show that the elemental content is very close to the nominal compositions used. Chromium is statistically distributed with gallium within the polycrystalline products. The averaged Cr:Ga ratios are in good agreement with the nominal composition used. The observed EDX results are shown in the Table 2.4.

Table 2.4. SEM/EDX results of $Bi_2Cr_xGa_{4-x}O_9$ solid solution series

Nominal composition $Bi_2Cr_xGa_{4-x}O_9$	Used (calculated) Cr/Ga	Observed (EDX) Cr/Ga
0.2	0.053	0.042(11)
0.4	0.111	0.090(13)
0.6	0.176	0.165(11)
0.8	0.250	0.238(18)
1.0	0.333	0.291(16)
1.2	0.429	0.401(21)
1.4	0.538	0.492(11)
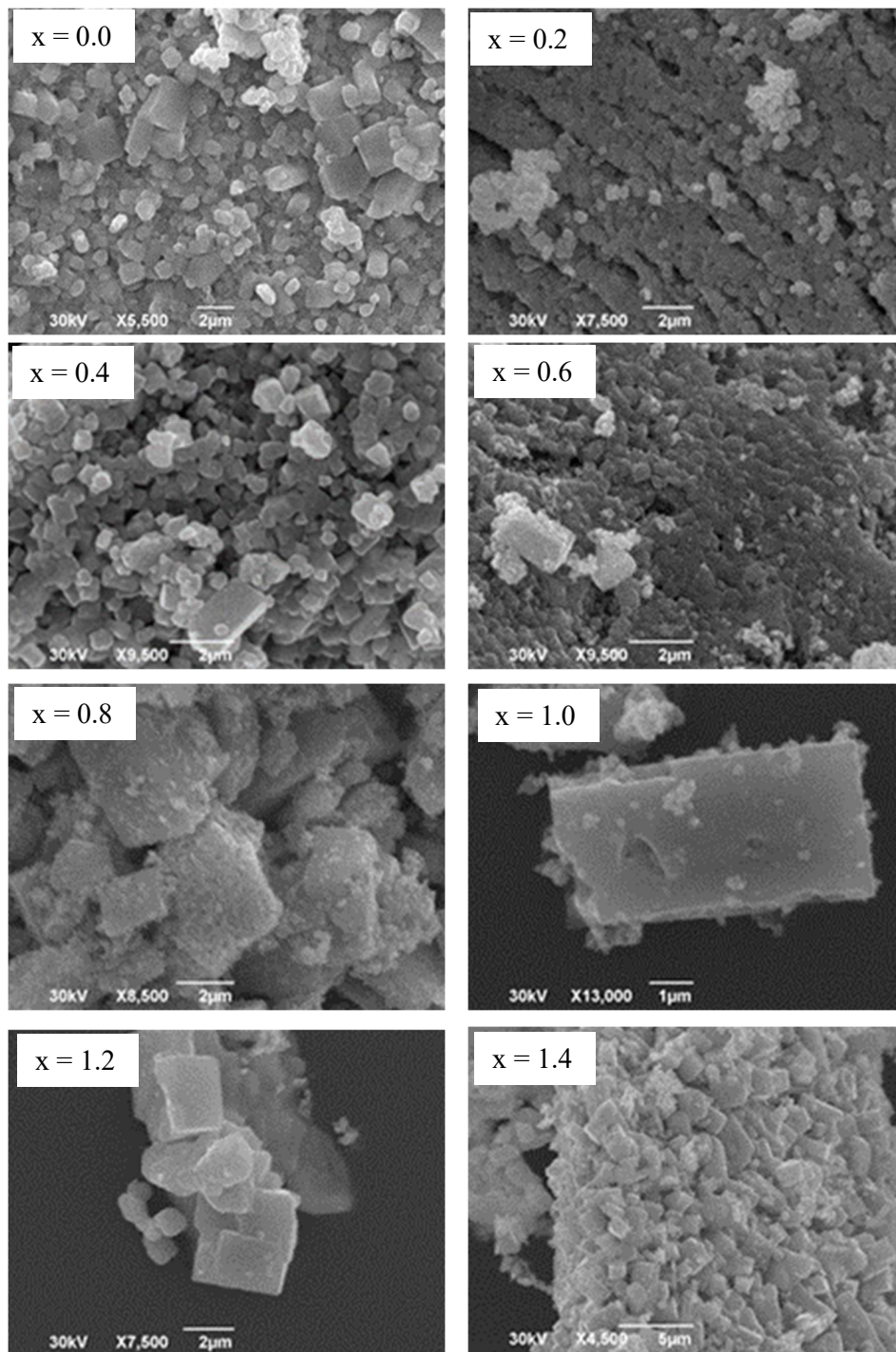
Fig. 2.14. SEM image of $Bi_2Cr_xGa_{4-x}O_9$ at different nominal compositions at 800ºC.

2.3.2 Results and discussion of Bi$_2$Fe$_x$Al$_{4-x}$O$_9$ series

A solid solution series of general formula Bi$_2$Fe$_x$Al$_{4-x}$O$_9$ (x = 0, 1, 2, 3 and 4) were prepared from the appropriate amount of Bi(NO$_3$)$_3$.9H$_2$O, Fe(NO$_3$)$_3$.9H$_2$O, and glycerin by the gel combustion method. Each member of this series belongs to the orthorhombic mullite type family, which is characterized by MO$_6$ edge-shared octahedra forming chains parallel to the crystallographic c-axis. The AlO$_6$ octahedral chains are interconnected through double M$_2$O$_7$ tetrahedra by a shared oxygen vertex [63]. The Bi^{3+} cation exists in the framework networks forming a nido-like trigonal pyramidal BiO$_4$E (E = LEP functioning as an extra ligand that is stereochemically active) coordination where the nido-position provides space for the stereo-active 6s lone electron pair. XRD, SEM and FT-IR analyses revealed that the results found are in good agreement with those of earlier reports, indicating that structurally Bi$_2$Fe$_x$Al$_{4-x}$O$_9$ solid solution series has been formed which belongs to the orthorhombic mullite type structure backbone at temperatures 700-900ºC.

2.3.2.a XRD analysis of Bi$_2$Fe$_x$Al$_{4-x}$O$_9$ series

The XRD patterns of Bi$_2$Fe$_x$Al$_{4-x}$O$_9$ (x = 1, 2, 3, and 4) solid solutions at different temperatures are shown in Figs. 2.15 - 2.17. The diffraction patterns of Bi$_2$Fe$_3$AlO$_9$, Bi$_2$Fe$_2$Al$_2$O$_9$ and Bi$_2$FeAl$_3$O$_9$ at all temperatures are found comparable to the reported pattern of mullite type orthorhombic phase of Bi$_2$Fe$_4$O$_9$ and Bi$_2$Al$_4$O$_9$ [ICSD Pattern; card no. 00-025-0090, 01-072-1832, 01-083-1995 and 00-025-1048]. The broad diffraction peak of Bi$_2$Fe$_2$Al$_2$O$_9$ and Bi$_2$FeAl$_3$O$_9$ may correspond to the nano-crystalline phase of the analyzed samples. It is also observed that with increasing Al concentration from Bi$_2$Fe$_3$AlO$_9$ to Bi$_2$FeAl$_3$O$_9$, the peak becomes broader, corresponding to the small crystallite size. The crystallite size increases again in the case of Bi$_2$Al$_4$O$_9$ having the highest amount of Al, indicated by the sharper and intense nature of the diffraction peak. Observing carefully the XRD pattern of the Bi$_2$Fe$_x$Al$_{4-x}$O$_9$ series also reveals that in the sample with increasing Al content form Bi$_2$Fe$_4$O$_9$ and Bi$_2$Al$_4$O$_9$, the peaks are shifted toward the higher angles region. This shifting is associated with the distance between crystalline planes, resulting into the reduction of lattice parameters [84].
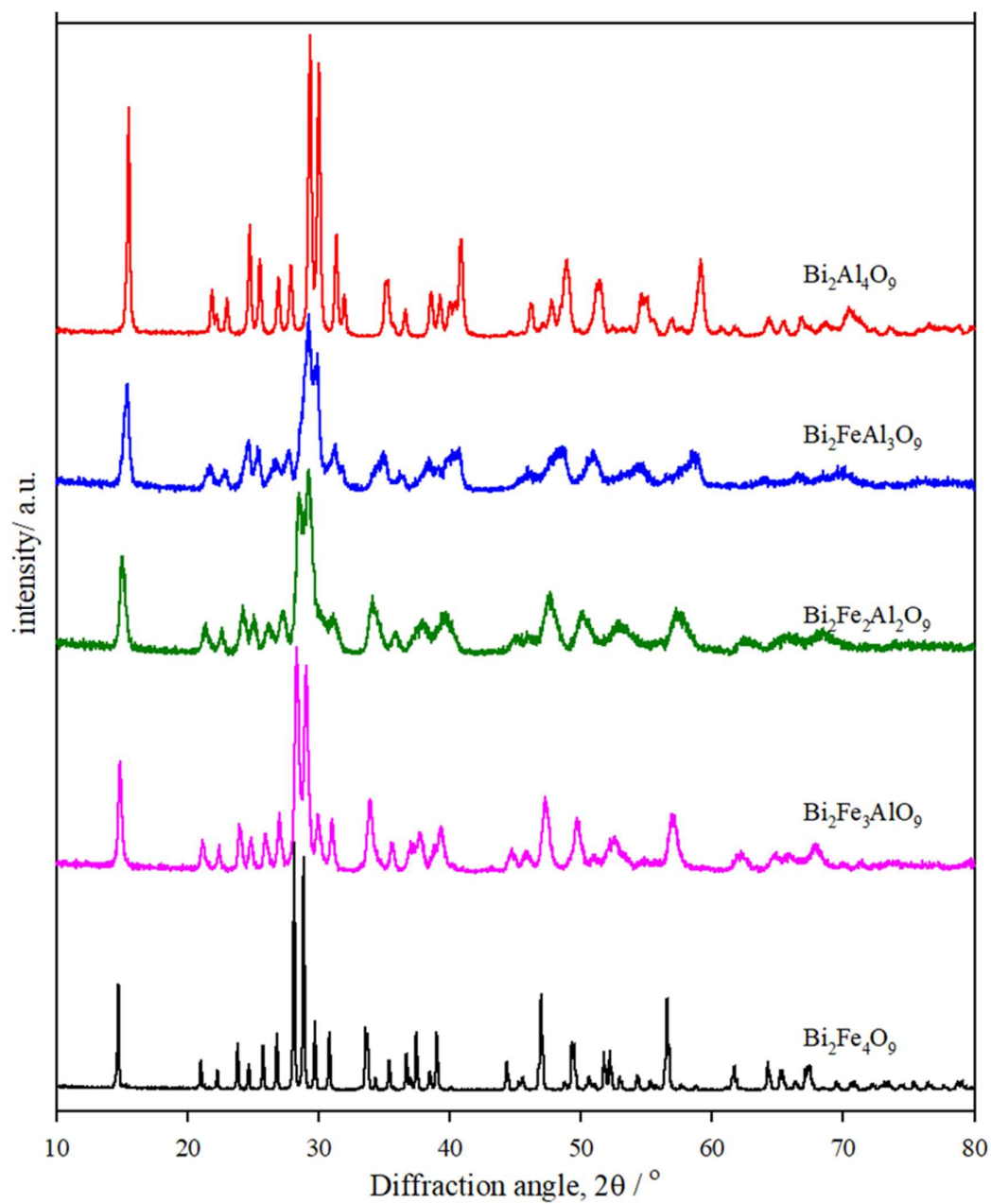
Fig. 2.15. XRD patterns of $Bi_2Fe_xAl_{4-x}O_9$ with different nominal compositions at 700°C. For clarity, the diffraction patterns are vertically plotted. The patterns show the orthorhombic phase.

Fig. 2.16. XRD pattern of $Bi_2Fe_xAl_{4-x}O_9$ with different nominal compositions at 800^oC. For clarity, the diffraction patterns are vertically plotted. The patterns show orthorhombic phase.
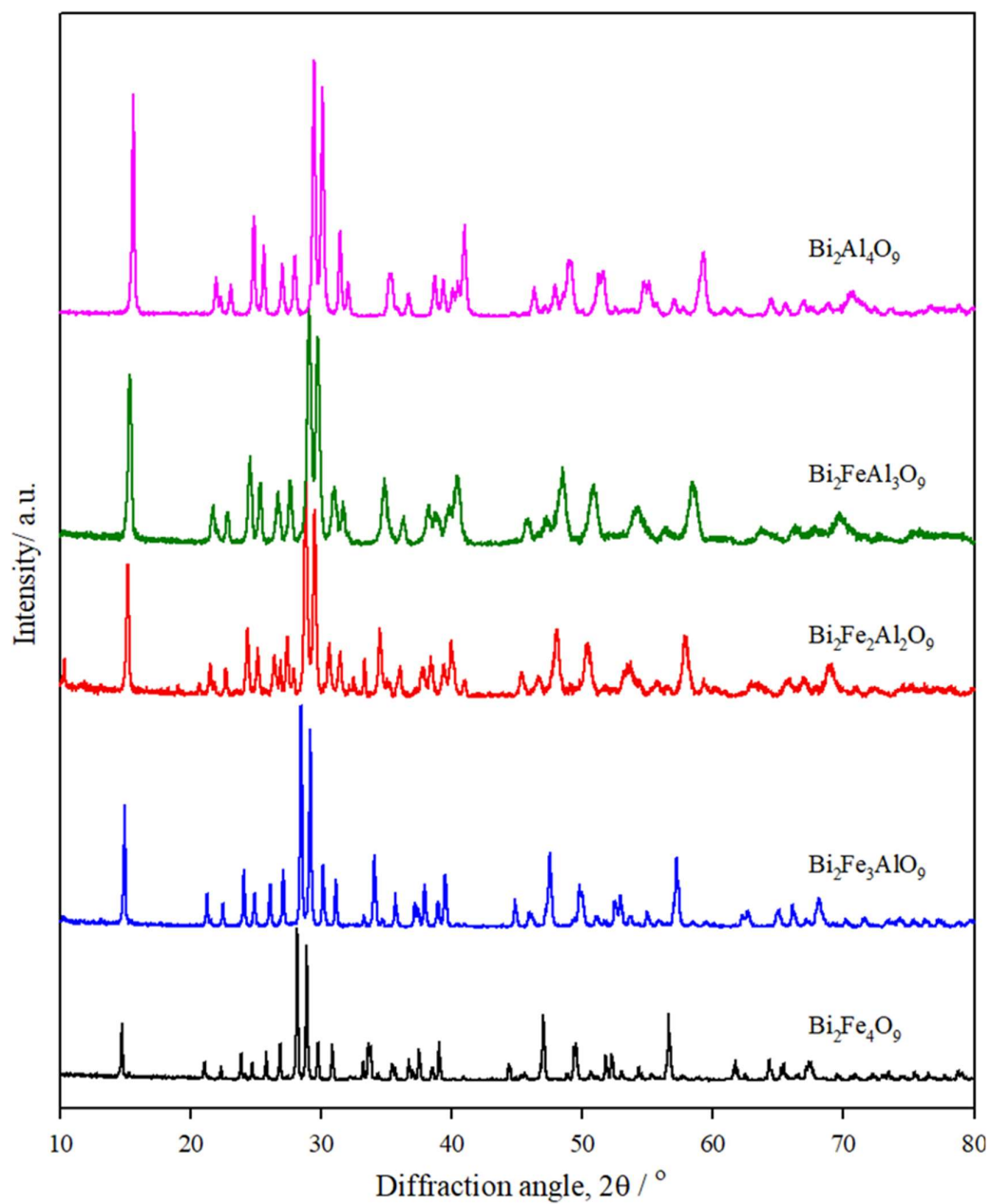
Fig. 2.17. XRD pattern of $Bi_2Fe_xAl_{4-x}O_9$ with different nominal compositions at 900°C. For clarity, the patterns are vertically plotted.

2.3.2.b FT-IR analysis of $Bi_2Fe_xAl_{4-x}O_9$ series

The Fourier transform infrared spectra of the as-prepared $Bi_2Fe_xAl_{4-x}O_9$ (x = 0, 1, 2, 3 and 4) samples are shown in Fig. 2.18. Three distinct characteristic bands are observed that are shifted to higher wave numbers, going from $Bi_2Fe_4O_9$ to $Bi_2Al_4O_9$. This shifting can be described as an increase of the vibrational force constant due to smaller Al-O compared to Fe-O bond distance. The band at 923 cm^{-1} in $Bi_2Al_4O_9$ and at 812 cm^{-1} in $Bi_2Fe_4O_9$ can be assigned as Al-O or Fe-O stretching mode of the tetrahedral units according to the spectroscopic data of mullite type structure [33]. These high energetic vibrations are responsible for the relatively short tetrahedral Al-O/Fe-O formed by sharing the connecting oxygen atom of the tetrahedral pairs. This band splits and formed characteristic band triplet in intermediate $Bi_2Fe_2Al_2O_9$ compounds; the higher energy band is associated with stretching modes of Al-O-Al while lower energy band with Fe-O-Fe respectively. Small shifting of the bands to higher wave numbers with increasing Al content indicates a gradual increase of the tetrahedral Al-O and Fe-O distance.
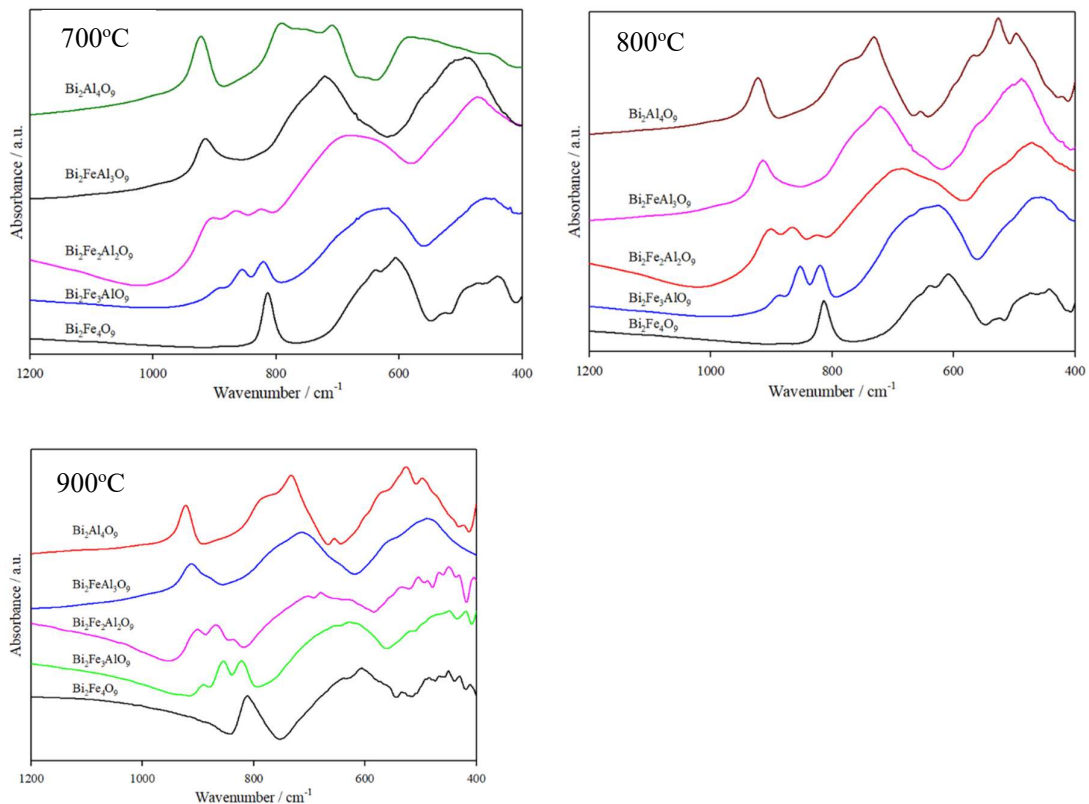
Fig. 2.18. FT-IR spectra of $Bi_2Fe_xAl_{4-x}O_9$ (x = 0, 1, 2, 3, 4) with different compositions at different temperatures. For clarity, the spectra are plotted vertically. Characteristic bands for mullite are observed that are shifted to higher wave numbers, going from $Bi_2Fe_4O_9$ to $Bi_2Al_4O_9$.

2.3.2.c. SEM analysis of Bi₂FeₓAl₄₋ₓO₉ series

SEM analyses have been done for morphology and size distribution of the synthesized particles, shown in Fig. 2.19. Compound $Bi_2Al_4O_9$ exists as aggregated spherical particles, whereas $Bi_2Fe_4O_9$ as cuboid particles. SEM images also demonstrate that cuboid particles appear with increasing the concentration of Fe. The crystal size increases with increasing temperature agree well with X-ray diffraction studies.

700°C	800°C	900°C
Bi$_2$Al$_4$O$_9$	Bi$_2$Al$_4$O$_9$	Bi$_2$Al$_4$O$_9$
Bi$_2$FeAl$_3$O$_9$	Bi$_2$FeAl$_3$O$_9$	Bi$_2$FeAl$_3$O$_9$
Bi$_2$Fe$_2$Al$_2$O	Bi$_2$Fe$_2$Al$_2$O$_9$	Bi$_2$Fe$_2$Al$_2$O$_9$
Bi$_2$Fe$_3$AlO$_9$	Bi$_2$Fe$_3$AlO$_9$	Bi$_2$Fe$_3$AlO$_9$
Bi$_2$Fe$_4$O$_9$	Bi$_2$Fe$_4$O$_9$	Bi$_2$Fe$_4$O$_9$
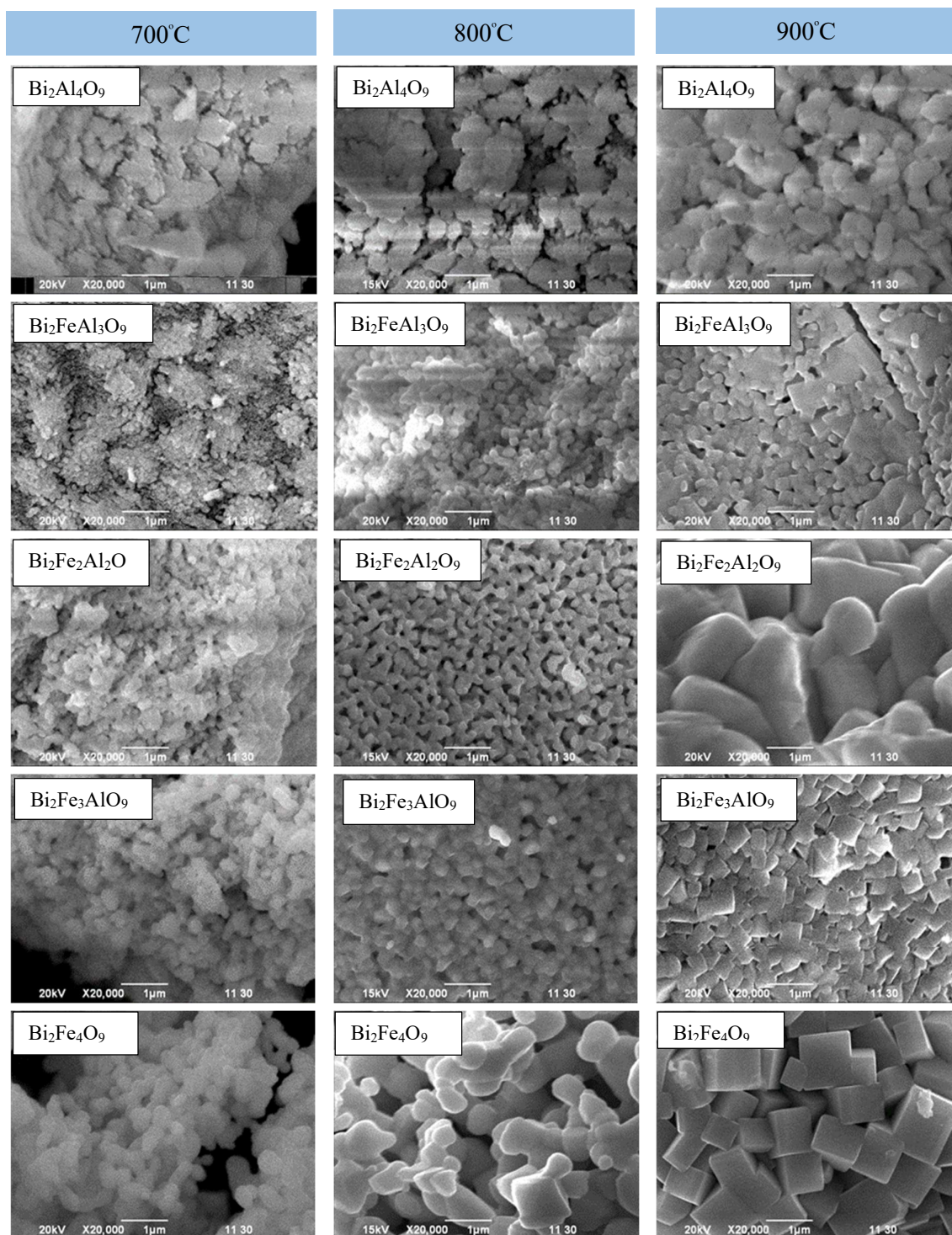
Fig. 2.19. SEM images of Bi$_2$Fe$_x$Al$_{4-x}$O$_9$ at different temperatures. SEM images show that the particles changes shape from spherical to cuboid with increasing Fe concentration.

2.3.2.d Color of the prepared $Bi_2Fe_xAl_{4-x}O_9$ series

It is observed that color of the prepared $Bi_2Fe_xAl_{4-x}O_9$ samples changes from off-white to deep red with increasing Fe content.

2.3.3 Results and discussion of $Bi_2Fe_3(Cr_xAl_{1-x})O_9$ series

$Bi_2Fe_3(Cr_xAl_{1-x})O_9$ is a mixed oxide solution series with nominal compositions x = 0.0, 0.2, 0.4, 0.5 and 0.6. They were prepared by glycerin combustion method comprises making of a homogeneous gel of appropriate amount of metal nitrates, $M(NO_3)_3.xH_2O$ (M = Bi, Fe, Cr, and Al) with glycerin, followed by calcination and the calcination temperature varied from 700 to 900°C. The obtained crystalline product was characterized by XRD, FT-IR spectroscopy and scanning electron microscopy (SEM). Not all the members of this series belong to the orthorhombic mullite type family at all studied compositions and temperatures.

2.3.3.a XRD analysis of $Bi_2Fe_3(Cr_xAl_{1-x})O_9$ series

The XRD pattern of $Bi_2Fe_3(Cr_xAl_{1-x})O_9$ solid solutions (x = 0.0, 0.2, 0.4, 0.5 and 0.6) at calcined at 900°C shown in Fig. 2.20 and other temperatures are given in the appendix. All the XRD peaks of $Bi_2Fe_3AlO_9$ and $Bi_2Fe_3Cr_{0.2}Al_{0.8}O_9$, nominal composition of x = 0 and x = 0.2 of $Bi_2Fe_3(Cr_xAl_{1-x})O_9$ were indexed as mullite-type orthorhombic phase at all temperatures. Presence of any extra line other than orthorhombic phase was not detected, ensuring single phase formation of the product. Samples with nominal compositions of x = 0.4, and x = 0.5 show mullite-type orthorhombic phase at > 700°C. At 900°C all composition shows mullite orthorhombic phase with increasing calcination temperature whereas the XRD peaks become sharper indicating increase of crystallite size. XRD pattern of the compounds also shows a few added lines associated to the presence of Cr in the crystal lattice, suggesting a successful doping of Cr in the $Bi_2Fe_3(Cr_xAl_{1-x})O_9$ solid solution series that could be seen up to x = 0.6 at 900°C. The pure orthorhombic phase of $Bi_2Fe_3(Cr_xAl_{1-x})O_9$ series were refined by the Rietveld method using space group *Pbam* with the profex software [45]. As shown in Fig. 2.21, the calculated and measured XRD patterns are well-fitted. The cell parameters are slightly increases with nominal compositions, indicating partial doping of chromium occurs. According to the literature, substitution of metal ions takes place in the octahedral site in mullite. Due to the close values of their crystal radii, Al^{3+} (67.5 pm) and or Cr^{3+} (75.5 pm) are expected to be able to replace Fe^{3+} (78.5 pm) ions in the $Bi_2Fe_3(Cr_xAl_{1-x})O_9$ solid solution series.
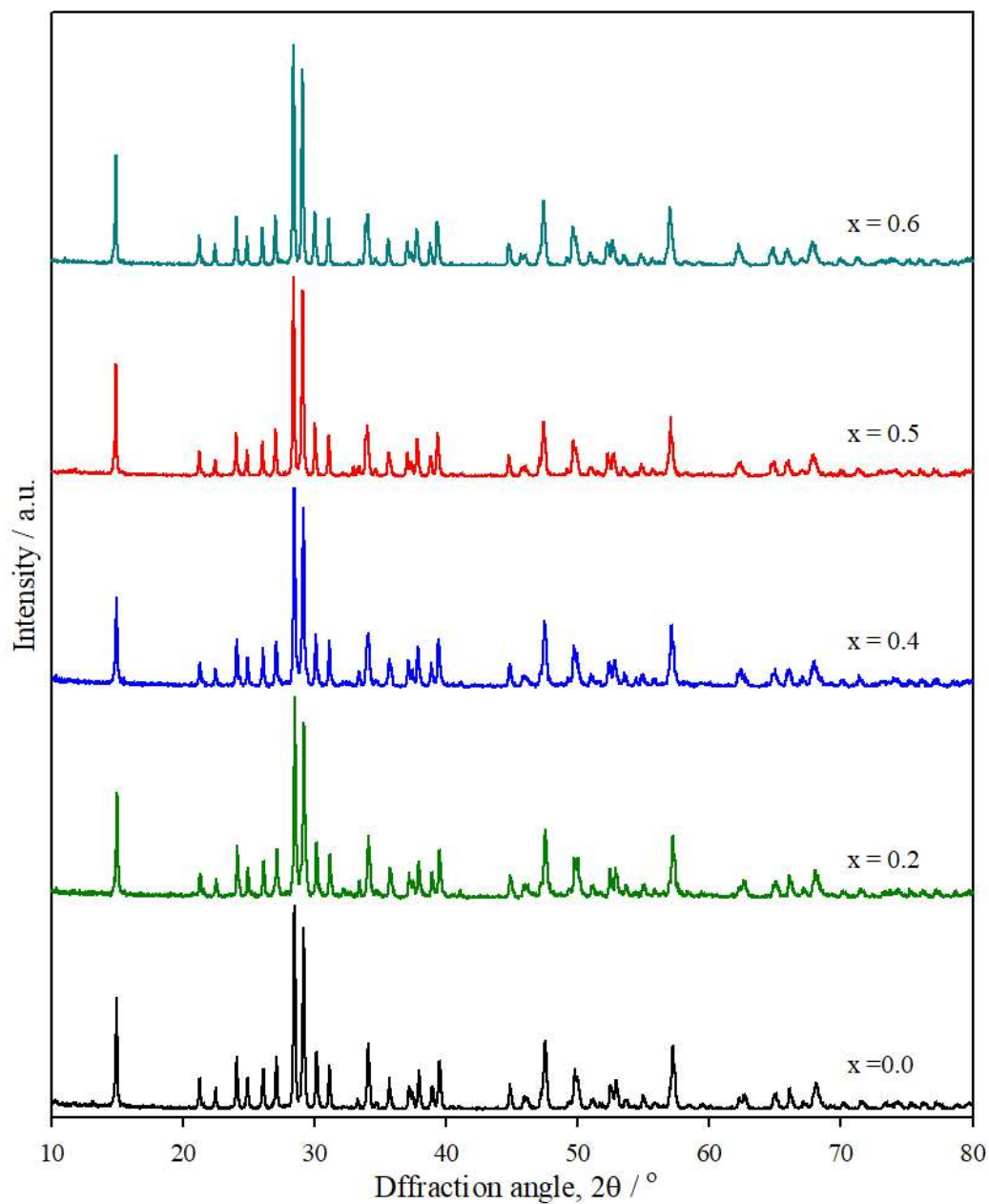
Fig. 2.20. XRD patterns of $Bi_2Fe_3(Cr_xAl_{1-x})O_9$ with different nominal compositions at 900°C. For clarity, the diffraction patterns are vertically plotted. All compositions show orthorhombic mullite-type phase.
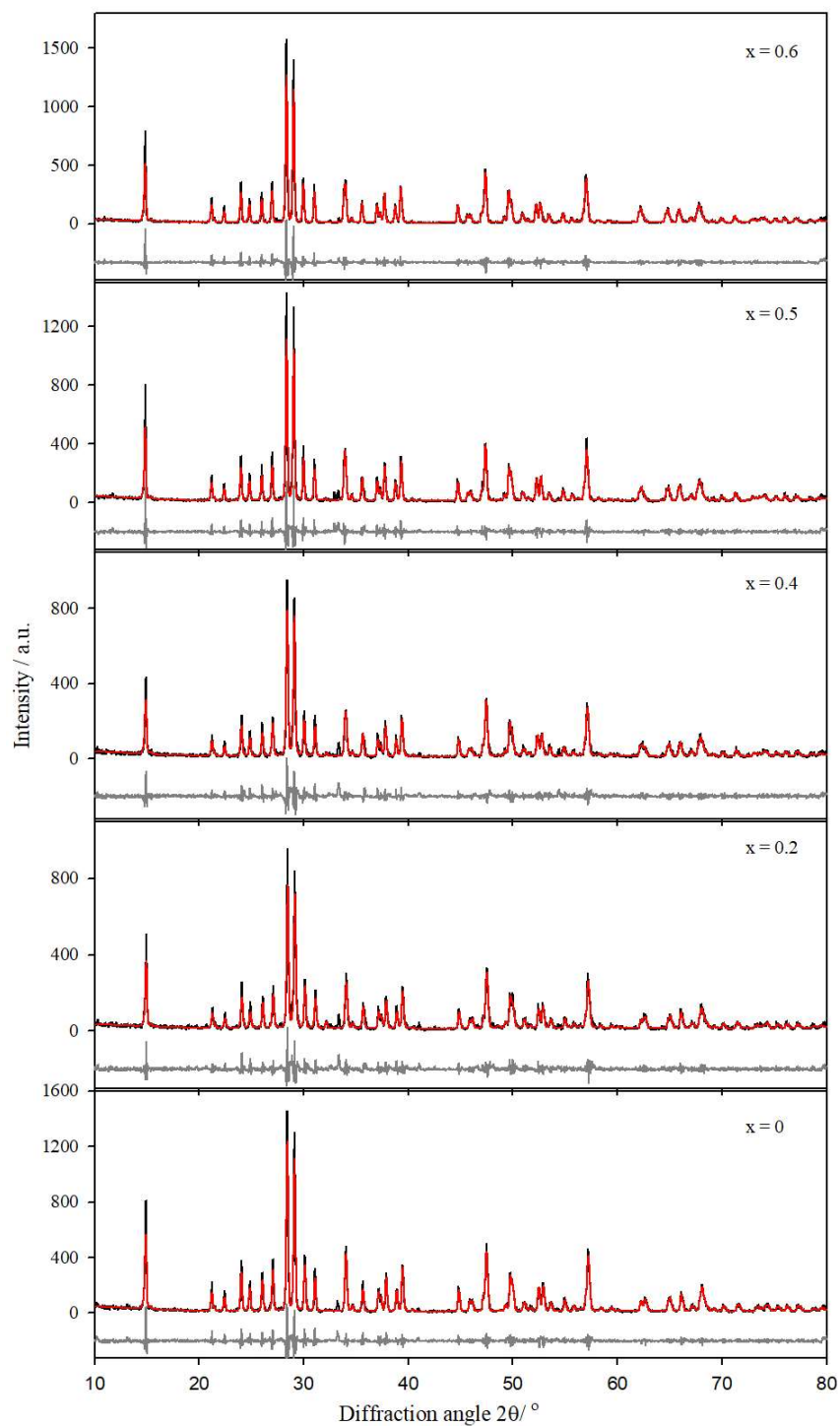
Fig. 2.21. Rietveld refinements fit of the $Bi_2Fe_3(Cr_xAl_{1-x})O_9$ (x = 0, 0.2, 0.4, 0.5 and 0.6) series at 900ºC. The black spectrum represents observed/measured spectrum, and the red spectrum represents calculated data. The black curve below the spectrum represents the difference spectrum.

Table 2.5 Cell parameter of $Bi_2Fe_3(Cr_xAl_{1-x})O_9$ at 900ºC

Nominal Compositions, x	a / pm	b / pm	c / pm
0.0	0.7915	0.8358	0.5928
0.2	0.7922	0.8363	0.5939
0.4	0.7929	0.8371	0.5951
0.5	0.7932	0.8376	0.5957
0.6	0.7942	0.8380	0.5963

2.3.3.b FT-IR analysis of $Bi_2Fe_3(Cr_xAl_{(1-x)})O_9$ series

FT-IR spectrum of $Bi_2Fe_3(Cr_xAl_{1-x})O_9$ show that the characteristics band for mullite type orthorhombic phase found at about 450, 630, and 850 cm^{-1} wavenumber. The band centered at about 850 cm^{-1} can be arbitrated for M-Oc-M stretch (O_3M-Oc-MO_3 dimer); band about 630 cm^{-1} for M-O stretch (MO_4), M-O-M bend (MO_4) and band about 450 cm^{-1} for O-M-O band (MO_4), M-O stretch (MO_6), M-O-M bend (MO_6) [32]. The distinctive triplet band observed at 850 cm^{-1} in the absorption spectrum of $Bi_2Fe_3(Cr_xAl_{1-x})O_9$ indicate that Al-O-Al conjunction are still present in these iron rich compounds. High energy band centered at about 890 cm^{-1} can be assigned as stretching modes for tetrahedral pairs with Al on both sides (Al-O-Al), the band centered about 850cm^{-1} can be assigned for stretching vibration where Al and Fe both are present in tetrahedral sites (Al-O-Fe and Fe-O-Al, respectively) and the low energy band (about 825 cm^{-1}) can be ascribed as stretching modes with Fe on both tetrahedral sites (Fe-O-Fe) [33]. A slight but continuous shift of absorption bands toward lower wave number was observed with increasing Cr doping in mullite phase indicates that the Cr^{3+} doping in mullite phase is associated with a local structural change.
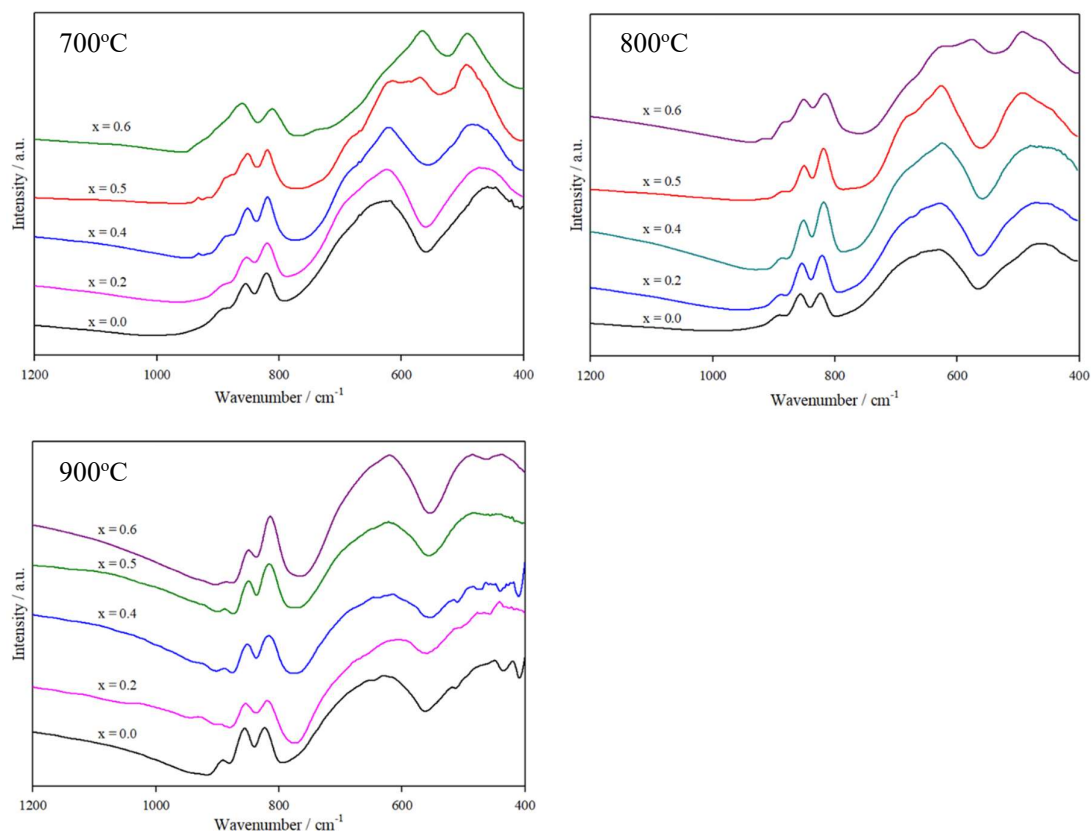
Fig. 2.22. FT-IR spectra of $Bi_2Fe_3(Cr_xAl_{(1-x)})O_9$ with different nominal compositions at different temperatures. For clarity, the spectra are vertically plotted.

2.3.3.c SEM / EDX analysis of $Bi_2Fe_3(Cr_xAl_{(1-x)})O_9$ series

Scanning electron micrographs of $Bi_2Fe_3(Cr_xAl_{(1-x)})O_9$ at different compositions and calcined temperatures are shown in Fig. 2.23. The particles are cuboidal at all temperatures ranging from 700 to 900°C and at all compositions. However, the particle size increases with increasing x (the Cr^{3+} content) and annealing temperatures. Thus, the doping with Cr^{3+} ions obviously modify the surface morphologies and grain sizes. Increase in particle sizes occurs with an increase in calcination temperature, may as a result of the Ostwald ripening process. According to this process, smaller particles merge to form large particles by solid state diffusion as a result of potential energy difference between small and large particles. The results from SEM analysis agree well with the results obtained from XRD. The EDX spectrum indicates that the synthesized sample contains Bi, Fe, Al, O and Cr, no foreign elements were present. The EDX results show that the actual level of chromium doping and predetermined chromium doping content is very close. It was also observed that with the decrease of aluminum content, the chromium content increase, which is expected.

700ºC	800ºC	900ºC
x = 0	x = 0	x = 0
x = 0.2	x = 0.2	x = 0.2
x = 0.4	x = 0.4	x = 0.4
x = 0.5	x = 0.5	x = 0.5
x = 0.6	x = 0.6	x = 0.6
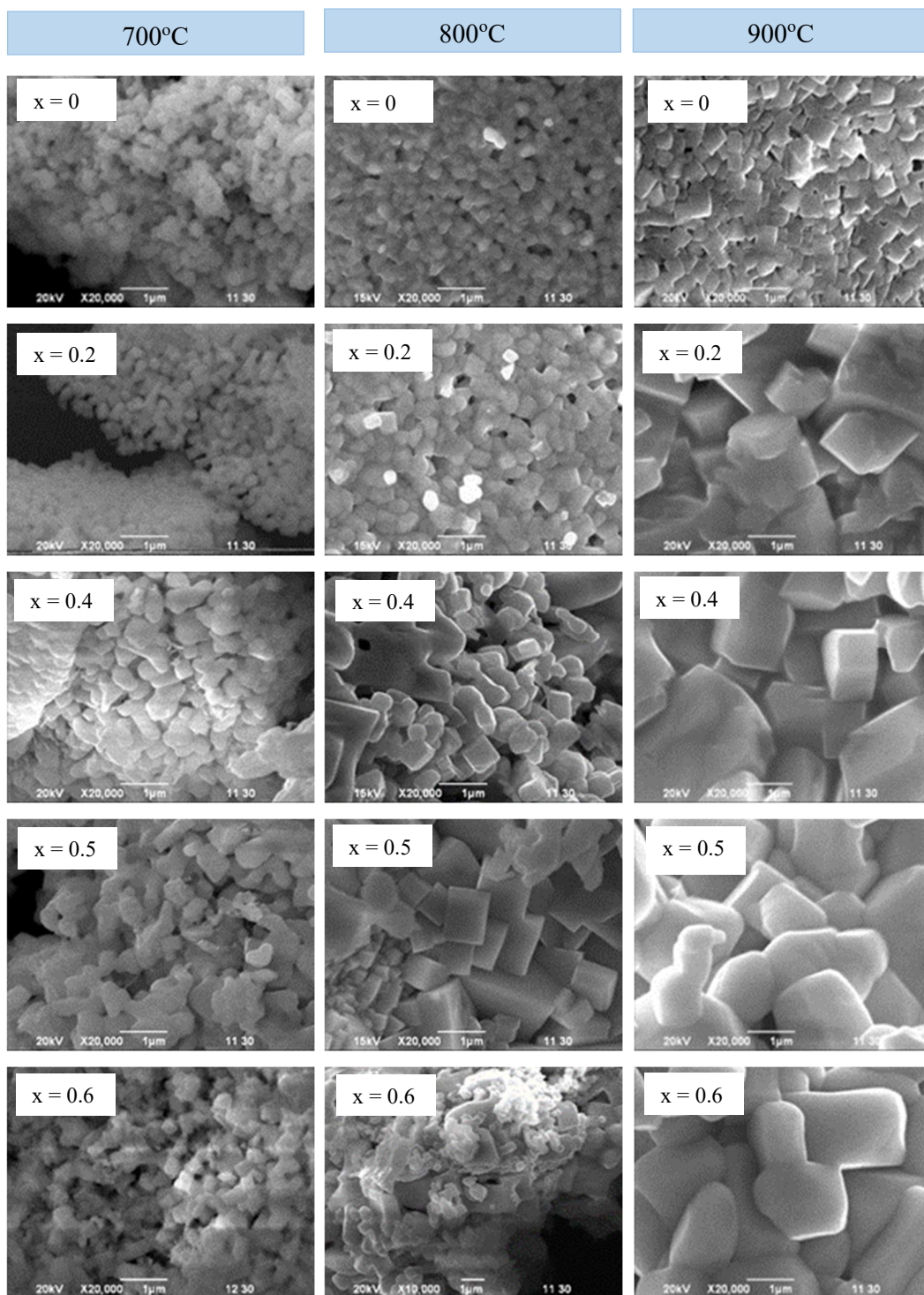
Fig. 2.23. SEM images of $Bi_2Fe_3(Cr_xAl_{1-x})O_9$ at different compositions and calcination temperatures.

Table 2.6 Chemical composition of $Bi_2Fe_3(Cr_xAl_{1-x})O_9$ solid solution prepared at 900°C by EDX analysis.

Nominal Composition	Element	Weight % used	Weight % found	Cr/Al used	Cr/Al observed
x = 0	Bi	55.25	57.97	-	-
	Fe	22.14	14.06		
	Al	3.57	5.12		
	O	19.04	22.86		
x = 0.2	Bi	54.89	50.17	0.404	0.397
	Fe	22.00	21.80		
	Al	4.43	4.65		
	Cr	1.79	1.72		
	O	18.91	21.65		
x = 0.4	Bi	54.53	49.60	1.284	1.054
	Fe	21.86	23.90		
	Al	2.11	3.32		
	Cr	2.71	3.50		
	O	18.78	19.67		
x = 0.5	Bi	54.35	58.55	1.931	2.657
	Fe	21.78	12.45		
	Al	1.75	2.86		
	Cr	3.38	7.60		
	O	18.73	18.55		
x = 0.6	Bi	54.18	49.04	2.885	2.786
	Fe	21.71	27.19		
	Al	1.40	2.01		
	Cr	4.04	5.60		
	O	18.67	16.16		

2.3.3.d Color of $Bi_2Fe_3(Cr_xAl_{(1-x)})O_9$ series

It is observed from the $Bi_2Fe_3(Cr_xAl_{1-x})O_9$ color chart in the appendix, the color of the doped samples systematically changes from reddish brown to black red with increasing Cr content and with temperature.

2.3.4 Results and discussion of $Bi_2Fe_2(Cr_xAl_{1-x})_2O_9$ series

The $Bi_2Fe_2(Cr_xAl_{1-x})_2O_9$ solid solution is a mixed oxide solution with x ranging between 0.1 and 0.6. It was prepared by making a homogeneous gel of appropriate amount of metal nitrates, $M(NO_3)_3.xH_2O$ (M = Fe, Al and Cr) and glycerin. Then the prepared gel calcined and characterized by XRD, FT-IR and SEM. Not all the members of this series belong to the orthorhombic mullite type family at all studied compositions and temperatures.

2.3.4.a XRD analysis of $Bi_2Fe_2(Cr_xAl_{(1-x)})_2O_9$ series

The XRD diffraction pattern of $Bi_2Fe_2(Cr_xAl_{1-x})_2O_9$ (x = 0.0, 0.2, 0.4, 0.5 and 0.6) annealed at 700, 800 and 900°C are presented in Figs. A.2.9, A.2.10, 2.24 and the lines are compared to those observed in the same region for $Bi_2Fe_2Al_2O_9$. The diffracted lines of $Bi_2Fe_2Al_2O_9$ are indexed as mullite type orthorhombic phase at 700 and 800°C. Presence of any extra line other than orthorhombic phase was not detected, which ensure single phase formation of the product. At nominal composition, x = 0.2 the compound shows mullite type orthorhombic phase at > 700°C. At 900°C, samples with all studied compositions show orthorhombic mullite-type phase, except x = 0.6 and x = 0.0. A few lines other than mullite type orthorhombic phase are, however, observed at 900°C demonstrating the phase transformation begins to occur around this temperature. X-ray results that with increasing calcination temperature, the intensity of peaks increases and the diffraction peaks become sharper and narrower. This indicates the increment of the crystallinity. Presence of additional peaks in the XRD pattern of the compounds indicates successful doping of Cr in the $Bi_2Fe_2Al_2O_9$ solid solution up to x = 0.5 (25%) at 900°C.

The pure orthorhombic phase of $Bi_2Fe_2(Cr_xAl_{1-x})_2O_9$ series at 900°C (nominal composition x = 0, 0.2, 0.4, 0.5) were refined by the Rietveld method using space group *Pbam* with the profex software [45]. The calculated and measured XRD patterns are well-fitted, shown in Fig. 2.25. According to the literature, substitution of metal ions takes place in the octahedral site in mullite. Due to the close values of their crystal radii, Al^{3+} (67.5 pm) and or Cr^{3+} (75.5 pm) are expected to be able to replace Fe^{3+} (78.5 pm) ions in the $Bi_2Fe_3(Cr_xAl_{1-x})O_9$ solid solution series. The cell parameters are slightly increases with nominal compositions indicating metal ions partially substitute by chromium in the octahedral site in mullite.
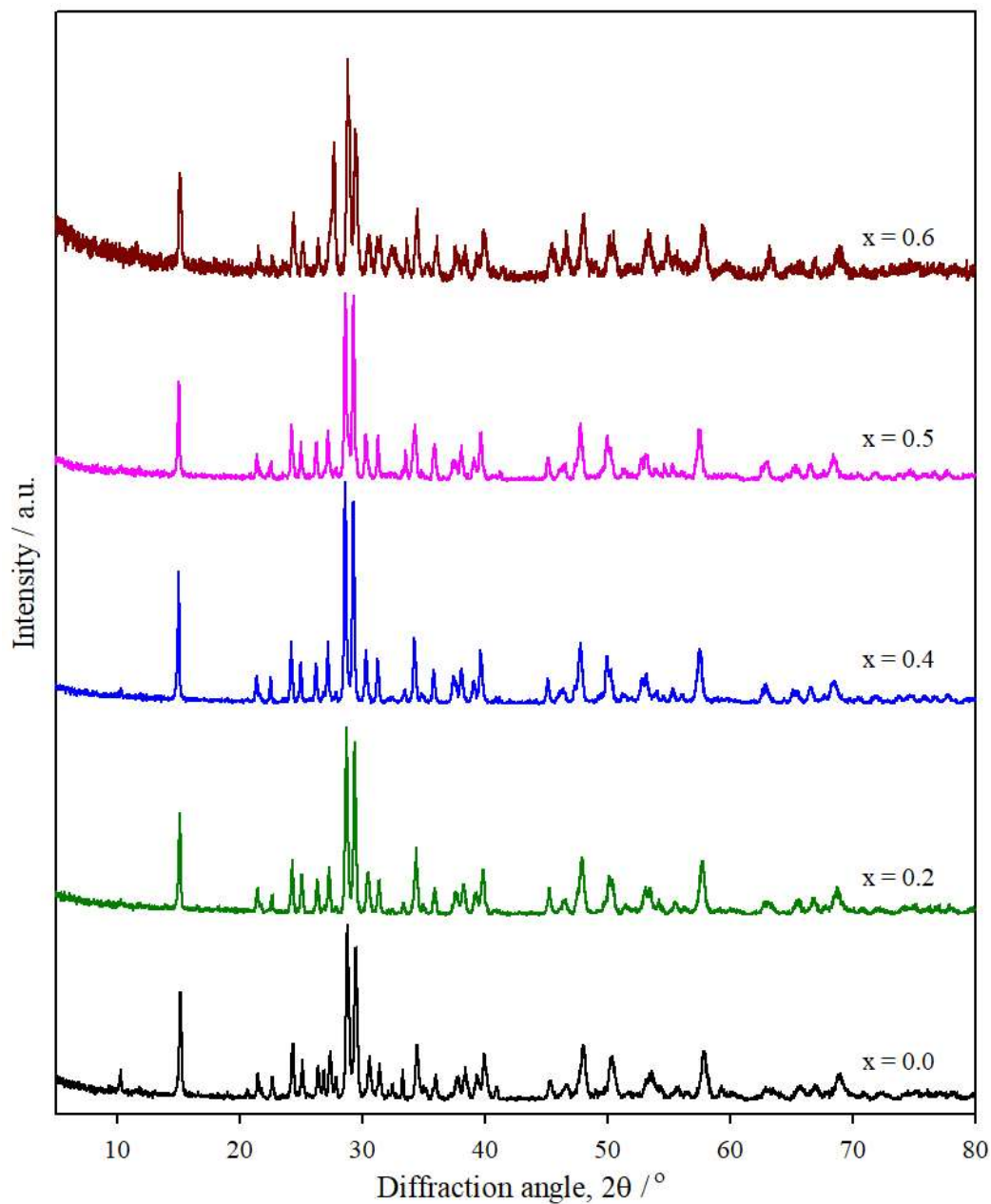
Fig. 2.24. XRD patterns of $Bi_2Fe_2(Cr_xAl_{1-x})_2O_9$ with different nominal compositions at 900°C. For clarity, the diffraction patterns are vertically plotted. All compositions show orthorhombic mullite-type phase, except x = 0.6 and x = 0.0.
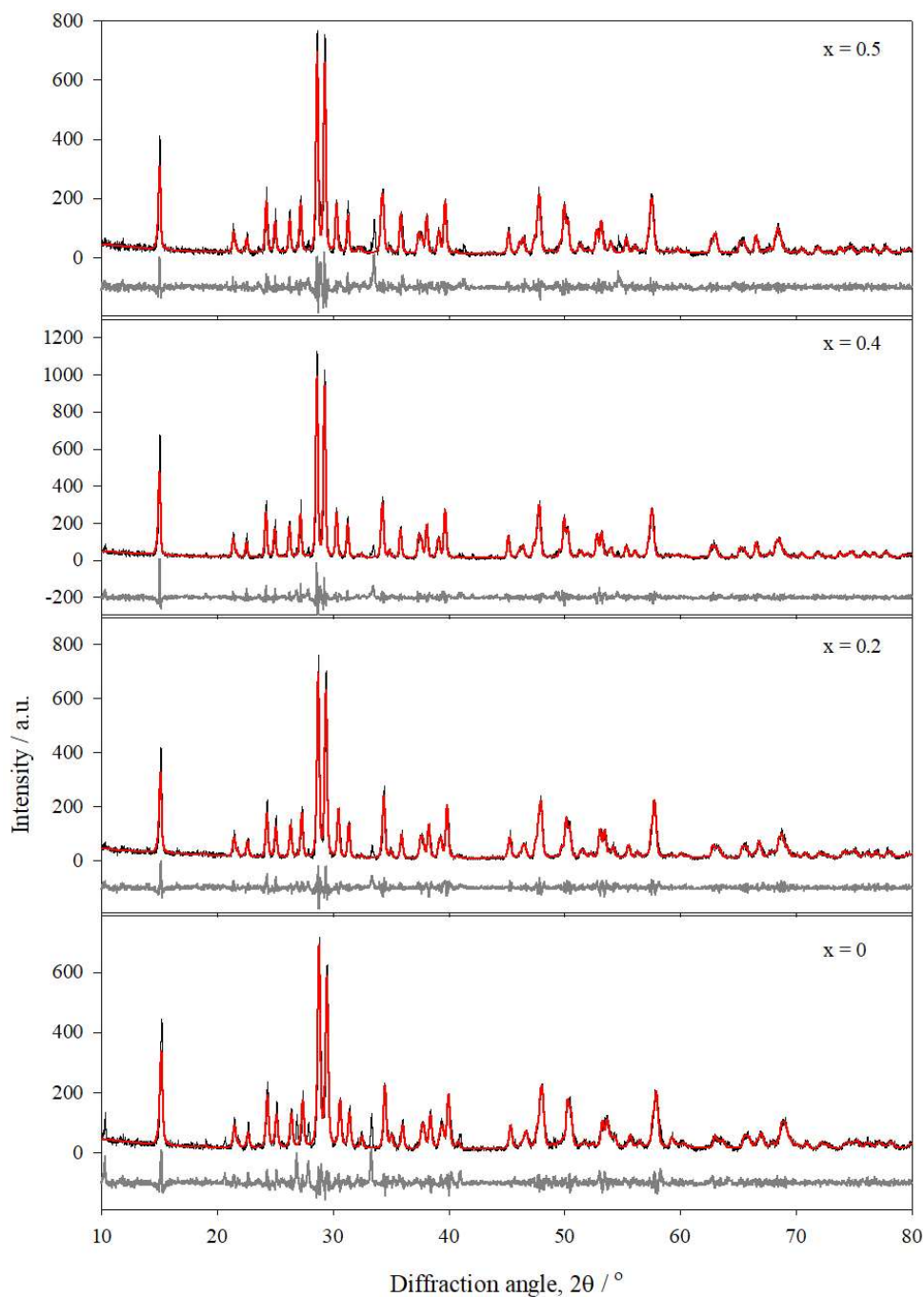
Fig. 2.25. Rietveld refinements fit of the $Bi_2Fe_2(Cr_xAl_{1-x})_2O_9$ (x = 0, 0.2, 0.4, and 0.5) series at 900°C. The black spectrum represents observed/measured spectrum, and the red spectrum represents calculated data. The black curve below the spectrum represents the difference spectrum.

Table 2.7 Cell parameter of $Bi_2Fe_2(Cr_xAl_{1-x})_2O_9$ at 900°C

Nominal compositions, x	a / pm	b / pm	c / pm
0.0	0.7852	0.8276	0.5846
0.2	0.7870	0.8287	0.5870
0.4	0.7892	0.8305	0.5897
0.5	0.7895	0.8306	0.5905

2.3.4.b FT-IR analysis of $Bi_2Fe_2(Cr_xAl_{1-x})_2O_9$

For all samples of $Bi_2Fe_2(Cr_xAl_{1-x})_2O_9$ series, the FT-IR spectra indicates the existence of absorption band in the region 500 to 900 cm^{-1} wave number which are a common feature of the mullite type orthorhombic phase of $Bi_2M_4O_9$ ($M = Al^{3+}$, Fe^{3+}, Ga^{3+}). The absorption band centered at about 860 cm^{-1} is due to M-Oc-M stretch (O_3M-Oc-MO_3 dimer), the band at 700 cm^{-1} for M-O stretch (MO_4), M-O-M bend (MO_6), O-M-M bend (MO_6) [32]. The higher frequency absorption band at 860 cm^{-1} split into a triplet, which is a characteristic spectral feature of mullite type $Bi_2Fe_2Al_2O_9$ phase. Voll *et al.* [33] reported that the high energy band centered at 900 cm^{-1} is due to stretching modes of tetrahedral pairs with Al on both sides (Al-O-Al), the band centered at about 866 cm^{-1} is assigned to stretching vibrations of the tetrahedral sides with Al and Fe (Al-O-Fe and Fe-O-Al) and the low energy band at about 826 cm^{-1} is owing to stretching modes with Fe on both tetrahedral sites (Fe-O-Fe). Debnath *et al.* [32] described that Cr can only partially substitute the octahedrally coordinated M in $Bi_2M_4O_9$, but no substitution of Cr occurs in MO_4 tetrahedra. Shifting of absorption bands toward lower wave numbers with increasing Cr^{3+} doping in mullite phase is associated with a local structural change.
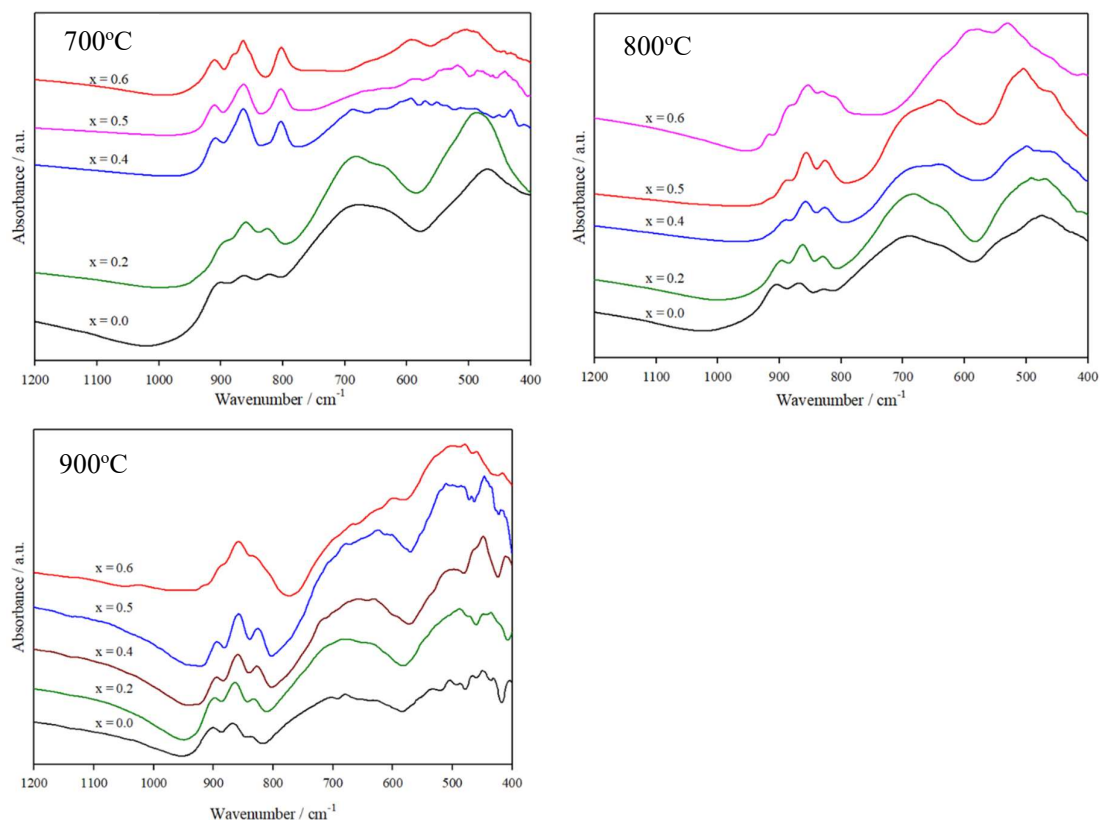
Fig. 2.26. FT-IR spectra of $Bi_2Fe_2(Cr_xAl_{1-x})_2O_9$ with different nominal compositions at 700°C. For clarity, the spectra are plotted vertically.

2.3.4.c SEM analysis of $Bi_2Fe_2(Cr_xAl_{1-x})_2O_9$

The surface morphology and microstructure of $Bi_2Fe_2(Cr_xAl_{1-x})_2O_9$ are observed using scanning electron microscopy (SEM) as shown in Fig. 2.27. The SEM images of $Bi_2Fe_2(Cr_xAl_{1-x})_2O_9$ clearly indicates that particle size increase with increasing calcination temperature. At nominal composition x = 0, cuboid-like particles are found at all studied temperatures but at x = 0.2, x = 0.4 cuboidal particles are observed only at ≥ 800°C. At x ≥ 0.5, the samples are polycrystalline at 900°C.

700°C	800°C	900°C
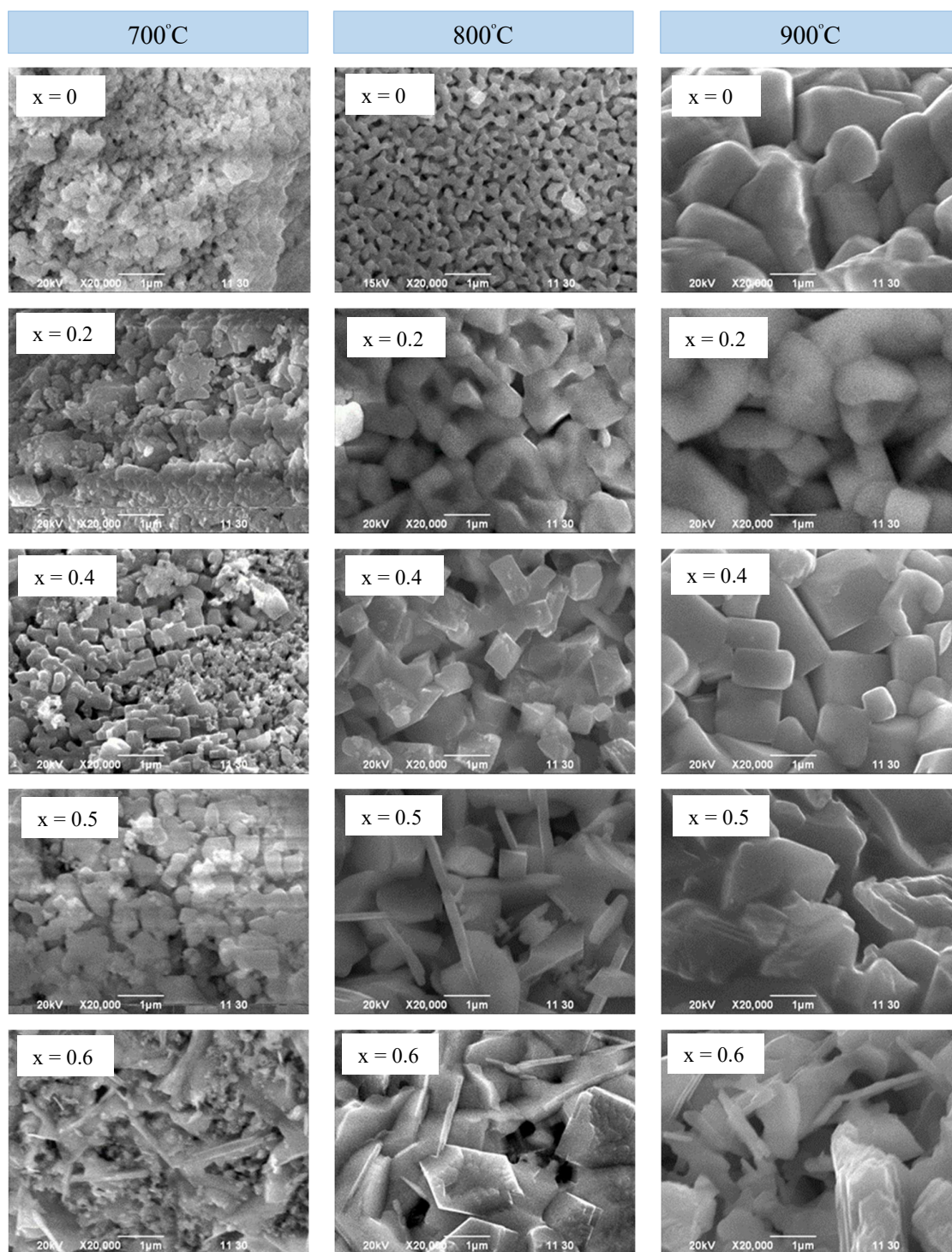
Fig. 2.27. SEM images of $Bi_2Fe_2(Cr_xAl_{1-x})_2O_9$ with different compositions at different temperatures.

2.3.4.d Color of Bi₂Fe₂(CrₓAl₍₁₋ₓ₎)₂O₉ solid solution series

It is observed that with increasing Cr content in mullite type $Bi_2Fe_2(Cr_xAl_{1-x})_2O_9$ system, the color of the doped samples systematically changes from deep red to black red.

2.3.5 Bi₂Fe(CrₓAl₁₋ₓ)₃O₃ series

The nonstoichiometric oxide solid solution $Bi_2Fe(Cr_xAl_{1-x})_3O_9$ series comprises a mixed oxide solution with x ranging 0, 0.2, 0.4, 0.5 and 0.6. This series of compounds was prepared from a homogeneous gel made by mixing the appropriate amount of metal nitrates, $M(NO_3)_3 \cdot xH_2O$ (M = Bi, Fe, Cr and Al) and glycerin. The new solid was obtained by the gel combustion method, calcined at 700, 800 and 900°C temperature and characterized by XRD, FT-IR spectroscopy and SEM microscopy. The members with nominal composition 0.0, 0.2 and 0.4 of this series belong to the family of orthorhombic mullite type crystal structures at studied temperature. In this context, we can conclude that the combustion method used in the present study characterizes an effective, simple and low cost protocol to synthesize $Bi_2Fe(Cr_xAl_{1-x})_3O_9$ solid solutions.

2.3.5.a XRD analysis of Bi₂Fe(CrₓAl₁₋ₓ)₃O₃ series

The XRD pattern of $Bi_2Fe(Cr_xAl_{1-x})_3O_9$ solid solutions (x = 0.0, 0.2, 0.4, 0.5 and 0.6) calcined at different calcined temperature are shown in Figs. 2.28, A.2.12 and A.2.13. The XRD pattern of $Bi_2FeAl_3O_9$ with nominal composition of x = 0.0 of ($Bi_2Fe(Cr_xAl_{1-x})_3O_9$ series) was indexed as mullite type orthorhombic phase at all temperatures. Presence of any extra line other than orthorhombic phase was not detected, ensuring a single phase formation of the product. The peaks become sharper with increasing calcination temperature, indicating increasing crystallite size. Compound with x = 0.2 show mullite type orthorhombic phase at > 700°C and with x = 0.4 show mullite type orthorhombic phase only at 900°C. Nominal composition with x = 0.5 and x = 0.6 does not show any mullite type orthorhombic phase even up to 900°C. It was reported earlier that the doped cations normally occupy the octahedral site in mullite in replacing Al^{3+}, though minor amount can enter into the oxygen tetrahedra. X-ray pattern of the compounds also indicates successful doping of Cr in the studied solid solution up to x = 0.4 (8.56 %) at 900°C. Thus, the incorporation of Cr^{3+} cation in the octahedral chain site is low even at higher temperature. Note that the incorporation of foreign cations in mullite depends on oxidation states and ionic radii, in addition to the temperature, pressure and chemical environment during incorporation. Profex software was used to refine the pure orthorhombic phase of

Bi$_2$Fe(Cr$_x$Al$_{1-x}$)$_3$O$_9$ series at 900°C (nominal composition x = 0, 0.2, 0.4) [45]. The calculated and measured XRD patterns are well-fitted, shown in Fig. 2.28. The calculated cell parameters are presented in Table 2.8. Cell parameter *a, c* slightly decreases then increase, but cell parameter *b* increases slightly with compositions.
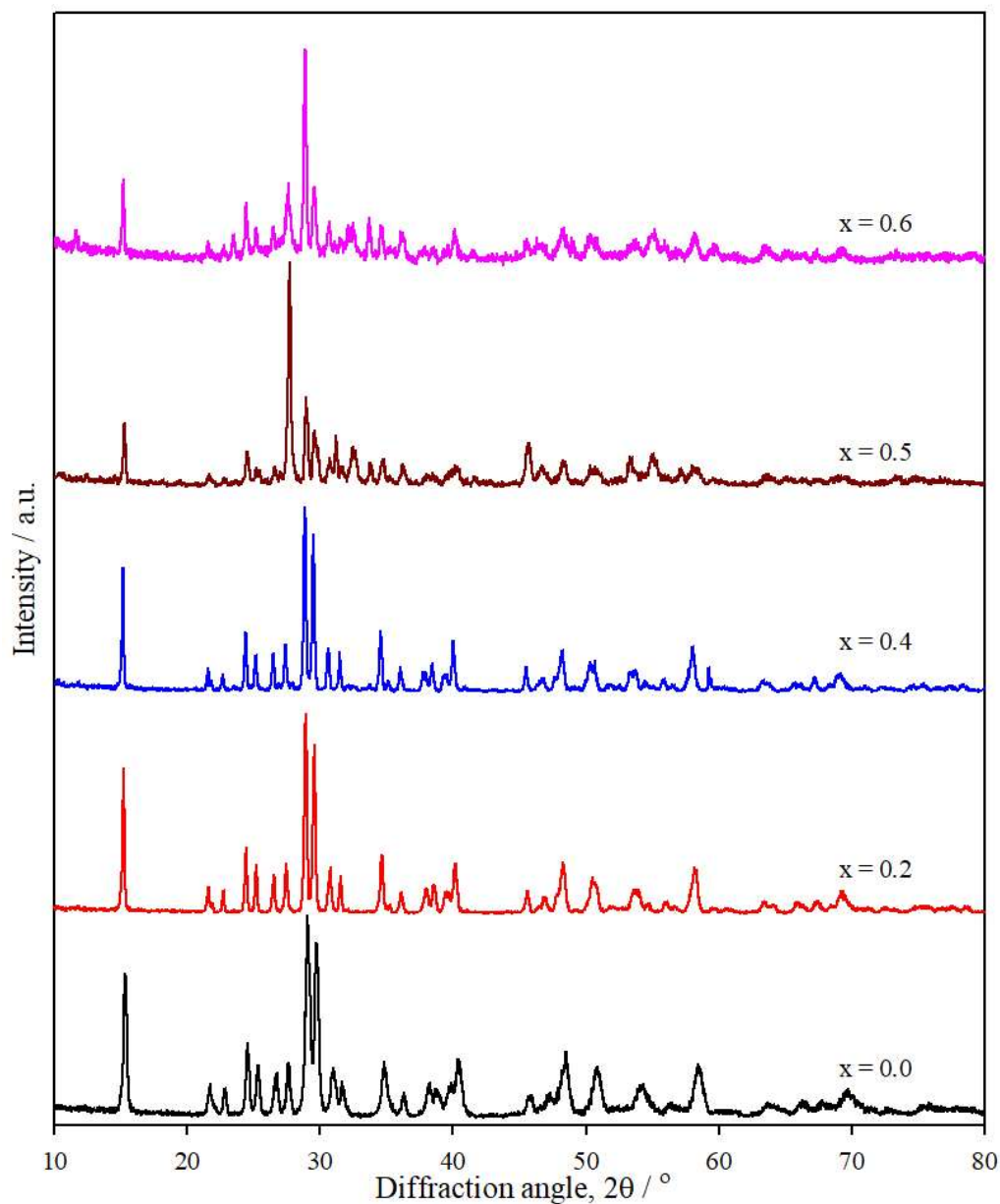
Fig. 2.28. XRD patterns of Bi$_2$Fe(Cr$_x$Al$_{1-x}$)$_3$O$_9$ with different nominal compositions at 900°C. For clarity, the diffraction pat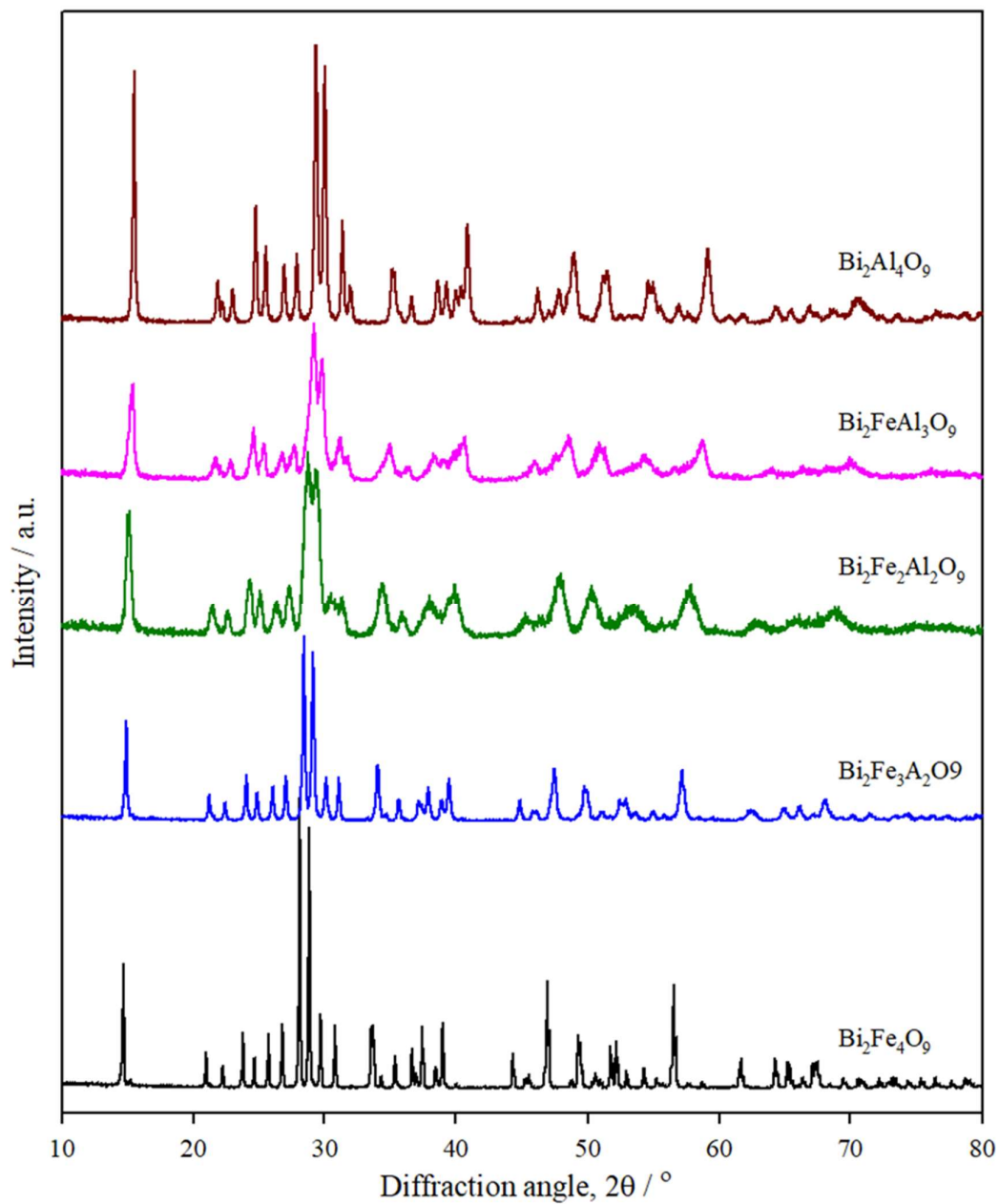terns are vertically plotted. The XRD patterns show that the nominal compositions, x = 0, 0.2, 0.4 form mullite type orthorhombic phase.
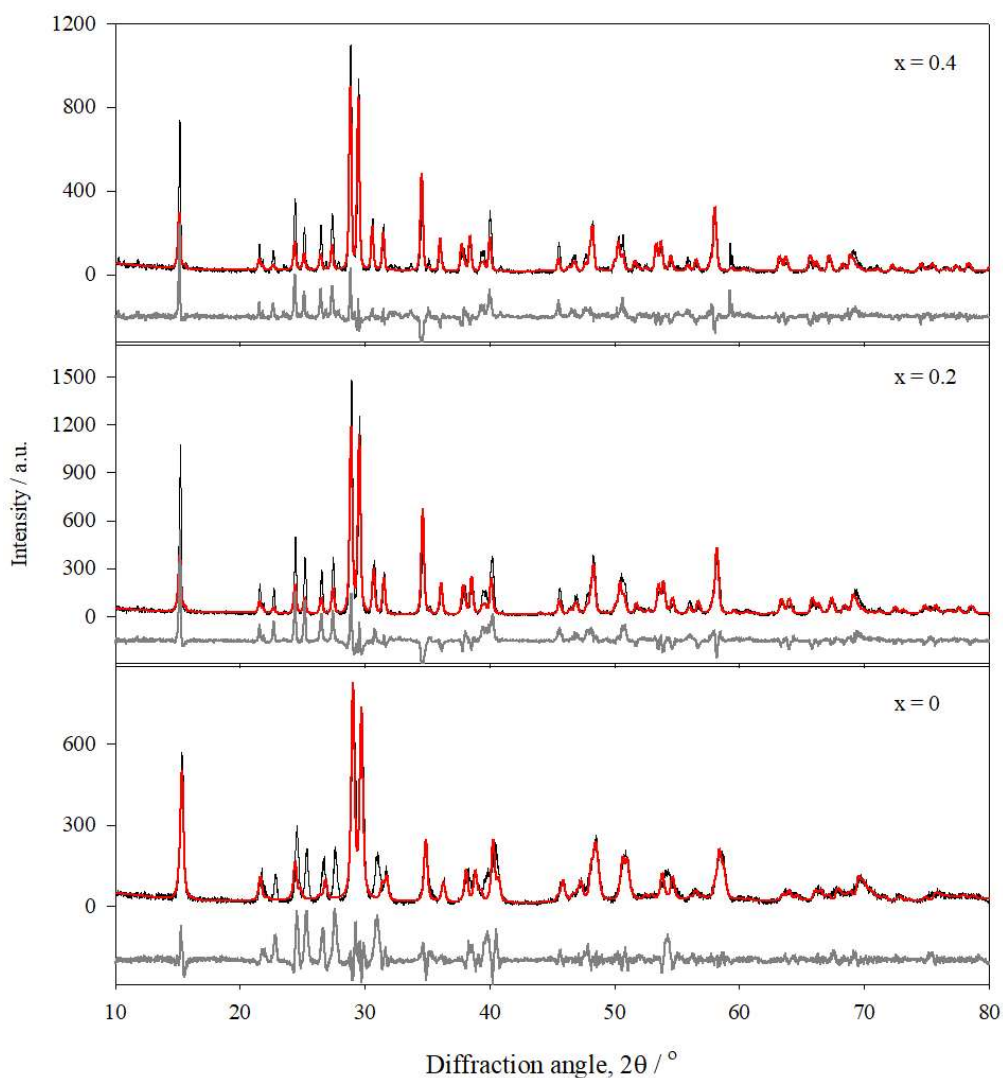
Fig. 2.29. Rietveld refinements fit of the $Bi_2Fe(Cr_xAl_{1-x})_3O_9$ (x = 0, 0.2, and 0.4) series at 900°C. The black spectrum represents observed/measured spectrum, and the red spectrum represents calculated data. The black curve below the spectrum represents the difference spectrum.

Table 2.8 Cell parameter of $Bi_2Fe(Cr_xAl_{1-x})_3O_9$ at 900°C

Nominal compositions, x	a / pm	b / pm	c / pm
0.0	0.7861	0.8078	0.5941
0.2	0.7818	0.8222	0.5810
0.4	0.7843	0.8239	0.5839

2.3.4.b FT-IR analysis of $Bi_2Fe(Cr_xAl_{1-x})_3O_3$

The FT-IR absorption spectra of $Bi_2Fe(Cr_xAl_{1-x})_3O_9$ (x = 0.0, 0.2, 0.4, 0.5, 0.6) are shown in Fig. 2.30. and the bands are compared to those observed in the same region for $Bi_2M_4O_9$ (M = Al^{3+}, Ga^{3+}, Fe^{3+}). Three broad bands centered around 590, 700 and 900 cm^{-1} are recognized as characteristics bands for the mullite-type orthorhombic phase. The bands are assigned as follows: at 900 cm^{-1} for M–Oc–M stretch (O_3M–Oc–MO_3 dimer), at 700 cm^{-1} for M-O stretch (MO_4), M-O-M band for (MO_4) and at about 590 cm^{-1} for O-M-O band (MO_6) [32]. However, the band at 900 cm^{-1} split, which is characteristics for $Bi_2Fe_yAl_{4-y}O_9$ compounds. Voll et al. [33] explained that the high energy band centered at about 900 cm^{-1} is due to the stretching modes of the tetrahedral pairs with Al on both sides (Al-O-Al). The band with maximum intensity centered about 866 cm^{-1} is assigned for stretching vibrations where Al and Fe enter tetrahedral sites (Al-O-Fe and Fe-O-Al) respectively and the low energy band (about 826 cm^{-1}) is assigned due to stretching modes with Fe on both tetrahedral site (Fe-O-Fe). Debnath et al. [32] explained that Cr can partially substitute only the octahedral coordinated M in $Bi_2M_4O_9$ and no substitution of Cr in MO_4 tetrahedra can occur. It is also observed that absorption bands shifted to lower wave numbers with increasing Cr doping in mullite phase is due to a change in local structure begin to occur. FT-IR spectra also comply with XRD pattern.
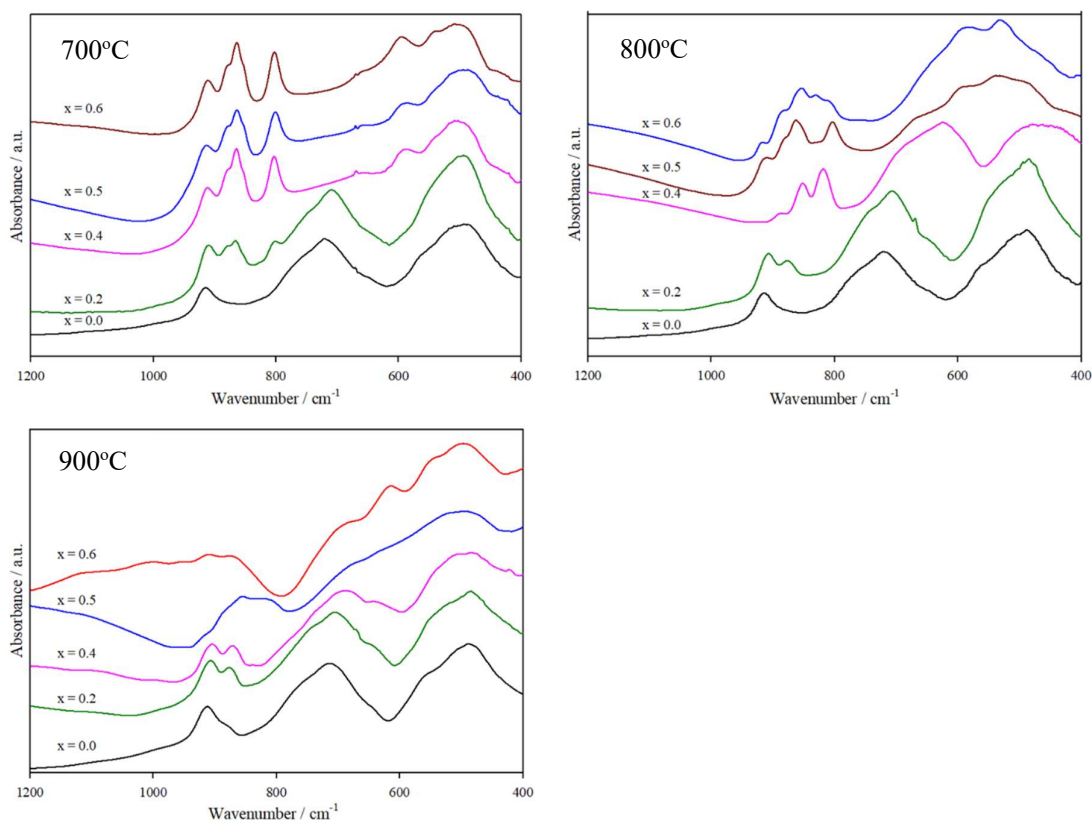
Fig. 2.30. FT-IR spectra of $Bi_2Fe(Cr_xAl_{1-x})_3O_9$ with different nominal compositions at different temperatures. For clarity, the spectra are plotted vertically.

2.3.4.c SEM analysis of $Bi_2Fe(Cr_xAl_{(1-x)})_3O_3$

The size and morphology of $Bi_2Fe(Cr_xAl_{1-x})_3O_9$ particles are examined by SEM (scanning electron microscopy). It is clearly observed from SEM images that the particle size increase with increasing calcination temperature. The shape of the particles changes from spherical to cuboid with increasing in Fe concentration. The images, at composition x = 0.0 shows granular spherical uniform particle at all temperatures while at x = 0.2 granular particle at $\geq 800^{\circ}C$. The particles are uniform cuboid only at $900^{\circ}C$ with composition x = 0.4. At higher composition x = 0.5 and x = 0.6, the samples are polycrystalline at all temperatures.

700°C	800°C	900°C
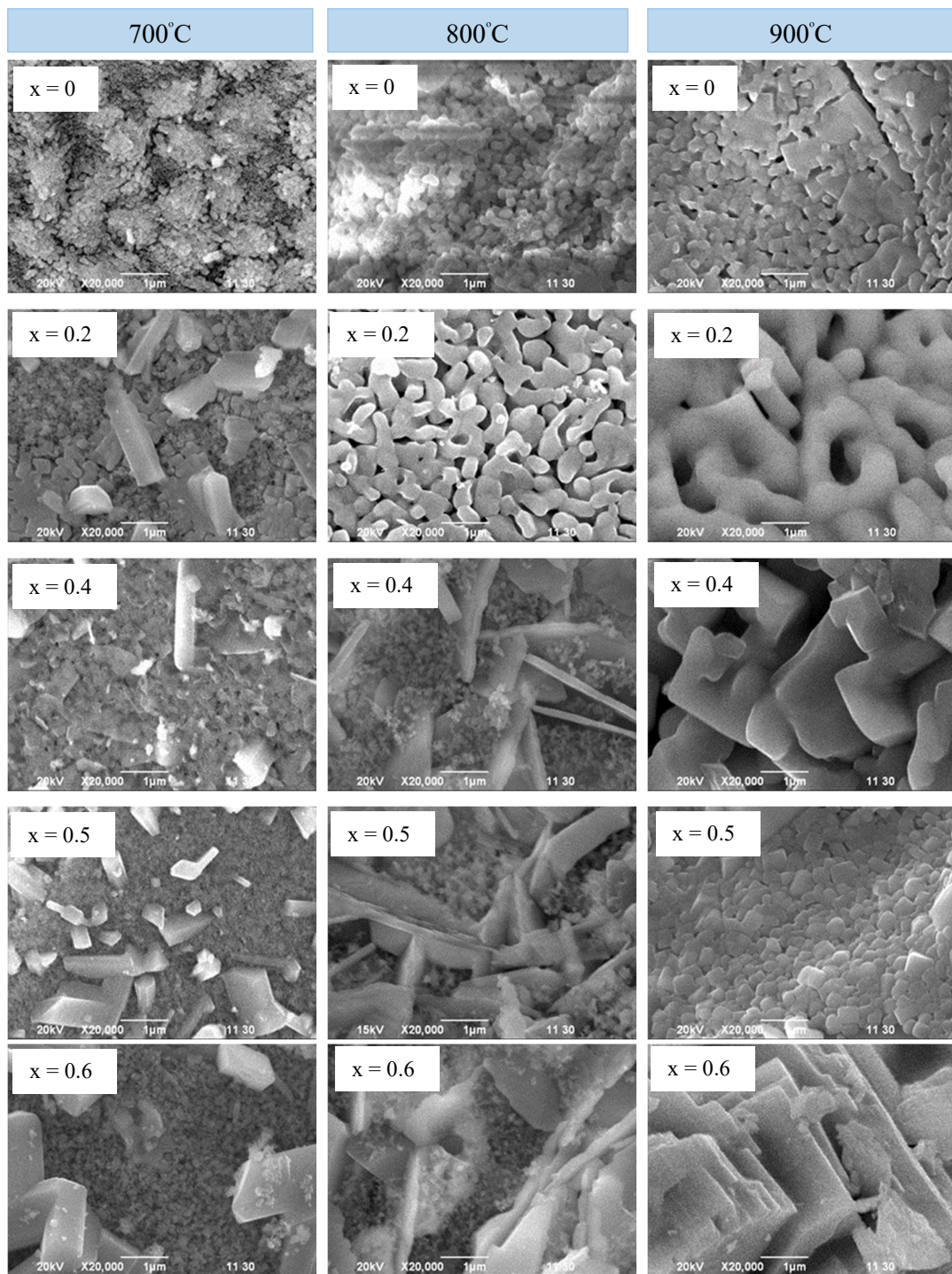
Fig. 2.31. SEM images of $Bi_2Fe(Cr_xAl_{1-x})_3O_9$ with different compositions at different temperatures.

2.3.4.d Color of the prepared $Bi_2Fe(Cr_xAl_{(1-x)})_3O_9$ series

It is observed that color of the prepared $Bi_2Fe(Cr_xAl_{1-x})_3O_9$ samples changes from yellowish red to greenish black with increasing Cr content.

Conclusion of bismuth metallates

This work aims to study bismuth metalates solid solution obtained by gel combustion synthesis a modified solution combustion synthesis (SCS) was developed in the mid-1980s. In some cases, SCS and sol-gel combustion synthesis are used in the same way. However, there is a difference between these methods. In the case of gel combustion synthesis (GCS), the initially prepared form can be a gel or an aqueous solution that is dried at a temperature below the boiling point of the solvent for the gel-type media. The gelatin process provides accurate control of cationic stoichiometry and a homogeneous mixture of metal ions at the atomic level. The gel in a glass or ceramic container was placed on a hot plate or inside a hot furnace. Generally, the temperature of a furnace or hot plate can reach 300-500°C. Heating, formation and decomposition of the gel, self-ignition, combustion, and the solid-forming process continue in one technological step. This method is the most commonly used method of heating GCS. This process, in fact, is characterized by a hot, fast and independent reaction, the formation of high purity products of various sizes and shapes, simple processes, the use of simple machines and cheap reactants.

A new series of polycrystalline materials $Bi_2Cr_xGa_{4-x}O_9$ has been synthesized by gel combustion method using the mixture of corresponding metal nitrates and glycerin followed by calcination in air at 800°C. Rietveld refinement of XRD of powder data shows that the lattice parameter a remains almost constant with increasing nominal Cr content. But in case of b cell parameters decreases up to nominal composition 1.0 then remain almost constant. Cell parameters c increases slightly up to nominal composition 0.6, and then it remains almost constant. Unit cell volume remains almost constant. Characteristics four bands for the mullite type orthorhombic phase of $Bi_2M_4O_9$ observed clearly in FT-IR spectrum. No splitting of IR absorption peak of $(850\ cm^{-1})$ $O_3Ga-O_c-GaO_3$ stretching mode reveal that no $O_3Ga-O_c-CrO_3$ and $O_3Cr-O_c-CrO_3$ type bonding were present in $Bi_2Cr_xGa_{4-x}O_9$ solid solution series. This indicates that Cr partially substitutes only the octahedrally coordinated Ga in $Bi_2Ga_4O_9$. As the crystal radius of Cr^{3+} (75.5 pm) at six-fold coordination is very close to Ga^{3+} (76 pm) and due to strong ligand field stabilization

energy of Cr^{3+} in six-fold coordination, Cr^{3+} can substitute Ga^{3+} in GaO_6 octahedra and slightly shrinkage in octahedral site is favorably supported by XRD and FT-IR analysis. Characteristics absorption peak for Ga-O stretch at GaO_6 octahedra at 470 cm^{-1} slightly shifted to higher wavenumber with increasing Cr concentration due to decrease of octahedral Ga-O and Cr-O distance.

Crystalline $Bi_2Fe_xAl_{4-x}O_9$ (x = 0,1, 2, 3, and 4) has been synthesized by gel combustion method using appropriate amounts of nitrate salts of corresponding metals and glycerin, stirring to make a gel and then calcining in a calibrated furnace. Each member of this series at all studied temperatures belongs to the family of orthorhombic mullite type structures characterized by the edge sharing MO_6 octahedra forming chains running parallel to the crystallographic c-axis. The synthesized samples are well crystalline, and both the crystallinity and the grain growth develop with increasing calcination temperature. The XRD, FT-IR and SEM analysis strongly support this observation. Careful observation of the XRD pattern of the $Bi_2Fe_xAl_{4-x}O_9$ series also reveals that in the sample with increasing Al content form $Bi_2Fe_4O_9$ and $Bi_2Al_4O_9$, the peaks have been shifted to higher angles. This shift is related to the distance between crystalline planes, leading to the reduction of lattice parameters [84].

Bismuth based solid solution series, $Bi_2Fe_3(Cr_xAl_{1-x})O_3$ (x = 0.0, 0.1, 0.2, 0.4, 0.5, 0.6), $Bi_2Fe_2(Cr_xAl_{(1-x)})_2O_3$ (x = 0.0, 0.1, 0.2, 0.4, 0.5, 0.6) and $Bi_2Fe(Cr_xAl_{1-x})_3O_3$ (x = 0.0, 0.1, 0.2, 0.4, 0.5, 0.6) have been synthesized by the gel combustion method in the present study. The initial precursor has been made by taking appropriate amounts of nitrate salts of corresponding metals and glycerin according to desired stoichiometry at room temperature, stirring vigorously to make an excellent chemically homogeneous gel followed by calcination treatment at temperatures varying from 700 to 900ºC. XRD, FT-IR and SEM data showed that members of each series at least at an x composition and at a temperature adopt mullite type phase. From XRD pattern, it is revealed that solid solution series $Bi_2Fe_3(Cr_xAl_{1-x})O_9$ form mullite type orthorhombic phase at all studied composition at 900ºC. For $Bi_2Fe_2(Cr_xAl_{1-x})_2O_9$ series, all studied compositions show orthorhombic mullite-type phase except x = 0.6 compounds. But solid solution series $Bi_2Fe(Cr_xAl_{1-x})_3O_9$ form mullite type orthorhombic phase only up to nominal composition x = 0.4. FT-IR spectra follow the similar trend as XRD pattern. It is reported that depending on the synthesis temperature and atmosphere, mullite is able to incorporate a number of transition/non-transition metal cations and other foreign atoms. As the crystal radius values

of Al^{3+} (67.5 pm) and Cr^{3+} (75.5 pm) are close to that of Fe^{3+} (78.5 pm) so, it is likely that Al^{3+} and/or Cr^{3+} cations can substitute Fe^{3+} ion in the lattice of bismuth based solid solution series. Substitution by metal ions primarily occurs in the octahedral site in mullite, although minor amounts can also enter the oxygen tetrahedra, MO_4, cited in the literature. Particle size of mullite type phase increased gradually with increasing combustion temperature and Cr content. The increase in the particle sizes could be due to the merging of the smaller particles into larger ones with increasing temperature. The crystal structure, phase formation, and crystallite size were confirmed with XRD, FT-IR and SEM data.

Chapter Three
Alkali Metal Tungsten Oxides

3.1 Structures and properties of tungsten oxides, tungsten bronzes and tungsten bronzoids

Stoichiometric tungsten oxide generally denoted by WO_3 coexists with a little amount of WO_2 also [85]. These two crystal phases are made from WO_6 building blocks, as shown in Fig. 3.1. Here, six oxygen ions form an octahedron around the tungsten ions, with each oxygen ion exactly positioned between two tungsten ions. In WO_3, each oxygen ion is shared by two corner shared blocks. On the other hand, in WO_2 each oxygen ion is shared by three edge-shared blocks.
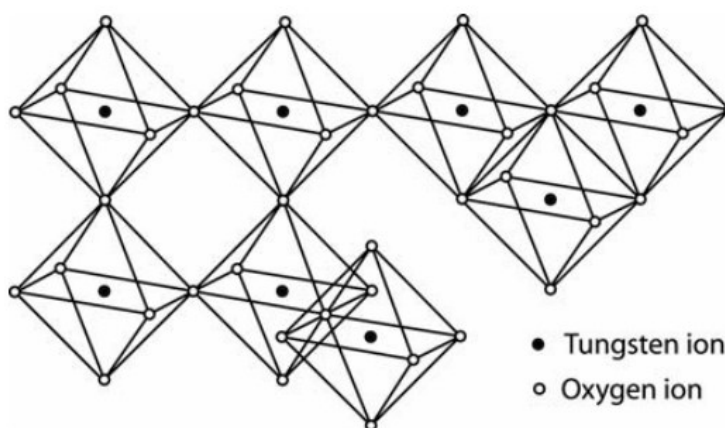
Fig. 3.1. Schematics of the construction of WO_6 blocks where each tungsten ion is octahedrally surrounded by six oxygen ions and one oxygen ion exists in between two tungsten ions. The left side shows corner-shared oxygen ions (WO_3) and the right side shows edge-shared oxygen (WO_2) [85].

However, tungsten tri-oxide (WO_3) undergoes complex structural distortion upon heating and experiences numerous transitions. Due to the distortion of the WO_6 octahedra, all of the polymorphs have very low symmetry. The structure of WO_3 is sensitive to both temperature and pressure, and an increase in either will lead to a slightly distorted structure and a corresponding symmetry change. Howard *et al.* reviewed the detailed determination of phase transition by high resolution neutron powder diffraction from room temperature to 1000°C [86, 87]. The WO_3 structure changes with temperature, from low temperature monoclinic (below ~ - 43°C), via triclinic structure (~ - 43°C – 17°C), room temperature monoclinic structure (~17°C – 330°C), orthorhombic (~ 330°C – 740°C) and to tetragonal structure (above ~ 740°C) [88, 89]. Electrochromic devices based on WO_3 are being studied for smart film

applications with changeable modulations in optical spectra [90]. Semiconductor tungsten trioxide (WO_3), structurally very similar to perovskite, can be used for many chromic windows [91].

A collective name of materials where ions are incorporated into the crystalline tungsten oxide is termed tungsten bronzes (TB). The general formula of TB can be written as A_xWO_3, where A is usually an alkali metal (Li, Na, K, Rb or Cs) or any other mono or divalent metal of appropriate size. The name bronze was first given in 1823 by the German chemist Friedrich Wöhler due to the metallic shine of the compounds [92, 93]. Tungsten bronzes are essentially non-stoichiometric compounds having a common formula, A_xWO_3, which is formed by a WO_3 matrix and doped cation A^{n+} with different x compositions ($0 < x < 1$) [89, 94 and 95]. Here, the cation (A^{n+}) is an electropositive element of group 1, 2, 12, or 13, lanthanide series. The doped ions that are responsible for the coloration travel through the relatively larger tunnels between the WO_6 blocks. The sites of A ions in the tunnel are, in most cases, only partly occupied, and the tungsten atoms are slightly moved from the center. As a result, octahedra are slightly distorted. The electronic properties of the materials can be modified by the cations' mobility in the WO_3 framework.

Crystal structure of tungsten bronzes changes with various alkali metals (A) and x. When $0.15 \leq x \leq 0.33$, $(Cs, K \text{ and } Rb)_xWO_3$ exists in a hexagonal structure, though Na_xWO_3 shows a different crystal structure with increasing x value (0 to 1) undergoing transition from monoclinic-orthorhombic, then tetragonal, and lastly, cubic. In hexagonal alkali tungsten bronze, A_xWO_3, the corner-shared WO_6 octahedra form six member rings such as a channel along the c-axis and alkali metal ion (A^+) ions reside in the central position of the channel. The radius of the hexagonal channels is nearly 1.63 Å, while the radius of alkali metal ions, namely Cs^+, Rb^+, and K^+, are 1.69, 1.47, 1.33 Å, respectively. The K^+ ion is lighter and smaller compared to Cs^+ and Rb^+, so they bind less strongly in the WO_3 lattice. Tungsten bronzes also exhibit a wide range of interesting physicochemical properties [96-103]. Some of the properties of tungsten bronzes are described below in brief:

Electrical properties: In 1963, shanks *et al.* described when $x > 0.25$, the alkali metal tungsten bronzes $(Li, Na, K)_xWO_3$ show metallic behavior and when $x < 0.25$ show semiconducting properties [104]. The electrical resistivity is independent of the alkali metal type but depends

on x-composition. It has been suggested that electrons, released when the inserted alkali atoms are ionized, are conducted readily through the tungsten t_{2g} and oxygen π orbitals.

Electronic properties: The superconducting properties of tungsten bronze have been known for long [100]. The alkali metal hexagonal tungsten bronzes, $(K, Rb, Cs)_xWO_3$ exhibit superconductivity with T_c around 1.5 K. [105, 106]. Since the empty W 5d orbitals were hybridized with the O 2p, that results an empty valance band and conduction band, the WO_3 matrix is an insulator. Alkali metal cations contribute to their s electrons to the conduction band of the matrix of WO_3 and generate metallic as well as superconducting transitions [96].

Magnetic properties: It was reported that rubidium, a few lithium and potassium bronzes show diamagnetism, though sodium bronzes' paramagnetic property is low [23, 107]. Magnetic susceptibility measurements of cubic Na_xWO_3 single crystal cubes (x = 0.49, 0.76 and 0.85) revealed that they were paramagnetic and become temperature independent from 70 K to 300 K [108]. Similar observations were found for the powder alkali metal tungsten bronze [109].

Optical properties: An identical relationship among the color and valance of metal atoms has been reported for tungsten bronzes. The proportion of pentavalent and hexavalent tungsten atoms in the crystal lattice is greatly connected with color changes of these types of oxides. The deep blue color of hexagonal $K_{0.3}WO_3$ has been found to have faded to a creamy color due to the continuous dilution of W^{5+} with Ta^{5+} in the $K_{0.3}(W^{6+}_{0.7}W^{5+}_{0.3-y}Ta_y)O_3$ solid solution series. Similar findings were made for the $K_{0.3}(W^{6+}_{0.7}W^{5+}_{0.3-y}V_y)O_3$ series, whose color ranges from deep blue to brownish blue [110]. Donor atoms introduce electrons into the WO_3 lattice in tungsten bronzes $A_x(W^{6+}_{1-x}W^{5+})O_3$, which are induced by electron-phonon coupling strongly and form polarons instead of free electrons. Due to this property, tungsten bronzes show strong absorption properties in the near infrared region, which can be tailored by increasing metal concentration in the visible region. Therefore, the optical appearance of sodium tungsten bronze changes from green-blue-grey due to the concentration of polaron increasing from zero to over the metal insulator transition [111-114]. It is also found that cubic Na_xWO_3 shows various colors depending on the ratio of W^{5+}/W^{6+} cations present in the lattice.

Chemical properties*:* The chemical analysis of tungsten bronzes is very difficult due to the inertness of these types of compounds toward water and other common solvents. Due to this

inertness, elevated activation energy is required for the transmission of alkali metal in WO_3-matrix [115]. Tungsten bronzes react with the chemicals which can attack WO_3 lattice, thus introducing cations in tunnels protected from the common reagent. Therefore, strong acids do not react with tungsten bronze. Tungsten bronzes have many interesting applications based on these properties, such as in strong acidic solutions, where these materials can be used as catalysts. In alkali media, tungsten bronzes are known to be the oxidized to tungstate of A^+ cation and they can convert ammoniacal silver nitrate, which can be used for the quantitative analysis of this type of material. Strong acceptors of electron such as tungsten (VI) or iodine are able to degrade Na_xWO_3 to a very close composition of WO_3 compound, and molecular hydrogen (electron donors) can convert compounds composition closer to $NaWO_3$, [116-118]. Hydrogen tungsten bronze (H_xWO_3) is closely related to the structure of Na_xWO_3 and is very reactive [119, 120]. They have the tendency to be attacked by air gradually and oxidized quickly by hot chromic acid.

The nonstoichiometric tungsten bronzes of type $A_x(W^{5+}_xW^{6+}_{1-x})O_3$ indicate the existence of W^{5+} and W^{6+} in the same bronze composition. Substitution of pentavalent W with other pentavalent metals like Nb/Ta is possible [24, 25, 99 and 121]. As a result, the fully oxidized phases of tungsten oxide material W^{5+} cation are completely substituted by other low valence cations, forming a structure similar to bronzes known as bronzoid [121]. The resultant phases are completely oxidized compounds. Li^+, Mg^{2+}, Cr^{3+}, Ti^{4+}, Mo^{6+} cations can partially replace tungsten in tungsten bronze. Due to this substitution, the properties of tungsten bronze are expressively modified. Replacement of W^{5+} cations by Nb^{5+} and Ta^{5+} is very common in literature. This type of compound shows greater electrical resistivity because of the d^0 electronic configuration of Nb^{5+} and Ta^{5+} cations, but their compositional and structural views are the same as bronze compounds [122-126].

Miyamoto *et al.* prepared a solid solution series $Na(Nb_xW_{1-x})O_3$ at 1823 K and 6 GPa and discovered five perovskite-related phases: three orthorhombic phases (for $0 \le x \le 0.16$, $0.20 \le x \le 0.40$ and $0.40 \le 0.52$) and two cubic phases (for $x = 0.16$ and $0.52 \le x \le 1$)[125]. Dey *et al.* reported Nb and Mo substituted cubic Li_xWO_3 and hexagonal Cs_xWO_3 tungsten bronze systems [37, 124]. Dudson *et al.* worked on Ta substituted Na_xWO_3 [99, 126]. Hussain *et al.* reported Nb^{5+} substitution in hexagonal potassium and rubidium tungsten bronze [23]. In addition, Debnath *et al.* reported Nb^{5+} substitution in cubic Na_xWO_3 and tetragonal K_xWO_3

[21, 26]. Also, Ta^{5+}, V^{5+} substituted hexagonal potassium tungsten bronze was prepared by Shakil *et al.* using the solid state synthesis method. [36].

For different value of x ranging from 0 to 1, one or more structural phase transitions of tungsten bronzes $A_x(W^{5+}_xW^{6+}_{1-x})O_3$ are known. The high value of x results in high symmetry and the low value of x produces low-symmetry phase [99, 127]. The crystal structure of tungsten bronzes or bronzoids, $A_x(W^{5+}_xW^{6+}_{1-x})O_3$, is made up of corner-shared WO_6 octahedra that form various types of channels in which A^+ cations are found. These octahedral units form a 3 to 6 membered ring, which depends on the type of A^+ cation and concentration x. Tungsten bronzes are classified into several types based on the amount, size of the atom of interstitial metal and the temperature of synthesis.

In 1953, Magnéli invented the HTB structure for $Rb_{0.29}WO_3$ [95]. Because the HTB channel is larger than the PTB and TTB channels, large cations can easily be located [128]. Cations of alkali metals (K, Rb, Cs) and other cations/ions such as NH_4^+, Ba, Ca, Tl, Sn, Nd etc. formed HTB structures [129-132] and the theoretical metal content $x_{max} = 0.33$, when the hexagonal tunnels are completely occupied. For x = 0.19 to 0.33, a similar oxidized structure is known as HTB bronzoid [133-135].

● W and V
● O
● K/Rb/Cs

b

a
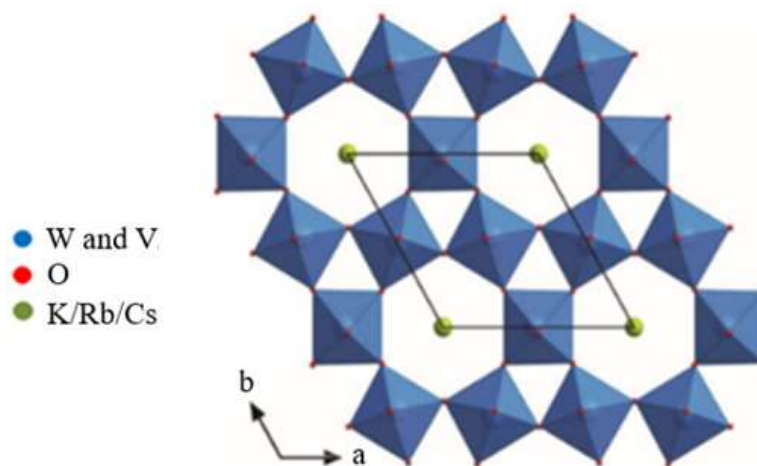
Fig. 3.2. Crystal structure of hexagonal tungsten bronze/bronzoid (HTB)

Bronzoid can be represented with a general formula $A_xT_xW_{1-x}O_3$, where A is K, Rb and Cs; T is V or Nb or Ta; x ranges from 0.20 - 0.30. The higher value of hexagonal tungsten bronzoid

and reduced bronzes is the same (0.33) [133, 134]. But the lower limit is 0.20 when A = K or Rb and T = Nb or Ta, and when A = Cs and T = Nb, x is 0.20 - 0.25. In intergrowth tungsten bronze (ITB) a hexagonal tunnel of a single row is detached by n slabs of WO_6 octahedra, where n = 2, 3, 4, 5, which is known as (n)-ITB, and a twin row is detached by n slabs of WO_6 octahedra known as (1, n)–ITB [135]. Sharma *et al.* [24] described an intergrowth tungsten bronzoid (ITB) series $Cs_xNb_xW_{1-x}O_3$ where x ranges from 0.08 to 0.12.

Table 3.1 Collected x value for different tungsten bronzes [96, 128, 135-137]

$A_x(W^{5+} W^{6+}_{1-x})O_3$	A = Li	A = Na	A = K	A = Rb	A = Cs
PTB	0-0.5	0-0.95			
TTB		0.26-0.3	0.4-0.59		
HTB			0.22-0.31	0.16-0.33	0.16-0.33
ITB			0.06-0.1	0.06-0.1	0.33-0.1

A_xWO_3 with nano size has significant solar-heat shielding properties while alkali ions like K, Rb and Cs are inserted to form a hexagonal structure. $Cs_{0.33}WO_3$ can be used in a variety of automotive and architectural windows as solar control films and laminated glasses [13, 139, 138]. Tungsten bronzes can also be used as heterogeneous catalysts. This opportunity stops the attraction of bronzes to oxygen atom and includes a transfer of electron between adsorbate-adsorbent, and the process is composition dependent [140-142]. Platinum bronze, Pt_yWO_3 electrode where y is a minimum of 0.5, catalytic activity is equal to Pt electrode but cheaper than Pt electrode and more corrosion resistant. This electrode is useful for fuel cells where an acid electrode (H_2SO_4 or H_3PO_4) is used and can be employed as an oxygen (cathode) electrode [140]. Tungsten bronze electrodes can be used in different electrochemical systems as indicators. The bronze electrodes can be used as potentiometric indicator electrodes for dissolved oxygen in aqueous media, which is useful in the field of environmental research due to the high sensitivity and the magnitude of potential change per unit variation of the conversion of oxygen [143]. They can used for pH, pM determination for some specific reducible species like Ag and Hg to monitor the change in potential involve in some redox systems [140].

Thus, bronzes of tungsten or bronzoid materials have a variety of appealing properties like intense color, metallic shine, and metallic or semi-metallic conductivity towards acids and

alkalis. Their electrical, optical and magnetic properties are also very interesting. However, these properties vary significantly with inserted cations' concentration and nature; synthesis methods, preparation temperature and pressure, keeping environment.

3.2 Experimental of alkali metal tungsten oxides

3.2.1 Preparation of nonstoichiometric alkali metal tungsten oxides

Solid solution series $K_xV_xW_{1-x}O_3$ (x = 0.15, 0.20, 0.25, 0.30)

Nonstoichiometric compounds with the formula $K_xV_xW_{1-x}O_3$ are fully oxidized because all tungsten atoms are in the W^{6+} state. Solid solutions with nominal compositions $K_xV_xW_{1-x}O_3$ (x = 0.15, 0.20, 0.25 and 0.30) were synthesized via the solution combustion synthesis (SCS) method. The precursor materials used were of the highest quality reagent grade KNO_3 (Sigma Aldrich, Germany), NH_4VO_3 (Sigma Aldrich, Germany), NH_4NO_3 (Sigma Aldrich, Germany), H_2WO_4 (Sigma Aldrich, Germany) and aqueous ammonia (Sigma Aldrich, Germany). All reactants were taken appropriate molar proportion according to the following equation:

$$xKNO_3 \ + \ xNH_4VO_3 \ + \ (1-x) H_2WO_4 \ \rightarrow \ K_xV_xW_{1-x}O_3 \dots\dots\dots\dots\dots\dots..eq. 3.1$$
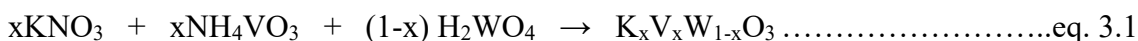
An exact amount of tungstic acid and potassium nitrate (KNO_3), ammonium vanadate (NH_4VO_3), and ammonium nitrate (NH_4NO_3) were dissolved in minimum volume of aqueous ammonia. Glycerin was added to this mixture. Ammonium nitrate and glycerin acted here as an oxidizer and a fuel, respectively. The ratio of n(glycerin) to n(NH_4NO_3) = 1:8 was kept in all the experiments. The solutions were then heated at 120°C to a viscous gel to prevent premature ignition. The gel was then heated at 200°C for 3 hours, which led to the formation of the fluffy mass. The fluffy mass was then grounded in an agate mortar to get the fine powder and then placed in a porcelain crucible. Finally, the fine powder was calcined in a muffle furnace at temperatures through the range of 300°C to 800°C with a 100°C interval for 24 hours in each case to get the desired products.

Solid solution series $Cs_xV_xW_{1-x}O_3$ (x = 0.15, 0.20, 0.25, 0.30)

Attempts were taken to prepare the $Cs_xV_xW_{1-x}O_3$ (x = 0.15, 0.20, 0.25, 0.30) series using the same procedure as described for the preparation of the $K_xV_xW_{1-x}O_3$ solid solution series. But in this case, cesium carbonate was used as a source of cesium and the reactants were taken in appropriate molar proportions according to the following equation:

$x/2$ Cs_2CO_3 + xNH_4VO_3 + $(1-x)$ H_2WO_4 → $Cs_xV_xW_{1-x}O_3$ …………………………eq. 3.2
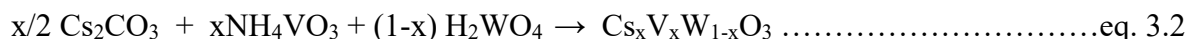
Solid solution series $Rb_xV_yW_{1-y}O_3$ (x = 0.25, 0.30 and 0.0 ≤ y ≤ x)

The series of compounds $Rb_xV_yW_{1-y}O_3$ with composition y < x can be described as a reduced solid solution phase because of the presence of both W^{6+} and W^{5+} in these compounds. A non-oxidizing atmosphere is required to prepare these types of nonstoichiometric solid solutions. Polycrystalline compounds with nominal compositions of $Rb_xV_yW_{1-y}O_3$ (x = 0.25, 0.30 and 0.0 ≤ y ≤ x) are collected from Istiak [144] for further characterization. They were synthesized by the conventional solid state method in evacuated SiO_2 glass ampoules. Appropriate amount of the reactants were taken according to the equation 3.3 and mixed thoroughly in an agate mortar and transferred into dried silica glass tubes (6.0 mm inner diameter and about 100 mm long, preheated at 700°C for overnight). The samples tubes were then evacuated at 10^{-2} Torr at room temperature by means of a mechanical pump for two hours and sealed. The prepared reaction tubes were isothermally heated in a Muffle furnace at 700°C for 4 days and finally quenched in water within a few seconds after the tubes were taken out of the Muffle furnace.

$x/2$ Rb_2WO_4 + $(1-x-y/2)WO_3$ + $(x/2-y/2)WO_2$ + $y/2V_2O_5$ → $Rb_xV_yW_{1-y}O_3$…...eq. 3.3
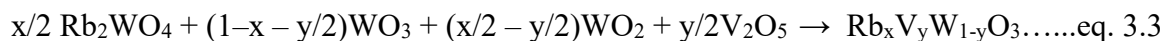
Reagent grade rubidium carbonate, tungsten(VI) oxide (99.998% pure; Alfa Aesar), tungsten(IV) oxide (99.9% pure; Alfa Aesar), vanadium(V) oxide (99.998% pure; Alfa Aesar) were used as starting materials. Before use, reagent grade rubidium carbonate and tungsten (VI) oxide were heated overnight at 100°C and 700°C, respectively. Rubidium tungstate, Rb_2WO_4, was prepared by heating an equimolar mixture of Rb_2CO_3 and WO_3 in an open crucible at 750°C for 24 hours. The purity of the Rb_2WO_4 was checked with XRD and FTIR.

3.2.2 Characterization of alkali metal tungsten oxides

The X-ray powder diffraction data of the samples ($Rb_xV_yW_{1-y}O_3$) were collected on a Bruker D8 diffractometer (CuK_α radiation) equipped with a secondary Ni filter having a Bragg-Brentano geometry. The measurement was carried out at room temperature in a range between 10° and 120° 2θ with a step size of 0.02° and a data collection time of 25s/step. The structures were refined with the Rietveld program 'Diffrac Plus Topas-4.2′ (Bruker AXS, Karlsruhe, Germany). For the calculation of the reflex profiles, fundamental parameters were used on the

basis of instrumental parameters calculated out of a LaB_6 standard measurement. As an additional general parameter, the sample displacement of the centre was varied and a polarization parameter was fixed. The starting atomic coordinates were taken from literature [145]. The occupancy of V in the 6g site was constrained so that occ.[V] = 1 – occ.[W]. To cross-check the X-ray results obtained by the Guinier-Hägg focusing camera, the X-ray powder patterns of a few samples were also recorded by a Bruker D4 diffractometer. The X-ray powder diffractogram of the prepared samples $Cs_xV_xW_{1-x}O_3$ and $K_xV_xW_{1-x}O_3$ was determind with an X-ray powder diffractmeter (Model- Rigaku Ultima IV, Japan) eqipped with CuK_α radiation. The 2θ range for collecting XRD patterns was 5 to 70° in a continuous scan mode. The structures of $Cs_xV_xW_{1-x}O_3$ and $K_xV_xW_{1-x}O_3$ were refined with the Rietveld program profex [45].

Infrared absorption spectra of $Rb_xV_yW_{1-y}O_3$ were recorded on a Bruker Vertex 80v FT-IR spectrometer under vacuum. For the IR spectroscopic measurements (in the range of 370-5000 cm^{-1}), 1.0 mg of the finely ground sample was dispersed into 199 mg potassium bromide (KBr) and pressed into a pellet (13 mm in diameter). The spectrum of pure KBr pellet prepared in the same way was used as a reference. On the other hand, a Fourirer Transform Infrared (FT-IR) spectometer (Moldel IR Prestige-21, Shimadju, Japan) was used for the molecular characterization of the prepared $Cs_xV_xW_{1-x}O_3$ and $K_xV_xW_{1-x}O_3$ samples. In this method, the ground powdered samples were mixed with KBr (1 mg sample and 199 mg KBr) and pressed to prepare pellets. The results are presented and discussed separately in the following sections.

SEM-EDX was used in this work for studying the morphology and the elemental composition of the samples of the series $Rb_{0.30}W_{1-y}V_yO_3$, $Cs_xV_xW_{1-x}O_3$ and $K_xV_xW_{1-x}O_3$. Measurements were conducted using a JEOL JSM 6490 LA instrument equipped with an EDX detector operated at an accelerating voltage of 20 kV. The prepared samples were smeared on adhesive carbon films and coated with platinum by the vacuum sputtering method. The EDX spectra were recorded in the range of 0-20 keV. The microanalyses gave information about the Rb:W and Cs:V:W or K:V:W ratios in at %. The whole spectrum was used in the quantification. About 10 to 12 measurements were carried out in each sample. The mean values of Rb/W (= x) and V/(V+W) (= y) are used for $Rb_{0.30}W_{1-y}V_yO_3$.

3.3 Results and discussion alkali metal tungsten oxides

3.3.1 $Rb_xV_yW_{1-y}O_3$ (x = 0.25 and 0.0 ≤ y ≤ 0.25; x =0.30 and 0.0 ≤ y ≤ 0.30) series

3.3.1.a XRD analysis of $Rb_xV_yW_{1-y}O_3$ (x = 0.25 and 0.0 ≤ y ≤ 0.25; x =0.30 and 0.0 ≤ y ≤ 0.30) series

The XRD patterns of the polycrystalline samples with nominal compositions $Rb_{0.30}V_yW_{1-y}O_3$ (0.0 ≤ y ≤ 0.30) and $Rb_{0.25}V_yW_{1-y}O_3$ (0.0 ≤ y ≤ 0.25) are shown in Fig. 3.3 and Fig. 3.4 respectively. All the X-ray diffraction peaks of samples with x = 0.30, 0.0 ≤ y ≤ 0.18 and x = 0.25, 0.0 ≤ y ≤ 0.15 could be indexed as a single HTB phase. The diffraction lines are systematically shifted with increasing nominal vanadium content. This shift is significant up to nominal composition y = 0.18 for the $Rb_{0.30}V_yW_{1-y}O_3$ series and y = 0.15 for the $Rb_{0.25}V_yW_{1-y}O_3$ series. These shifts are associated with the change in the values of the cell parameters, which is a function of vanadium content, y. The XRD pattern of samples with nominal compositions x = 0.30, 0.20 ≤ y ≤ 0.30 and x = 0.25, 0.18 ≤ y ≤ 0.25 showed the presence of some weak reflection which could not be indexed as HTB. Results of Rietveld refinements using space group $P6_3/mcm$ (No. 193) of the selected samples of y = 0.05, 0.18, 0.25 and 0.3 of the $Rb_{0.30}V_yW_{1-y}O_3$ (0 ≤ y ≤ 0.30) solid-solution series are shown in Fig. 3.5. The calculated curves rather well fit the experimental pattern, showing up the weak extra reflections seen for y > 0.18 composition. Similar results are obtained for the x = 0.25 series. The cell parameters obtained from Rietveld refinement of all samples are given in Table 3.2. The cell parameters as a function of vanadium content, y, for $Rb_{0.30}V_yW_{1-y}O_3$ and $Rb_{0.25}V_yW_{1-y}O_3$ are shown in Fig. 3.6 (a-d), including the unit cell volumes in Fig. 3.6 (e and f). Both series show the same trend. The lattice parameters (Fig. 3.6 (a, c)) only slightly decrease between y = 0 to y = 0.05, followed by a steep decrease up to y = 0.18 and 0.15 for x = 0.30 and 0.25, with increasing vanadium content. The c lattice parameter (Fig. 3.6 (b, d)) decreased slightly for y = 0.0 to 0.05, followed by a steep increase up to y = 0.18 and 0.15 for $Rb_{0.30}V_yW_{1-y}O_3$ and $Rb_{0.25}V_yW_{1-y}O_3$, respectively. The calculated unit cell volume shows a sharp decrease from y = 0 to y = 0.05, followed by a smooth overall decrease with an increase of y. For the x = 0.3 series, the values for y = 0.15 and 0.25 could be somehow overestimated and underestimated, respectively. The reason for this is, presently, not clear. Results with a similar trend have been observed on vanadium doped hexagonal potassium tungsten bronze, too [35].
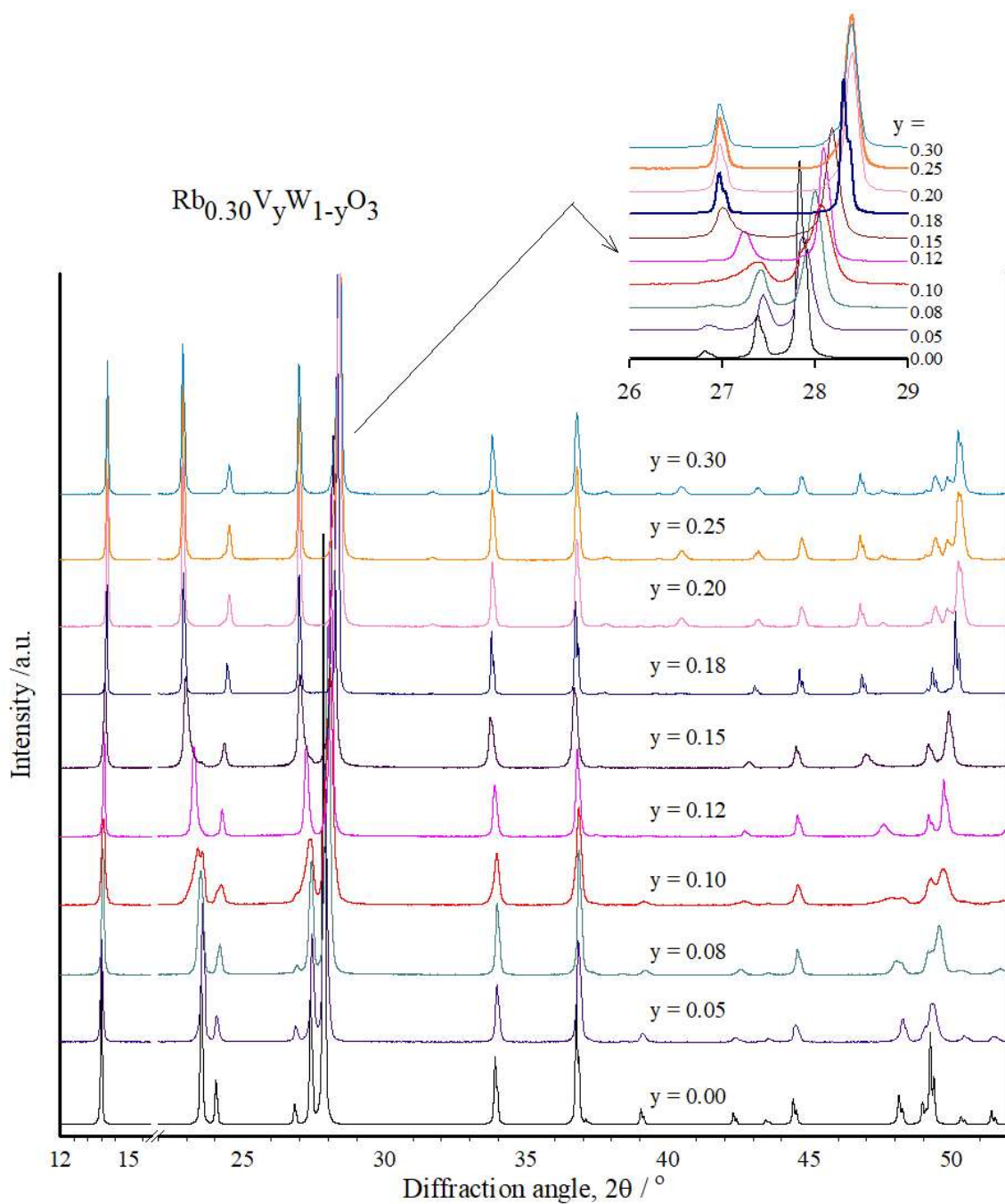
Fig. 3.3. XRD pattern of $Rb_{0.30}V_yW_{1-y}O_3$ ($0.0 \leq y \leq 0.30$) prepared at 700^oC. For clarity, the diffraction patterns are plotted vertically. The figure shows a pure HTB type bronze phase formed at nominal compositions $0.0 \leq y \leq 0.18$ and the diffraction lines systematically shift with increasing nominal vanadium content.
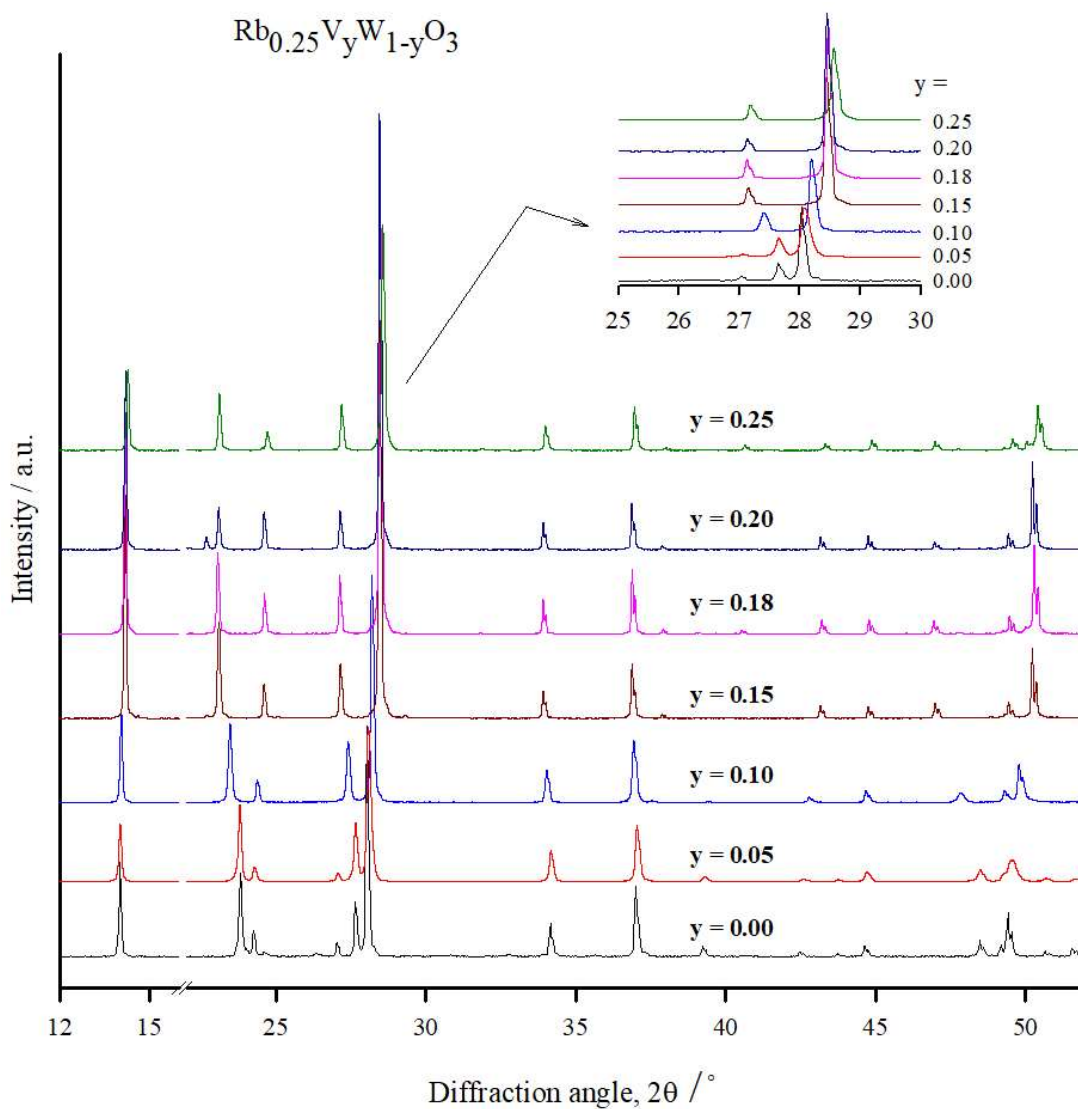
Fig. 3.4. The XRD pattern of $Rb_{0.25}V_yW_{1-y}O_3$ ($0.0 \leq y \leq 0.25$) prepared at 700°C. For clarity, the diffraction patterns are plotted vertically. The figure shows a pure HTB type bronze phase formed at nominal compositions $0.0 \leq y \leq 0.15$ and the diffraction lines systematically shift with increasing nominal vanadium content.
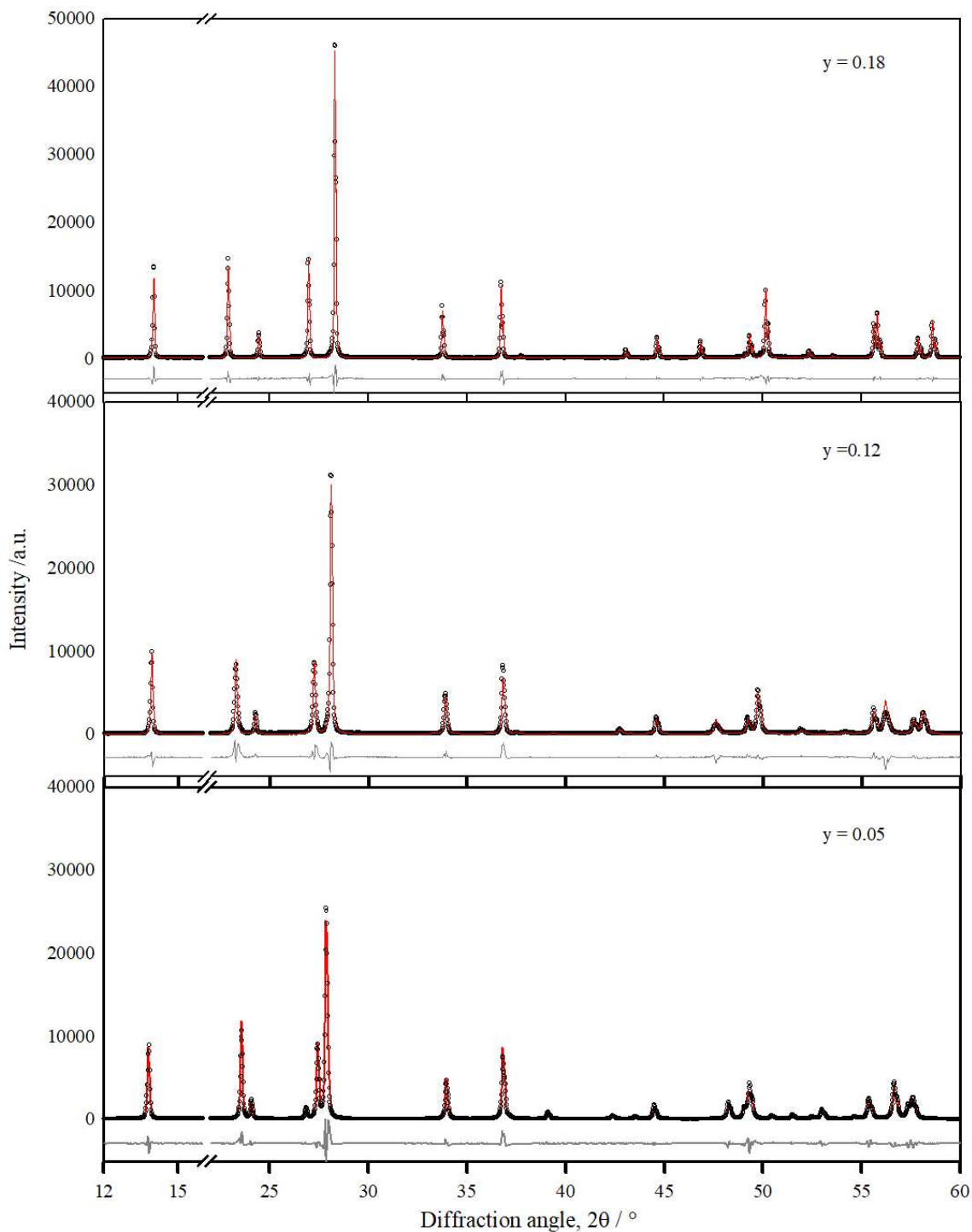
Fig. 3.5. Rietveld refinements fit three selected samples of the $Rb_{0.30}V_yW_{1-y}O_3$ ($0.0 \leq y \leq 0.30$) series. The black spectrum represents observed/measured spectrum, and the red spectrum represents calculated data. The black curve below the spectrum represents the difference spectrum.
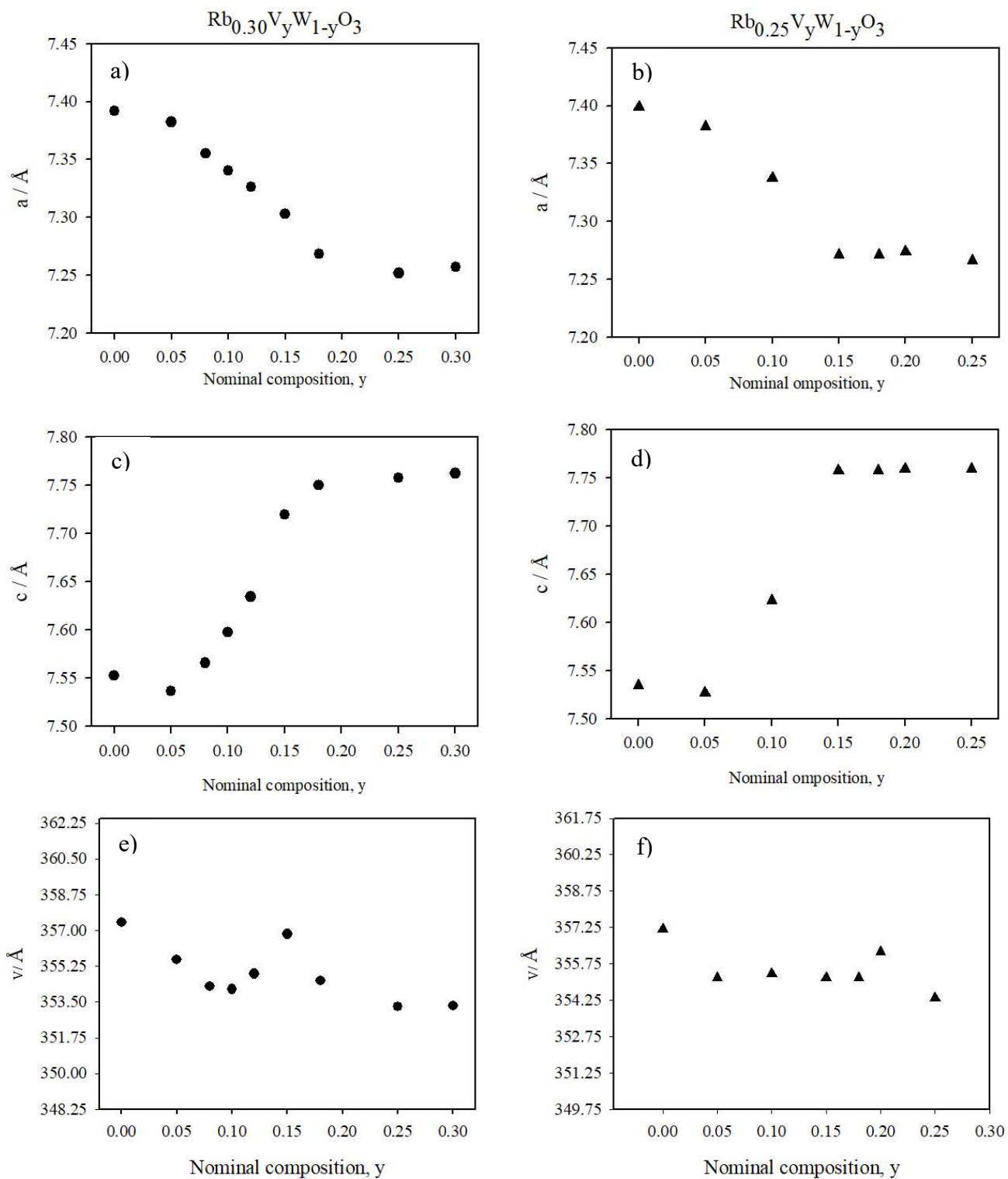
Fig. 3.6. Lattice parameters (*a, c, V*) of $Rb_{0.30}V_yW_{1-y}O_3$ ($0.0 \le y \le 0.30$) and $Rb_{0.25}V_yW_{1-y}O_3$ ($0.0 \le y \le 0.25$) as a function of nominal composition, y.

Table 3.2 At 700°C, cell parameters of $Rb_{0.30}V_yW_{1-y}O_3$ with different nominal compositions are prepared.

Composition (x)	Cell parameters / pm		Cell volume (Å³)	Occupancy			Rwp
	a	c		Rb^{1+} (oct)	W^{6+} (oct)	V^{5+} (oct)	
0.00	7.3921	7.5525	357.4115(54)	0.8500(57)	1.000(20)	0.000(20)	7.668
0.05	7.3813	7.5358	355.576 (13)	0.800(13)	0.956(26)	0.044(26)	5.447
0.08	7.3542(1)	7.5640(2)	354.291(19)	0.800(16)	0.841(30)	0.159(30)	7.240
0.10	7.3381(4)	7.5942(5)	354.146(46)	0.800(24)	0.844(45)	0.156(45)	8.881
0.12	7.3264(1)	7.63470(1)	354.900(15)	0.800(14)	0.779(26)	0.221(26)	8.258
0.15	7.3042(2)	7.7229(2)	356.829(24)	0.800(17)	0.710(30)	0.290(30)	8.367
0.18	7.2681	7.7500	354.5336(87)	0.836(17)	0.820(31)	0.180(31)	12.518
0.25	7.2517(2)	7.7573(3)	354.285(24)	0.800(24)	0.697(43)	0.300(43)	10.953
0.30	7.2523(2)	7.7570(3)	353.334(26)	0.800(25)	0.671(42)	0.329(42	13.355

Table 3.3 Details of the positional parameters of different atoms of the $Rb_{0.30}V_yW_{1-y}O_3$ series obtained from the Rietveld refinements X-ray data.

Atomic site	Coordinate	Nominal composition, $Rb_{0.30}V_yW_{1-y}O_3$								
		0.00	0.05	0.08	0.10	0.12	0.15	0.18	0.25	0.30
2b	x	0.0000	0.0000	0.0000	0.0000	0.0000	0.0000	0.0000	0.0000	0.0000
	y	0.0000	0.0000	0.0000	0.0000	0.0000	0.0000	0.0000	0.0000	0.0000
	z	0.0000	0.0000	0.0000	0.0000	0.0000	0.0000	0.0000	0.0000	0.0000
6g	x	0.4791	0.4791 (1)	0.4857 (1)	0.4873 (3)	0.4936 (3)	0.4942 (5)	0.4968 (5)	0.4925 (4)	0.4933 (6)
	y	0.0000	0.0000	0.0000	0.0000	0.0000	0.0000	0.0000	0.0000	0.0000
	z	0.2500	0.2500	0.2500	0.2500	0.2500	0.2500	0.2500	0.2500	0.2500
6g	x	0.4791	0.4791 (1)	0.4857 (1)	0.4873 (3)	0.4936 (3)	0.4942 (5)	0.4968 (5)	0.4925 (4)	0.4933 (6)
	y	0.0000	0.0000	0.0000	0.0000	0.0000	0.0000	0.0000	0.0000	0.0000
	z	0.2500	0.2500	0.2500	0.2500	0.2500	0.2500	0.2500	0.2500	0.2500
6f	x	0.5000	0.5000	0.5000	0.5000	0.5000	0.5000	0.5000	0.5000	0.5000
	y	0.0000	0.0000	0.0000	0.0000	0.0000	0.0000	0.0000	0.0000	0.0000
	z	0.0000	0.0000	0.0000	0.0000	0.0000	0.0000	0.0000	0.0000	0.0000
12j	x	0.4249(8)	0.4224 (11)	0.4258 (13)	0.4166 (19)	0.4207 (12)	0.4213 (13)	0.4244 (15)	0.4160 (20)	0.4175 (23)
	y	0.2159(8)	0.2141 (12)	0.2147 (17)	0.1950 (29)	0.2045 (24)	0.1875 (37)	0.1791 (25)	0.1944 (36)	0.2037 (50)
	z	0.2500	0.2500	0.2500	0.2500	0.2500	0.2500	0.2500	0.2500	0.2500

Table 3.4 Comparison of cell parameter changes with a few structurally related systems.

HTB Phases	y	Decrease of cell Parameter, a (%)	Increase of cell Parameter, c (%)
$K_{0.30}W_{1-y}Ta_yO_3$ [36]		0.06	0.15
$K_{0.30}W_{1-y}V_yO_3$ [35]	0.15	1.87	2.12
$Rb_{0.30}W_{1-y}V_yO_3$ (Present study)		1.69	2.45

The significant change in lattice parameters indicates most clearly the substitution of tungsten by vanadium along $Rb_xV_yW_{1-y}O_3$ within the HTB structure. The decrease of the cell parameter a indicates that the average distances between the six fold coordinated metal atoms (M) and the oxygen (O) decrease in the xy hexagonal plane. The MO_6 octahedra units become more squeezed. The increase of the cell parameter c thus indicates an elongation of the MO_6 units along c. The extent of squeezing and elongation of WO_6 octahedra depends on the vanadium content. Obviously, these two effects seem to be limited to the x = 0.3 series at about y = 0.18 composition. For the x = 0.25 series, this limit is obtained at y = 0.15. The change in cell parameters of some pentavalent M^{5+} doped bronzes is compared in Table 3.4. This comparison shows that when 50% (y = 0.15) of the W^{5+} is replaced, the cell parameters for V and Ta substituted bronzes are noticeably different. This could be due to the difference in their ionic size. Since Ta^{5+} (0.73 Å) has a larger size compared to V^{5+} (0.68 Å), the distortion (squeezing) of WO_6 octahedra is less pronounced for tantalum when substituting larger W^{5+} (0.76 Å) ions.

It has been reported that for the system $K_xTa_yW_{1-y}O_3$ cell parameters remains almost constant up to y = 0.15 and then a decreases and c increases with a further increase in y. Hussain *et al.* [23], however, reported that in the Nb substituted HTB type $K_{0.30}Nb_yW_{1-y}O_3$ system, both the cell parameters a and c decrease with increasing nominal Nb content. It has also been reported that the lattice parameter a decreases and c increases up to y = 0.15 in the $K_xV_yW_{1-y}O_3$ system. With this information, it could be concluded that there is some critical value for the substitution of pentavalent W by other pentavalent ions, which depends on the amount of W^{5+} (= x) in the initial composition. For the case of the $Rb_{0.30}V_yW_{1-y}O_3$ ($0 \leq y \leq 0.30$) and $Rb_{0.25}V_yW_{1-y}O_3$ ($0 \leq y \leq 0.25$) series, the limiting values of y are 0.18 and 0.15, respectively. Considering the ratio of V^{5+}/W^{5+}, it becomes y/x = 0.18/0.30 = 0.60 for the series $Rb_{0.30}V_{0.18}W_{0.82}O_3$ and also y/x = 0.15/0.25 = 0.60 for $Rb_{0.25}V_{0.15}W_{0.85}O_3$. This reveals that the vanadium doped hexagonal Rb_xWO_3 allows the contraction of the lattice when about 60% of the W^{5+} is replaced by V^{5+} and then, with more incorporation of V^{5+} the structure remains rigid and shows other non-bronze phases along with doped the HTB phase. Previous research [23, 35 and 36] on hexagonal $K_xNb_yW_{1-y}O_3$, $Rb_xNb_yW_{1-y}O_3$, $K_xV_yW_{1-y}O_3$, and $K_xTa_yW_{1-y}O_3$ systems show that about 50-60% W^{5+} could only be substituted by the respective pentavalent ions such as Nb^{5+} and Ta^{5+}, i.e., the limiting value is about 60%. The question arises if in the $Rb_xV_yW_{1-y}O_3$ systems considered here, a further substitution could be possible.

3.3.1.b FT-IR analysis of $Rb_xV_yW_{1-y}O_3$ (x = 0.25 and 0.0 ≤ y ≤ 0.25; x = 0.30 and

0.0 ≤ y ≤ 0.30) series

Infrared absorption spectra of polycrystalline samples of the series $Rb_{0.30}W_{1-y}V_yO_3$ and $Rb_{0.25}W_{1-y}V_yO_3$ measured at room temperature are shown in Fig. 3.7. The spectra are measured in the range of 370 cm^{-1} - 4000 cm^{-1}. Spectra above 2000 cm^{-1} are featureless and not shown in figures. The samples without vanadium, i.e., with nominal composition y = 0.0 do not show any significant phonon absorption. Similar results have been reported for the Ta-doped HTB system [36]. When W^{5+} ions are gradually replaced by V^{5+}, the screening of phonons by the polarons disappears gradually. Consequently, they develop phonon absorption feature as a function of y. The spectra observed for the sample $Rb_xV_yW_{1-y}O_3$ are in good agreement with the powder related spectra of $Cs_xW_{1-y}Nb_yO_3$-HTB reported by Dey *et al.* [37].

Due to the broadness of the bands, the assignment to specific vibrations is difficult. A discussion of the IR spectra of hexatungstates as reported by Maczka *et al.* [146] could be helpful. However, hexatungstate could be related to the HTB structure, which comprises a large number of vacancies on W sites. Such vacancies could be introduced by oxidation of HTB. Brusetti *et al.* [146] investigated the oxidation process of rubidium bronzes Rb_xWO_3 and found that at high rubidium content (0.33 ≤ x ≤ 0.28), hexatungstate is formed in equilibrium with an impoverished HTB phase. Therefore, some of the selected samples of $Rb_{0.30}W_{1-y}V_yO_3$ were heated in the air at 700°C to form the corresponding hexatungstate. The oxidation of $Rb_{0.30}WO_3$ bronzes involves the conversion of all W^{5+} to W^{6+} and the color of the samples changes from dark blue to white, showing that all polarons disappear. XRD of the oxidized sample reveals the HTB type phase with more broadening of diffraction lines. This implies a significant decrease in crystal sizes. The observed IR spectra of the oxidized $Rb_{0.30}WO_3$ is in agreement with the IR spectrum given by Maczka *et al.* [148]. The IR absorption spectra of the oxidized bronzes (i.e., hexatungstates) are directly compared with the respective samples before heating in Fig. 3.8. It is observed that the spectra of the samples before and after oxidation become more similar with increasing y > 0.18. For example, for y = 0.20, the difference can only be observed by a small shift of about 5 cm^{-1} wavenumber of the peak centered at 886 cm^{-1}. For y = 0.25, there seems to be no change. The color of the sample changes from deep brown to light brown. The decreasing change in the IR spectra on

oxidation may thus indicate an increasing counter doping effect with increasing y also for $y >$ 0.18. It is observed that the bands at 818 cm^{-1} and 870 cm^{-1} for oxidized $Rb_{0.3}WO_3$ (i.e., $y =$ 0.0) are systematically shifted into low and high wavenumbers respectively, with increasing vanadium content. It has been reported that the band at 870 cm^{-1} in Rb-hexatungstate is related to vibrations of equatorial oxygen atoms, i.e., the atoms which form W-O bonds within the pseudo-hexagonal xy layers, and the band at about 818 cm^{-1} is related to the vibrations of axial oxygen atoms. The shifting of these bands in the oxidized $Rb_xV_yW_{1-y}O_3$ could be related with the $< V/W–O >$ bond distances decreasing in the xy plane and increasing in the z direction with increasing vanadium content.
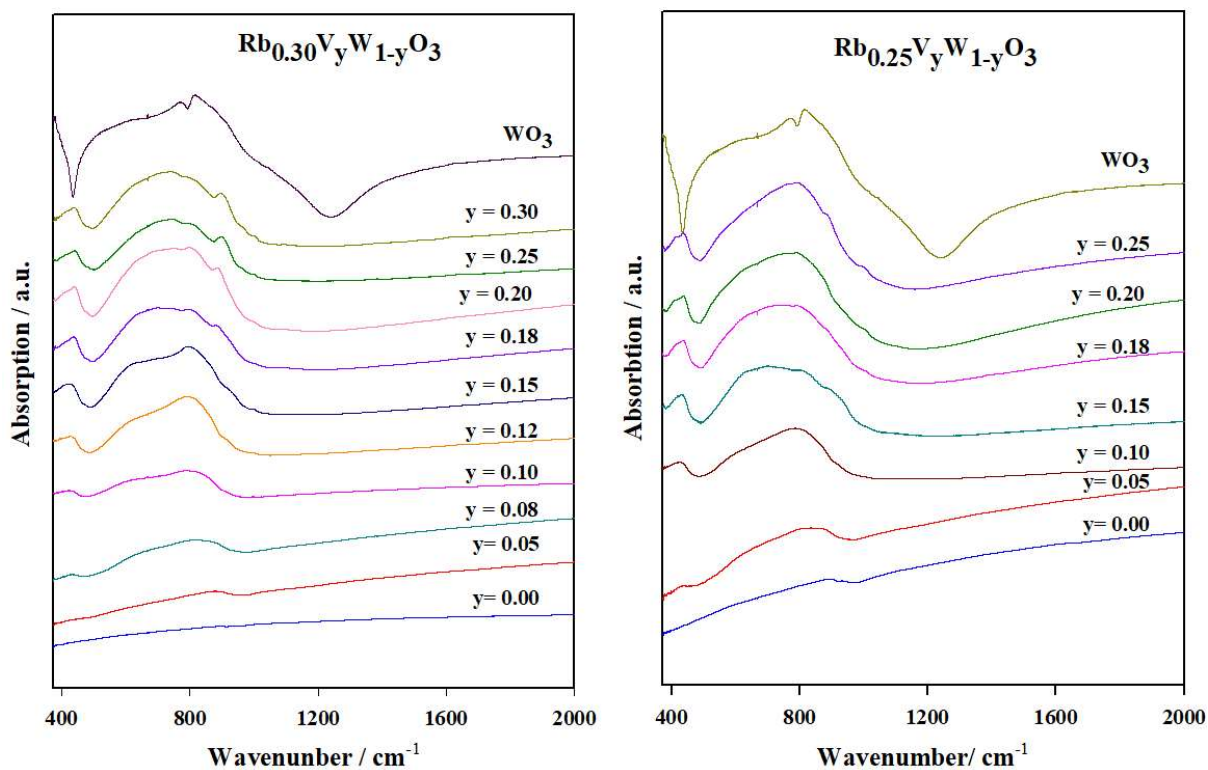
Fig. 3.7. FT-IR absorption spectra of the $Rb_{0.30}W_{1-y}V_yO_3$ and $Rb_{0.25}W_{1-y}V_yO_3$ series. For clarity the spectra are plotted vertically.
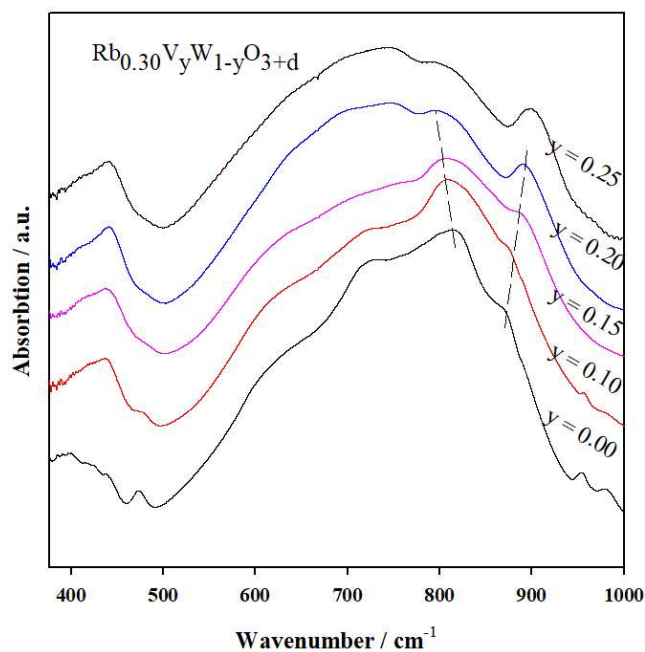
Fig. 3.8. FT-IR absorption spectra of some selected samples of the $Rb_{0.30}W_{1-y}V_yO_3$ series calcined 700°C in air. For clarity the spectra are plotted vertically.

89

3.3.1.c SEM / EDX analysis of $Rb_xV_yW_{1-y}O_3$ (x = 0.25 and 0.0 ≤ y ≤ 0.25; x = 0.30 and 0.0 ≤ y ≤ 0.30) series

The morphology of the samples were examined by scanning electron microscopy, which showed the presence of hexagonal shaped crystals along with irregular shaped crystals (Fig. 3.9). The crystals are of micrometer size. Energy dispersive X-ray (EDX) was used to estimate the elemental compositions of the prepared samples. The spectra clearly reveal the presence of Rb, W and V in the samples, $Rb_{0.30}W_{1-y}V_yO_3$. The quantitative estimation was carried out by counting the peak areas of the respective elements using JEOL software. Although the EDX study showed that the rubidium and vanadium content vary from crystal to crystal, their mean values are close to their nominal ones. The mean values of x and y are given in Table 3.5 based on 10 to 12 analyzed crystals from each sample. Table 3.5 shows that the composition of vanadium, y obtained from the EDX analysis, shows excellent consistency with their nominal ones, indicating the systematic incorporation of vanadium in the $Rb_xW_{1-x}O_3$ system. To check the homogeneity of the elemental composition in crystals SEM/ EDX line scan were performed. As a typical example SEM/EDX line scan of a crystal with nominal composition x = 0.3, y = 0.18 is shown in Fig. 3.10. The relative intensities of each element remain constant throughout the length of the crystal indicating the compositional homogeneity.
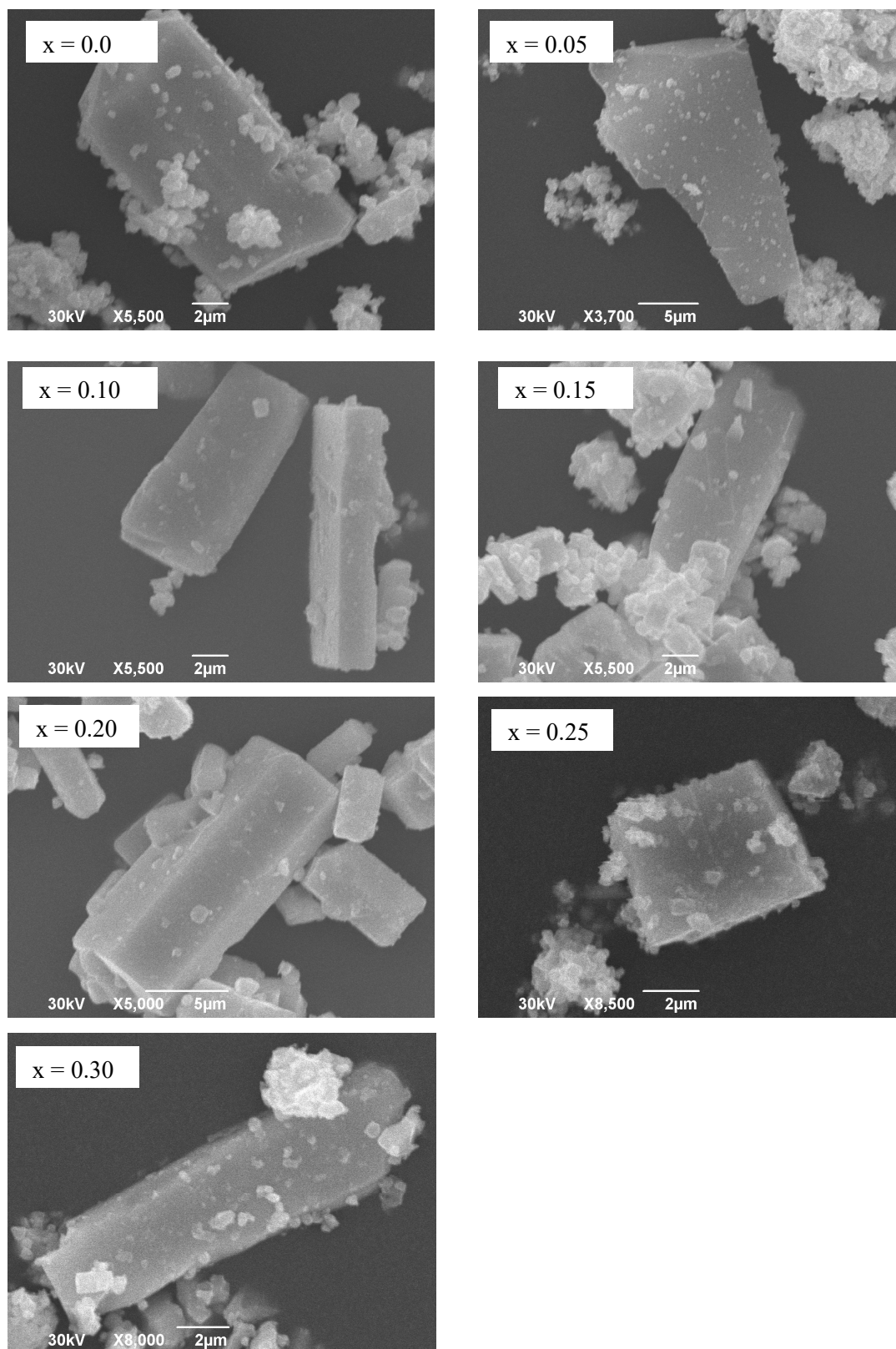
Fig. 3.9. SEM images of $Rb_{0.30}W_{1-y}V_yO_3$ series.
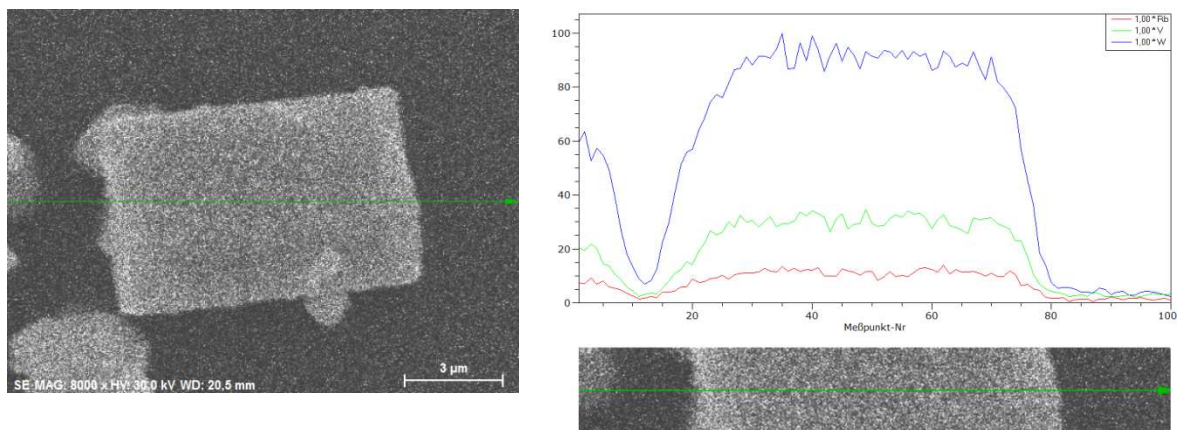
Fig. 3.10. Line scan of SEM / EDX to check the homogeneity of the elemental composition in a single crystal with x = 0, y = 0.18.

Table 3.5 The mean values of x and y in the samples, $Rb_xW_{1-y}V_yO_3$ obtained from EDX analysis.

Nominal composition	Mean value of x	Mean value of y
$Rb_{0.30}WO_3$	0.33 (3)	-------
$Rb_{0.30}W_{0.95}V_{0.05}O_3$	0.31 (2)	0.049 (6)
$Rb_{0.30}W_{0.90}V_{0.10}O_3$	0.29 (3)	0.10 (2)
$Rb_{0.30}W_{0.85}V_{0.15}O_3$	0.30(2)	0.15 (2)
$Rb_{0.30}W_{0.80}V_{0.20}O_3$	0.29 (3)	0.19 (3)
$Rb_{0.30}W_{0.75}V_{0.25}O_3$	0.32 (2)	0.24 (3)
$Rb_{0.30}W_{0.70}V_{0.30}O_3$	0.29 (3)	0.28 (4)

3.3.2 $Cs_xV_xW_{1-x}O_3$ series

3.3.2.a XRD analysis of $Cs_xV_xW_{1-x}O_3$ series

At temperatures ranging from 300-700°C, samples with nominal compositions $Cs_xV_xW_{1-x}O_3$ (x = 0.15, 0.20, 0.25, and 0.30) are prepared. The XRD patterns of the these samples are shown in Figs. 3.11, 3.12, 3.13 and 3.14 for compostion x = 0.15, 0.20, 0.25 and 0.30, respectively. The XRD patterns reveal that peak broadening decreases for all compositions with increasing preparation temperature. This broadening of XRD patterns indicates the formation of nanocrystalline samples below 500°C. The diffraction patterns for samples prepared at 500°C or higher temperatures can be indexed mostly as hexagonal tungsten bronze (HTB) kind phase (Fig. A.3.1) (ICSD pattern; card no. 01-083-13333. The pattern however, shows a second unidentified phase at higher temperature (≥ 600°C) for nominal composition x = 0.15, the pattern whereas with x = 0.20, the second phase appears at (≥ 700° C) (Fig. A.3.2). Rietveld refinements using space group $P6_3/mcm$ (No. 193) of $Cs_xV_xW_{1-x}O_3$ (x = 0.15, 0.20, 0.25, and 0.30) were carryout with the Profex software [45]. The XRD pattern of samples with nominal compositions x = 0.15 (≥ 600°C) showed the presence of some weak reflection which could not be indexed as HTB. The calculated cell parameters for the samples prepared at 500°C and 600°C show a small but significant shift, indicating the partial substitution of W by V in the $Cs_xV_xW_{1-x}O_3$ (x = 0.15, 0.20, 0.25, and 0.30) series.
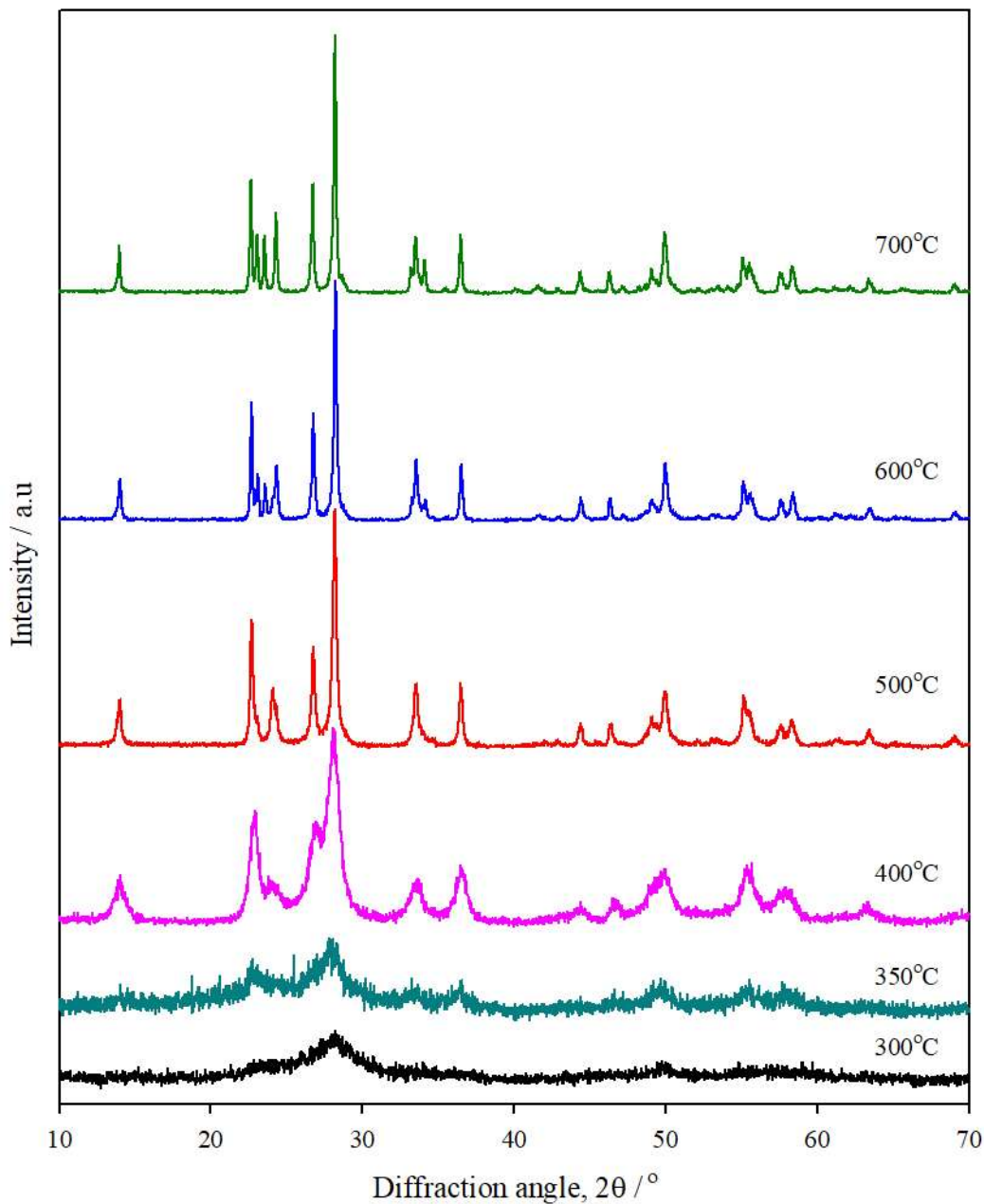
Fig. 3.11. XRD pattern of $Cs_xV_xW_{1-x}O_3$ (x = 0.15) at different temperatures and the diffraction patterns are plotted vertically for clarity. Figure also shows that the HTB type bronze phase started to form at 350°C temperature but a second unknown phase (between the values of 2θ, 22.8 to 24.1) is observed at ≥ 600°C.
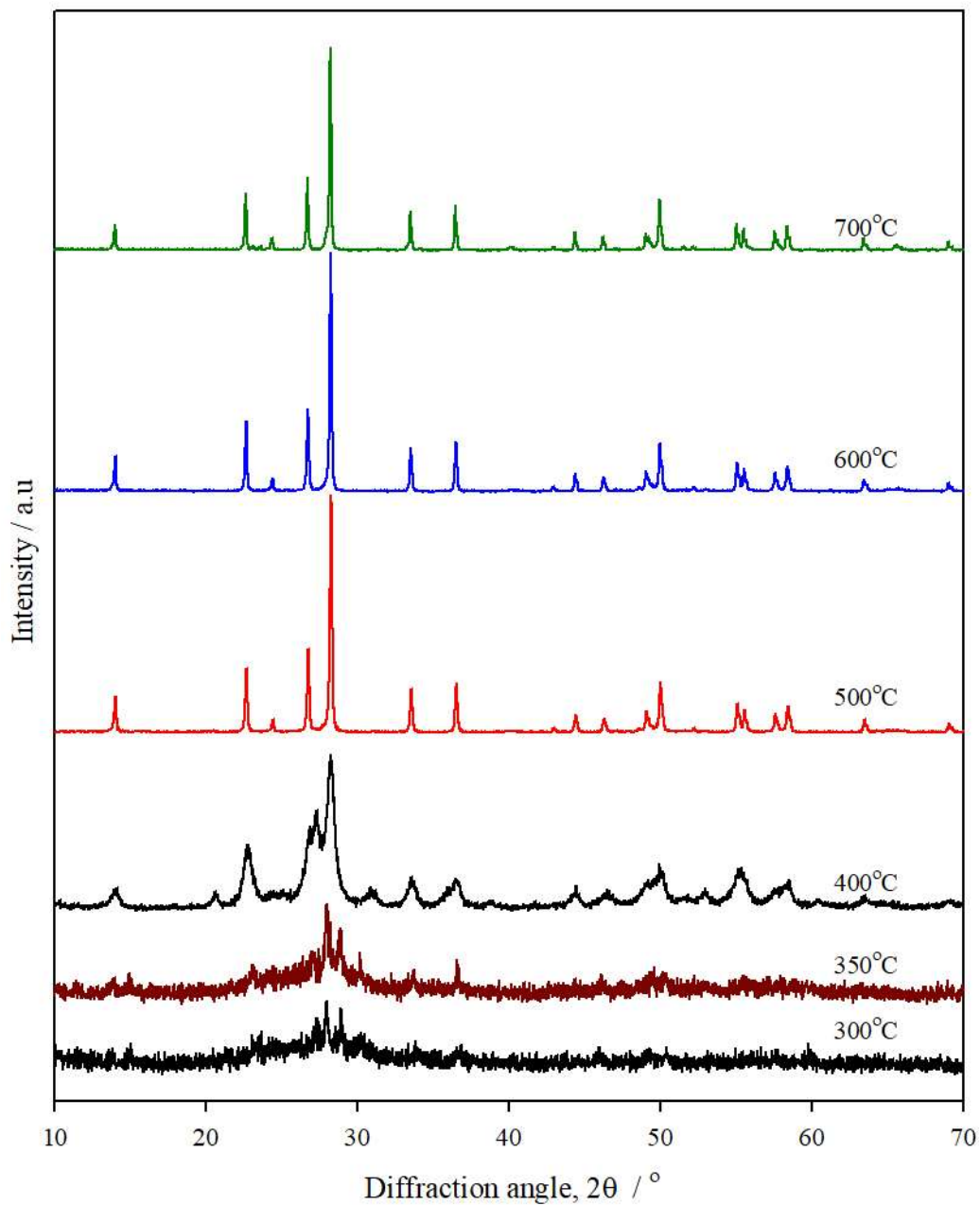
Fig. 3.12. XRD pattern of $Cs_xV_xW_{1-x}O_3$ (x = 0.20) at different temperatures and the diffraction patterns are plotted vertically for clarity. The HTB type bronze phase started to be formed at 400°C but a second unknown phase (between the values of 2θ, 22.5 to 24.3) is observed at 700°C.
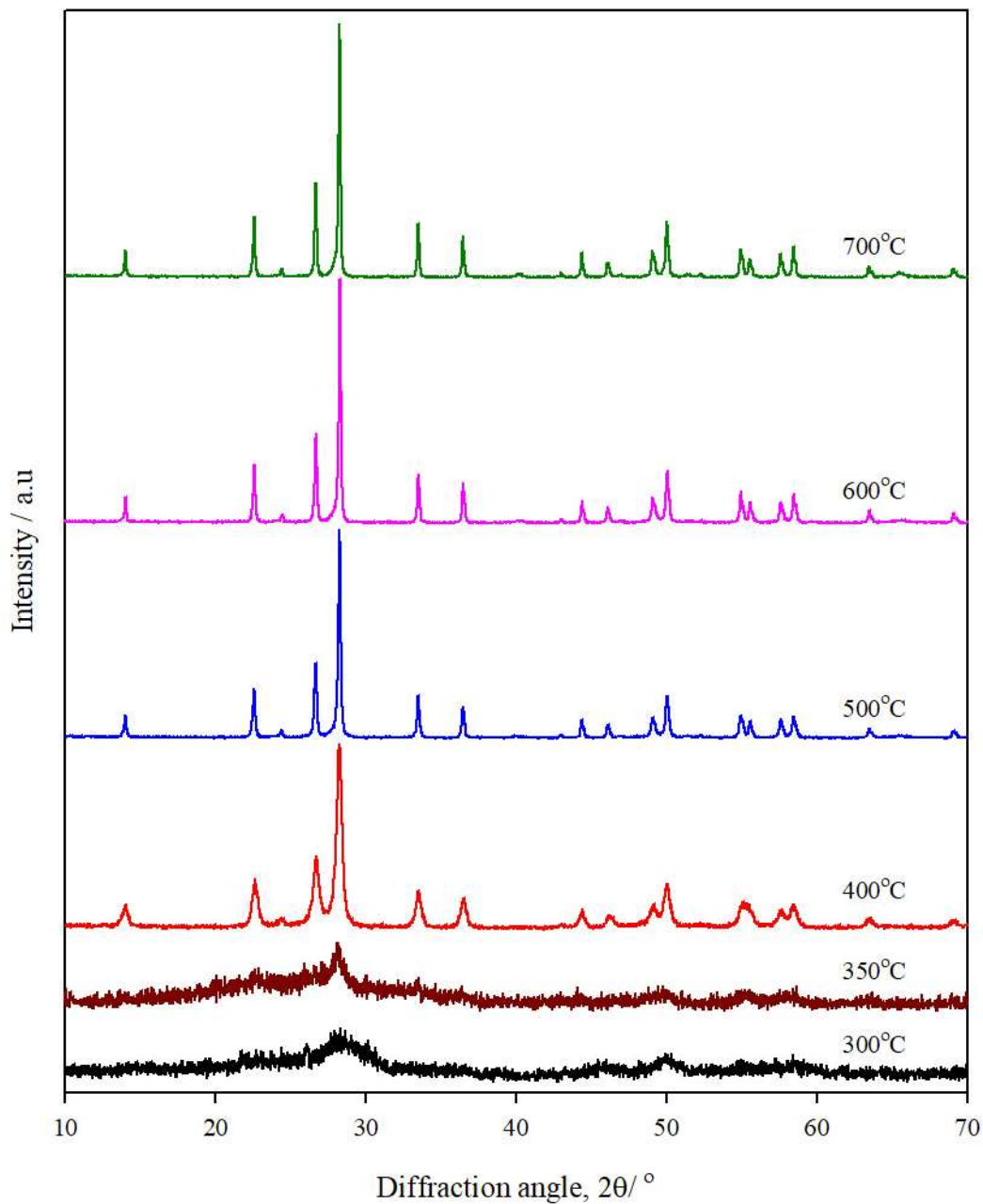
Fig. 3.13. XRD pattern of $Cs_xV_xW_{1-x}O_3$ (x = 0.25) at different temperatures. For clarity, the diffraction patterns are plotted vertically. The HTB type bronze phase is formed at 400-700°C temperatures.
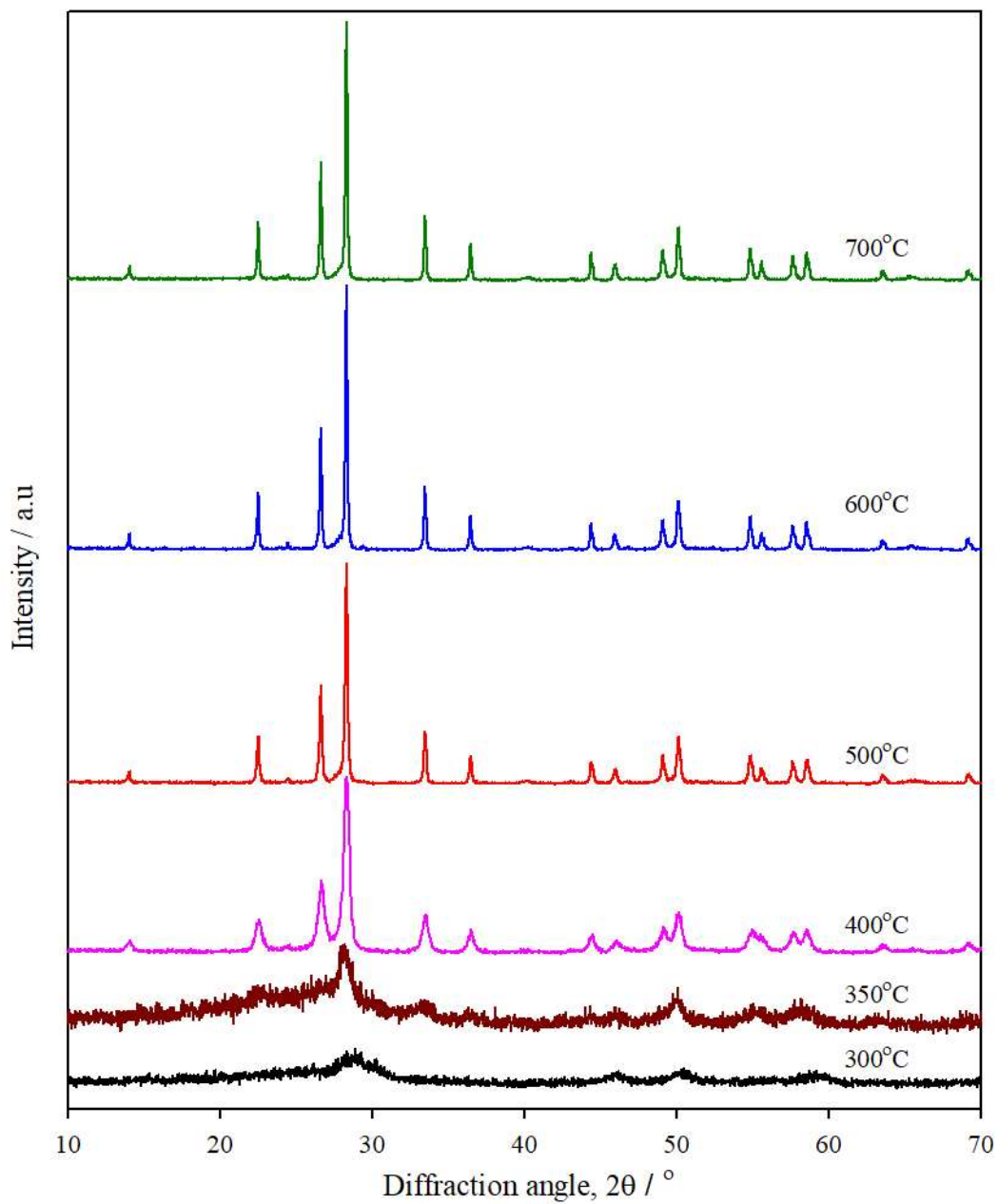
Fig. 3.14. XRD pattern of $Cs_xV_xW_{1-x}O_3$ (x = 0.30) at different temperatures. The diffraction patterns are plotted vertically, for clarity. The HTB type bronze phase is formed at 400-700°C temperatures.
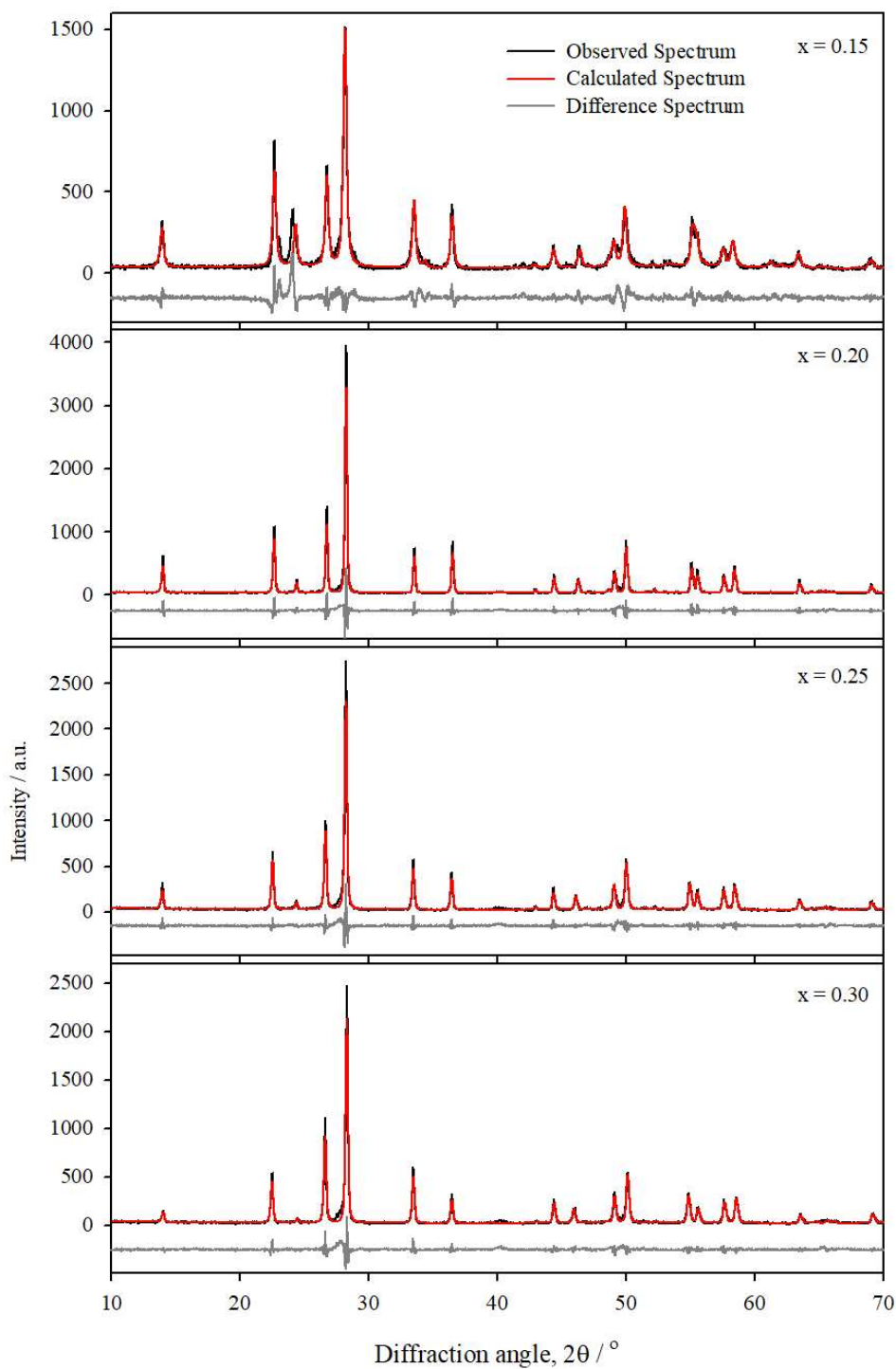
Fig. 3.15 Rietveld refinements fit of the $Cs_xV_xW_{1-x}O_3$ (x = 0.15, 0.20, 0.25, and 0.30) series at 500°C. The black spectrum represents observed/measured spectrum, and the red spectrum represents calculated data. The black curve below the spectrum represents the difference spectrum.
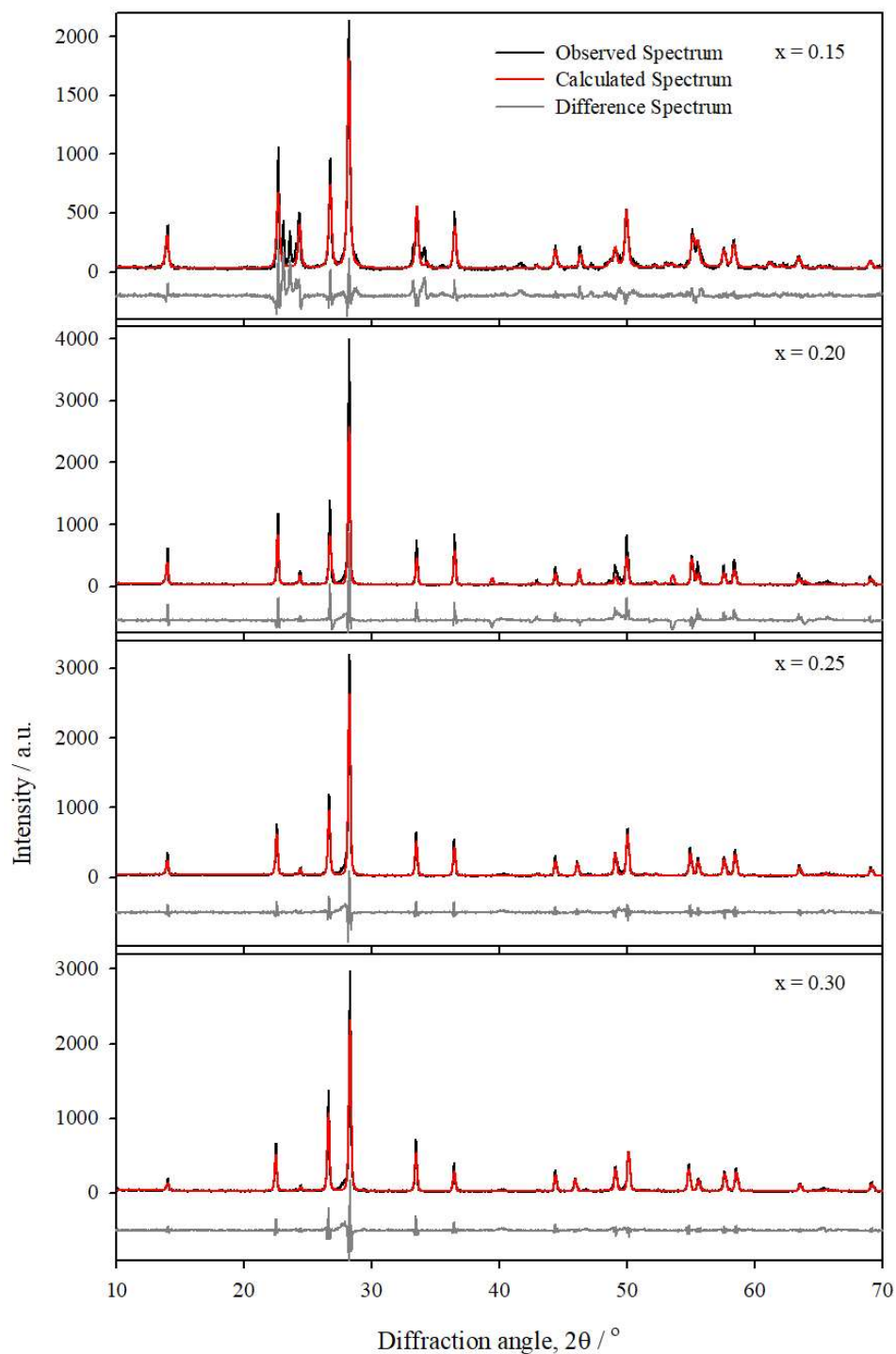
Fig. 3.16. Rietveld refinements fit of $Cs_xV_xW_{1-x}O_3$ (x = 0.15, 0.20, 0.25, and 0.30) series at 600ºC. The black spectrum represents observed/measured spectrum, and the red spectrum represents calculated data. The black curve below the spectrum represents the difference spectrum.
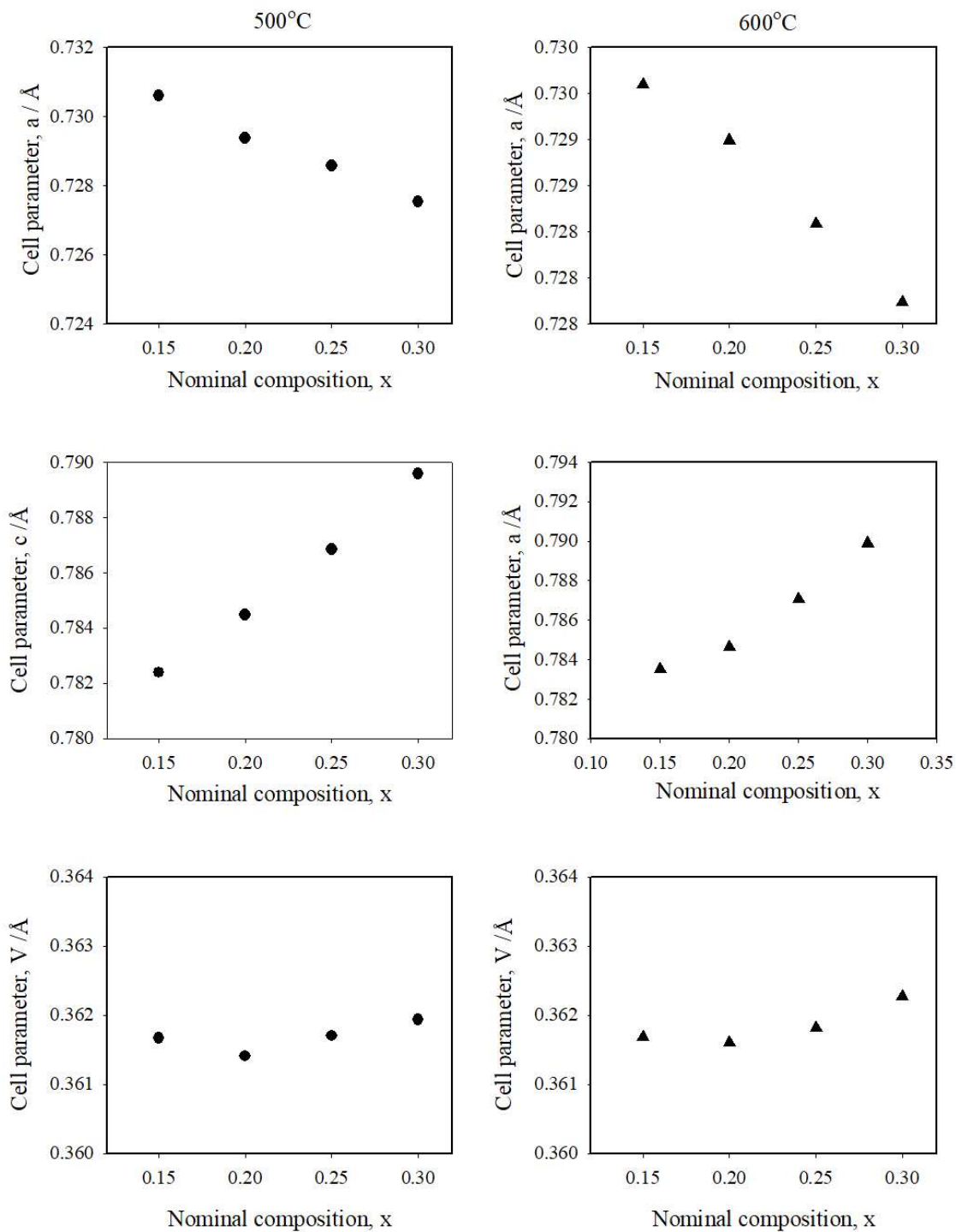
Fig. 3.17. Cell parameters (*a, c, V*) of $Cs_xV_xW_{1-x}O_3$ as a function of nominal composition, x at 500°C and 600°C.

In order to evaluate the crystalline size of the prepared bronzoid $Cs_xV_xW_{1-x}O_3$ with different x-composition and at different calcined temperatures calculated from XRD peak broadening (the full width at half maximum, FWHM) using Debye-Scherrer equation. It is also observed that with increase in calcined temperature, the FWHM of the more intense diffraction peak decreases, which reveals that the average crystallite size increases.

$$\tau = \frac{K\lambda}{\beta cos\theta}$$

where τ for the the mean crystallite size, K for the shape factor (0.089) and it is dimensionless, λ for the wavelength of X-ray radiation (1.5406 Å for CuK_α radiation), β repesents full width at half maximum (FWHM) of the more intense peak for the HTB phase after subtracting the instrumental line broadening, and θ represents the Bragg angle. The calculated crystallite size of the synthesized product is represented in Table A.3.1. It is observed that the average crystallite size of $Cs_xV_xW_{1-x}O_3$ varies from 11-200 nm, and the size increases with an increase in calcination temperatures.

3.3.2.b FT-IR analysis of $Cs_xV_xW_{1-x}O_3$ Series

The FT-IR absorption spectra of samples $Cs_xV_xW_{1-x}O_3$ (x = 0.15, 0.20, 0.25, and 0.30) were measured in the region of 400-400 cm^{-1} wavenumber and shown in Fig. 3.18. Broad absorption bands in the 500-1050 cm^{-1} range are caused by the stretching vibration of MO_6 octahedra found in $Cs_xV_xW_{1-x}O_3$ compounds where M is W or V [37, 99]. The weak absorption peaks found under 430 cm^{-1} represent bending mode of vibration for M-O-M joining bonds. The spectra are featureless for higher wavenumbers (> 1200 cm^{-1}). Therefore, absorption spectra are shown and compared in the region of 1200-400 cm^{-1} only. The FT-IR spectra of the studied compounds are also similar to the FT-IR spectra reported by Dey *et al.* for the $Cs_{0.25}W_{1-y}Nb_yO_3$ and $Cs_{0.3}W_{1-y}Nb_yO_3$ series [37]. The peak position centered at 430 cm^{-1} wavenumber systematically shifts to a higher wavenumber with increasing nominal composition x, which may indicate substitution of W by V in the $Cs_xV_xW_{1-x}O_3$ series (Fig. A.3. 5).
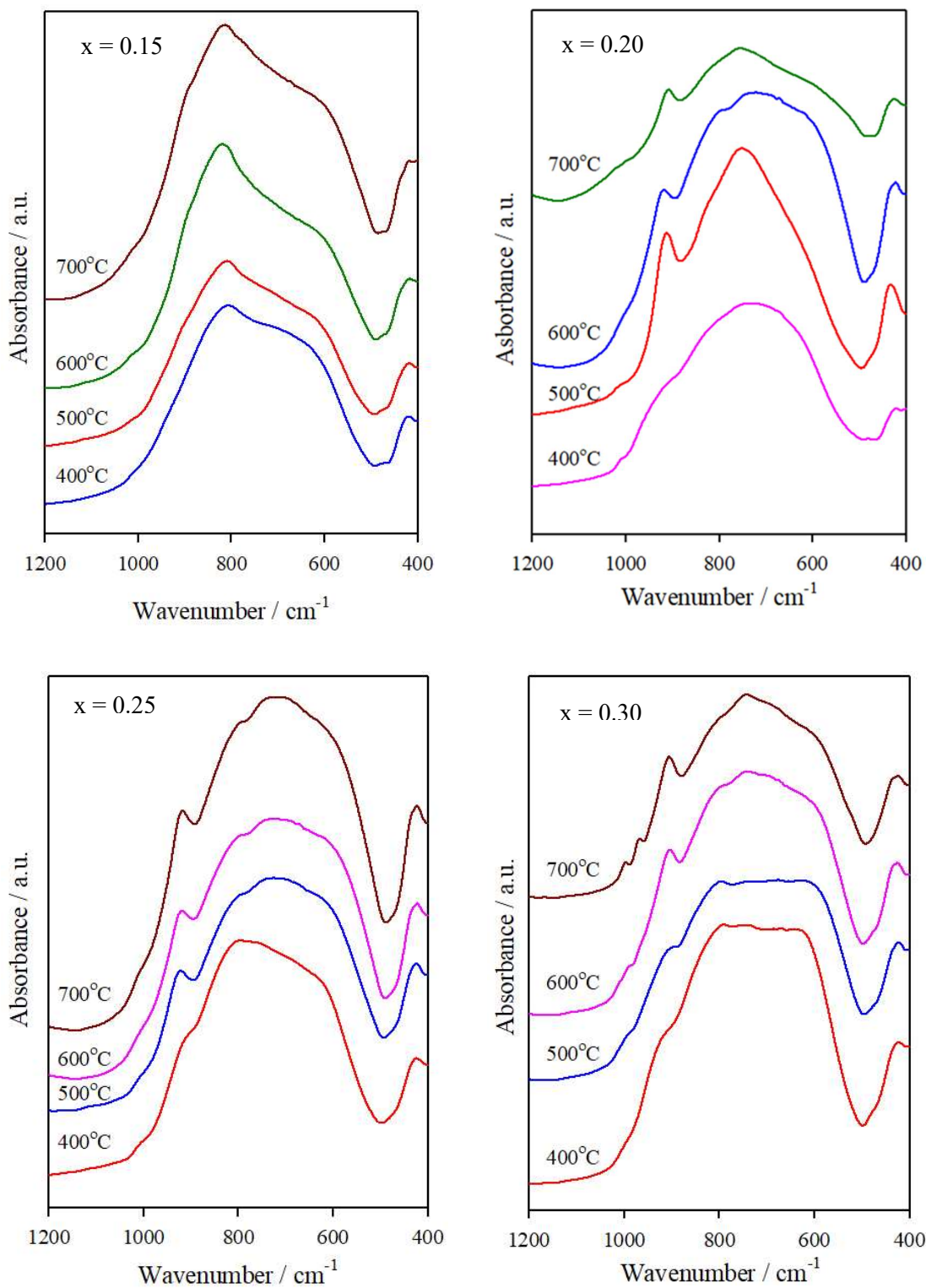
Fig. 3.18. FT-IR spectra of $Cs_xV_xW_{1-x}O_3$ (x = 0.15-0.30) at different temperatures. For clarity, the spectra are plotted vertically.

3.3.2.c. SEM/EDX analysis of $Cs_xV_xW_{1-x}O_3$ Series

The SEM images of some selected samples (prepared at a temperature of 500ºC) of the $Cs_xV_xW_{1-x}O_3$ series are shown in Fig. 3.19. The rest of the SEM images are given in appendices. The SEM images show that the calcination temperature noticeably influences the size and shape of the particles. Nanometer-sized particles are cleary visible in compounds prepared at low temperatures.

The elemental compositions obtained from EDX measurements are listed in Table 3.6. The EDX spectra of the samples $Cs_xV_xW_{1-x}O_3$ are given in appendices. The results are compared to the nominal composition used for the sample preparation. The observed ratio of vanadium to tungsten is in good covenant with the nominal composition.
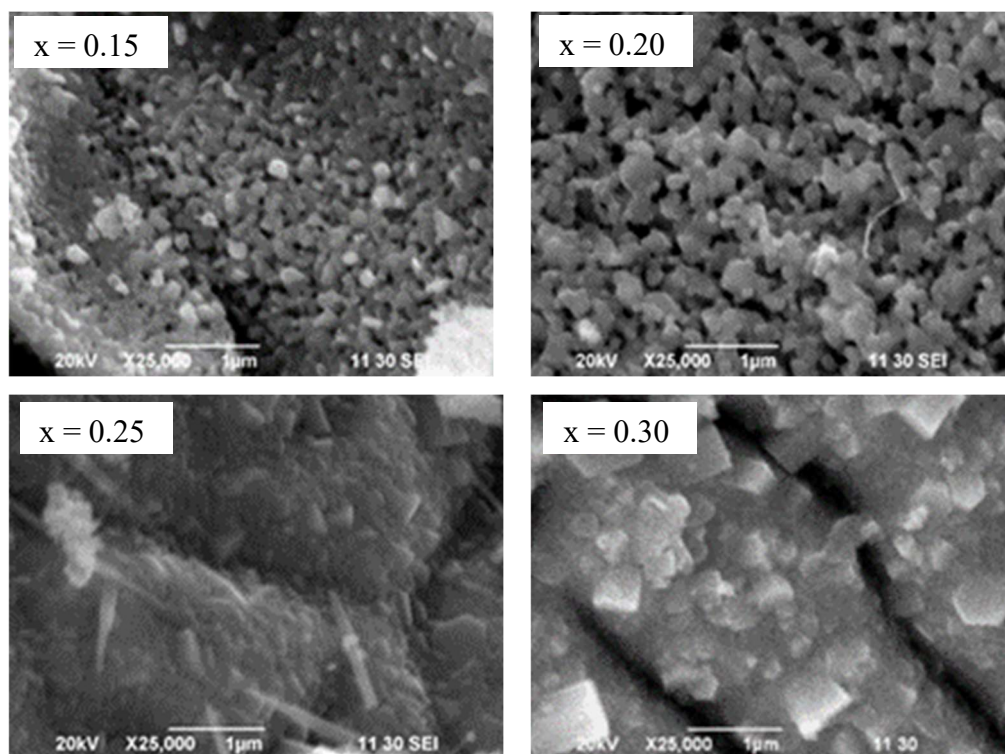
Fig. 3.19. SEM micrographs of $Cs_xV_xW_{1-x}O_3$ at 500ºC.

Table 3.6 EDX results of $Cs_xV_xW_{1-x}O_3$ (x = 0.15 – 0.30) series.

Nominal composition, x	V: W	
	Taken	Found
0.15	0.049	0.049
0.20	0.069	0.062
0.25	0.092	0.092
0.30	0.119	0.116

3.3.3 $K_xV_xW_{1-x}O_3$ series

The vanadium substituted potassium tungsten bronzoids with the general formula $K_xV_xW_{1-x}O_3$ are a series of nonstoichiometric compounds containing both hexagonal and trigonal tunnels which are formed by corner-shared WO_6 octahedra. Here the K^+ ions are situated in the hexagonal tunnel and the metal quantity x is in the range of $0.15 \leq x \leq 0.30$. Replacement of W^{6+} in WO_6 by V^{5+} occurs in only a small quantity that causes a fractional negative charge to be neutralized by the K^+ ion. This allows one to write the chemical formula of bronzoids as $A^+_x(V^{5+}_xW^{6+}_{1-x})O_3$. The solution combustion synthesis (SCS) method was used to create bronzoid type $A^+_x(V^{5+}_xW^{6+}_{1-x})O_3$ from an ammoniated solution containing an appropriate amount of KNO_3, NH_4VO_3, H_2WO_4 as metal sources, oxidants, and glycerin as a fuel. Structural morphology, phase composition, and unique properties of the studied materials were characterized using FT-IR, SEM, and EDX analysis.

3.3.3.a XRD analysis of $K_xV_xW_{1-x}O_3$ series

The XRD pattern of the samples, $K_xV_xW_{1-x}O_3$ (x = 0.15, 0.20, 0.25, and 0.30) prepared by SCS method, is shown in Figs. 3.20-3.23. A similar trend was observed in case of $K_xV_xW_{1-x}O_3$ to those of $Cs_xV_xW_{1-x}O_3$ producing similar XRD patterns. All the peaks of the diffraction pattern may be indexed as hexagonal tungsten bronze (HTB) like phase (ICSD pattern; card nos.01-081-0005 and 00-049-0541. At a higher temperature (≥ 600°C), the XRD pattern of the samples with nominal composition x = 0.15 and x = 0.20 shows the appearance of a second unknown phase (Fig. A.3.3(b)), whereas other compositions form a pure HTB phase. It is also observed that the peak intensity increases with temperature and becomes sharper and narrower. The improvement of the crystalinity may be initiated by the increrment

of the ratio of crystalline volume because of the size expansion of the nuclei [100]. Profex software was used for Rietveld refinements of $K_xV_xW_{1-x}O_3$ (x = 0.15, 0.20, 0.25, and 0.30) series with space group *P6₃/mcm* (No. 193) [45]. At 600ºC, the XRD pattern of samples with nominal compositions x = 0.15 showed the presence of some weak reflection which could not be indexed as HTB. The calculated cell parameters for the samples prepared at 500ºC and 600ºC show a small shift, indicating the partial substitution of W by V in the $K_xV_xW_{1-x}O_3$ (x = 0.15, 0.20, 0.25, and 0.30) series. The crystalline size of the prepared bronzoid $K_xV_xW_{1-x}O_3$ with different x-composition and at different calcined temperatures was calculated using Debye-Scherrer equation. The calculated crystallite size of the synthesized product is represented in Table A.3.2. It is observed that the average crystallite size of $K_xV_xW_{1-x}O_3$ varies from 14-118 nm and the size increases with an increase in calcination temperatures.
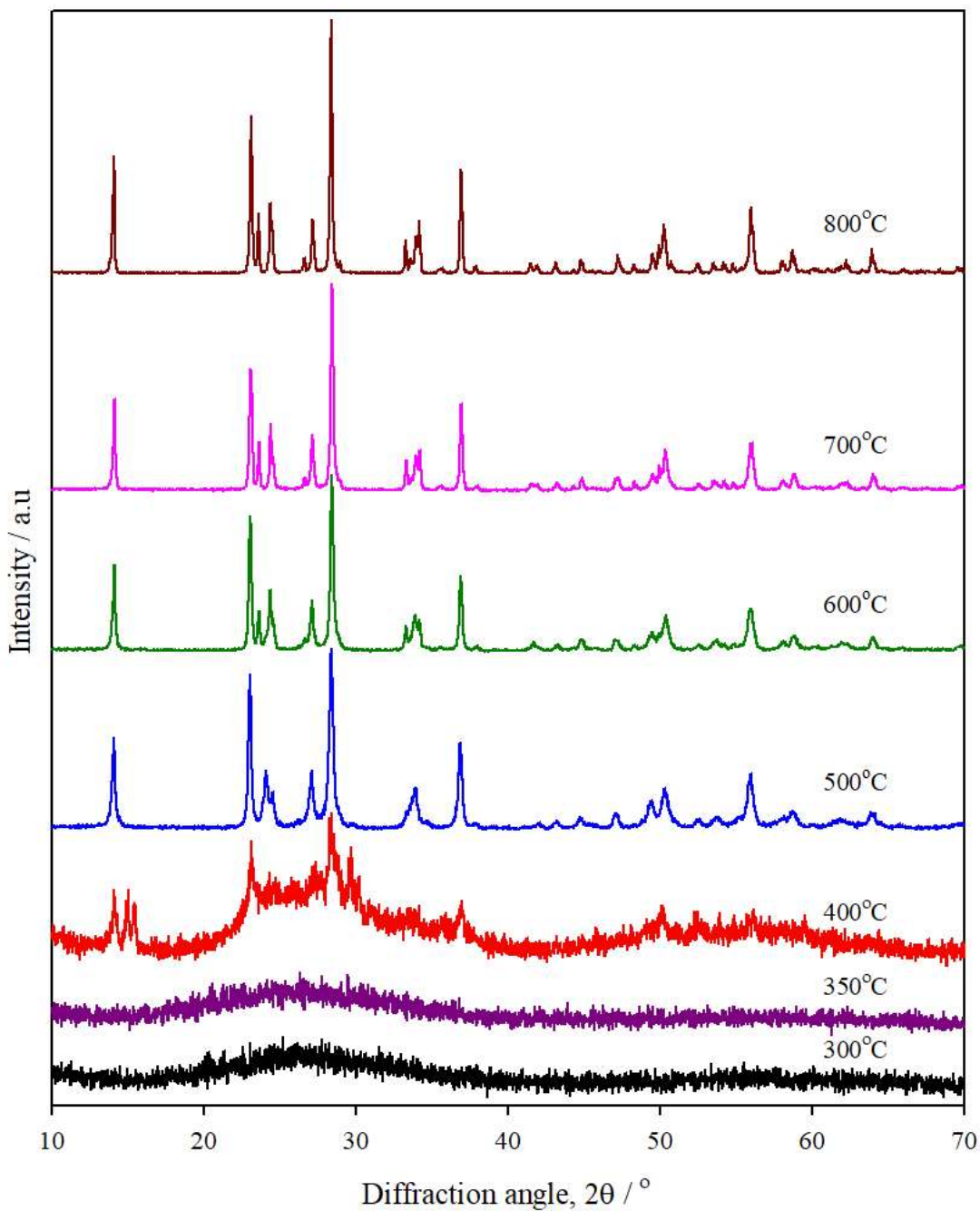
Fig. 3.20. XRD pattern of $K_xV_xW_{1-x}O_3$ at nominal composition, x = 0.15, at different temperatures. For clarity, the diffraction patterns are plotted vertically. At 400°C, the HTB type bronze phase began to form, but a second unknown phase (between 2θ = 23.0 and 24.4) appeared between 600°C and 800°C.
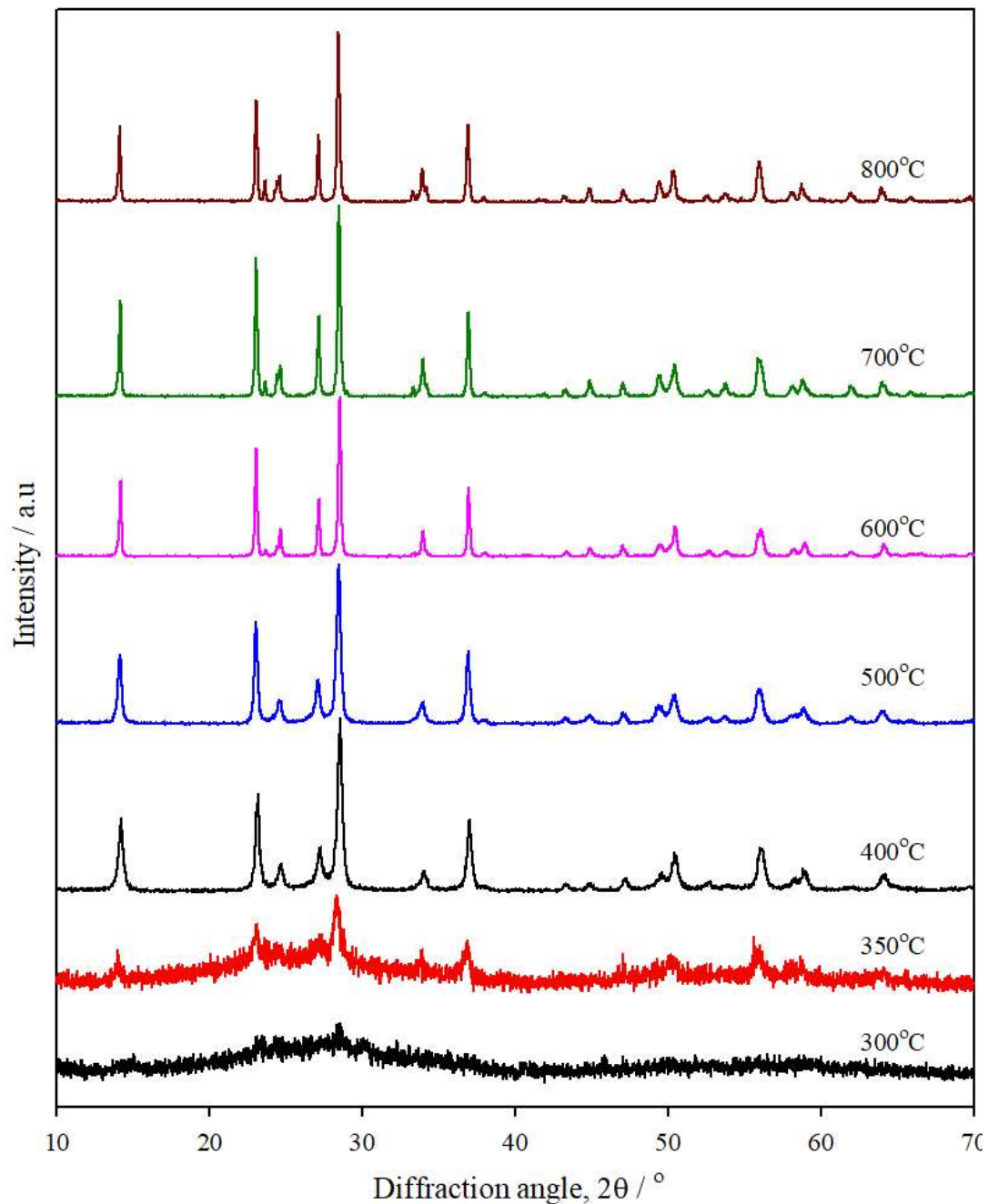
Fig. 3.21. XRD pattern of $K_xV_xW_{1-x}O_3$ at nominal composition, x = 0.20 at different temperatures. For clarity, the diffraction patterns are plotted vertically. At 400°C, the HTB type bronze phase began to form, but a second unknown phase (between 2θ = 23.0 and 24.4) appeared between 600°C and 800°C.
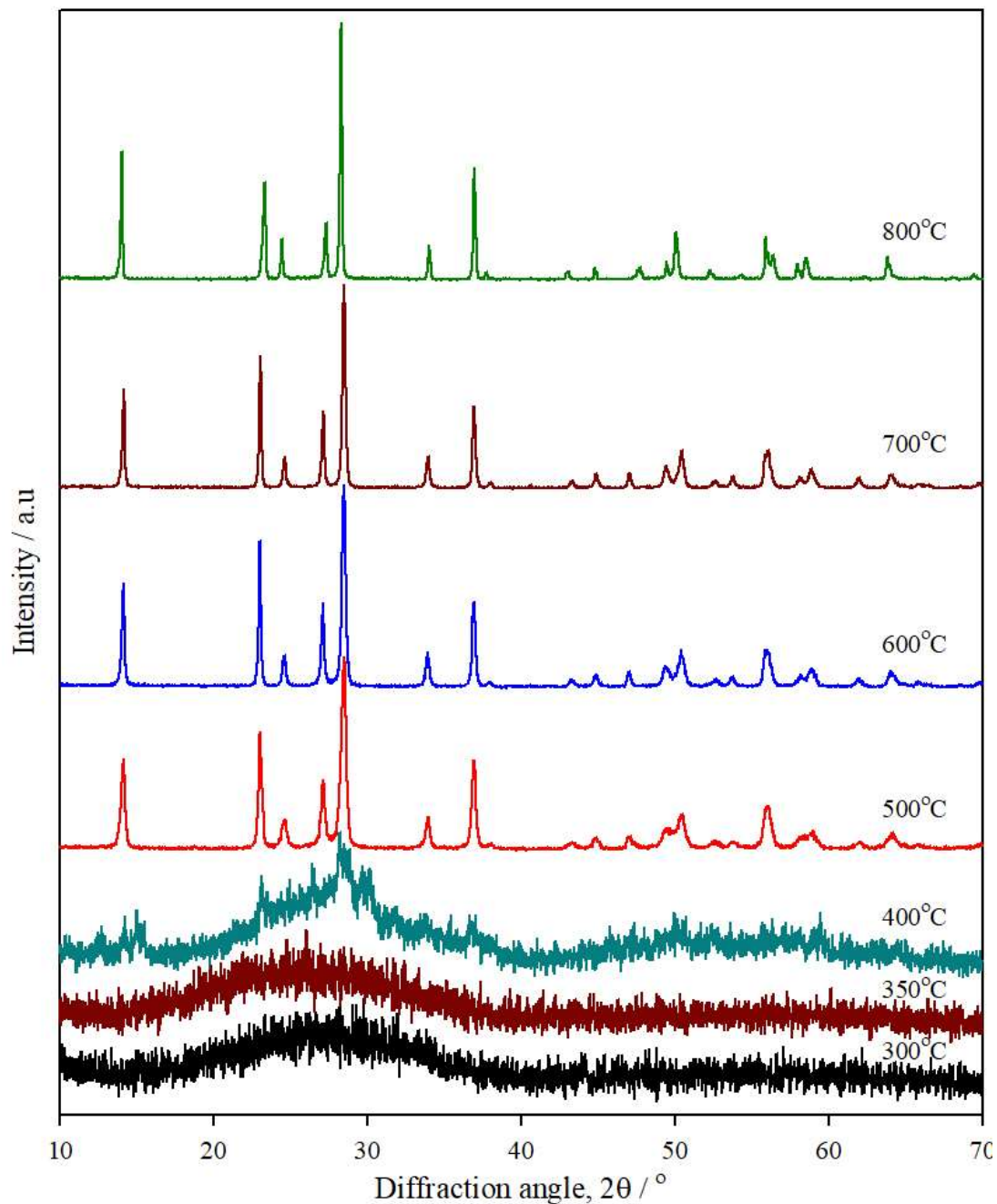
Fig. 3.22. XRD pattern of $K_xV_xW_{1-x}O_3$ at nominal composition, $x = 0.25$ at various temperatures. For clarity, the diffraction patterns are plotted vertically. The HTB bronze phase formed at temperatures ranging from 400-800°C.
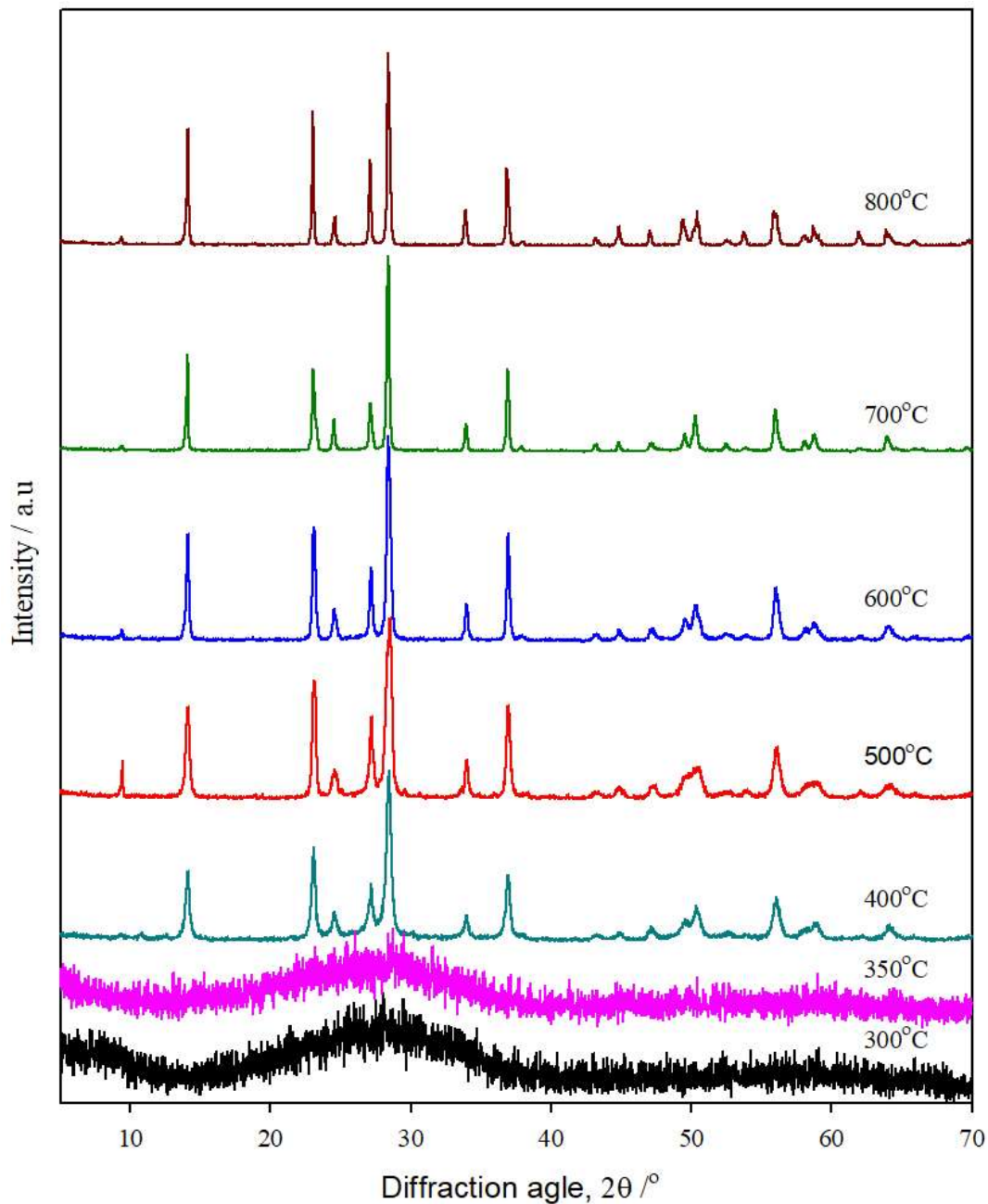
Fig. 3.23. XRD pattern of $K_xV_xW_{1-x}O_3$ at nominal composition, x = 0.30 at different temperatures. For clarity, the diffraction patterns are plotted vertically. At temperatures ranging from 400-800°C, a bronze phase of HTB type is formed.
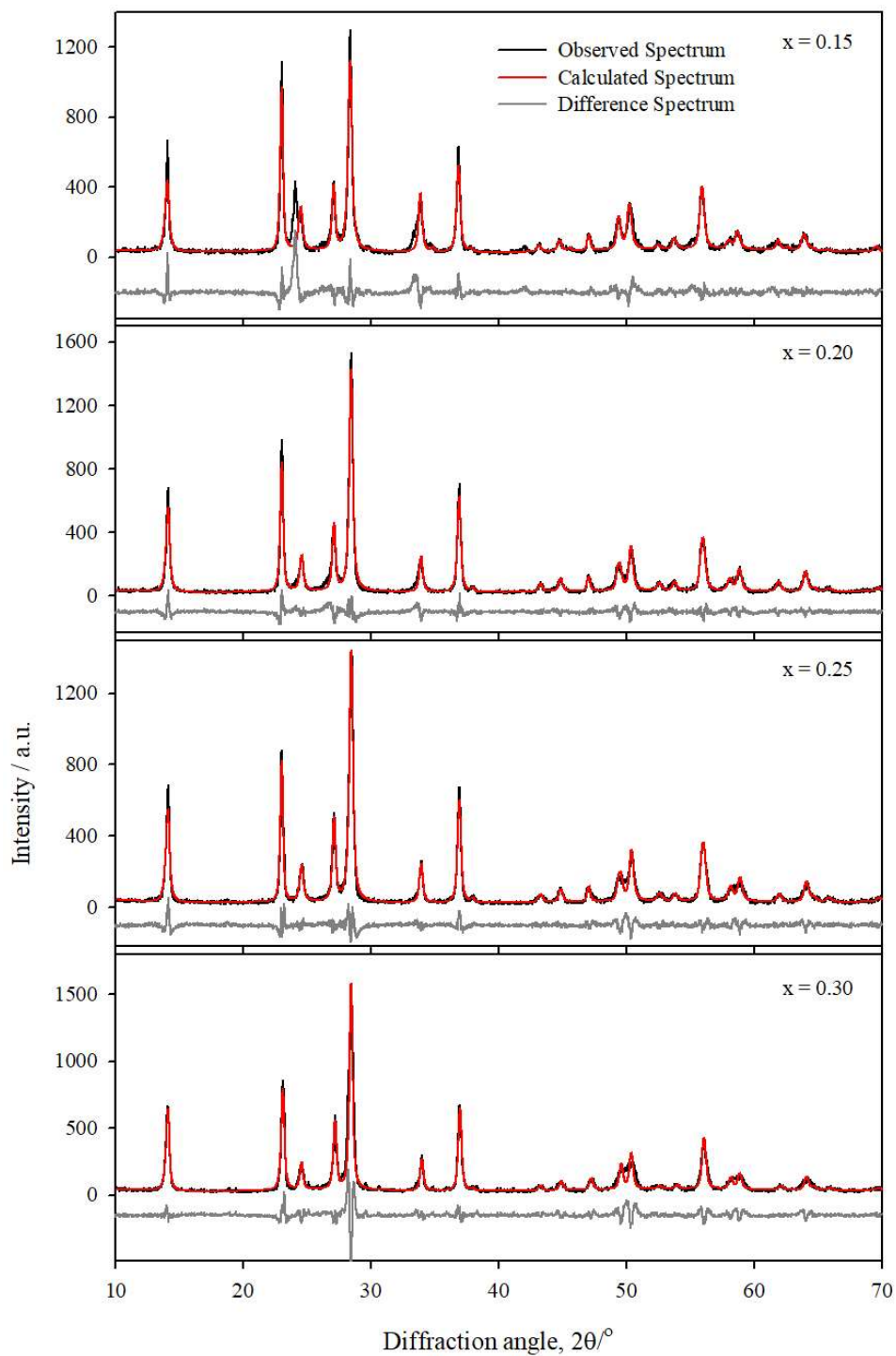
Fig. 3.24. Rietveld refinements fit of $K_xV_xW_{1-x}O_3$ (x = 0.15, 0.20, 0.25, and 0.30) series at 500°C. The black spectrum represents observed/measured spectrum, and the red spectrum represents calculated data. The black curve below the spectrum represents the difference spectrum.
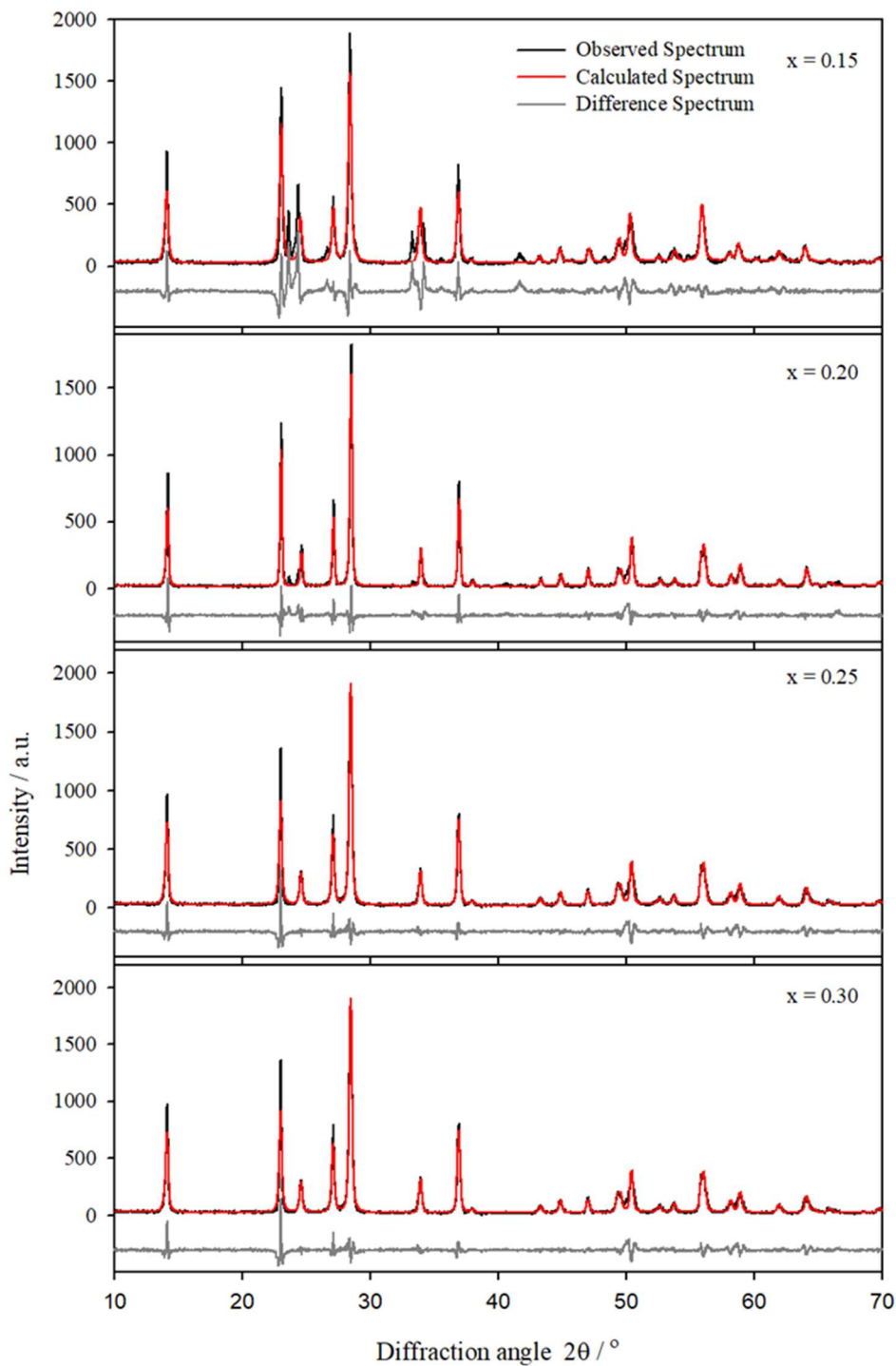
Fig. 3.25. Rietveld refinements fit of $K_xV_xW_{1-x}O_3$ (x = 0.15, 0.20, 0.25 and 0.30) series at 600°C. The black spectrum represents observed/measured spectrum, and the red spectrum represents calculated data. The black curve below the spectrum represents the difference spectrum.
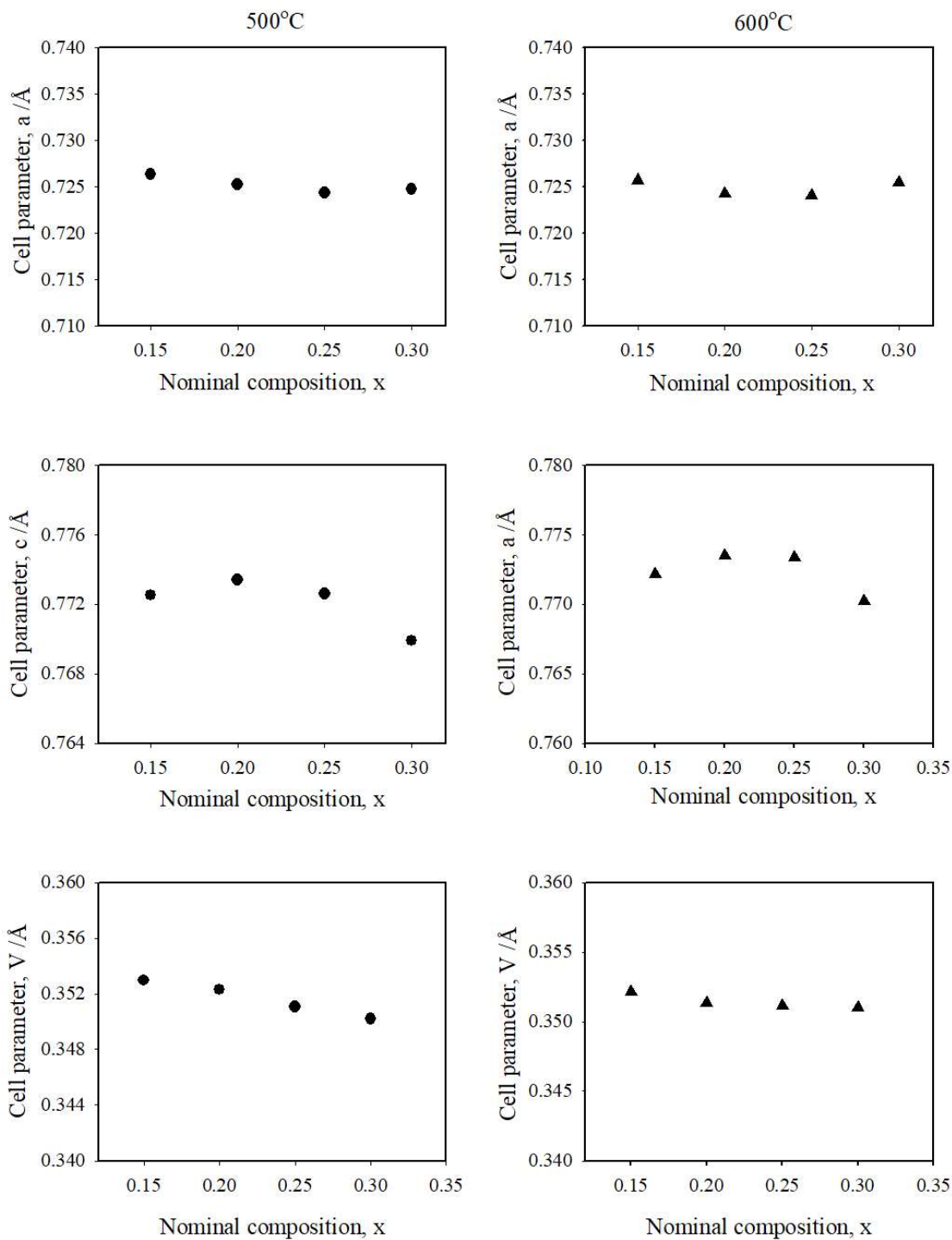
Fig. 3.26. Cell parameters (*a, c, V*) of $K_xV_xW_{1-x}O_3$ as a function of nominal composition, x at 500°C and 600°C.

3.3.3.b FT-IR analysis of of $K_xV_xW_{1-x}O_3$ series

Fig. 3.27 represent the FT-IR spectra of the prepared samples at different calcined temperatures. These spectra were collected in the 400-4000 cm^{-1} wavenumber range. The spectral pattern of both $Cs_xV_xW_{1-x}O_3$ and $K_xV_xW_{1-x}O_3$ are, in fact, very similar. The stretching vibration of MO_6 octehedra present in the $K_xV_xW_{1-x}O_3$ bronzoid where M is W or V, causes broad absoroption bands in the region of 500-1050 cm^{-1} [37, 99]. The weak absorption peaks found under 460 cm^{-1} represent the bending mode of the M-O-M joining bond [111]. In the higher wave number region (> 1000 cm^{-1}), no absopton band observed indicates the product is transparent in ths region (1050-4000 cm^{-1}) for the IR-radiation. The peak position centered at 440 cm^{-1} wavenumber systemically shifts to higher wavenumber with increasing nominal composition x, which may indicate substitution of W by V in the $K_xV_xW_{1-x}O_3$ series (Fig. A.3.6). The FT-IR spectra of the studied compounds are also similar to the FT-IR results found by Dey *et al.* for $Cs_{0.25}W_{1-y}Nb_yO_3$ and $Cs_{0.03}W_{1-y}Nb_yO_3$ series [37].
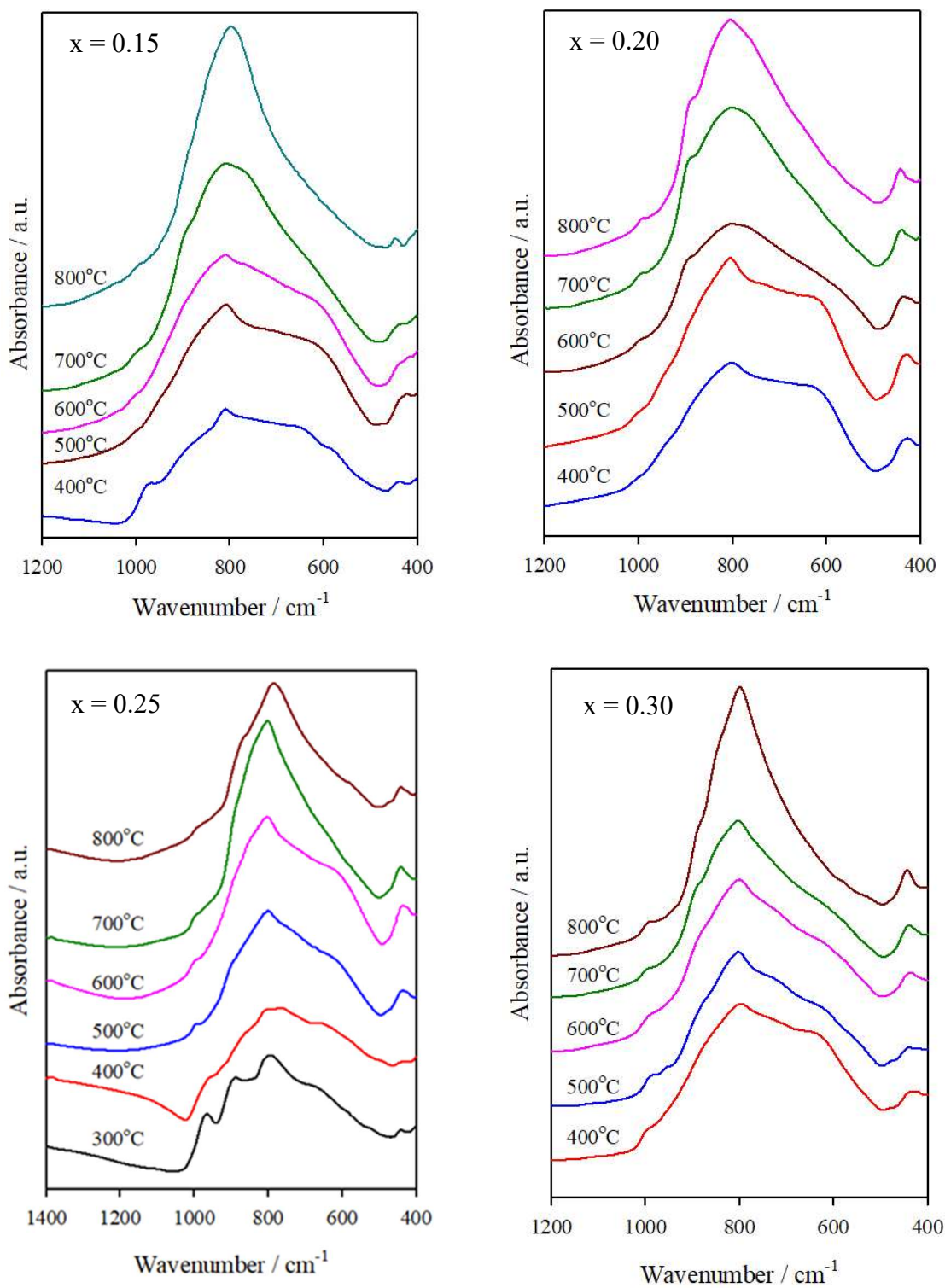
Fig. 3.27. FT-IR spectra of $K_xV_xW_{1-x}O_3$ at different compositions (x = 0.15 – 0.30) and at different temperatures. The spectra are plotted vertically for the sake of clarity.

3.3.3.c SEM/EDX analysis of $K_xV_xW_{1-x}O_3$ series

The size and morphology of $K_xV_xW_{1-x}O_3$ (x = 0.15-0.30) were studied by SEM. Fig. 3.28 presents the SEM micrographs of the samples prepared at 500°C. At comparatively higher temperatures, the synthesized $K_xV_xW_{1-x}O_3$ compound exhibits a rod-like structure having a diameter of 100-200 nm and a length of numerous micrometers. It is also observed that both the crystallinity and particle size increase gradually with increasing calcination temperatures, which agrees well with the result obtained from XRD analysis. It is observed from EDX results that the K^+ content is very close to the taken compositions. The close results from different spots of the sample indicate the satisfactory distribution of V^{5+} on the W^{5+} site in the products. The average ratios of potassium to tungsten and vanadium to tungsten are in good covenant with the nominal composition. At different nominal composition, the calculated and observed V:W values from EDX analysis are present in Table 3.7.
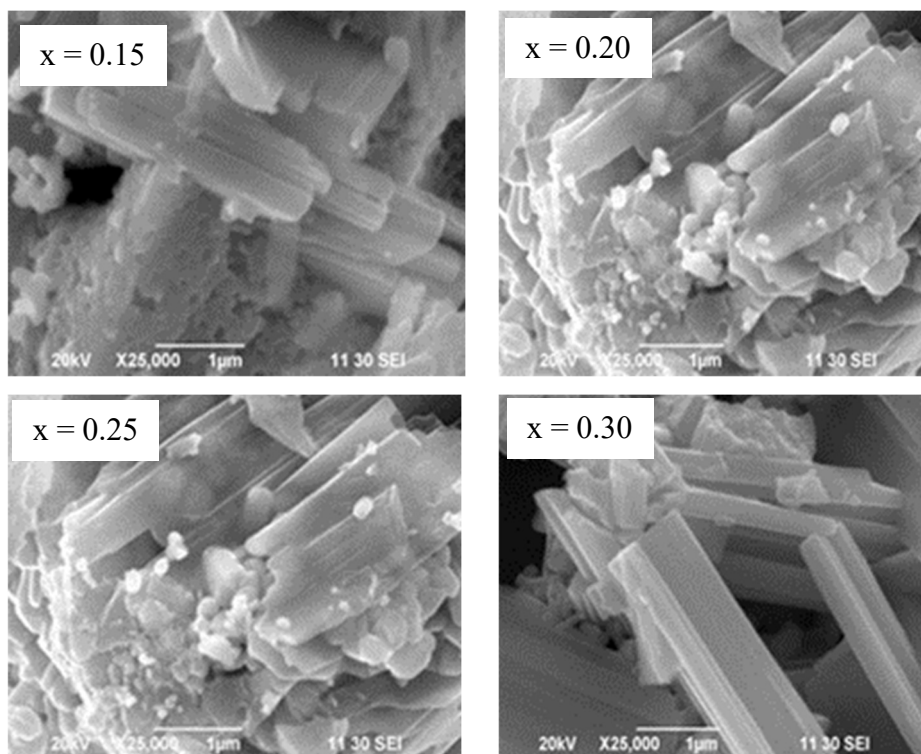
Fig. 3.28. SEM micrographs of $K_xV_xW_{1-x}O_3$ at 500°C.

Table 3.7 EDX results of $K_xV_xW_{1-x}O_3$ (x = 0.15 - 0.30) compound.

Composition, x	V:W	
	Taken	Found
0.15	0.049	0.049
0.20	0.069	0.077
0.25	0.092	0.090
0.30	0.119	0.130

Conclusion of alkali metal tungsten oxides

It has been shown that a series of polycrystalline samples with nominal composition $Rb_{0.30}W_{1-y}V_yO_3$ (y = 0.0 - 0.30) and $Rb_{0.25}W_{1-y}V_yO_3$ (y = 0.0 - 0.25) could be synthesized by solid state synthesis method at 700˚C in an evacuated silica glass tube. Analysis of X-ray powder diffraction data revealed the formation of single-phase hexagonal tungsten bronze (HTB). The samples with y ≥ 0.20 showed the presence of a small amount of other phases along with HTB. An overall decreasing trend of the calculated unit cell volume was observed with increasing vanadium content. The IR absorption spectrum y = 0.0 sample shows a featureless increase in intensity with increasing wavenumber due to the screening of phonons by the polarons. This effect gradually disappears with the successive replacement of W^{5+} ions by V^{5+}. Consequently, they develop a phonon absorption feature as a function of y. The incorporation of vanadium in the $Rb_xW_{1-y}V_yO_3$ system was also verified by SEM/EDX analysis. It is concluded that the substitution of V^{5+} for W^{5+} causes a strong elongation of the MO_6 polyhedra along z, compromised by a strong compression in the xy plane. Therefore, the unit cell volume only slightly decreases with increasing y related to the smaller radius of V^{5+} compared to W^{5+}.

Because of their appealing crystal chemistry, optical, electrical and magnetic properties, research on alkai metal tungsten bronzes $A_x(W^{5+}_xW^{6+}_{1-x})O_3$ with $0 < x \leq 1$ is abundant. These properties are mainly related to the associated W^{5+} and W^{6+} ions situated in the same crystallographic position. The properties of bronzoids also depend on the concentation, type, and radius of the A^+ cation. The crystal structure of HTB bronzoid is manily formed by corner-shared WO_6 octahedra forming channels and A^+ cation is situated there. The number of WO_6

octahedra forms a ring leading to tetragonal and hexagonal channels depending on size, concentration, and type of A^+ cation. However, fewer reports are found in the literature on the substituted alkali metal tungsten bronzoids, especially with transition metals, in spite of the fact that when both oxidation state and ionic radii are same/comparable.

Vanadium substituted alkali metal tungsten bronzoids, $A_xV_xW_{1-x}O_3$ (A = K, Cs) were synthesized by the solution combustion method, a simple, convenient and promising method for the preparation of oxide bronzes, bronzoids and other related compounds. The tungsten bronzoids, $A_xV_xW_{1-x}O_3$ (A = K, Cs) crystallized in the HTB phase within the range under study, $0.15 \leq x \geq 0.30$. It is reported that the HTB structure is made by corner-shared WO_6/VO_6 octahedra, which gives rise to tri- and hexagonal channels formed by the linkage of 3 and 6 octahedra, respectively. The trigonal channels are too small to accommodate alkali ions like K^+ and Cs^+. The alkali ions in HTB are thus located in the hexagonal channels. In this $A_xV_xW_{1-x}O_3$ composition, V^{5+} could only be substituted up to x = 0.33. The XRD pattern of the prepared samples confirms that HTB forms at all temperatures investigated. Calcining of these bronzoids at higher temperatures results in the decomposition of the products. The XRD pattern of $A_xV_xW_{1-x}O_3$ (A = Cs and K) at nominal composition x = 0.15 and 0.20 shows the appearance of an unknown second phase at higher temperature. Other samples in the series with nominal composition x = 0.25 and x = 0.30 posses pure HTB phase. It is also observed that the peak intensity increases with temperarue and becomes sharper and narrower. Due to the partial substitution of W by V, the diffraction lines systematically shifted with increasing the V content of the samples. The formation of the HTB structure is also confirmed by the FT-IR spectral data of the synthesized products. SEM images show rod like nanoparticles for $K_xV_xW_{1-x}O_3$ and flex- like for $Cs_xV_xW_{1-x}O_3$, the sizes of which increase with increasing temperatures. Both the observed K and V contents agree well with nominal compositions found in EDX analysis of $K_xV_xW_{1-x}O_3$.

The calculated cell parameters for the samples prepared at 500°C and 600°C show a small shift, indicating the partial substitution of W by V in these series. Our study reveals that vanadium substituted alkali metal tungsten bronzoids can be prepared by the SCS method. Both the temperature and composition play a crucial role in the formation of HTB phases of vanadium substituted alkali metal tungsten bronzoids. The size of the alkali metal ion is also an important factor.

Chapter Four

Tungsten Metaphosphates

4.1 Phosphate tungsten bronzes and their structural features

Metal phosphates are one of the most promising materials which can be used as catalysts, fluorescent materials, ceramic materials, dielectric substances, food additives, fuel cells, pigments, metal surface treatment [149-152]. However, higher functional properties of the material were observed when rare earth elements were added. The addition of rare earth elements to phosphates increased specific surface area and particle size, which improved the catalytic activity of metal phosphates. Phosphates with transition metals are very fascinating in solid state chemistry due to their economically advantageous properties. Depending on the methods and condition of synthesis, the structure and properties of transitional phosphates can be varied.

4.2 Phosphate tungsten bronzes (PTB)

PTB's are a family of mixed-valence compounds and their structure is built by the covalent phosphate layers association with a metallic ReO_3-type matrix. These are amazing non-stoichiometric compounds depending on several physical and chemical factors [153]. Raveau and his co-workers in 1978 synthesized the first crystal of phosphate tungsten bronze [154]. The phosphate tungsten bronzes have a great variety of crystal structures. Eight WO_6 octahedra share corners in the main frame of the structure of different phosphate tungsten bronzes, like the classical perovskite enclosure. When one WO_6 octahedra is replaced by one PO_4 form monophosphate tungsten bronzes (MPTB), and two adjacent WO_6 octahedra are replaced by a P_2O_7 diphosphate group sharing a common oxygen form diphosphate tungsten bronze (DPTB) shown in Fig. 4.1. Due to these substitutions inducing minor local deformations, the classical O-O distance in PO_4 tetrahedron (~2.4 Å) is always less than WO_6 octahedron (~2.7 Å). Three different types of deformation are known [7], namely: (i) a distortion of the adjacent WO_6 octahedra, which entails a lengthening of some of their O-O distances; (ii) a possible tilting of these octahedra; and (iii) a possible displacement of the W atoms within the octahedra, involving an off-centered W position and consequently different distributions of the six W-O distances.
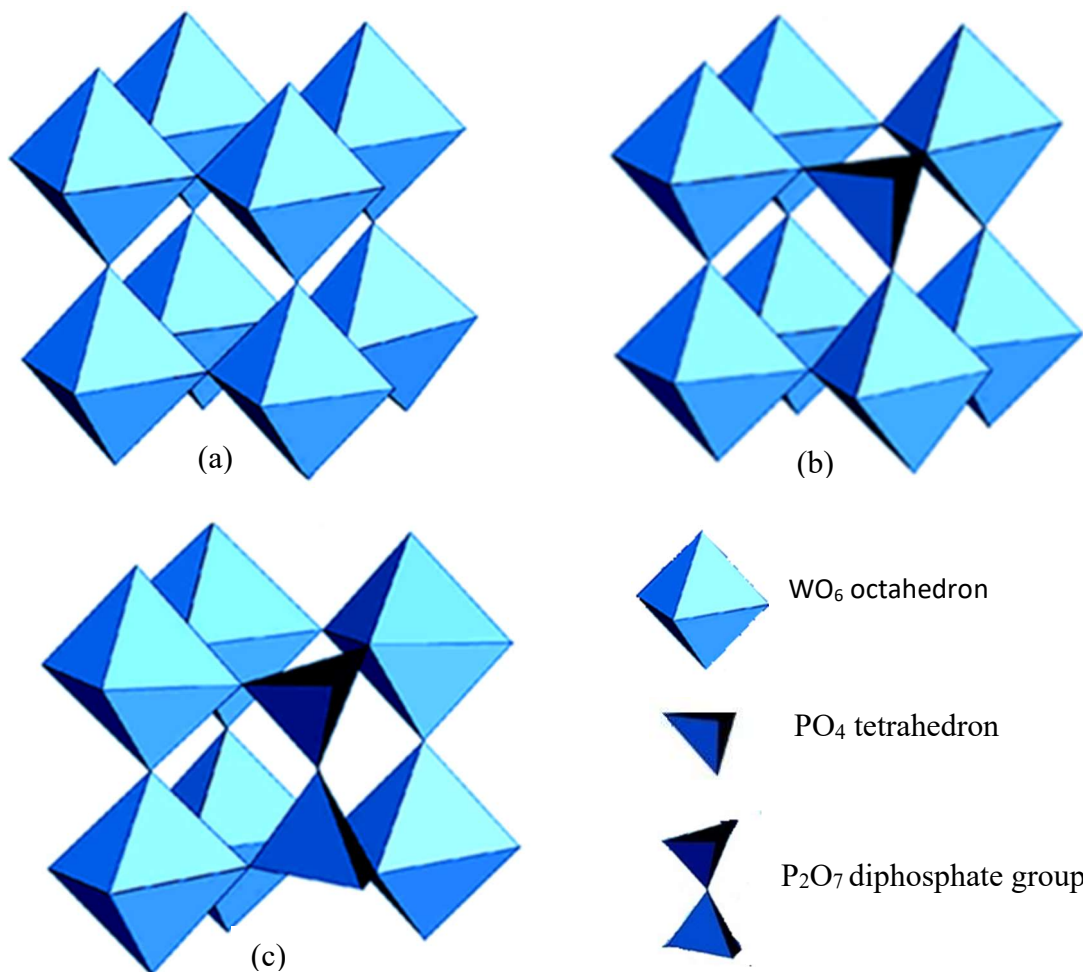
Fig. 4.1. (a) Classical perovskite cage, (b) Monophosphate tungsten bronzes (MPTB), and (c) Diphosphate tungsten bronzes (DPTB).

The PO$_4$ tetrahedra or the P$_2$O$_7$ groups are joined to one octahedral slab, leaving only one oxygen per tetrahedron to connect to a neighboring slab. The tetrahedra are then included in the slab, to make the boundaries on each side which contribute towards the thickness of the slab. The thickness of stacking of WO$_3$-type slabs is indicated by the value of m.

4.2.1 Monophosphate tungsten bronzes (MPTB)

The monophosphate tungsten bronzes (MPTB) can be described by the formulations A$_x$(WO$_3$)$_{2m}$(PO$_2$)$_4$ and (WO$_3$)$_{2m}$(PO$_2$)$_4$ depending on the presence or absence of an inserted cation (A) in the structure's tunnels, where x is the cation stoichiometry (A = Na, K, Pb) and m is an integer other than zero [156-159]. Two forms of monophosphate tungsten bronzes are known as MPTBp having pentagonal tunnels and MPTBh having hexagonal tunnels.

Depending on orientations, the combination of WO_3 and phosphate slices creates hexagonal or pentagonal tunnels.

The orientation of the WO_3 slabs with relation to the perovskite axes [100]p, [010]p, and [001]p can be described. In an MPTB compound, all of the slabs are typically the same thickness and parallel to (112)p. Two neighboring slabs probably linked in one of two ways to create MPTBp and MPTBh:

i)   Two subsequent slabs connected by O atoms are turned 180 degrees to create their images; at the edge, cages with pentagonal windows appear and form MPTBp.

ii)   Two neighboring slabs connected by O atoms undergo translation, resulting in the formation of cages with hexagonal windows, or MPTBh.
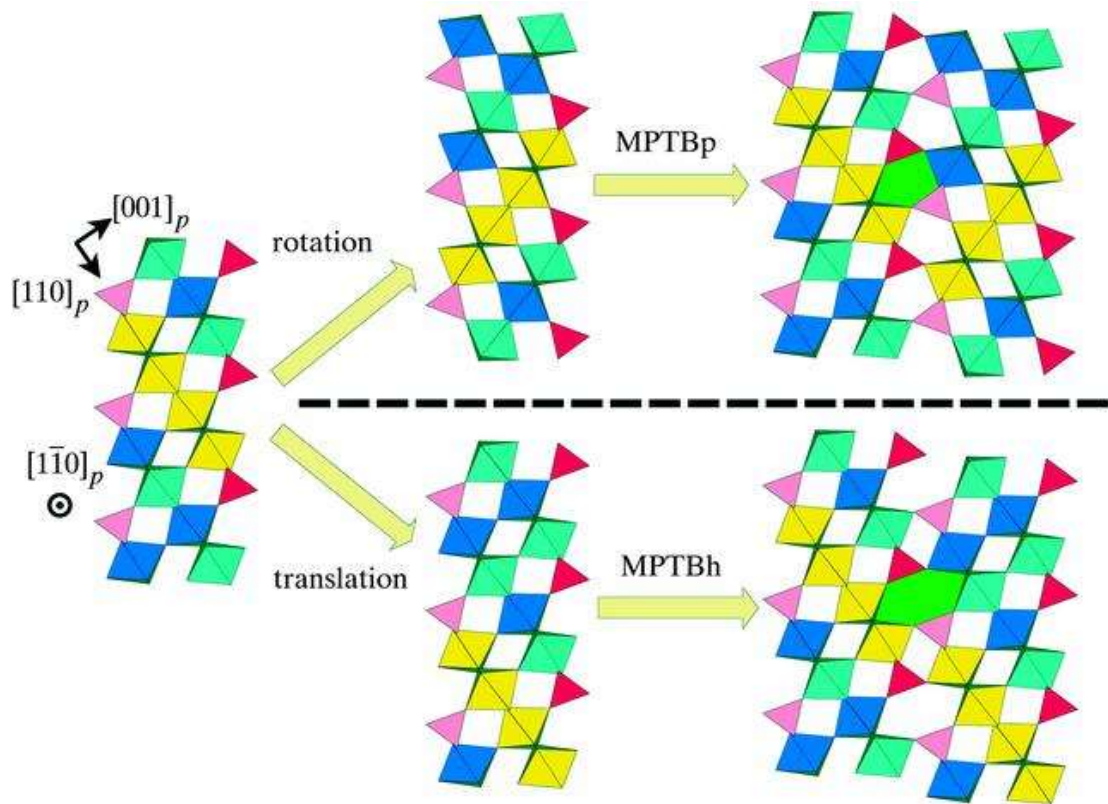
Fig. 4.2. Structural relations among the MPTBp family and MPTBh family.

4.2.2 Monophosphate tungsten bronzes with pentagonal tunnels (MPTBp)

MPTBp has the general formula $(PO_2)_4(WO_3)_{2m}$ where m is an integer (2, 4-16) is a homologous series [155, 160-162]. Again, an MPTBp structure is formed by $A_x(PO_2)_4(WO_3)_{2m}$ where A = Na, K and x < 1.0 [163]. As illustrated in Fig. 4.3(a), the screw axis connecting the two consecutive WO_3 slabs in the MPTBp with the formula $(PO_2)_4(WO_3)_{2m}$ is parallel to (010). Here it is observed that pentagonal tunnels open at the joint of the WO_3 and the phosphate slices [164]. The pentagonal tunnels are generally empty. Partial filling of pentagonal tunnels by Na^+ has been reported for the m = 4 and m = 6 members [164, 165].

(a)   (b)
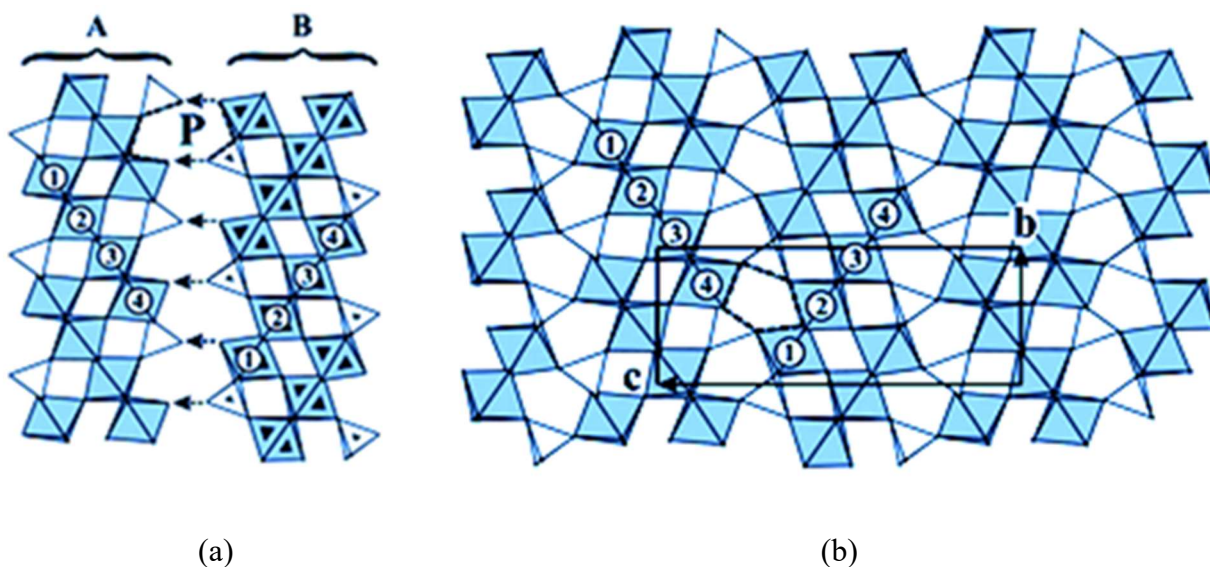
Fig. 4.3. (a) Structural arrangements of MPTBp, m = 4, from two slices A and B linked by 180° rotation. (b) Projection of MPTBp along a, here m = 4, i.e., four WO_6 octahedra describing the WO_3 slabs' thickness and numbered 1-4.

The thickness of the WO_3 slabs is denoted by m. For even-m members m/2, WO_6 octahedra are in the slabs (Fig. 4.4) and for odd-m members, (m+1)/2 and (m-1)/2 sequences of WO_6 octahedra alternate in adjacent WO_3 slabs which repeat in a zigzag fashion (Fig. 4.5).
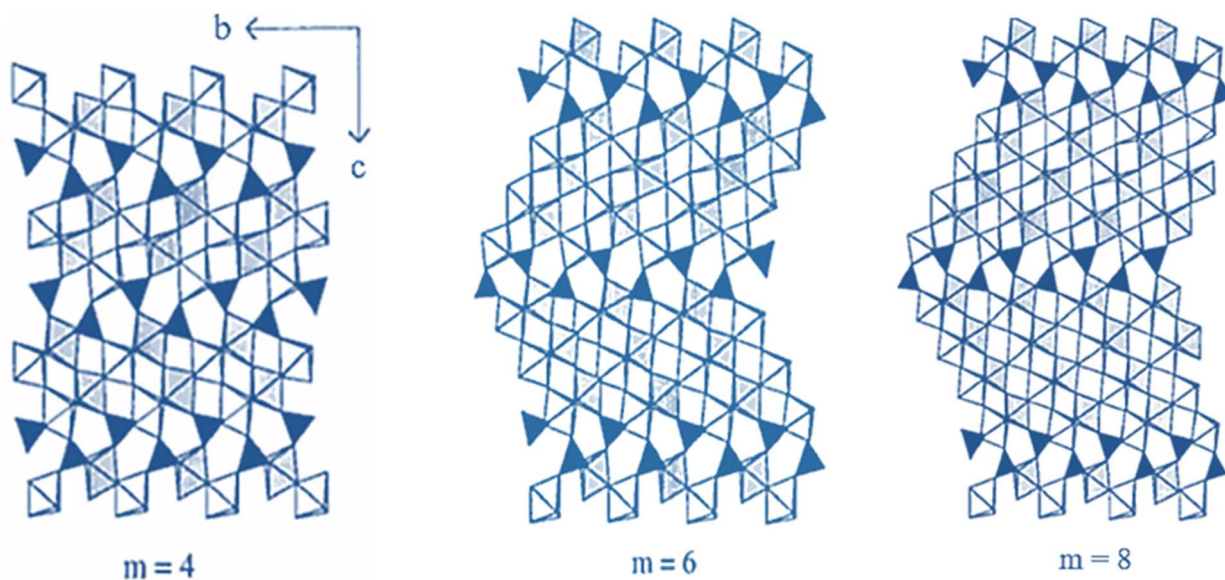
Fig. 4.4. Schematic structure of MPTBp, $(PO_2)_4(WO_3)_{2m}$, m = 4, 6, 8 with m/2-wide slabs of ReO_3-type WO_6 octahedra interconnected by PO_4 tetrahedra.
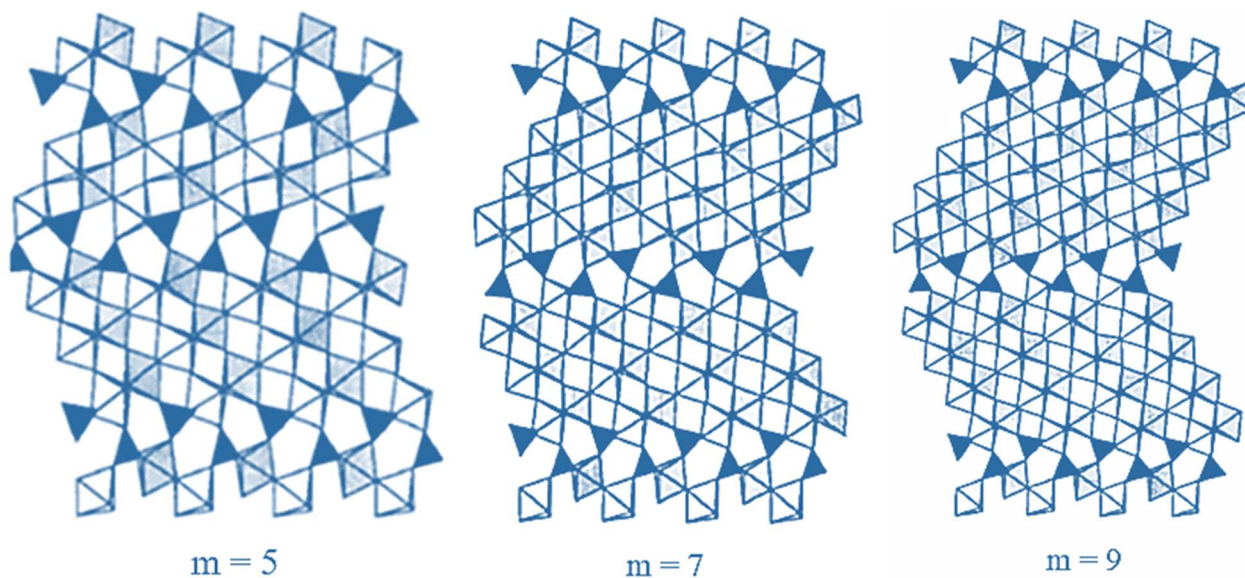
Fig. 4.5. Schematic structure of MPTBp, $(PO_2)_4(WO_3)_{2m}$, m = 5, 7, 9 with (m +1)/2 and (m-1)/2-wide slabs of ReO_3-type WO_6 octahedra interconnected by PO_4 tetrahedra.

4.2.3 Monophosphate tungsten bronzes with hexagonal tunnels (MPTBh)

MPTBh series having the general formula $A_x(PO_2)_4(WO_3)_{2m}$, where A is an inserted cation within the hexagonal tunnels such as Na^+, K^+ or Pb^{2+} (radius limited to ~1.33 Å) [164]. The compounds having m from 4 to 13 are known and the value of x, depending on the inserted cation, ranges from 1.75 to 3.00 [156, 163]. The structure of MPTBh is very similar to MPTBp, forming a ReO_3-type structure by corner-shared WO_6 slabs linked by PO_4 tetrahedra. At the shared point between two octahedral layers, the octahedral and tetrahedral corners share to form hexagonal tunnels, and the A cations are located there. The structural difference between MPTBp and MPTBh depends on the relative arrangement of the layers. The octahedral chain exhibits a gig-gag configuration for MPTBp, whereas in MPTBh the octahedral chain remains parallel from one ReO_3-type layer to the next.
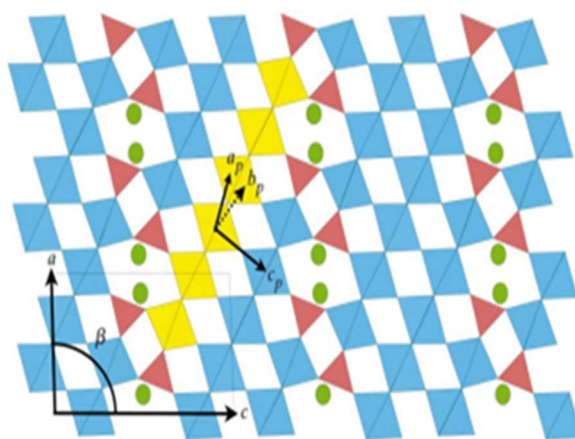
Fig. 4.6. $K_xP_4W_{12}O_{44}$ projected along (010), m = 6 terms of the family of MPTBh.

The symmetry of MPTBh is monoclinic with β as per monoclinic angle and c as the longest axis. Subsequently, b is perpendicular to the plan (Fig. 4. 6). The A cations seem to be at the level of the tetrahedral portions and can be visualized through the hexagonal windows visible at the interface of two slabs of WO_3-type. When the cations Na^+ or Pb^{2+} are introduced, the c parameter becomes double for all members of the series [165]. $K_x(PO_2)_4(WO_3)_{2m}$ series for x = 2 and m = 4, 6, 7, 8 and 10 were isolated and studied by X-ray diffraction and scanning electron microscopy [166]. Three types of defects are noticed in the crystals which are (i) the distribution of the phosphate planes with respect to the ReO_3-type slabs, (ii) the distribution of the K^+ ions in the channels, and (iii) the irregular arrangements of the phosphate planes.

4.2.4 Mixed metal monophosphate tungsten bronze

Recently, another type of monophosphate tungsten bronze known as mixed metal monophosphate tungsten bronze has been observed. For the monophosphate tungsten bronze $W^{5+}OPO_4$ (2nd member of the MPTB series, i.e., $(PO_4)_2(WO_3)_{2m}$ with m = 2, it was shown that co-replacement of pentavalent tungsten by hexavalent tungsten and trivalent cations is possible ($Cr^{3+}_{1/3}W^{6+}_{2/3}OPO_4$). It was also demonstrated [167] that $(PO_2)_4(W^{5+}O_3)_4(W^{6+}O_3)_4$ (MPTB with m = 4) can be modified by [167] substituting W^{5+} for W^{6+} and another transition metal of appropriate oxidation state, and the substituted phases with m = 4, $(M^{3+}_{1/6}W^{6+}_{5/6}O_3)_8(PO_2)_4$ (M = V and Cr) were detected.
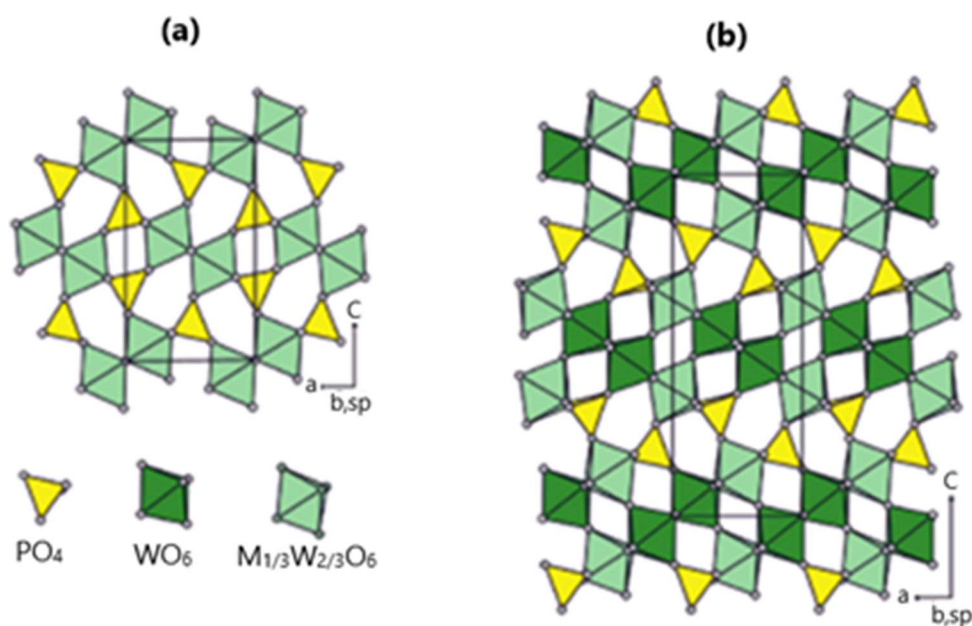
Fig. 4.7. Crystal structure of (a) $WOPO_4$ and (b) W_8O_{24} $(PO_2)_4$. Light green octahedron indicates mixed vacancy ($M^{3+}_{1/3}W^{6+}_{2/3}$) for the metal located in the isotopic mixed metal – MPTB ($M^{3+}W^{6+}_{2/3})OPO_4$ and $M^{3+}_{4/3}W^{6+}_{20/3}O_{24}(PO_2)_4$ [167].

Roy *et al.* also demonstrates the possibility of changing $(W^{5+}O_3)_4(W^{6+}O_3)_4(PO_2)_4$ (MPTB with m = 4) by replacing W^{5+} with W^{6+} and another transition metal with a suitable oxidation state (Fig. 4.7(b)). The replaced phases with m = 4 member $(M^{3+}_{1/6}W^{6+}_{5/6}O_3)_8(PO_2)_4$ (M = V and Cr) were prepared. It has been shown by Roy *et al.* that complete substitution of W^{5+} by either $(Ti^{6+}_{1/2} W^{6+}_{1/2})$ or $(M^{3+}_{1/3}W^{6+}_{2/3})$ through M^{3+} = V, Cr, Mo, Fe is possible in monophosphate tungsten bronzes $(WO_3)_{2m}(PO_2)_4$ with m = 2 and 4. These mixed metal monophosphate

tungsten bronzoids (mm-MPTB) do not show the characteristic bronze color of MPTB; instead, their colors, characteristic of M^{3+} ions, suggest localized electrons and insulating behavior.

4.2.5 Diphosphate tungsten bronzes (DPTB)

The general formula for diphosphate tungsten bronzes (DPTB) is $A_x(WO_3)_{2m}(P_2O_4)_2$, where the inserted cation A is of larger size (K, Ba, Rb, Tl, Ba and Cs) and belongs to $4 \leq m \leq 10$ [168, 169]. Their host-lattice $(WO_3)_{2m}$ is made by ReO_3-type slabs which are connected through planes of diphosphate group [156]. The first diphosphate tungsten bronze was isolated by Giroult in 1980 with the composition $Rb_{0.8}P_4W_{16}O_{56}$. The official name was given by Kihlborg (1982) [168, 170]. The structural principles of diphosphate tungsten bronzes and monophosphate tungsten bronzes are nearly identical. The identical slabs of ReO_3-type in diphosphate tungsten bronzes are cut parallel to (102) of the perovskite reference axes, which is the dissimilarity with MPTB. The diphosphate tungsten bronzes (DPTB), the tetrahedral slice containing diphosphate groups and their interconnections with WO_6 octahedra, build channels in which large-sized cations are inserted. In the diphosphates, the horizontal P_2O_7 group is toughly connected to four O atoms of four WO_6 octahedra of the slab, leaving two free O atoms to join a similar slab. The perovskite slabs are nearly regular and their perovskite channels are empty. In DPTB, the ReO_3-type slabs have corner sharing octahedral in the $[100]_p$ direction with a variable m and the even m members differ from the odd members by a translation of one phosphate plane out of two. As a result, the perovskite slabs are built up of identical chains of m/2 octahedra in the $[010]_p$ direction of the even members. For odd-m members, the octahedral chains parallel to $[010]_p$ of one slab are alternately former of (m + 1)/2 and (m - 1)/2 octahedra [156]. According to the length of the segments, these slabs, with variable thickness, are bound on each side by P_2O_7 diphosphate groups, and two successive slabs are connected through these groups. Theoretically, two structural types are possible: (i) the diphosphate tungsten bronzes with hexagonal channels (DPTBh) and (ii) the diphosphate tungsten bronzes with pentagonal channels (DPTBp). When two consecutive slabs are linked by a mirror plane which passes through the diphosphate groups, channels with a pentagonal section seem at the connection. However, in contrast to MPTB, two structure types are often encountered: only the diphosphates with hexagonal channels are synthesized, while

pentagonal channels are only seen in the electron microscope and have numerous defects [168].

4.2.6 Diphosphate tungsten bronzes with hexagonal tunnels (DPTBh)

The general formula for DPTB with hexagonal tunnels (DPTBh) is $A_x(WO_3)_{2m}(P_2O_4)$ ($4 \leq m \leq 10$), where different monovalent or divalent cations such as K^+, Tl^+, Rb^+ or Ba^{2+} can be inserted. They formed a ReO_3-type structure with regular stacking of identical slabs, having the same width slabs along a length that comprises monoclinic symmetry. As per the MPTBh family, b has been chosen along the twofold axis. The cations are positioned on the axis of the hexagonal channels due to large cages bound by eight WO_6 octahedra and two P_2O_7 groups stacking along b. The hexagonal plane is perpendicular to the channel axis and can be considered here as true tunnels [155]. The existing geometrical relations between the DPTBh family cell parameters and those of perovskite [159], shown in Fig. 4.8 for m = 4 ($Rb_xP_4W_8O_{32}$).
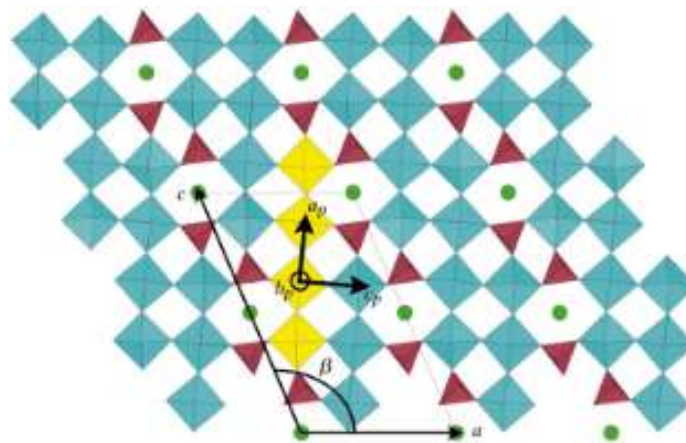
Fig. 4.8. $Rb_xP_4W_8O_{32}$ projected along (010) , m = 4 of the family of DPTBh.

4.2.7 Diphosphate tungsten bronzes with pentagonal tunnels (DPTBp)

The DPTB family has never been produced in a pure phase. In 1985, Hervieu *et al.* [155, 171] through high–resolution transmission electron microscopy (HRTEM), detected a few crystals of microstructure with ReO_3-type having several thicknesses related to identical domains. The identical boundary is inclined at 65 with respect to *c*-axis. As shown in Fig. 4.9, the boundary linked with pentagonal channels and surrounded by two groups of P_2O_7 with three WO_6

octahedra proposed a new structure of diphosphate tungsten bronzes, $(WO_3)_{2m}(P_2O_4)_2$ with pentagonal channels (DPTBp). The members of this family belong to an orthorhombic cell.
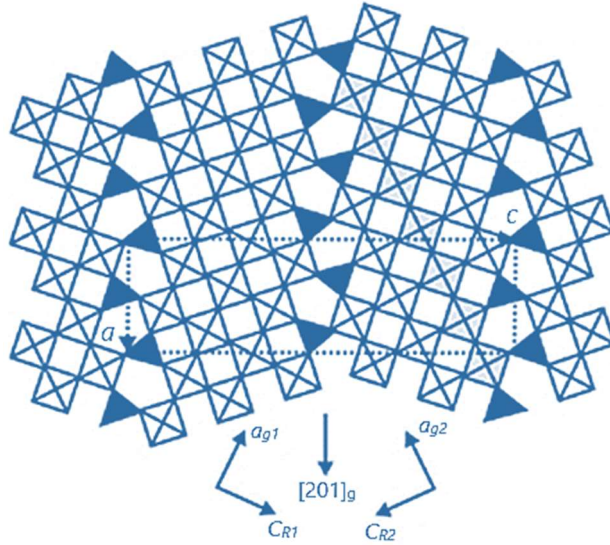
Fig. 4.9. Perfect projection of (010) for m = 7 member of the $(WO_3)_{2m}(PO_2)_4$ type structure. Here the identical boundary contains vacant pentagonal channels.

4.3 Synthesis of mixed metal monophosphate tungsten bronze, $A_{4/3-x}T_xW_{20/3}O_{24}(PO_2)_4$ (A/T = Cr, Fe, Al and x = 0, 1/3, 2/3, 3/3, 4/3)

The starting material used for the synthesis of $A_{4/3-x}T_xW_{20/3}O_{24}(PO_2)_4$ were high quality reagent grade $Fe(NO_3)_3.9H_2O$ (Sigma Aldrich, Germany), $Cr(NO_3)_3.9H_2O$ (Sigma Aldrich, Germany), $Al(NO_3)_3.9H_2O$ (Sigma Aldrich, Germany), NH_4NO_3 (Sigma Aldrich, Germany), H_2WO_4 (Sigma Aldrich, Germany), $NH_4H_2PO_4$ (Sigma Aldrich, Germany) and NH_4OH (Sigma Aldrich, Germany). The chemicals were used without any further purification. The $A_{4/3-x}T_xW_{20/3}O_{24}(PO_2)_4$ series were synthesized using the solution combustion synthesis (SCS) method. This method is based on a brief, exothermic burning reaction between oxidizing agents and organic fuel. It includes two steps: (i) formation of the precursor, and (ii) auto-ignition. Reactants were taken in appropriate molar proportions according to the following equation:

$$\left(\frac{4}{3} - x\right)A(NO_3)_3.9H_2O + xT(NO_3)_3.9H_2O + \left(\frac{20}{3}\right)H_2WO_4 + 4NH_4H_2PO_4 \rightarrow$$
$$A\left(\frac{4}{3} - x\right)T_xW_{\frac{20}{3}}(PO_2)_4, \text{ where A/T = Cr, Fe and Al.}$$
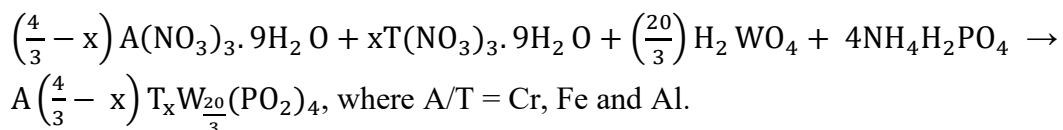
A calculated amount of tungstic acid H_2WO_4, metal such as [$Fe(NO_3)_3.9H_2O$, $Al(NO_3)_3.9H_2O$ and $Cr(NO_3)_3.9H_2O$], ammonium dihydrogen phosphate, $NH_4H_2PO_4$ and ammonium nitrate, NH_4NO_3 were dissolved in a minimum volume of aqueous ammonia, and glycerin was added in it. Metal nitrates, ammonium nitrate, ammonium dihydrogen phosphate acted as oxidizers and glycerin acted as a fuel. The ratio of n(glycerin) to n(NH_4NO_3) = 1: 8 was maintained in all experiments. The solutions were then evaporated ($\leq 100^oC$) carefully to a viscous gel to stop early ignition. Then the gel was heated in the burner until the release of the brown NO_x gases, which confirms the decomposition of the metal nitrates. The release of the brown gases led to the formation of fluffy masses. The fluffy mass was grounded in an agate mortar to get a fine powder and then placed in a porcelain crucible. Afterwards, the fine dry powder was calcined in a muffle furnace at a temperature in the ranges of 500-800^oC with a 50^oC interval for 24 hours in each case to get the desired product. The sample preparation process is schematically shown in the flow chart.
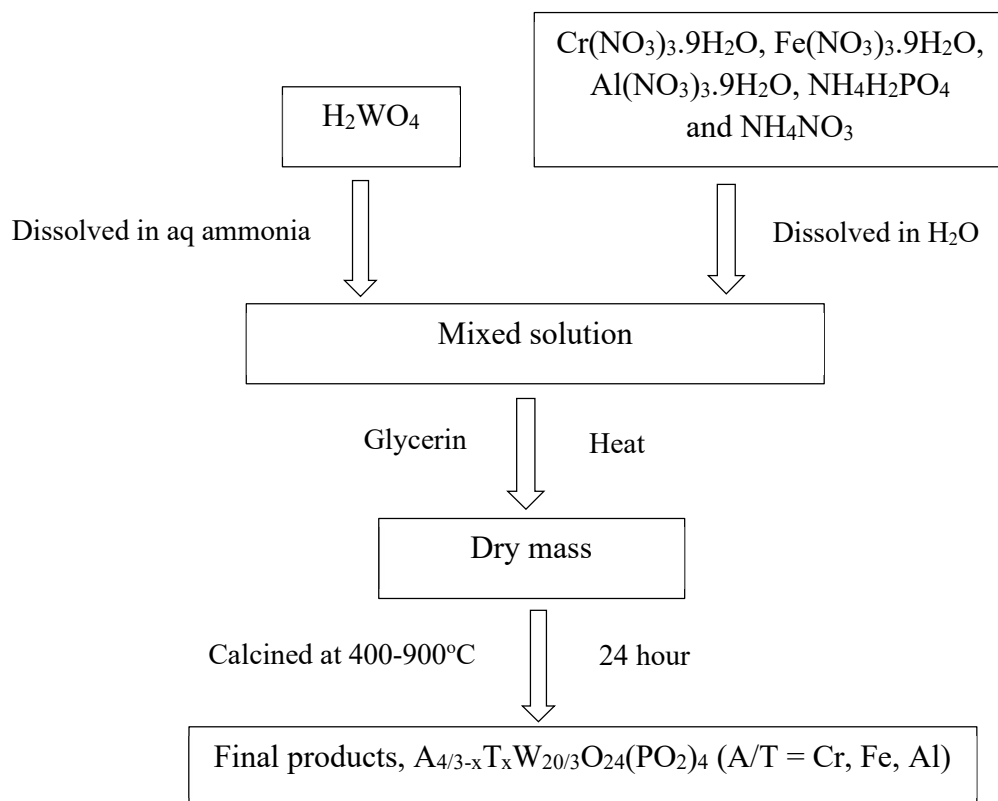
Fig. 4.10. Flow chart of the mixed metal monophosphate tungsten bronze, $A_{4/3-x}T_xW_{20/3}O_{24}(PO_2)_4$, (A/T = Cr, Fe, Al and x = 0, 1/3, 2/3, 3/3, 4/3) preparation method.

4.4 Characterization of mixed metal monophosphate tungsten bronze, with nominal composition $A_{4/3-x}T_xW_{20/3}O_{24}(PO_2)_4$, (A/T = Cr, Fe, Al and x = 0, 1/3, 2/3, 3/3, 4/3)

The crystlline structure of the prepared sample was determind with an X-ray Diffractometer (Model Rigaku Ultima IV, Japan), which is eqipped with CuK_α radiation. The 2θ range for collecting XRD patterns was 5 to 80° in a continuous scan mood. The cell parameters of some selected samples were refined using the Rietveld program profex [45]. Scaaning Electron Microscope (SEM) (Model JEOL JSM-6490LA, Japan) with an electron voltage of 20KV was used to examine the morphology and size distribution of the prepared sample. In this method sample were riding on a curved shaped stage, which is made of aluminum, and the maintaining work distace is 10 mm. The elemental composition of the prepared sample was estimated by an Energy Dispersive X-ray Spectometer (Model EDAX Team, EDAX, USA). A Fourirer Transform Infrared (FT-IR) Spectometer (Model IR Prestige-21, Shimadju, Japan) was used for the molecular characterization of the prepared samples. In this method, the ground powdered samples were mixed with KBr (1 mg sample and 199 mg KBr) and pressed to pepare pelletes.

4.5 Results and discussion of mixed metal monophosphate tungsten bronze with nominal composition $A_{4/3-x}T_xW_{20/3}O_{24}(PO_2)_4$,(A/T = Cr, Fe, Al and x = 0, 1/3, 2/3, 3/3, 4/3)

4.5.1 $Cr_{4/3-x}Fe_xW_{20/3}O_{24}(PO_2)_4$ series

The solution combustion method was used to prepare a mixed-metal monophosphate tungsten bronze, $Cr_{4/3-x}Fe_xW_{20/3}O_{24}(PO_2)_4$ (x = 0, 1/3, 2/3, 3/3, 4/3) series. The reactants were tungstic acid, metal nitrates, aqueous ammonia and glycerin. Both the tungstic acid and metal nitrates act as sources of metals and oxidizers, with aqueous ammonia as a solvent and glycerin as a fuel. The fluffy mass, formed after drying at 100^oC, was heated in a muffle furnace from 400^oC to 900^oC for 24 hours at every 50^oC step. The powder sample was then characterized using XRD, FT-IR, SEM, and EDX techniques.

4.5.1.a XRD analysis of $Cr_{4/3-x}Fe_xW_{20/3}O_{24}(PO_2)_4$ series

Figs. 4.11-4.15 show the XRD patterns of the synthesized $Cr_{4/3-x}Fe_xW_{20/3}O_{24}(PO_2)_4$ (x = 0, 1/3, 2/3, 3/3, 4/3) samples calcined at different temperatures.
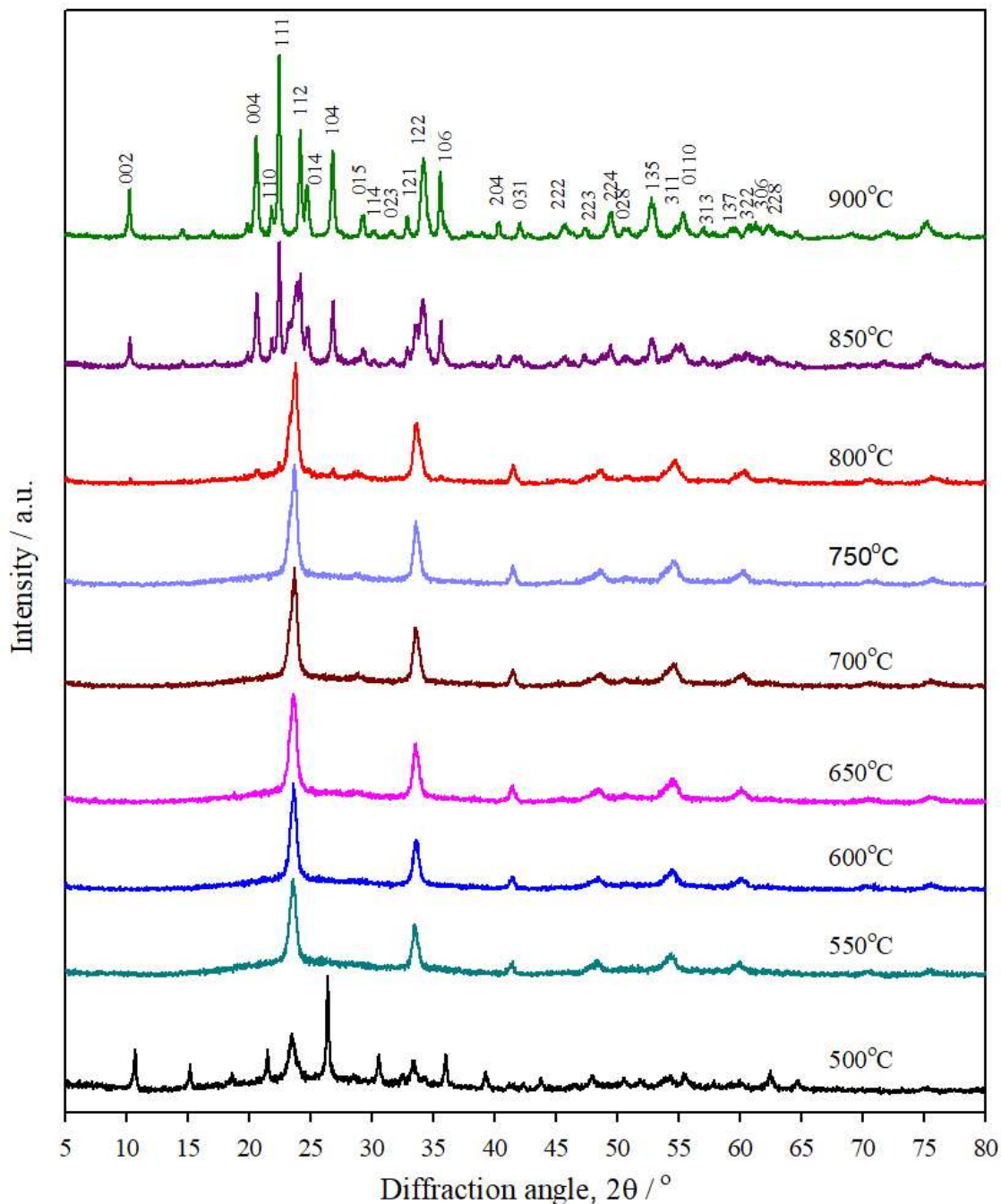
Fig. 4.11. XRD pattern of $Cr_{4/3-x}Fe_xW_{20/3}O_{24}(PO_2)_4$, x = 0 at different temperatures. For clarity, the diffraction patterns are plotted vertically. The patterns, up to 750°C, exhibit a cubic type crystalline phase. At 800°C, in addition to the cubic phase, some orthorhombic phase characteristic lines were observed, and at 850°C, the mixture completely transforms to the pure orthorhombic phase of $Cr_{4/3}W_{20/3}O_{24}(PO_2)_4$ (ICSD pattern; card no. 00-043-0390 and 01-075-2248).
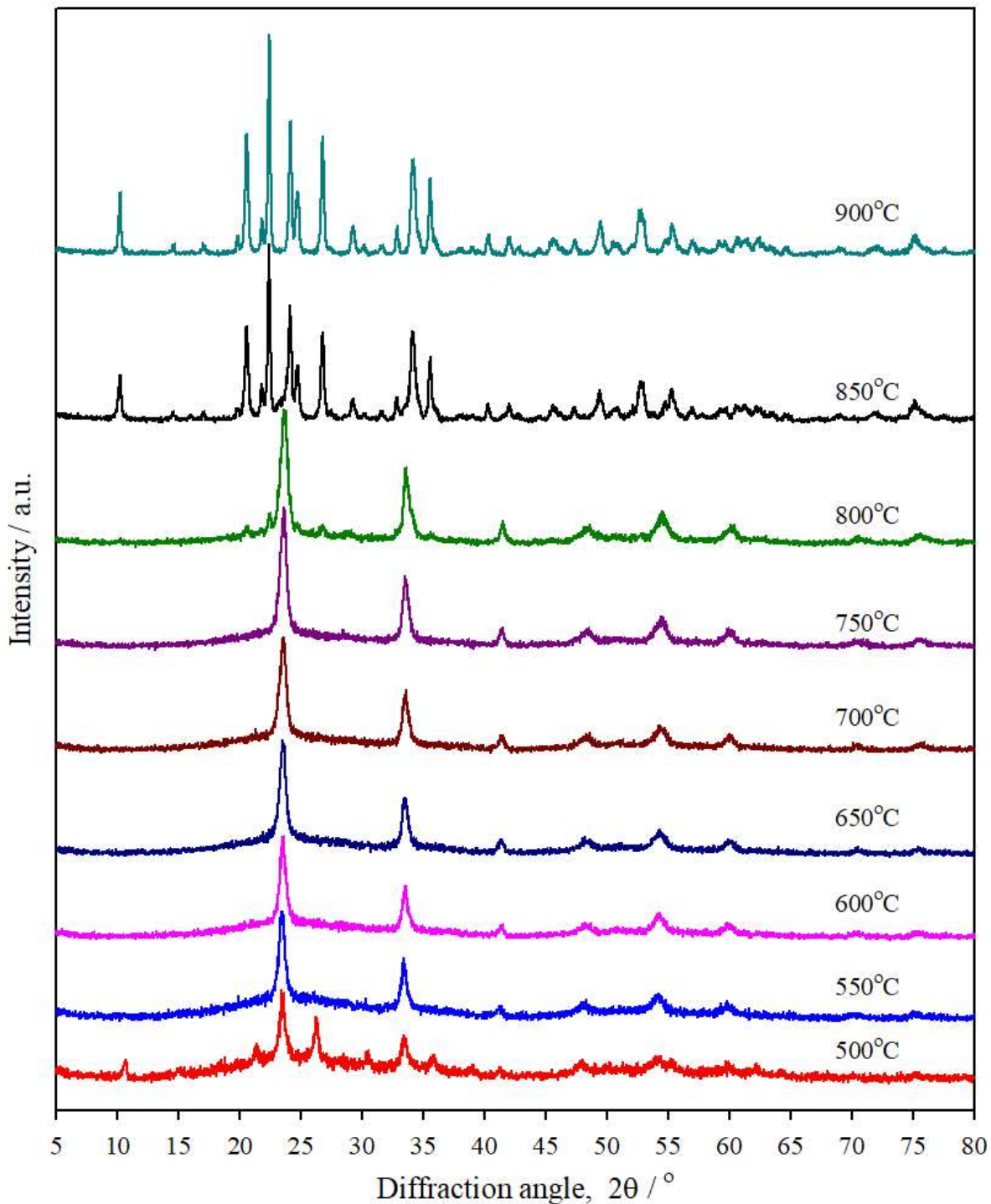
Fig. 4.12. XRD pattern of $Cr_{4/3-x}Fe_xW_{20/3}O_{24}(PO_2)_4$, x = 1/3 at different temperatures. For clarity, the diffraction patterns are plotted vertically. The patterns show a pure cubic phase up to 750°C, a mixed cubic and orthorhombic phase at 800°C and a pure orthorhombic phase at 850°C and 900°C.
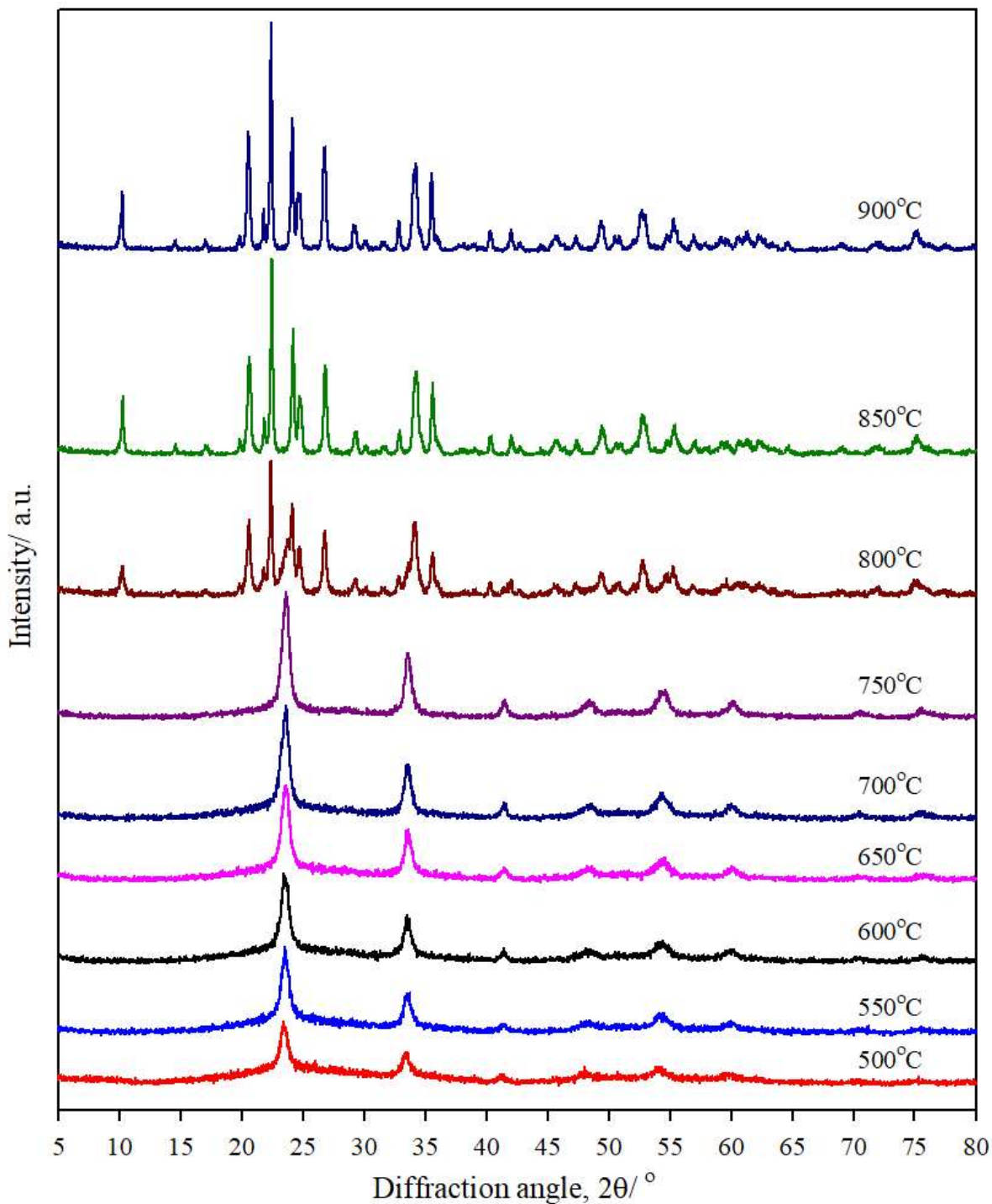
Fig. 4.13. XRD pattern of $Cr_{4/3-x}Fe_xW_{20/3}O_{24}(PO_2)_4$, x = 2/3 at different temperatures. For clarity, the diffraction patterns are plotted vertically. The patterns show a pure cubic phase up to 750°C, a mixed cubic and orthorhombic phase at 800°C, and a pure orthorhombic phase at 850°C and 900°C.
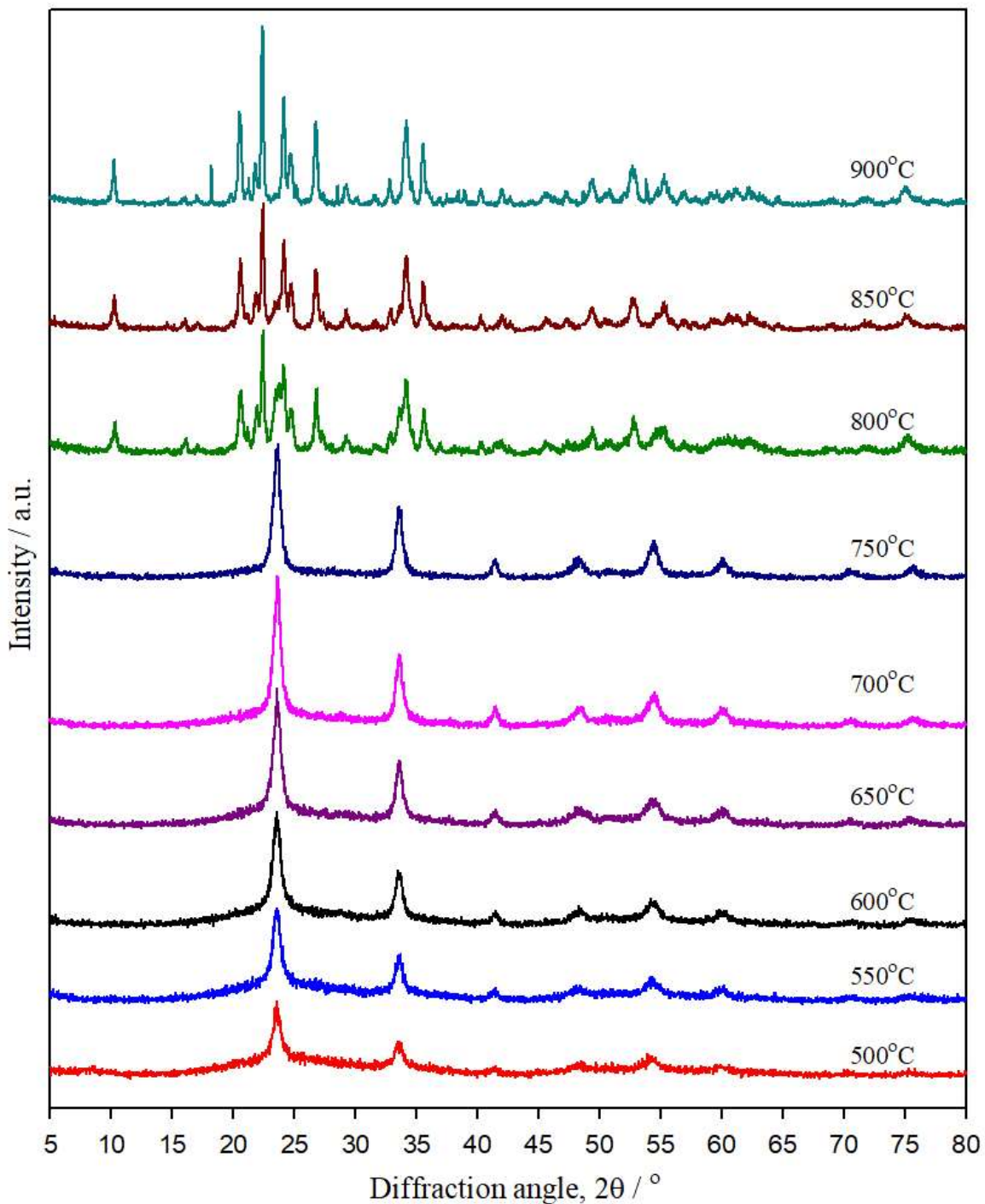
Fig. 4.14. XRD pattern of $Cr_{4/3-x}Fe_xW_{20/3}O_{24}(PO_2)_4$, x = 1 at different temperatures. For clarity, the diffraction patterns are plotted vertically. The patterns show a pure cubic phase up to 750°C, a mixed cubic and orthorhombic phase at 800°C, and a pure orthorhombic phase at 850°C and 900°C.
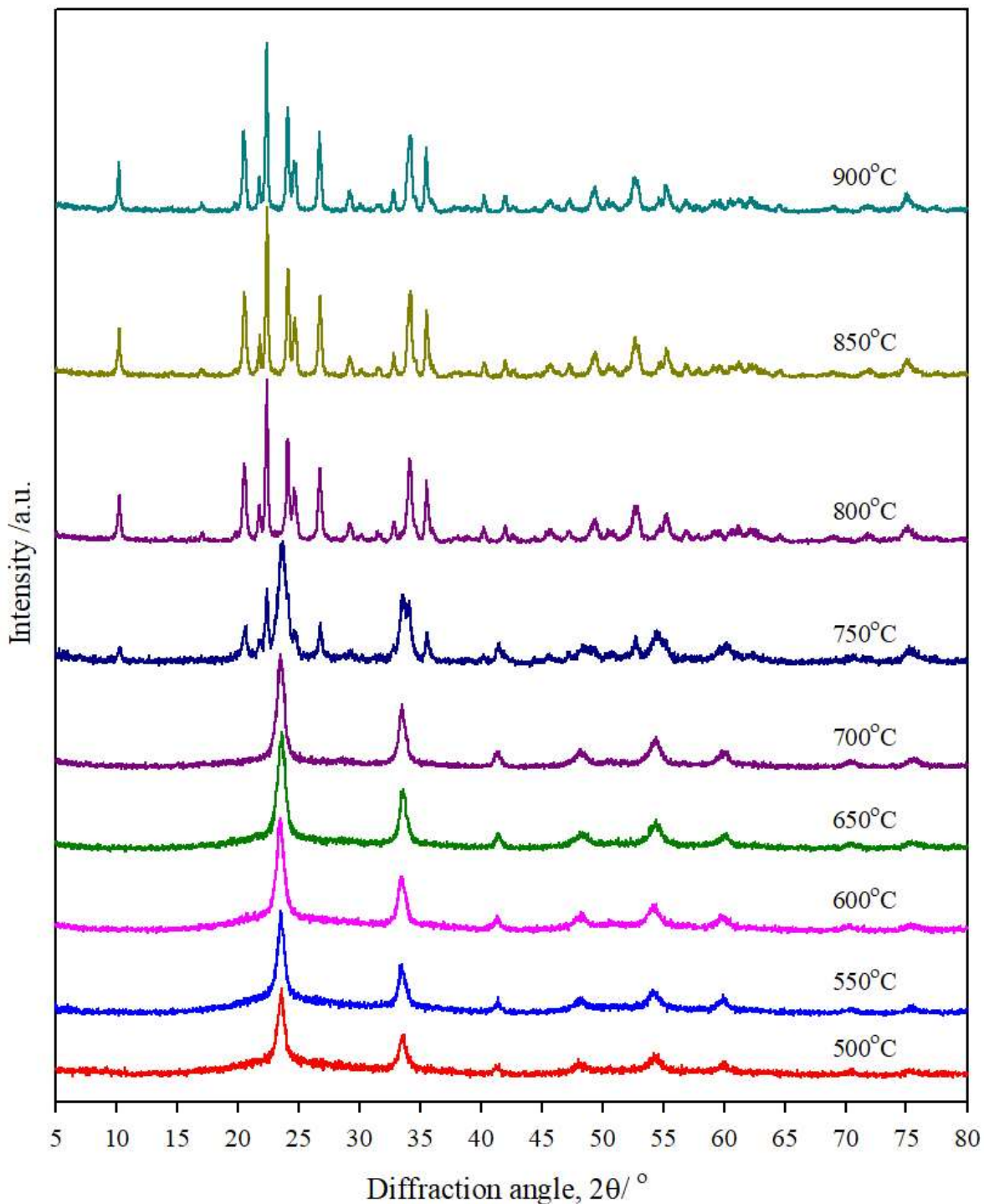
Fig. 4.15. XRD pattern of $Cr_{4/3-x}Fe_xW_{20/3}O_{24}(PO_2)_4$, x = 4/3 at different temperatures. For clarity, the diffraction patterns are plotted vertically. The patterns show a pure cubic phase up to 700°C, a mixed cubic and orthorhombic phase at 750°C and a pure orthorhombic phase at 800°C to 900°C.

The iron doped chromium monophosphate tungsten bonzes $Cr_{4/3-x}Fe_xW_{20/3}O_{24}(PO_2)_4$ with composition x = 0 are clearly converted into the $Cr_{4/3}W_{20/3}O_{24}(PO_2)_4$ series. The XRD patterns of $Cr_{4/3}W_{20/3}O_{24}(PO_2)_4$ at different temperatures are shown in Fig. 4.11. The patterns, up to 750°C, exhibit a number of Bragg reflections related to the (111), (200), (220), (311), and (222) reflections, suggesting the cubic type nanocrystalline phase. However, at 800°C, some characteristic lines related to the orthorhombic phase were observed in addition to the cubic phase. At 850°C, the mixture completely turns into a pure orthorhombic phase of $Cr_{4/3}W_{20/3}O_{24}(PO_2)_4$. The XRD pattern of iron doped Cr-MPTB with nominal composition x = 1/3, 2/3, and 1 shows very similar behavior; pure cubic phase up to 750°C, mixed cubic and orthorhombic phase at 800°C, and pure orthorhombic phase at 850°C.

At nominal composition x = 4/3, the sample turns into $Fe_{4/3}W_{20/3}O_{24}(PO_2)_4$ of which the X-ray diffraction pattern at different temperatures is shown in Fig. 4.15. The pattern up to 700°C indicates a cubic phase. However, as the heating temperature increases, the orthorhombic phase appears, and at the investigated temperature of 800-900°C, the XRD pattern could be perfectly indexed as the orthorhombic phase of $Fe_{4/3}W_{20/3}O_{24}(PO_4)_4$.

The cubic and orthorhombic phase structure parameters were refined by the Rietveld method. The Rietveld refinements were carried out using space group $P2_12_12_1$ (19) for the orthorhombic phase and Pm-$3m$ (221) for the cubic phase with the Rietveld program Profex [45]. There is an excellent agreement between the XRD patterns calculated and measured as shown in Figs. 4.16. and 4.17. The cell parameters are presented in Tables' 4.1 and 4.2. At 600°C and 650°C for cubic phase, it is found that the cell parameters slightly decrease up to nominal composition x = 1, then slightly increase. For orthorhombic phase cell parameters, *a, b, V* slightly increase, but *c* remains constant.

The influence of calcination temperature on the intensity and broadness of diffraction peaks was also studied. As calcination temperature rises, the diffraction peaks of prepared samples, $Cr_{4/3-x}Fe_xW_{20/3}O_{24}(PO_2)_4$ (x = 0, 1/3, 2/3, 3/3, 4/3) become progressively intense and sharp, which is an indication of better crystallinity. The Debye-Scherer equation was used to calculate the crystallite size of the cubic phase of prepared monophosphate tungsten bronze. The average crystallite size of the cubic $Cr_{4/3-x}Fe_xW_{20/3}O_{24}(PO_2)_4$ phase was estimated (Appendix, Table A. 4.1) and found to vary from 11-16 nm. Aggregation of small grains and the development of giant grains occur when grain size changes with temperature.
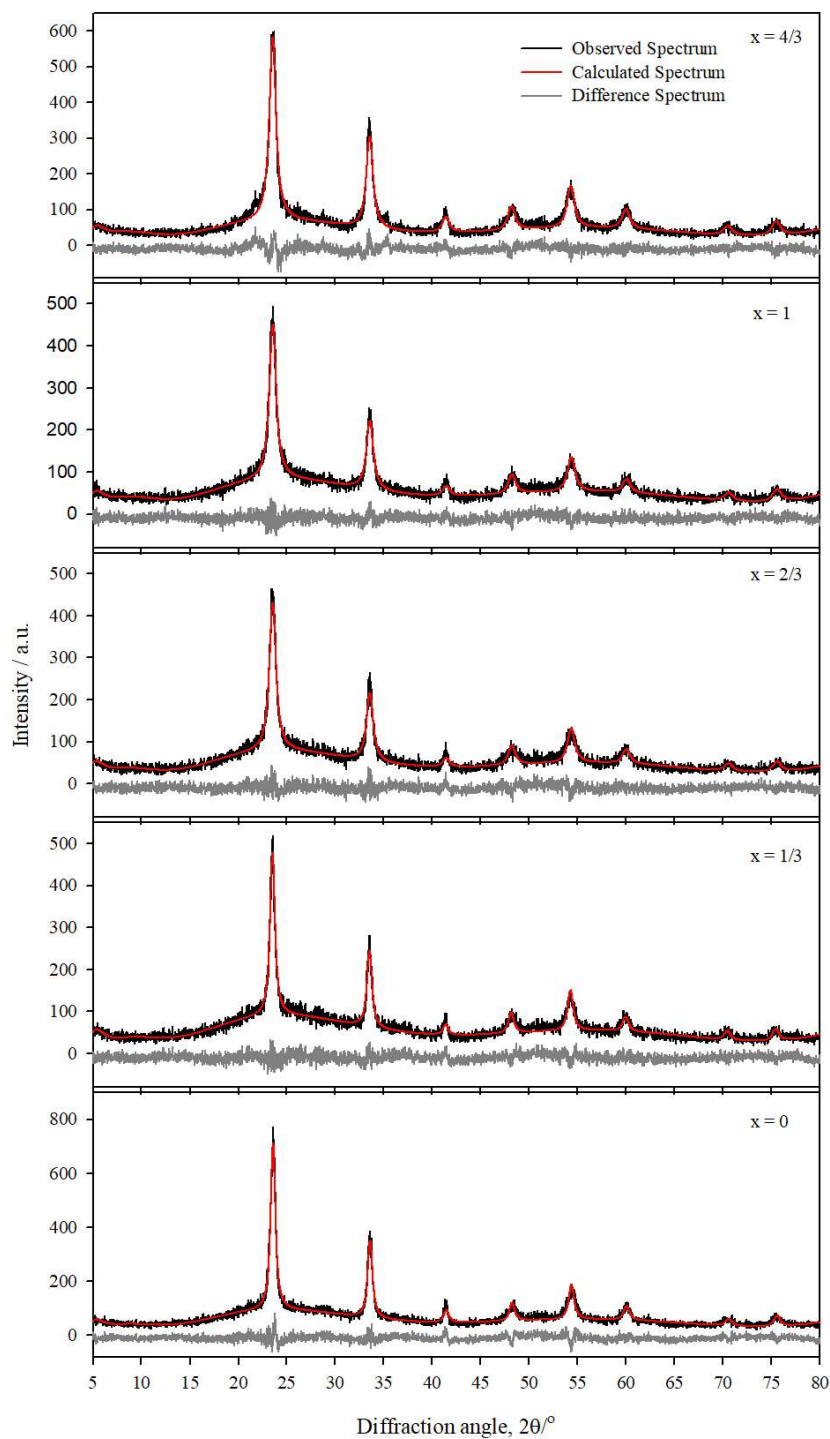
Fig. 4.16. Rietveld refinements fit of $Cr_{4/3-x}Fe_xW_{20/3}O_{24}(PO_2)_4$ series samples prepared at 600ºC. The black spectrum represents the observed/measured spectrum, and the red spectrum represents calculated data. The curve below the spectrum represents the difference spectrum.
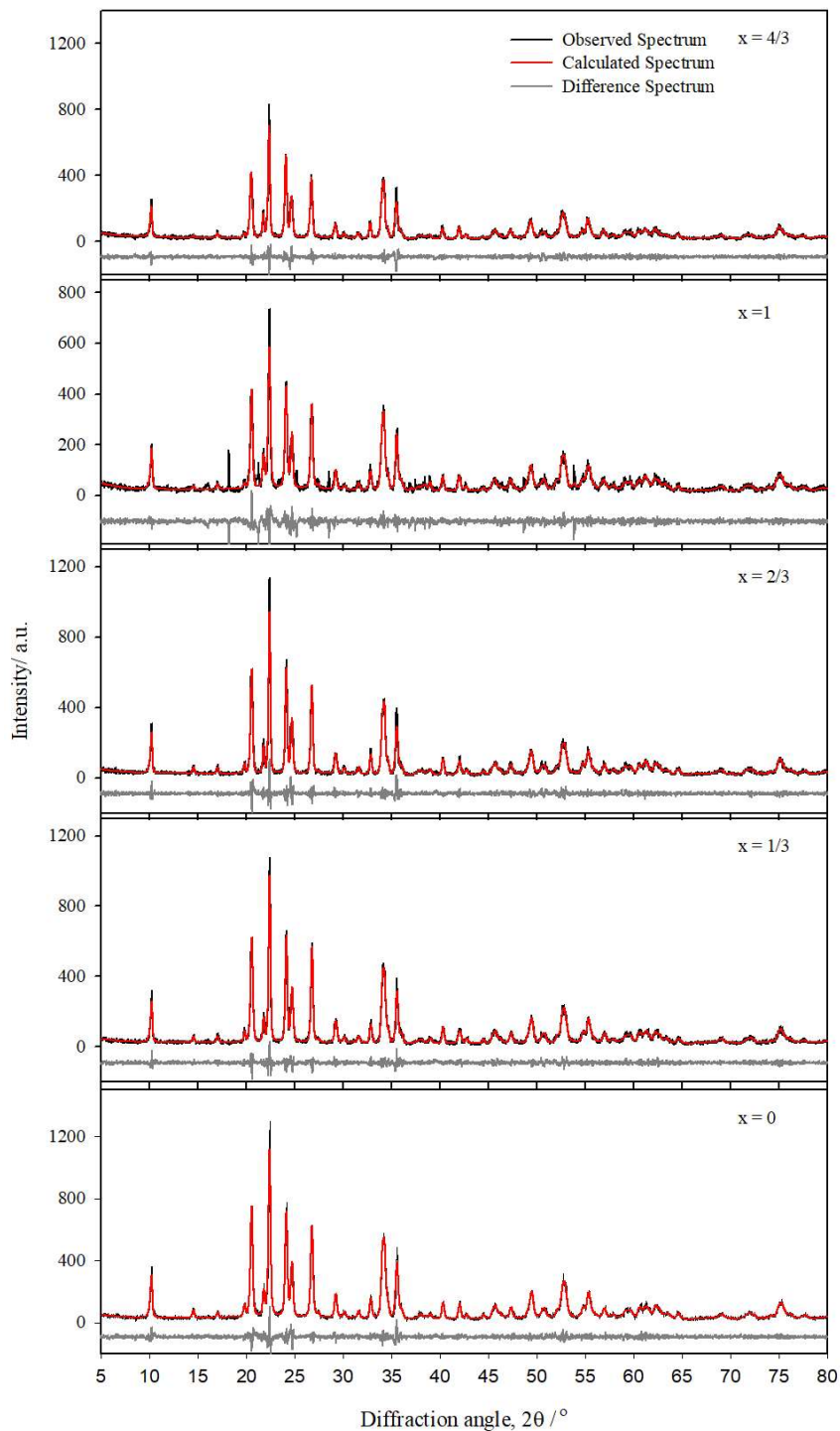
Fig. 4.17. Rietveld refinements fit of $Cr_{4/3-x}Fe_xW_{20/3}O_{24}(PO_2)_4$ series samples prepared at 900°C. The black spectrum represents the observed/measured spectrum, and the red spectrum represents calculated data. The curve below the spectrum represents the difference spectrum.

Table 4.1 Cell parameter of $Cr_{4/3-x}Fe_xW_{20/3}O_{24}(PO_2)_4$ with different nominal compositions prepared at 600°C and 650°C.

Nominal Compositions	Cell parameters a / Å	
	600°C	650°C
x = 0	0.3777	0.3772
x = 1/3	0.3782	0.3777
x = 2/3	0.3777	0.3776
x = 1	0.3776	0.3775
x = 4/3	0.3782	0.3777

Table 4.2 Cell parameter of $Cr_{4/3-x}Fe_xW_{20/3}O_{24}(PO_2)_4$ with different nominal compositions prepared at 900°C.

Nominal Compositions	Cell parameters			
	a / Å	b / Å	c / Å	V/ (Å^3)
x = 0	0.5229	0.6497	1.7292	0.5874
x = 1/3	0.5232	0.6501	1.7299	0.5883
x = 2/3	0.5231	0.6500	1.7307	0.5885
x = 1	0.5240	0.6505	1.7310	0.5901
x = 4/3	0.5236	0.6507	1.7307	0.5896
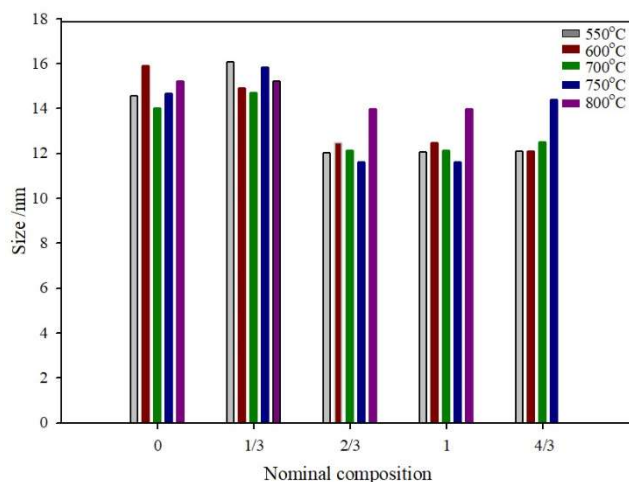
Fig. 4.18. Crystallite sizes of $Cr_{4/3-x}Fe_xW_{20/3}O_{24}(PO_2)_4$ (x = 0, 1/3, 2/3, 1, 4/3) were measured at different compositions and temperatures and ranged from 11-16 nm.

4.5.1. b FT-IR analysis of $Cr_{4/3-x}Fe_xW_{20/3}O_{24}(PO_2)_4$ series

Fig. 4.19 shows the FT-IR spectra of $Cr_{4/3-x}Fe_xW_{20/3}O_{24}(PO_2)_4$ (x = 0, 1/3, 2/3, 3/3, 4/3) at various temperatures. The spectra of $Cr_{4/3-x}Fe_xW_{20/3}O_{24}(PO_2)_4$ series at all compositions show three broad peaks at around 519, 812, 958 cm^{-1}. These are related to the stretching vibrational modes of W-O and O-W-O of WO_3. With increasing temperatures, these bands are shifted toward lower wave numbers. The shifting of the bands could be caused by the changing crystalline phase at higher temperatures. Thus, the spectral feature of the FT-IR absorption spectra of the samples supports the phase transition from cubic to orthorhombic. The fourth, at about 1082 cm^{-1}, is attributed to the P-O asymmetric mode of the phosphate group. At 850ºC and 900ºC, the absorption bands of all members of the solid solution series of $Cr_{4/3-x}Fe_xW_{20/3}O_{24}(PO_2)_4$ are nearly identical and correspond to the MPTB structure type. It is evident that the FT-IR spectra are completely in agreement with the XRD data (Fig. A. 4.1).
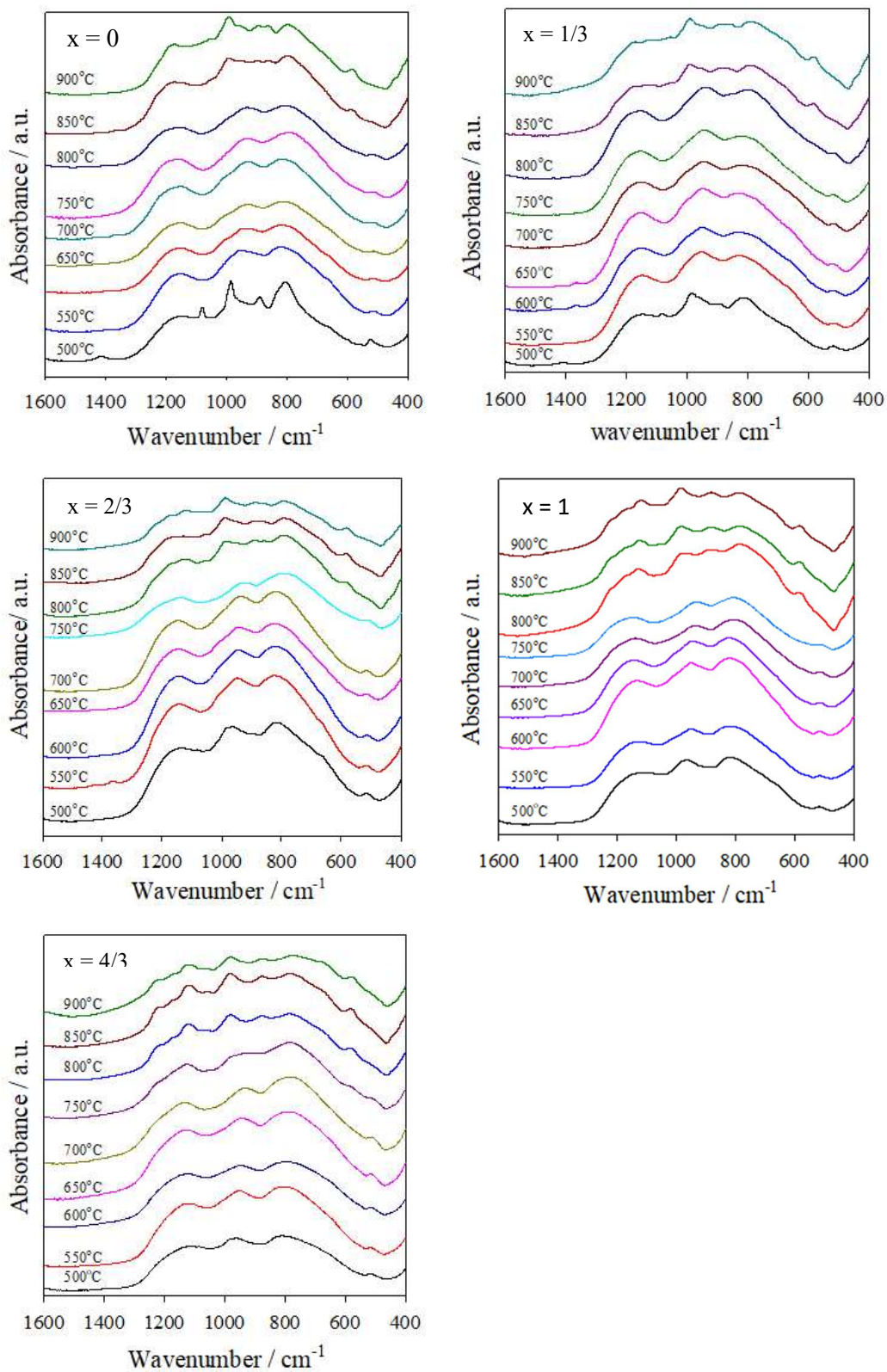
Fig. 4.19. FT-IR spectra of $Cr_{4/3-x}Fe_xW_{20/3}O_{24}(PO_2)_4$ with different nominal compositions at different temperatures.

4.5.1.c SEM / EDX analysis of $Cr_{4/3-x}Fe_xW_{20/3}O_{24}(PO_2)_4$ series

SEM measurements are one of the better tools to calculate grain size because of the image produced by the sample. The results of SEM analysis of $Cr_{4/3-x}Al_xW_{20/3}O_{24}(PO_2)_4$ with compositional variation at 900°C are shown in Fig. 4.20, with additional temperature SEM images shown in the appendix. It shows almost uniform spherical nanocrystalline particles for all compositions. This observation agrees well with the results of calculations using Scherer equation.

The EDX spectrum of $Cr_{4/3-x}Fe_xW_{20/3}O_{24}(PO_2)_4$ calcined at 900°C reveals (appendix) that the prepared sample contains Cr, Fe, W and P, with no foreign elements present. The EDX results show that with decreasing the ratio of Cr:W, the ratio of Fe:W increases, which is expected.
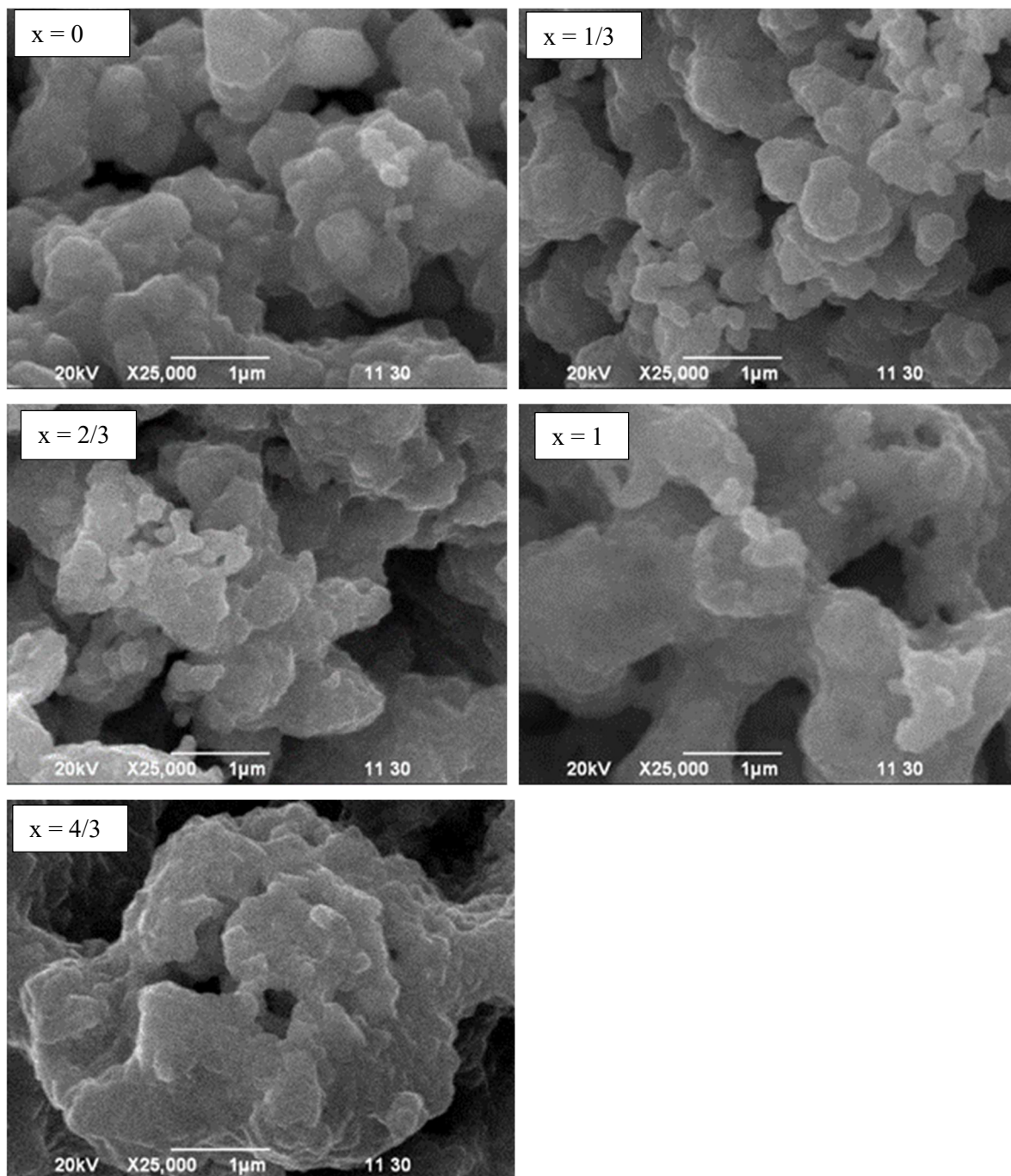
Fig. 4.20. SEM images of $Cr_{4/3-x}Fe_xW_{20/3}O_{24}(PO_2)_4$ with different nominal compositions at 900ºC.

Table 4.3 EDX results of $Cr_{4/3-x}Fe_xW_{20/3}O_{24}(PO_2)_4$

Composition			Weight % found	Cr/W	Fe/W
x = 0		Cr	5.22	0.08	-
		Fe	-		
		W	65.00		
		P	7.44		
x = 1/3		Cr	5.28	0.08	0.08
		Fe	5.17		
		W	64.12		
		P	6.00		
x = 2/3		Cr	4.56	0.07	0.11
		Fe	6.67		
		W	61.54		
		P	6.98		
x = 1		Cr	3.085	0.06	0.12
		Fe	8.305		
		W	62.005		
		P	8.415		
x = 4/3		Cr	-	-	0.13
		Fe	6.67		
		W	62.23		
		P	6.395		
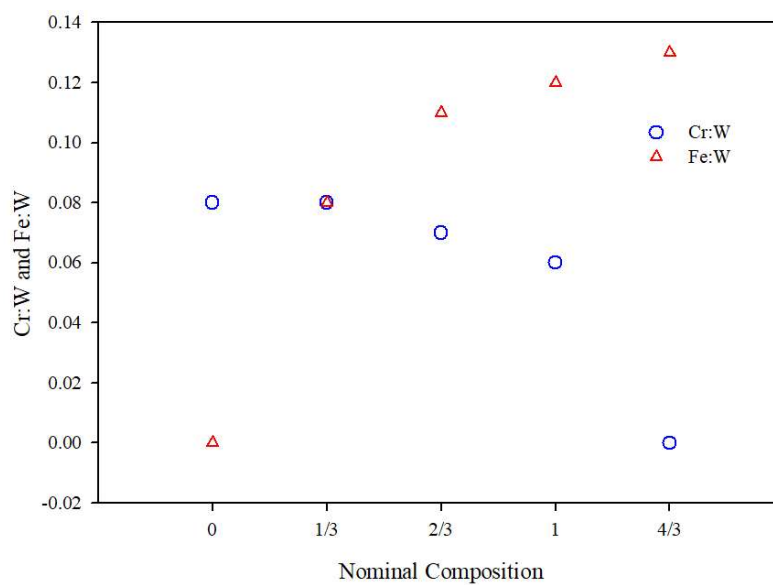
Fig. 4.21. EDX results of $Cr_{4/3-x}Fe_xW_{20/3}O_{24}(PO_2)_4$ with different nominal compositions at 900^oC.

4.5.2 $Cr_{4/3-x}Al_xW_{20/3}O_{24}(PO_2)_4$ series

Mixed-metal monophosphate tungsten bronzes, $Cr_{4/3-x}Al_xW_{20/3}O_{24}(PO_2)_4$ (x = 0, 1/3, 2/3, 3/3, 4/3) were synthesized by the solution combustion synthesis (SCS) method. The chosen reactants were tungstic acid and metal nitrates as a source of metals and oxidizers, aqueous ammonia as a solvent, and glycerin as a fuel. The fluffy mass, formed after drying at about 100ºC, was heated in a preheated muffle furnace from 400ºC to 900ºC for 24 hours at every 50ºC step, and then characterized by XRD, SEM and FT-IR spectroscopy techniques.

4.5.2.a XRD analysis of $Cr_{4/3-x}Al_xW_{20/3}O_{24}(PO_2)_4$ series

The XRD patterns of the samples $Cr_{4/3-x}Al_xW_{20/3}O_{24}(PO_2)_4$ (x = 0, 1/3, 2/3, 3/3, 4/3) with different calcination temperatures are given in Figs. 4.22 - 4.26.
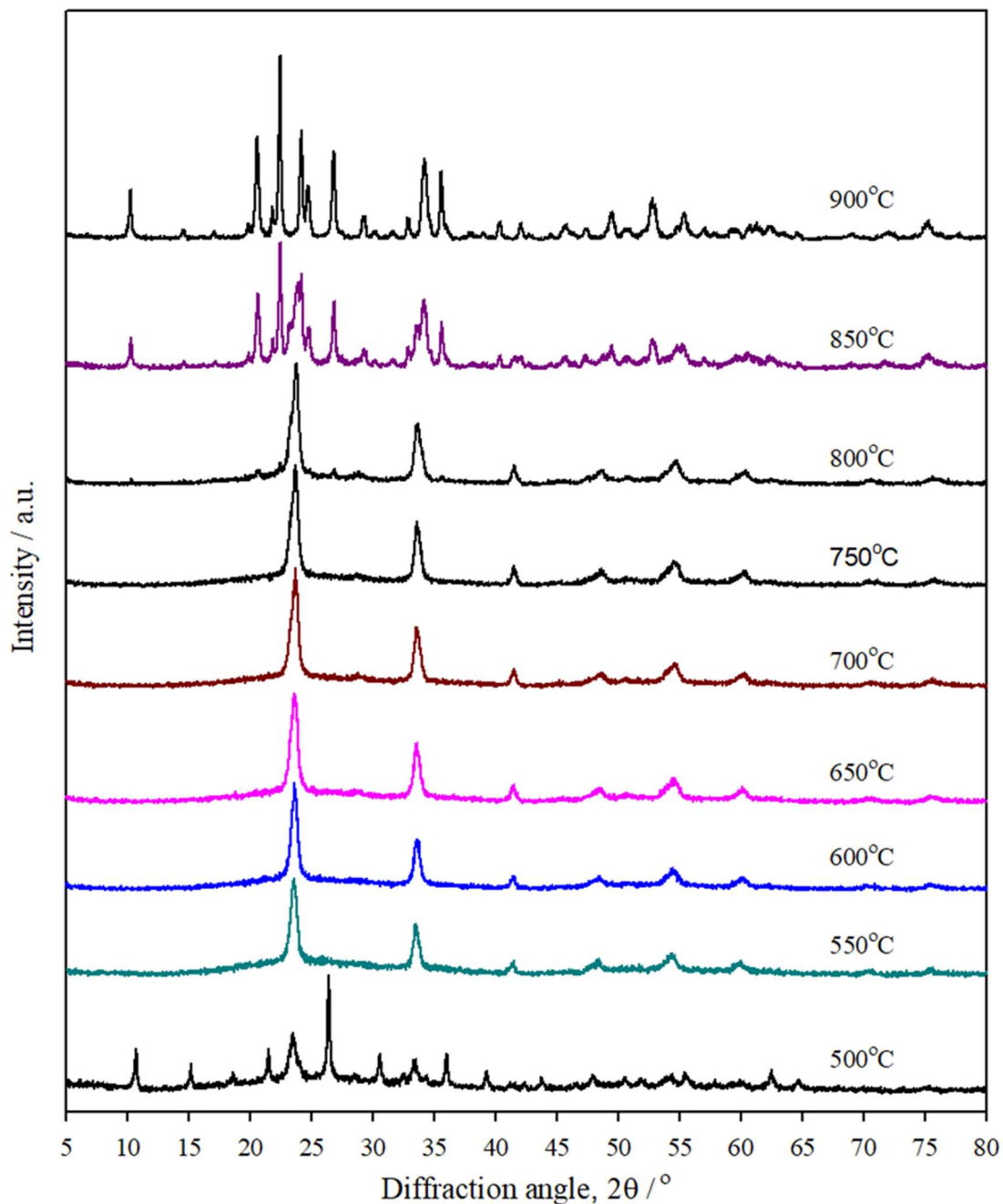
Fig. 4.22. XRD pattern of $Cr_{4/3-x}Al_xW_{20/3}O_{24}(PO_2)_4$ with nominal composition x = 0, at different temperatures. For clarity, the diffraction patterns are plotted vertically. The patterns, up to 750°C, exhibit a cubic type crystalline phase. At 800°C, some characteristic lines related to orthorhombic phase were observed in addition to the cubic phase, and at 850°C, the mixture completely turns to the pure orthorhombic phase of $Cr_{4/3}W_{20/3}O_{24}(PO_2)_4$.
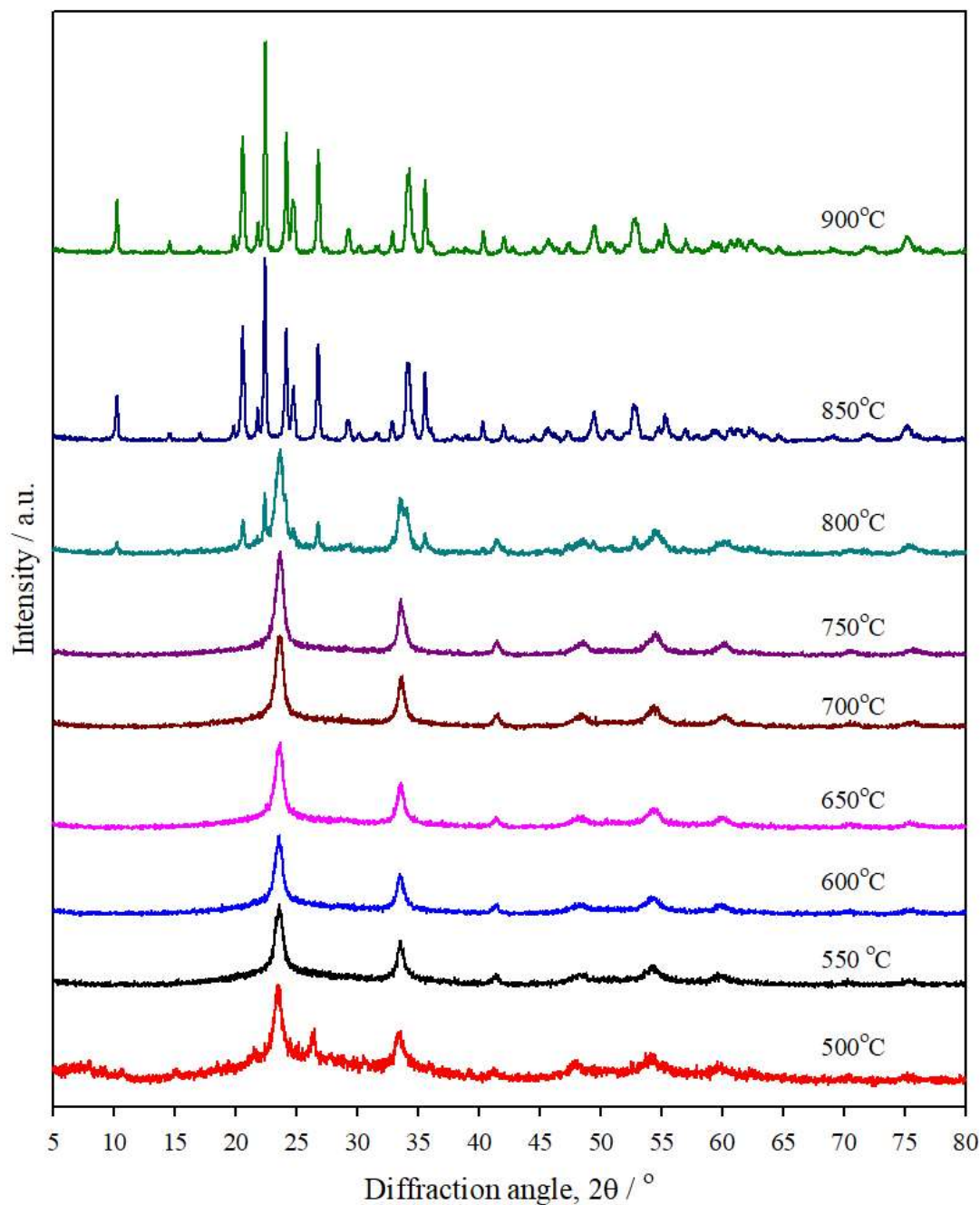
Fig. 4.23. XRD pattern of $Cr_{4/3-x}Al_xW_{20/3}O_{24}(PO_2)_4$ at nominal composition $x = 1/3$, at different temperatures. For clarity, the diffraction patterns are plotted vertically. The patterns show a pure cubic phase up to 750^oC, a mixed cubic and orthorhombic phase at 800^oC, and a pure orthorhombic phase at 850^oC and 900^oC.
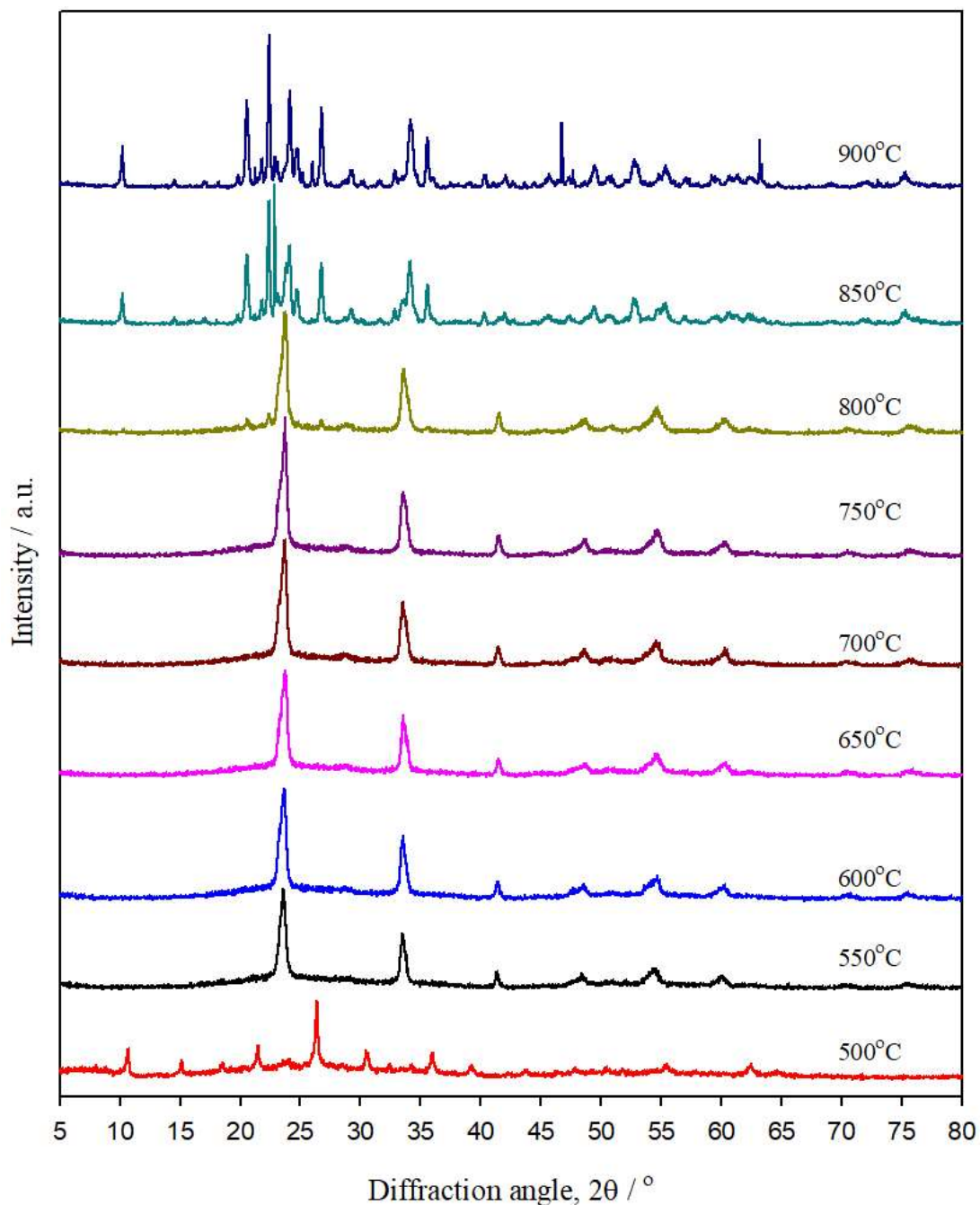
Fig. 4.24. XRD pattern of $Cr_{4/3-x}Al_xW_{20/3}O_{24}(PO_2)_4$ with nominal composition, x = 2/3, at different temperatures. For clarity, the diffraction patterns are plotted vertically. The patterns show a pure cubic phase up to 750°C, where a phase transition from cubic to orthorhombic starts to appear. On further heating, the pattern shows some additional lines along with an orthorhombic phase.
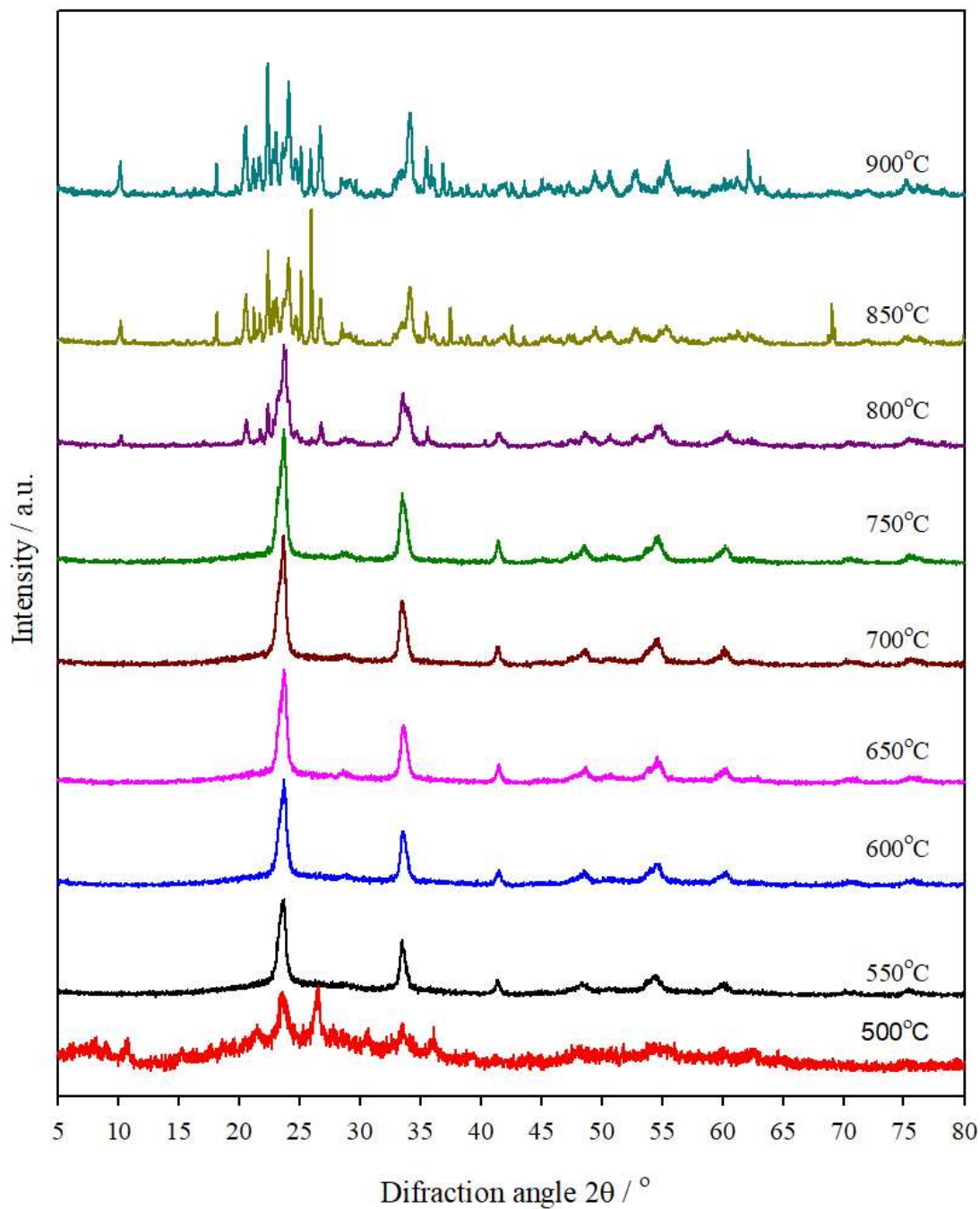
Fig. 4.25. XRD pattern of $Cr_{4/3-x}Al_xW_{20/3}O_{24}(PO_2)_4$ with nominal composition x = 1, at different temperatures. For clarity, the diffraction patterns are plotted vertically. The patterns show a pure cubic phase up to 750°C, where a phase transition from cubic to orthorhombic starts to appear. On further heating, the sample decomposes into another new phase.

Fig. 4.26. XRD pattern of $Cr_{4/3-x}Al_xW_{20/3}O_{24}(PO_2)_4$ with nominal composition x = 4/3, at different temperatures. For clarity, the diffraction patterns are plotted vertically. The patterns show a pure cubic phase up to 750°C, and at 800°C, a phase transition from cubic to orthorhombic starts to appear. On further heating, the sample decomposes into another new phase.

The X-ray diffraction pattern of ($Cr_{4/3}W_{20/3}O_{24}(PO_2)_4$) (i.e., at nominal composition x = 0) at different temperatures synthesized by the SCS method is shown in Fig. 4.22. A number Bragg reflections corresponding to the (111), (200), (220), (311) and (222) reflections of the cubic phase were observed. The high intensity peak of face centered cubic (FCC) materials [(111) reflection] is also observed here. The studied sample's cubic phases were maintained up to 750°C, but at 800°C, some characteristic lines related to the orthorhombic phase of $Cr_{4/3}W_{20/3}O_{24}(PO_2)_4$ were observed alongside the cubic phase lines. At 850°C and 900°C, the XRD pattern can be perfectly indexed as the orthorhombic phase of $Cr_{4/3}W_{20/3}O_{24}(PO_2)_4$. Observing the diffraction pattern of the $Cr_{4/3-x}Al_xW_{20/3}O_{24}(PO_2)_4$ series at nominal compositions of x = 1/3 yields a very similar explanation. At nominal composition x = 2/3, some extra lines appeared, i.e., at $2\theta \approx 23.06$, which are not related to the orthorhombic phase. Similar observations are found for nominal composition x = 1 (Fig. A.4.7). However, up to 750°C, the XRD patterns of $Al_{4/3}W_{20/3}O_{24}(PO_2)_4$ (when x = 4/3) are pure cubic phase. At 800°C, a phase transition from cubic to orthorhombic starts to appear. Further heating causes the sample to decompose into other new phases.

The cubic phase structure parameters of the $Cr_{4/3-x}Al_xW_{20/3}O_{24}(PO_2)_4$ series were refined by the Rietveld method using space group *Pm-3m* (221) with the Rietveld program profex. The calculated and measured XRD patterns are in very good agreement, as shown in Figs. 4.27. and A.4.9 The cell parameters at 600°C and 650°C for the cubic phase are shown in Table 4.4. It is found that the cell parameters slightly increase up to the nominal composition x = 1/3, then remain almost constant.

The influence of calcined temperature on crystallite sizes of $Cr_{4/3-x}Al_xW_{20/3}O_{24}(PO_2)_4$ at different compositions is also examined using the Debye-Scherer equation that relates the size of crystallites in a solid to the broadening of X-ray diffraction peaks. The crystallite sizes of $Cr_{4/3-x}Al_xW_{20/3}O_{24}(PO_2)_4$ (x = 0, 1/3, 2/3, 1, 4/3) compounds in cubic phase were estimated and are shown in (Table A.4.2). The sizes are in the range of 13-18 nm.
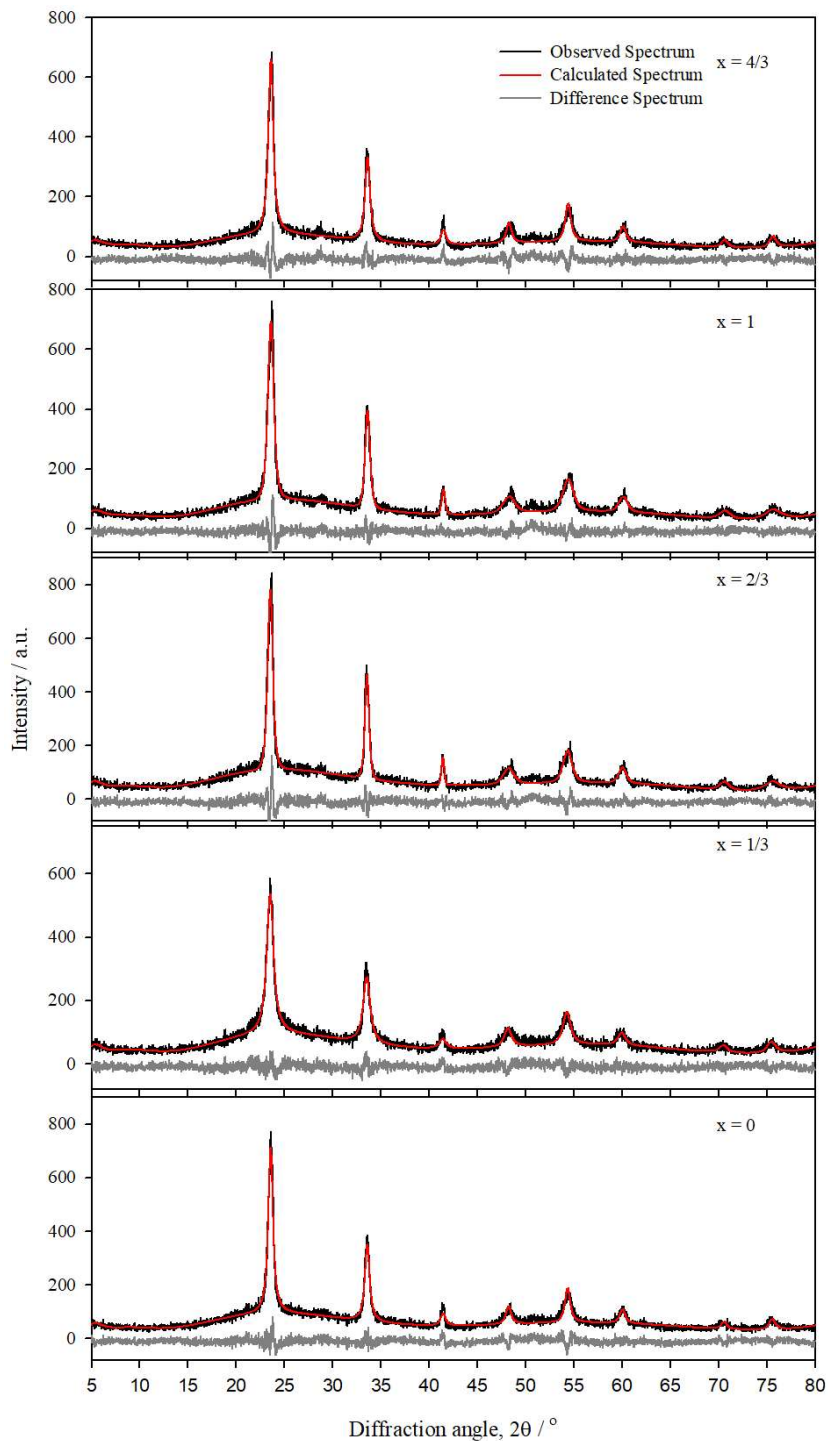
Fig. 4.27. Rietveld refinements fit of $Cr_{4/3-x}Al_xW_{20/3}O_{24}(PO_2)_4$ series samples prepared at 600ºC. The black spectrum represents the observed/measured spectrum, and the red spectrum represents calculated data. The curve below the spectrum represents the difference spectrum.

Table 4.4 Cell parameters of $Cr_{4/3-x}Al_xW_{20/3}O_{24}(PO_2)_4$ series at 600°C and 650°C.

Nominal Compositions	600°C	650°C
x = 0	0.377712	0.377234
x = 1/3	0.378007	0.377843
x = 2/3	0.377450	0.376888
x = 1	0.377310	0.376723
x = 4/3	0.377438	0.376840
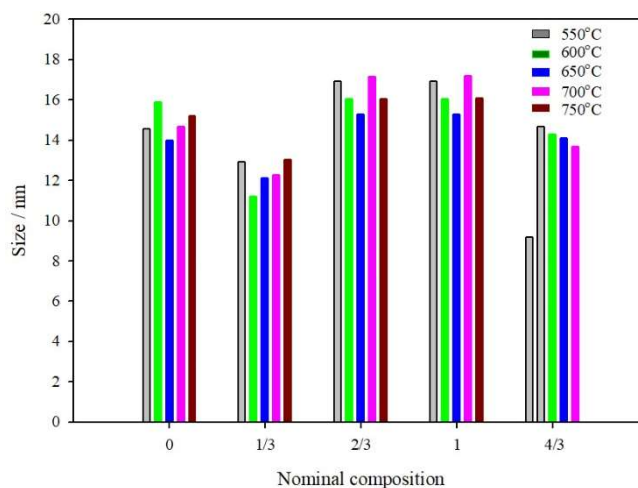
Fig. 4.28. Crystallite sizes of $Cr_{4/3-x}Al_xW_{20/3}O_{24}(PO_2)_4$ at different compositions and temperatures.

4.5.2.b FT-IR analysis of $Cr_{4/3-x}Al_xW_{20/3}O_{24}(PO_2)_4$ series

Fig. 4.29 shows the FT-IR spectra of the $Cr_{4/3-x}Al_xW_{20/3}O_{24}(PO_2)_4$ (x = 0, 1/3, 2/3, 1, 4/3) series at different temperatures.

The FT-IR spectra of $Al_{4/3}W_{20/3}O_{24}(PO_2)_4$ at all compositions show three bands at around 512, 805, 969 cm^{-1} wavenumbers, which can be assigned for the stretching vibrations of W-O, O-W-O bridging group of WO_3. These bands are shifted toward lower wave numbers with increasing temperature. Shifting of this type is possibly associated with the change of the crystalline phase from cubic to monoclinic at higher temperatures. The FT-IR spectra are thus in good agreement with the XRD findings. The band was observed at about 1142 cm^{-1} wavenumber due to the P-O asymmetric stretching vibration modes for the phosphate group. At 850°C and 900°C, the absorption bands of the first two members (x = 0 and 1/3) are identical and correspond to the MPTB structure type. However, at x = 2/3 and 1, some additional bands along with the MPTB structure type are observed. Moreover, the IR spectra of nominal composition x = 4/3 is completely different from the MPTB structure type. These results comply with the XRD analysis.
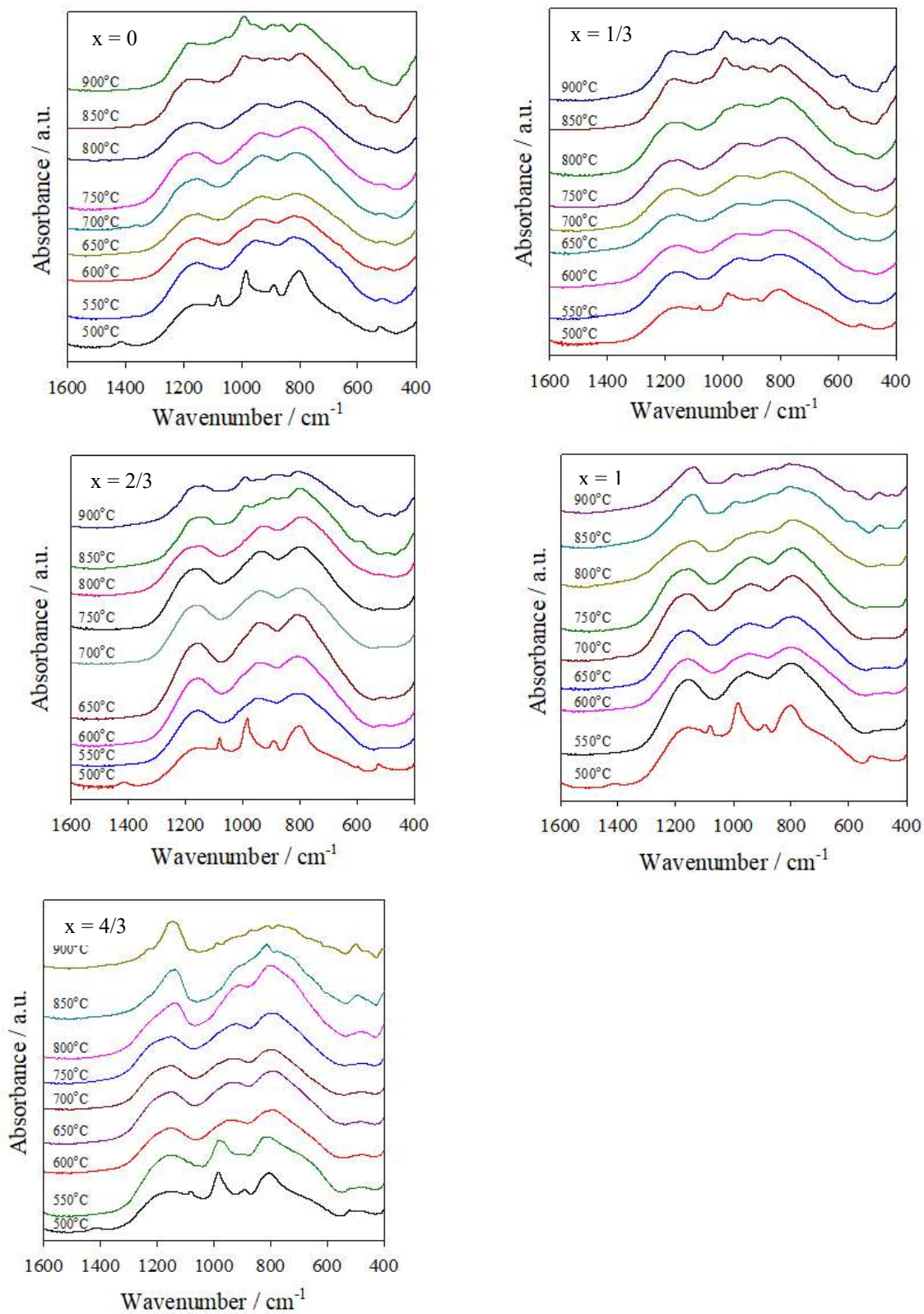
Fig. 4.29. FT-IR spectra of $Cr_{4/3-x}Al_xW_{20/3}O_{24}(PO_2)_4$ with different nominal composition at different temperatures.

4.5.2.c SEM analysis $Cr_{4/3-x}Al_xW_{20/3}O_{24}(PO_2)_4$ series

SEM images of $Cr_{4/3-x}Al_xW_{20/3}O_{24}(PO_2)_4$ (x = 0, 1/3, 2/3, 1, 4/3) samples at different temperatures were recorded and the SEM image at 900ºC shown in Fig. 4.30. The images show almost uniform spherical nanocrystalline particles for all compositions of the compound.
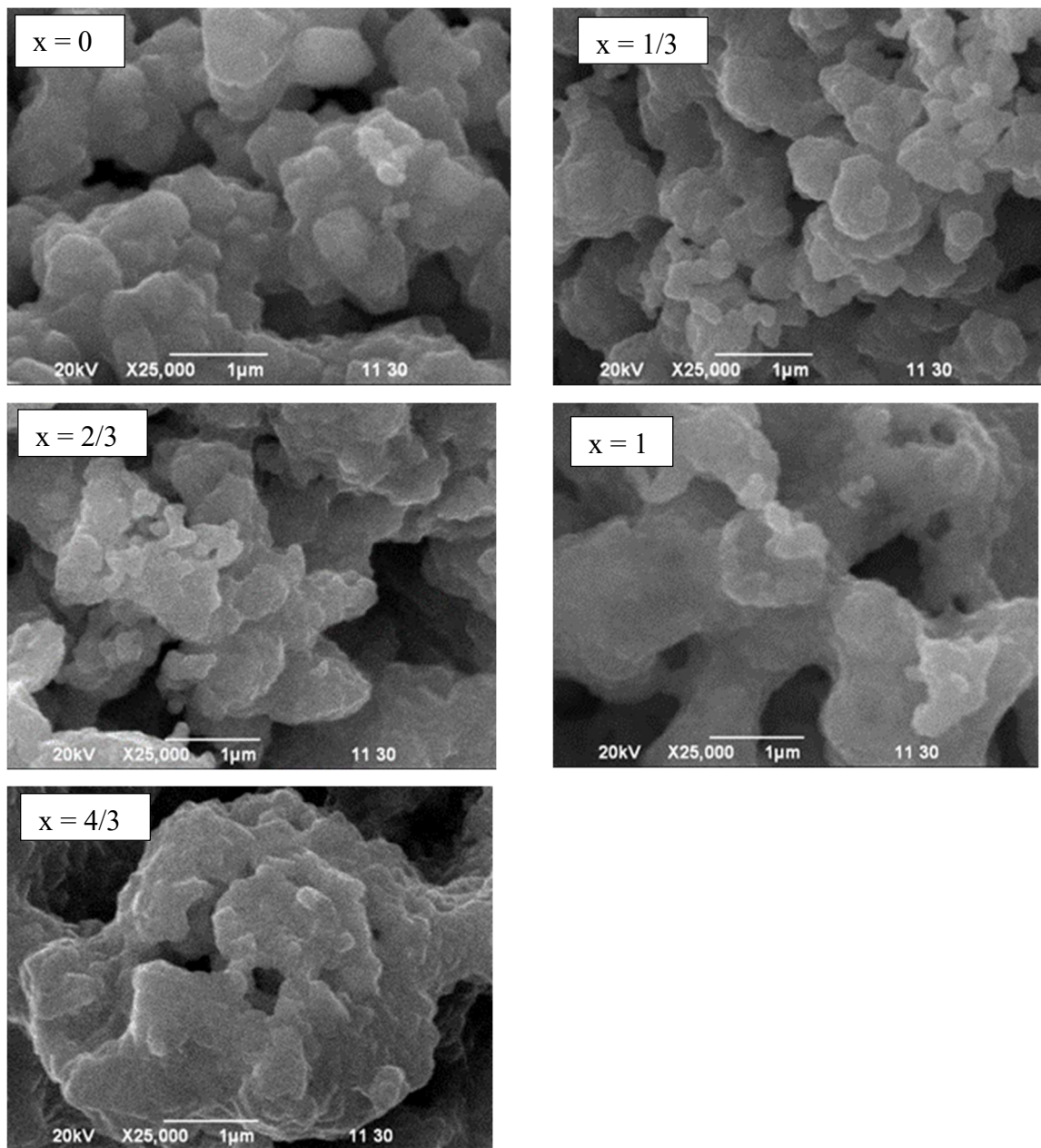
Fig. 4.30. SEM images of $Cr_{4/3-x}Al_xW_{20/3}O_{24}(PO_2)_4$ with different nominal compositions at 900ºC.

4.5.3 $Al_{4/3-x}Fe_xW_{20/3}O_{24}(PO_2)_4$ series

The SCS method was used to synthesize the $Al_{4/3-x}Fe_xW_{20/3}O_{24}(PO_2)_4$ (x = 0, 1/3, 2/3, 3/3, 4/3) series. Tungstic acid and metal nitrates as a source of metals and oxidizers, aqueous ammonia as a solvent, and glycerin as a fuel were chosen for their preparation. The gel that was formed after drying at 100°C was heated in a muffle furnace from 400°C to 900°C for 24 hours at every 50°C step. The synthesized samples were then characterized by XRD, FT-IR spectroscopy and SEM techniques.

4.5.3.a XRD analysis of $Al_{4/3-x}Fe_xW_{20/3}O_{24}(PO_2)_4$ series

Figs. 4.31-4.35 show the XRD patterns of the series, $Al_{4/3-x}Fe_xW_{20/3}O_{24}(PO_2)_4$, (x = 0, 1/3, 2/3, 1, 4/3) at different calcination temperatures.

The XRD pattern of $Al_{4/3}W_{20/3}O_{24}(PO_2)_4$ (i.e., at composition x = 0) is indexed at 500°C. It shows the presence of Braggs reflections of (111), (200), (311), (222) for the face center cubic (FCC) phase. Thus, the $Al_{4/3}W_{20/3}O_{24}(PO_2)_4$ sample crystallizes in the FCC system. When the sample is heated further up to 750°C, the pattern remains cubic, but at 800°C, some new lines appear which are not related to the orthorhombic phase. On further heating, the phase structure decomposes into a new phase different from the monoclinic phase. A similar pattern is observed for nominal compositions, x = 1/3 and 2/3. At nominal composition x = 1, the compound demonstrates a cubic phase up to 750°C. When the sample is heated further, i.e., at 750°C, some characteristic lines related to the orthorhombic phase were observed along with those of the cubic phase. At 850°C and 900°C, the X-ray pattern shows an orthorhombic phase with some additional lines.

The compound $Fe_{4/3}W_{20/3}O_{24}(PO_2)_4$ exhibits a very similar diffraction pattern (Fig. 4.35) up to 700°C at nominal composition x = 4/3. Indexing of the lines (111, 200, 220, 311, 222, and 400) in the pattern ends in a cubic phase. When the sample is heated further, i.e., at 750°C, some characteristic lines related to the orthorhombic phase of $Cr_{4/3}W_{20/3}O_{24}(PO_2)_4$ were observed along with those of the cubic phase. At 800-900°C, the X-ray pattern is indexed as the orthorhombic structure of $Fe_{4/3}W_{20/3}O_{24}(PO_2)_4$. The sharpening of the diffraction lines with increasing calcination temperature was due to an increase in crystalline size.
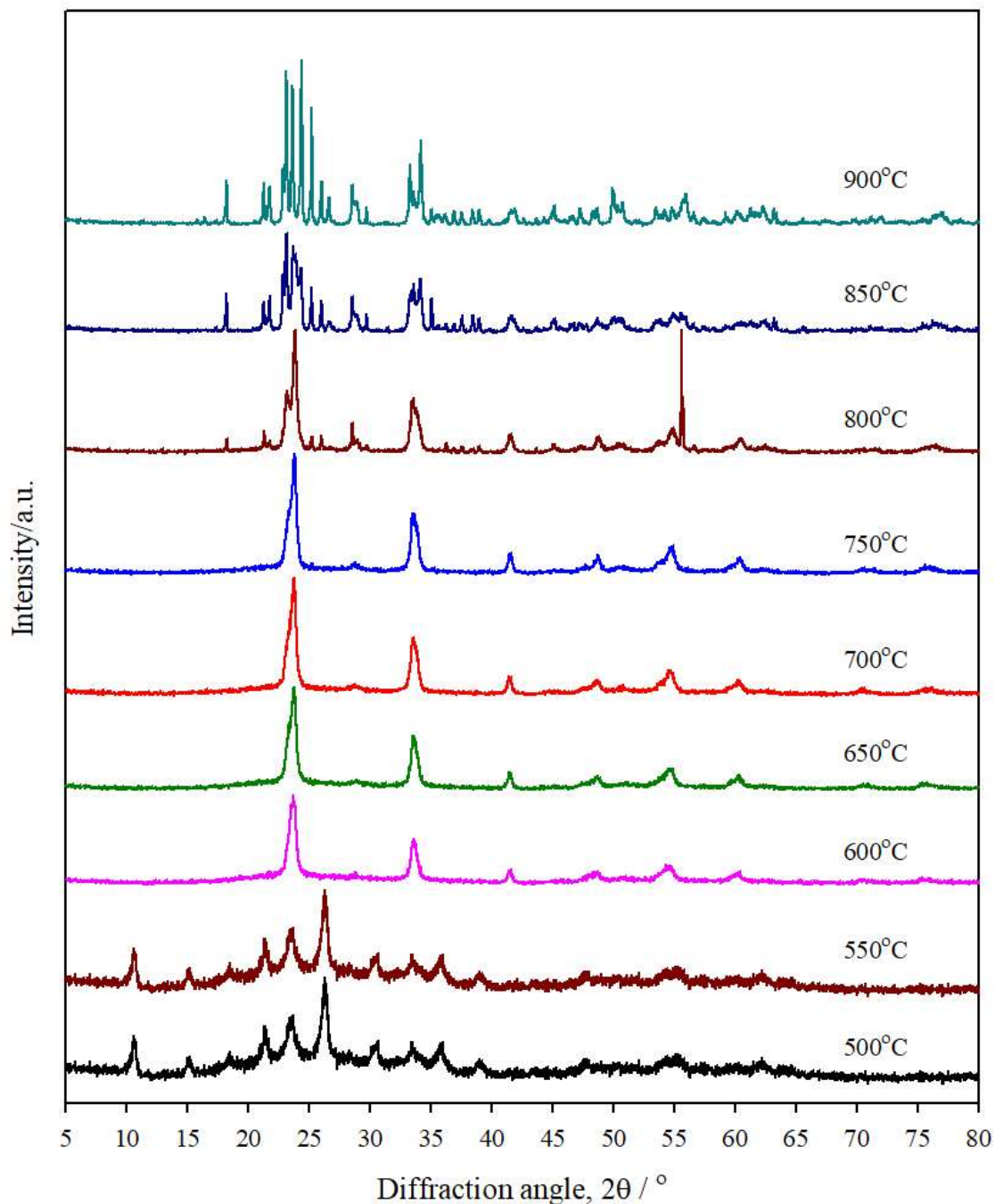
Fig. 4.31. XRD pattern of $Al_{4/3-x}Fe_xW_{20/3}O_{24}(PO_2)_4$ at nominal composition $x = 0$ at different temperatures. For clarity, the diffraction patterns are plotted vertically. The patterns show a pure cubic phase up to 750ºC, and at 800ºC, a phase transition from cubic to orthorhombic starts to appear. On further heating, the sample decomposes into another new phase.

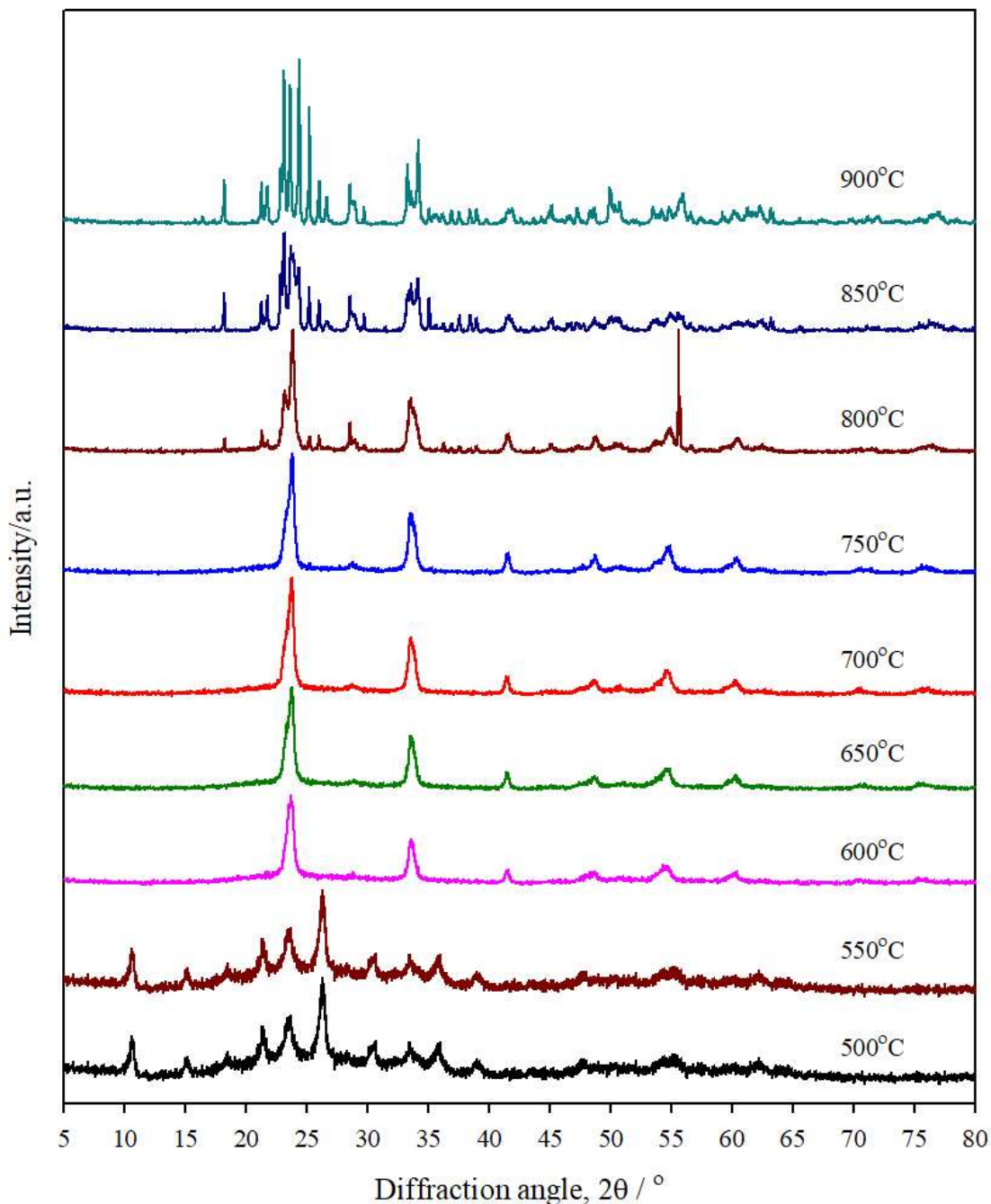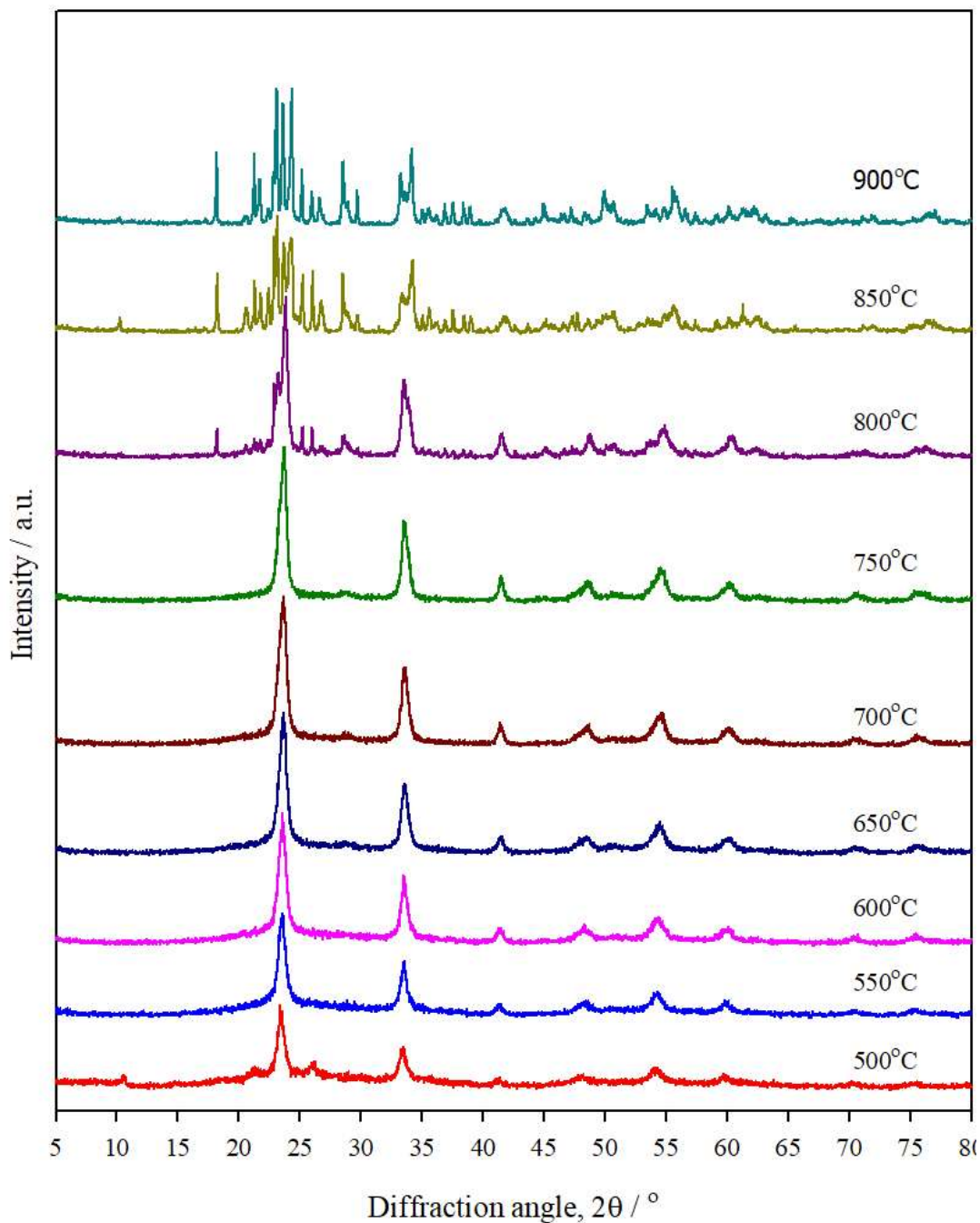Fig. 4.32. XRD pattern of $Al_{4/3-x}Fe_xW_{20/3}O_{24}(PO_2)_4$ at nominal composition x = 1/3 at different temperatures. For clarity, the diffraction patterns are plotted vertically. The patterns show a pure cubic phase up to 750°C, and at 800°C, some additional lines with cubic phase are observed. On further heating, the sample decomposes into another new phase.
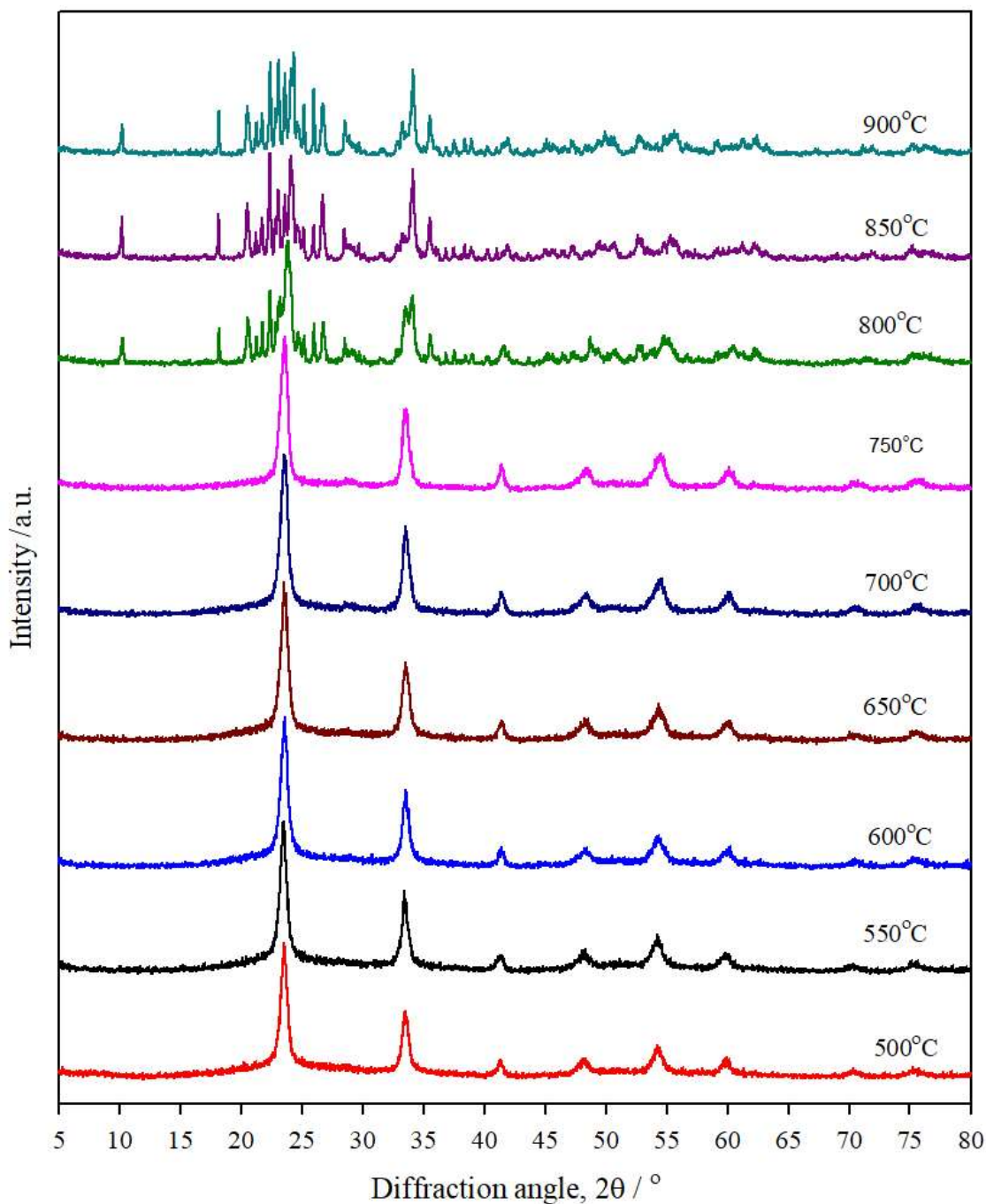
Fig. 4.33. XRD pattern of $Al_{4/3-x}Fe_xW_{20/3}O_{24}(PO_2)_4$ at nominal composition x = 2/3 at different temperatures. For clarity, the diffraction patterns are plotted vertically. The patterns show a pure cubic phase up to 750°C. On further heating, the sample decomposes into other new phase.
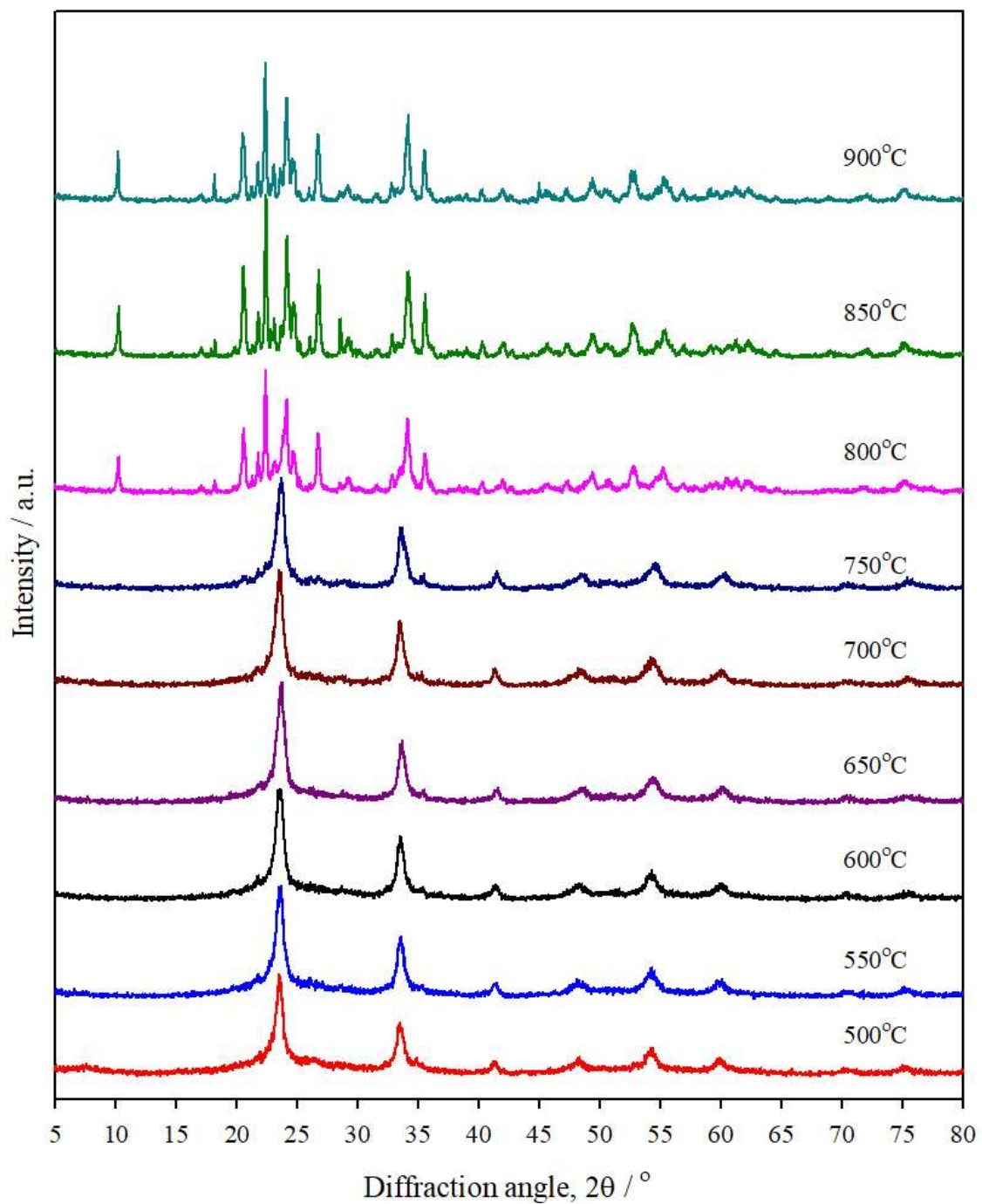
Fig. 4.34. XRD pattern of $Al_{4/3-x}Fe_xW_{20/3}O_{24}(PO_2)_4$ at nominal composition x = 1 at different temperatures.
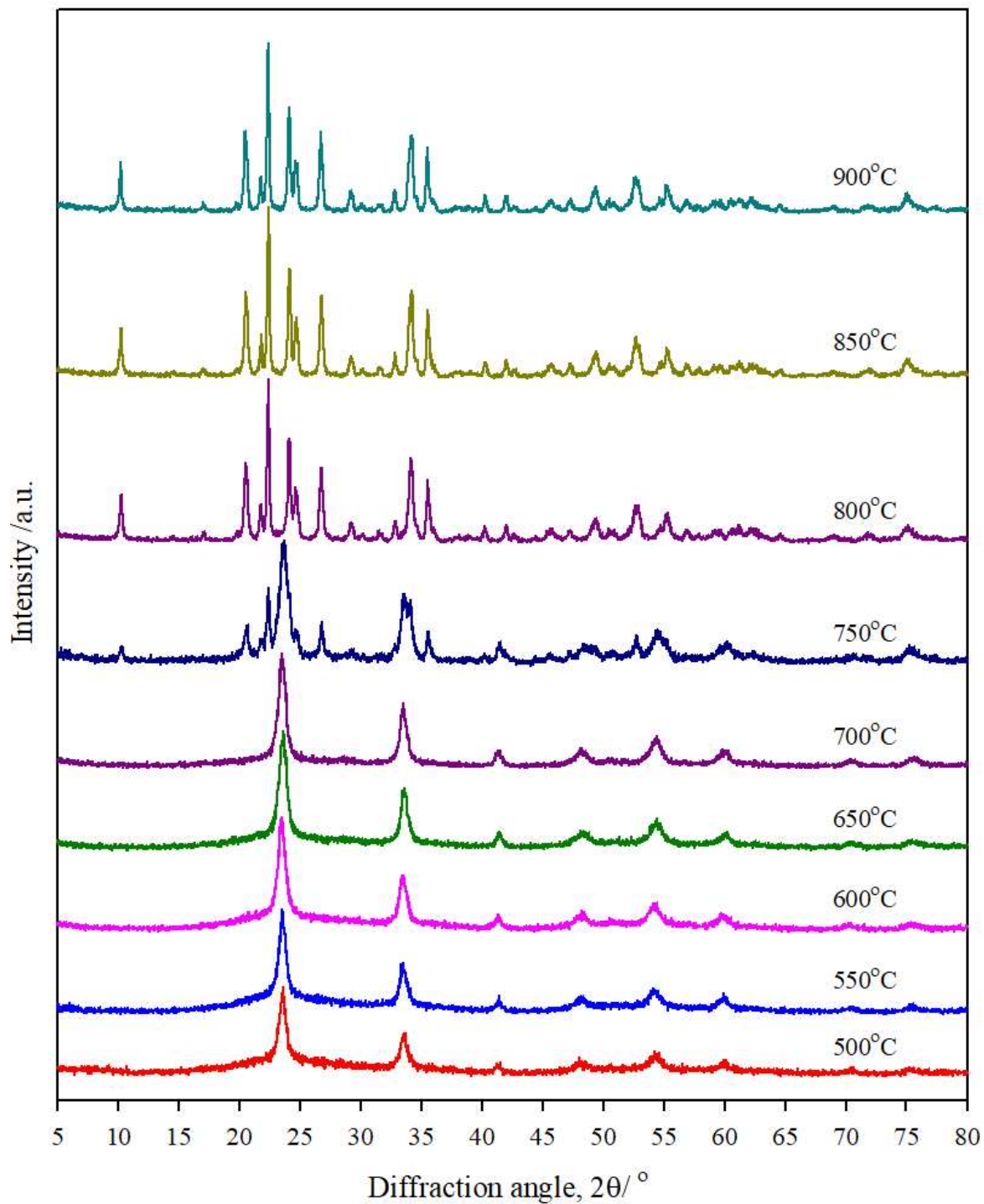
Fig. 4.35. XRD pattern of $Al_{4/3-x}Fe_xW_{20/3}O_{24}(PO_2)_4$ at nominal composition x = 4/3 at different temperatures.

The pure cubic phase structure parameters of the $Al_{4/3-x}Fe_xW_{20/3}O_{24}(PO_2)_4$ series were refined by the Rietveld method using space group *Pm-3m* (221) with the profex software. As shown in Figs. 4.36. and A.4.13, the calculated and measured XRD patterns are well fitted. The cell parameters at 600°C and 650°C for the cubic phase are shown in Table 4.4. It is found that the cell parameters slightly increase up to x = 2/3 and then slightly decrease.

The crystallite size of the prepared $Al_{4/3-x}Fe_xW_{20/3}O_{24}(PO_2)_4$ series was calculated using the Debye-Scherer equation. The sizes of cubic $Al_{4/3-x}Fe_xW_{20/3}O_{24}(PO_2)_4$ nanoparticles are tabulated in Table A.4.3. The estimated sizes are in the range of 8-13 nm.
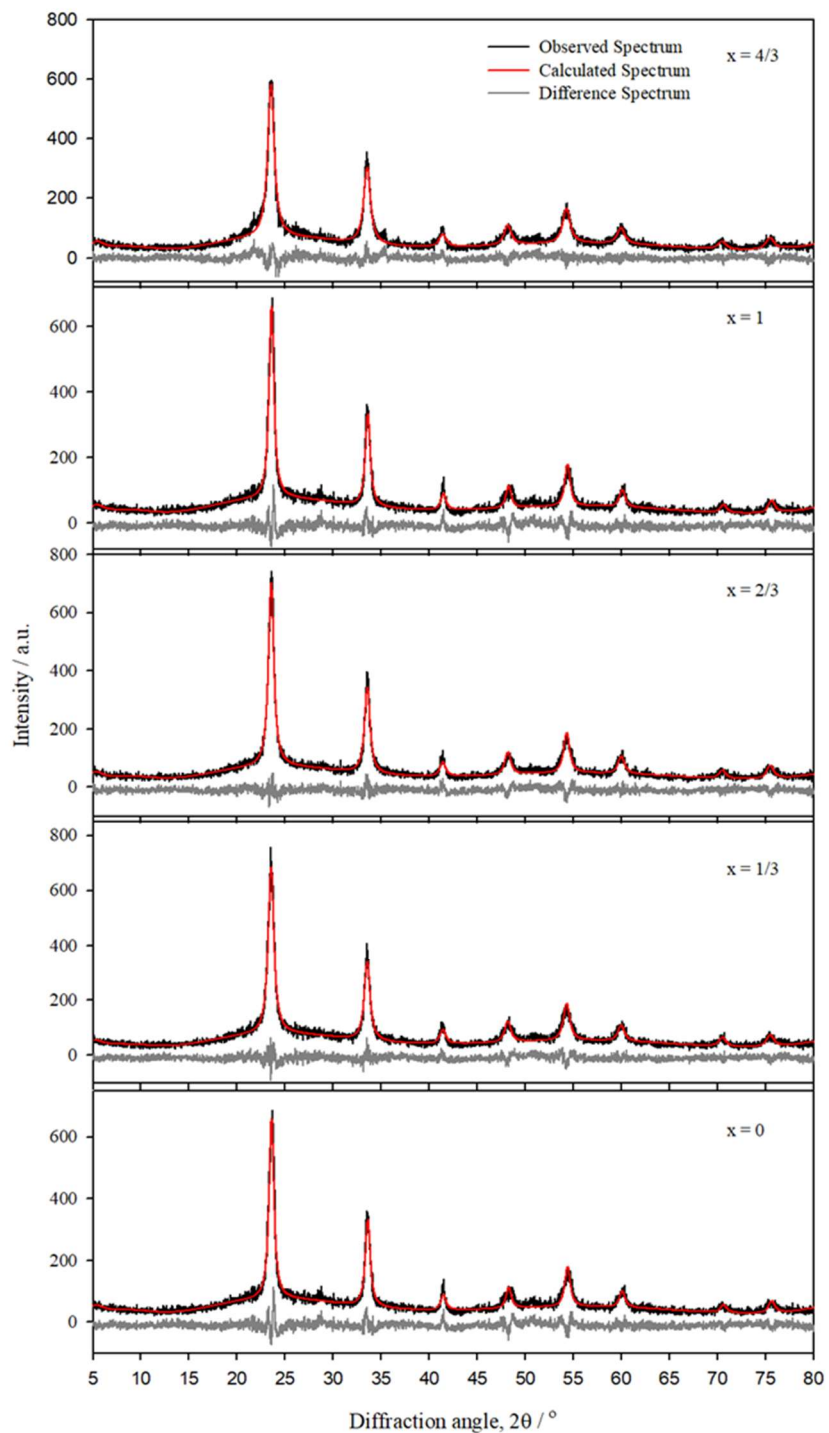
Fig. 4.36. Rietveld refinements fit of the $Al_{4/3-x}Fe_xW_{20/3}O_{24}(PO_2)_4$ series samples prepared at 600°C. The black spectrum represents the observed/measured spectrum, and the red spectrum represents calculated data. The curve below the spectrum represents the difference spectrum.

Table 4.5 Cell parameters of $Al_{4/3-x}Fe_xW_{20/3}O_{24}(PO_2)_4$ series at 600°C and 650°C.

Nominal Compositions	600°C	650°C
x = 0	0.3774	0.3768
x = 1/3	0.3780	0.3774
x = 2/3	0.3780	0.3778
x = 1	0.3774	0.3778
x = 4/3	0.3781	0.3777
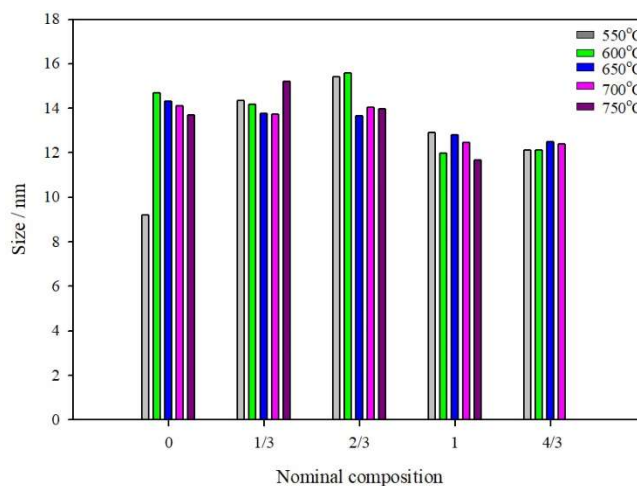
Fig. 4.37. Crystallite sizes of $Al_{4/3-x}Fe_xW_{20/3}O_{24}(PO_2)_4$ at different temperatures and compositions.

4.5.3.b. FT-IR analysis $Al_{4/3-x}Fe_xW_{20/3}O_{24}(PO_2)_4$ series

The FT-IR spectra of $Al_{4/3-x}Fe_xW_{20/3}O_{24}(PO_2)_4$ (x = 0, 1/3, 2/3, 1, 4/3) at various temperatures are shown in Fig. 4.38. The spectra of $Fe_{4/3}W_{20/3}O_{24}(PO_2)_4$ (i.e., at x = 4/3) show three bands around 519, 805, 940 cm^{-1} wavenumber and they can be compared with the vibrations of W-O, O-W-O of WO_3. With increasing temperatures, these bands are shifted toward lower wave numbers. This spectral property may be associated with the change of a crystalline phase at higher temperatures. The band for P-O stretching modes of the phosphate group was detected at 1127 cm^{-1} wavenumber. Similar observations are found for all other nominal compositions, x. At higher temperatures, only nominal composition x = 4/3 corresponds to the MPTB structure type. The decomposition of the phase with increasing calcination temperatures is visible in the pattern of FT-IR spectra for other compositions. FT-IR spectra at nominal compositions x = 1/3, 2/3 and 1 show all the absorption bands of the MPTB type along with additional bands. But, the IR spectra of nominal composition x = 0 is completely different from the MPTB structure type. These results comply with the XRD analysis.
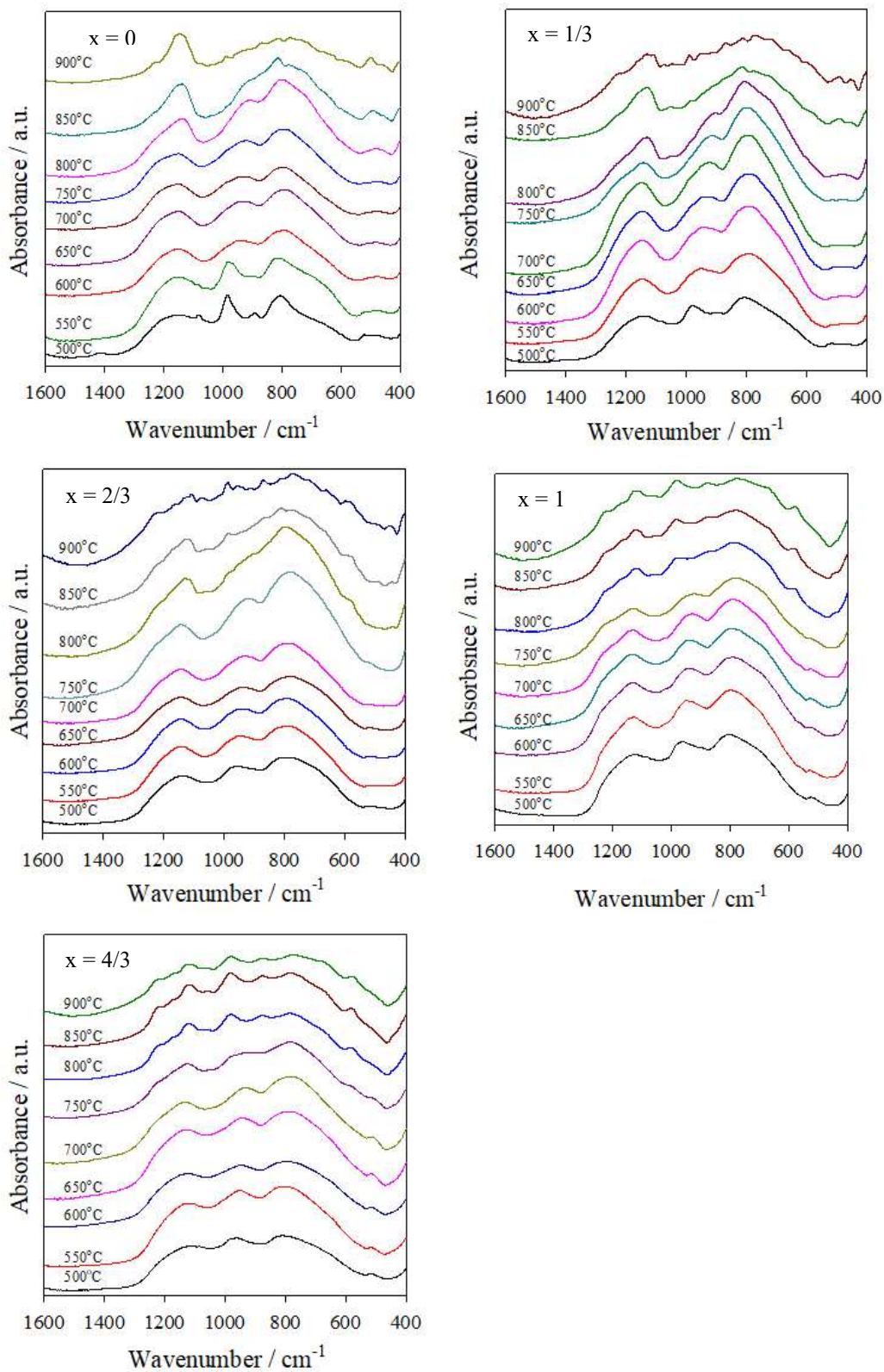
Fig. 4.38. FT-IR spectra of $Al_{4/3-x}Fe_xW_{20/3}O_{24}(PO_2)_4$ with different nominal compositions at different temperatures.

4.5.3.c. SEM analysis of Al$_{4/3-x}$Fe$_x$W$_{20/3}$O$_{24}$(PO$_2$)$_4$ series

Fig. 4.39 shows the SEM images of Al$_{4/3-x}$Fe$_x$W$_{20/3}$O$_{24}$(PO$_2$)$_4$ (x = 0, 1/3, 2/3, 1, 4/3) with compositional variations at 900°C. Other temperature SEM images are shown in the Appendix. A nearly uniform spherical nanocrystalline particle distribution was found for all studied compositions.
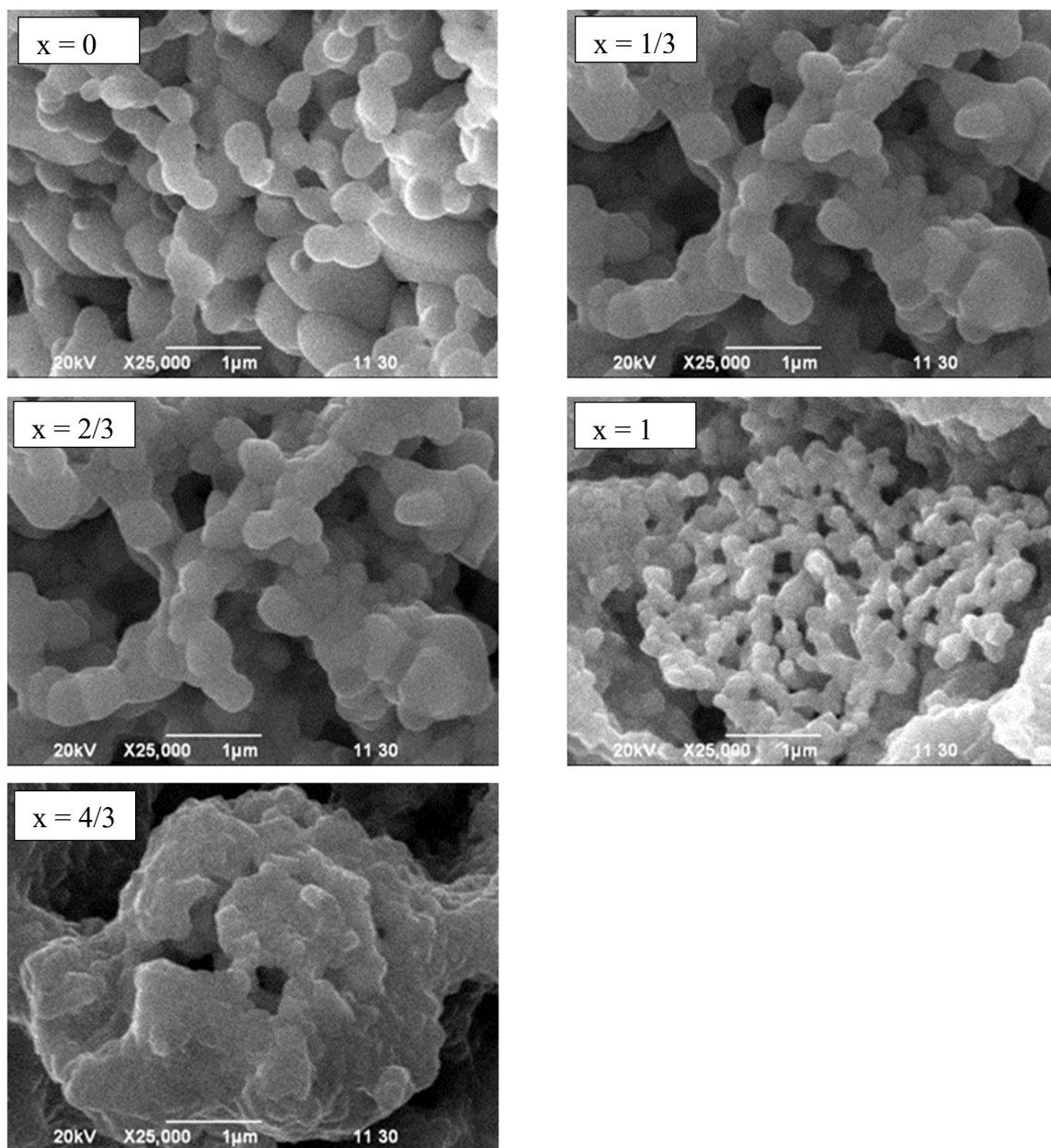
Fig. 4.39. SEM images of Al$_{4/3-x}$Fe$_x$W$_{20/3}$O$_{24}$(PO$_2$)$_4$ with different nominal compositions at 900°C.

Conclusion of phosphate tungsten bronze $(A_{4/3-x}T_xW_{20/3}O_{24}(PO_2)_4)$ **series**

Finally, we present a relatively simple SCS method for producing three series of mixed-metal monophosphate tungsten bronzes $Cr_{4/3-x}Fe_xW_{20/3}O_{24}(PO_2)_4$, $Cr_{4/3x}Al_xW_{20/3}O_{24}(PO_2)_4$ and $Fe_{4/3-x}Al_xW_{20/3}O_{24}(PO_2)_4$, with nominal compositions x = 0, 1/3, 2/3, 1, 4/3. Since the method uses a solution, it has all the possibility of a wet chemical process like stoichiometry and the desired amount of doping control. The temperature as well as composition-structure relationship of the synthesized sample were studied.

The prepared samples were characterized by X-ray powder diffraction, Fourier transform infrared spectroscopy (FT-IR), scanning electron microscopy (SEM) and energy dispersive X-ray spectroscopy (EDX). XRD analysis of the solid solution series, $(Cr_{4/3-x}Fe_xW_{20/3})O_{24}(PO_2)_4$ with nominal compositions $0.00 \leq x \leq 1$ exhibits cubic phase up to 700°C, but cubic phase up to 700°C for x = 4/3. When the samples were heated further, a few lines related to the orthorhombic phase were noticed for $Cr_{4/3}W_{20/3}O_{24}(PO_2)_4$, additionally with the cubic phase. At 850°C, the X-ray pattern could be perfectly indexed as the orthorhombic structure of $Cr_{4/3}W_{20/3}O_{24}(PO_2)_4$. The FT-IR results support the XRD findings that the phase change occurs from cubic to orthorhombic at the indicated temperature and composition. Cell parameters for cubic phase at 600°C and 650°C slightly decrease up to nominal composition x = 1, then slightly increase. For orthorhombic phase cell parameters, *a, b,* and *V* slightly increase, but *c* remains constant. The broadening of XRD peaks for all cubic phases reveal the nanocrystallinity of the compounds, which was supported by SEM images. Investigation of SEM analysis reveals that they form aggregated nanocrystalline particles. The EDX confirms the presence of all the experimental elements.

A solid solution series of $Cr_{4/3-x}Al_xW_{20/3}O_{24}(PO_2)_4$ with nominal compositions of x = 0, 1/3, 2/3, 1, 4/3 was also prepared using the SCS method. Up to 750°C, the X-ray powder pattern of $Cr_{4/3-x}Al_xW_{20/3}O_{24}(PO_2)_4$ with nominal composition $0.00 \leq x \leq 4/3$ shows cubic phase. But at 800°C, some differences in composition variation were observed. For x = 0, 1/3 characteristic lines related to the orthorhombic phase were observed with a mixture of cubic phase. At 850°C and 900°C, the X-ray pattern could be perfectly indexed as the orthorhombic structure, which is in agreement with $P_4W_8O_{32}$. At nominal composition x = 2/3, some extra lines appeared, i.e. at $2\theta \approx 23.06$, which are not related to the orthorhombic phase. Similar

observations were found for nominal composition x = 1. However, up to 750°C, the XRD patterns of $Al_{4/3}W_{20/3}O_{24}(PO_2)_4$ (when x = 4/3) are pure cubic phase. At 800°C, a phase transition from cubic to orthorhombic starts to appear. On further heating, the diffraction pattern shows complete decomposition into some new phase. Therefore, the diffraction patterns for all compositions except nominal composition x = 4/3 are orthorhombic at 900°C with a small orthorhombic impurity for nominal composition x = 2/3 and 1. The cell parameters at 600°C and 650°C for cubic phase show that the cell parameters slightly increase up to nominal composition x = 1/3, then remains almost constant. The FT-IR results also show the same systematic change with the composition change. SEM image investigation shows that they form aggregated nanocrystalline particle.

The third series, $Al_{4/3-x}Fe_xW_{20/3}O_{24}(PO_2)_4$, also exhibits a cubic crystalline phase with composition changes up to 750°C. Only nominal composition x = 4/3 shows an orthorhombic phase at 850°C and 900°C. But for other nominal compositions, when the sample is heated further at 800°C, some new lines appear which are not related to the orthorhombic phase. On further heating, the product may be converted to another phase. The calculated cell parameters for cubic phase at 600°C and 650°C show that the cell parameters increase slightly up to nominal compositions x = 2/3 and then decrease.

Considering all the information, it is possible to conclude that Cr and Fe can form a complete solid solution series $(A_{4/3-x}T_xW_{20/3})O_{24}(PO_2)_4$ with an MPTB structure. Other two series, however, $(Cr_{4/3-x}Al_xW_{20/3})O_{24}(PO_2)_4$ and $(Al_{4/3-x}Fe_xW_{20/3})O_{24}(PO_2)_4$, exhibit composition dependent structural variation.

References

References

[1]   J. -L. Zhang, and G. -Y. Hong, "Nonstoichiometric Compounds," *In Modern Inorganic Synthetic Chemistry*, Elsevier, 329–354, 2017, doi: 10.1016/B978-0-444-63591-4.00013-6.

[2]   J. S. Anderson, "Nonstoichiometric compounds: A critique of current structural views," *Proc. Indian Acad. Sci. - Chem. Sci.*, *93(6)*, 861-904, 1984, doi: 10.1007/BF02840335.

[3]   P. Dubey and N. Kaurav, "Stoichiometric and Nonstoichiometric Compounds," *In Structure Processing Properties Relationships in Stoichiometric and Nonstoichiometric Oxides*, 2020, doi: 10.5772/intechopen.89402.

[4]   D. Chen, C. Chen, Z. M. Baiyee, Z. Shao, and F. Ciucci, "Nonstoichiometric oxides as low-cost and highly-efficient oxygen reduction/evolution catalysts for low-temperature electrochemical devices," *Chemical Reviews*, *115(18)*, 9869-9921, 2015, doi: 10.1021/acs.chemrev.5b00073.

[5]   T. J. Daou, G. Pourroy, S. Bégin-Colin. J. M. Grenèche, C. Ulhaq-Bouillet, P. Legaré, P. Bernhardt, and G. Rogez, "Hydrothermal synthesis of monodisperse magnetite nanoparticles," *Chem. Mater.*, *18*, 4399-4404, 2006, doi: 10.1021/cm060805r.

[6]   G. Centi, "Role of non-stoichiometry and soft chemistry in the preparation of advanced catalysts," *Diffus. Defect Data. Pt A Defect Diffus. Forum*, Vol. 191, pp. 17-34, 2001, doi: 10.4028/www.scientific.net/ddf.191.17.

[7]   S. Y. Udovichenko, A. N. Bobylev, D. A. Belotserkovtseva, and D. D. Shpindyuk, "Obtaining of non-stoichiometric titanium oxide using reactive magnetron sputtering," In *IOP Conference Series: Materials Science and Engineering*, Vol. 387, No. 1, p. 012080, 2018, doi: 10.1088/1757-899X/387/1/012080.

[8]   L. Li, M. Li, H. Zhang, I. M. Reaney, and D. C. Sinclair, "Controlling mixed conductivity in Na1/2Bi1/2TiO$_3$ using A-site non-stoichiometry and Nb-donor doping," *J. Mater. Chem. C*, *4(24)*, 5779-5786, 2016, doi: 10.1039/c6tc01719c.

[9]   P. Kofstad, Nonstoichiometry, diffusion, and electrical conductivity in binary metal oxides, Wiley-Interscience, New York, 1972.

[10]   A. J. Moulson, and J. M. Herbert, "*Electroceramics: Materials, Properties, Applications*," Wiley, 2003.

[11]   S. Samira, X. K. Gu, and E. Nikolla, "Design strategies for efficient nonstoichiometric mixed metal oxide electrocatalysts: correlating measurable oxide properties to electrocatalytic performance," *ACS Catal.*, *9(11)*, 10575-10586, 2019, doi: 10.1021/acscatal.9b02505.

[12]   X. K. Gu, J. S. A. Carneiro, S. Samira, A. Das, N. M. Ariyasingha, and E. Nikolla, "Efficient oxygen electrocatalysis by nanostructured mixed-metal oxides," *J. Am. Chem. Soc.*, *140(26)*, 8128-8137, 2018, doi: 10.1021/jacs.7b11138.

[13]   H. Takeda, and K. Adachi, "Near infrared absorption of tungsten oxide nanoparticle dispersions," *J. Am. Ceram. Soc.*, *90(12)*, 4059-4061, 2007, doi: 10.1111/j.1551-2916.2007.02065.x.

[14]   C. M. Wu, S. Naseem, M. H. Chou, J. H. Wang, and Y. Q. Jian, "Recent advances in tungsten-oxide-based materials and their applications," *Frontiers in Materials.*, *6*, 49, 2019, doi: 10.3389/fmats.2019.00049.

[15]   B. Bhuyan, B. Paul, S. S. Dhar, and S. Vadivel, "Facile hydrothermal synthesis of ultrasmall $W_{18}O_{49}$ nanoparticles and studies of their photocatalytic activity towards degradation of methylene blue," *Mater. Chem. Phys.*, *188*, 1-7, 2017, doi: 10.1016/j.matchemphys.2016.12.035.

[16]   M. Mehring, "From molecules to bismuth oxide-based materials: Potential homo- and heterometallic precursors and model compounds," *Coordination Chemistry Reviews.*, *251(7-8)*, 974-1006, 2007, doi: 10.1016/j.ccr.2006.06.005.

[17]   K. Wójcik, "The Synthesis, Structure and Reactivity of Iron-Bismuth Complexes: Potential Molecular Precursors for Multiferroic $BiFeO_3$," *Doctoral Dissertation*, Technische Universität Chemnitz, 2010.

[18]   O. Rohr, "Bismuth – the new ecologically green metal for modern lubricating engineering," *Industrial Lubrication and Tribology*, *54(4)*, 153-164, 2002, doi: 10.1108/00368790210431709.

[19]   I. Bloom, M. C. Hash, J. P. Zebrowski, K. M. Myles, and M. Krumpelt, "Oxide-ion conductivity of bismuth aluminates," *Solid State Ionics*, *53*, 739-747, 1992, doi: 10.1016/0167-2738(92)90249-O.

[20]   S. Zha, J. Cheng, Y. Liu, X. Liu, and G. Meng, "Electrical properties of pure and Sr-doped $Bi_2Al_4O_9$ ceramics," *Solid State Ionics*, *156(1-2)*, 197-200, 2003, doi: 10.1016/S0167-2738(02)00172-8.

[21]   T. Debnath, S. C. Roy, C. H. Rüscher, and A. Hussain, "Synthesis and characterization of niobium-doped potassium tetragonal tungsten bronzes, $K_xNb_yW_{1-y}O_3$," *J. Mater. Sci.*, *44(1)*, 179, 2009, doi: 10.1007/s10853-008-3101-4.

[22]   F. Galasso, L. Katz, and R. Ward, "Tantalum analogs of the tetragonal tungsten bronzes," *J. Am. Chem. Soc.*, *81(22)*, 5898-5899, 1959, doi: 10.1021/ja01531a013.

[23]   A. Hussain, A. Ul-Monir, M. M. Murshed, and C. H. Rüscher, "Synthesis and characterization of niobium substituted hexagonal tungsten bronzes," *Zeitschrift fur Anorg. und Allg. Chemie*, *628(2)*, 416-420, 2002, doi: 10.1002/1521-3749(200202)628:2<416::AID-ZAAC416>3.0.CO;2-A.

[24]   R. Sharma, and L. Kihlborg, "Structures and defects of new intergrowth tungsten bronze analogues revealed by high resolution electron microscopy," *Mater. Res. Bull.*, *16(4)*, 377-380, 1981, doi: 10.1016/0025-5408(81)90004-0.

[25]   R. Sharma, "Bronzoid phases in the pseudo-binary system $A_xNb_xW_{1-x}O_3$ with A = K and Cs," *Mater. Res. Bull.*, *20*(11), 1373-1381, 1985, doi: 10.1016/0025-5408(85)90132-1.

[26]   T. Debnath, "Structure, Chemical Composition and Optical Property Relationship of Alkali-Metal Tungsten Oxides and Niobium Tungsten Oxides," *Doctoral dissertation*, Hannover: Gottfried Wilhelm Leibniz Universität Hannover, 2008.

[27]   M. Greenblatt, "Monophosphate tungsten bronzes. A new family of low-dimensional, charge-density-wave oxides," *Acc. Chem. Res.*, *29(5)*, 219-228, 1996, doi: 10.1021/ar950157.

[28]   B. Raveau, "Numerous structures of oxides can be built up from the ReO_3-type framework," *Proc. Indian Acad. Sci. (Chem. Sci.), 52*, 67-101, 1986.

[29]   F. Deganello, and A. K. Tyagi, "Solution combustion synthesis, energy and environment: Best parameters for better materials," *Progress in Crystal Growth and Characterization of Materials., 64(2)*, 23-61, 2018, doi: 10.1016/j.pcrysgrow.2018.03.001.

[30]   T. Mimani, and K. C. Patil, "Solution combustion synthesis of nanoscale oxides and their composites," *Mater. Phys. Mech., 4(2)*, 134–137, 2001.

[31]   S. C. Roy, W. Assenmacher, T. Linden, L. Esser, W. Mader, and R. Glaum, "Substitution of W^{5+} in monophosphate tungsten bronzes by combinations Mn^+/W^{6+}," *Zeitschrift fur Naturforsch. - Sect. B J. Chem. Sci., 71(5)*, 543-552, 2016, doi: 10.1515/znb-2016-0036.

[32]   T. Debnath, A. Ullah, C. H. Rüscher, and A. Hussain, "Chromium substitution in mullite type bismuth aluminate: $Bi_2Cr_xAl_{4-x}O_9$ with $0 \leq x \leq 2.0$," *J. Solid State Chem., 220*, 167-171, 2014, doi: 10.1016/j.jssc.2014.08.021.

[33]   D. Voll, A. Beran, and H. Schneider, "Variation of infrared absorption spectra in the system $Bi_2Al_{4-x}Fe_xO_9$ (x = 0 - 4), structurally related to mullite," *Phys. Chem. Miner., 33(8)*, 623-628, 2006, doi: 10.1007/s00269-006-0108-8.

[34]   M. S. Hegde, G. Madras, and K. C. Patil, "Noble metal ionic catalysts," *Acc. Chem. Res., 42(6)*, 704-712, 2009, doi: 10.1021/ar800209s.

[35]   A. M. Abdullah, T. Debnath, C. H. Rüscher, and A. Hussain, "Synthesis and Characterization of Vanadium Substituted Potassium Tungsten Bronzes, $K_xV_yW_{1-y}O_3$," *J. Sci. Res., 4(2)*, 507, 2012, doi: 10.3329/jsr.v4i2.9349.

[36]   M. M. R. Shakil, T. Debnath, C. H. Rüscher, and A. Hussain, "Study of tantalum substituted potassium tungsten bronzes," *J. Bangladesh Chem. Soc., 25(1)*, 38-45, 2012, doi: 10.3329/jbcs.v25i1.11770.

[37]   K. R. Dey, T. Debnath, C. H. Rüscher, M. Sundberg, and A. Hussain, "Synthesis and characterization of niobium doped hexagonal tungsten bronze in the systems, $Cs_xNb_yW_{1-y}O_3$," *J. Mater. Sci., 46(5)*, 1388-1395, 2011, doi: 10.1007/s10853-010-4932-3.

[38]   S. Roy, B. Mallesham, V. B. Zade, A. Martinez, V. Shutthanandan, S. Thevuthasan, and C.V. Ramana, "Correlation between structure, chemistry, and dielectric properties of iron-doped gallium oxide ($Ga_{2-x}Fe_xO_3$)," *J. Phys. Chem. C*, *122(48)*, 27597-27607, 2018, doi: 10.1021/acs.jpcc.8b07921.

[39]   H. Lu, H. Li, Y. Chen, and H. Liu, "A facile hydrothermal method to synthesize ammonium tungsten bronze nanoplatelets for NIR absorption," *382(2)*, 0220622018, 2018, doi: 10.1088/1757-899X/382/2/022062.

[40]   C. H. Rüscher, K. R. Dey, T. Debnath, I. Horn, R. Glaum, and A. Hussain, "Perovskite tungsten bronze-type crystals of Li_xWO_3 grown by chemical vapour transport and their characterization," *J. Solid State Chem.*, *181(1)*, 90-100, 2008, doi: 10.1016/j.jssc.2007.10.033.

[41]   G. Huang, C. –H. Lu, and H. -H. Yang, "Magnetic nanomaterials for magnetic bioanalysis. *In Novel Nanomaterials for Biomedical, Environmental and Energy Applications*, 89-109, 2019, doi:10.1016/B978-0-12-814497-8.00003-5.

[42]   J. S. A. Carneiro, J. Williams, A. Gryko, L. P. Herrera, and E. Nikolla, "Embracing the complexity of catalytic structures: A viewpoint on the synthesis of nonstoichiometric mixed metal oxides for catalysis," *ACS Catalysis.*, *8(4)*, 3054-3066, 2020, doi: 10.1021/acscatal.9b04226.

[43]   C. Guo, S. Yin, L. Huang, and T. Sato, "Synthesis of one-dimensional potassium tungsten bronze with excellent near-infrared absorption property," *ACS Appl. Mater. Interfaces*, *3(7)*, 2794-2799, 2011, doi: 10.1021/am200631e.

[44]   M. S. Whittingham, J. D. Guo, R. Chen, T. Chirayil, G. Janauer, and P. Zavalij, "The hydrothermal synthesis of new oxide materials," *Solid State Ionics*, *75*, 257-268, 1995, doi: 10.1016/0167-2738(94)00220-M.

[45]   N. Doebelin and R. Kleeberg, "Profex: A graphical user interface for the Rietveld refinement program BGMN," *J. Appl. Crystallogr.*, *48(5)*, 1573-1580, 2015, doi: 10.1107/S1600576715014685.

[46]   C. Sherman Hsu, *Infrared Spectroscopy in Handbook of Instrumental Techniques for Analytical Chemistry*. Prentice Hall, Upper Saddle River, NJ/London, 1997.

[47]   T. P. Gujar, V. R. Shinde, C. D. Lokhande, R. S. Mane, and S. H. Han, "Bismuth oxide thin films prepared by chemical bath deposition (CBD) method: Annealing effect," *Appl. Surf. Sci.*, *250(1-4)*, 161-167, 2005, doi:10.1016/j.apsusc.2004.12.050.

[48]   C. M. B. Hincapié, M. J. P. Cárdenas, J. E. A. Orjuela, E. R. Parra, and J. J. O. Florez, "Physical-chemical properties of bismuth and bismuth oxides: Synthesis, characterization and applications," *Dyna*, *79(176)*, 139-148, 2012.

[49]   X. Y. Zhang, W. S. Hu, X. W. Qi, G. F. Sun, J. Q. Qi, H. H. Chen, and R. X. Zhong, "Synthesis and characterization of $Bi_2Al_4O_9$ powders," In *Advanced Materials Research*, *624*, 34-37, 2013, doi: 10.4028/www.scientific.net/AMR.624.34.

[50]   H. Schneider, and S. Komarneni, "*Mullite*," 2006, doi: 10.1002/3527607358.

[51]   H. Schneider, and S. Komarneni, "*Basic Properties of Mullite*," Wiley Online Library, 141-225, 2005.

[52]   H. Schneider, R. X. Fischer, and J. Schreuer, "Mullite: Crystal structure and related properties," *J. Am. Ceram. Soc.*, *98(10)*, 2948-2967, 2015, doi: 10.1111/jace.13817.

[53]   K. R. Gbashi, A. T. Salih, A. A. Najim, and M. A. H. Muhi, "Nanostructure characteristics of Bi_2O_3:Al_2O_3 thin films and the annealing temperature effect on morphological, optical, and mechanical properties," *Superlattices Microstruct.*, *146*, 106656, 2020, doi: 10.1016/j.spmi.2020.106656.

[54]   K. Cui, Y. Zhang, T. Fu, J. Wang, and X. Zhang, "Toughening mechanism of mullite matrix composites: A review," *Coatings*, *10(7)*, 672, 2020, doi: 10.3390/coatings10070672.

[55]   H. Schneider, J. Schreuer, and B. Hildmann, "Structure and properties of mullite-A review," *J. Eur. Ceram. Soc.*, *28(2)*, 329-344, 2008, doi: 10.1016/j.jeurceramsoc.2007.03.017.

[56]   B. Krüger (née Lazic), H. Krüger, R. Kaindi, and L. Perfler, "Superstructure of mullite-type $KA_{l9}O_{14}$," *Chem. Mater.*, *25(3)*, 496-502, 2013, doi: 10.1021/cm3038476.

[57]   A. Friedrich, J. Biehler, W. Morgenroth, L. Wiehl, B.Winkler, M. Hanfland, M. Tolkiehn, M. Burianek, and M. Mühlberg, "High-pressure phase transition of $Bi_2Fe_4O_9$," *J. Phys. Condens. Matter.*, *24(14)*, 145401, 2012, doi: 10.1088/0953-8984/24/14/145401.

[58]   N. Niizeki, and M. Wachi, "The crystal structures of $Bi_2Mn_4O_{10}$, $Bi_2Al_4O_9$ and $Bi_2Fe_4O_9$," *Zeitschrift für Krist. Mater.*, *127(1–6)*, 173, 1968, doi: 10.1524/zkri.1968.127.16.173.

[59]   A. G. Tutov, and V. Markin, "X-ray diffraction study of the antiferromagnetic $Bi_2Fe_4O_9$ and isotypic compounds," *Neorg. Mater*, *6*, 2014-2017, 1970.

[60]   I. Abrahams, A. J. Bush, G. E. Hawkes, and T. Nunes, "Structure and oxide ion conductivity mechanism in $Bi_2Al_4O_9$ by combined X-ray and high-resolution neutron powder diffraction and 27Al solid state NMR," *J. Solid State Chem.*, *147(2)*, 631-636, 1999, doi: 10.1006/jssc.1999.8427.

[61]   S. K. Filatov, S. V. Krivovichev, Yu. V. Aleksandrova, R. S. Bubnova, A. V. Egorysheva, P. Burns, Yu. F. Kargin, and V. V. Volkov, "Crystal-structure refinement, thermal expansion, and chemical distortion of $Bi_2Ga_4O_9$," *Russ. J. Inorg. Chem.*, *51(6)*, 878-883, 2006, doi: 10.1134/S0036023606060052.

[62]   A. Friedrich, E. A. Juarez-Arellano, E. Haussühl, R. Boehler, B. Winkler, L. Wiehl, W. Morgenroth, M. Burianek, and M. Mühlberg, "Persistence of the stereochemical activity of the Bi^{3+} lone electron pair in $Bi_2Ga_4O_9$ up to 50 GPa and crystal structure of the high-pressure phase," *Acta Crystallogr. Sect. B Struct. Sci.*, *66(3)*, 323-337, 2010, doi: 10.1107/S0108768110010104.

[63]   M. M. Murshed, C. B. Mendive, M. Curti, M. Šehović, A. Friedrich, M. Fischer, and T. M. Gesing, "Thermal expansion of mullite-type $Bi_2Al_4O_9$: A study by X-ray diffraction, vibrational spectroscopy and density functional theory," *J. Solid State Chem.*, *229*, 87-96, 2015, doi: 10.1016/j.jssc.2015.05.010.

[64]   K. L. Da Silva, V. Šepelák, A. Paesano, F. J. Litterst, and K. D. Becker, "Structural studies of $Bi_2(Fe_xAl_{1-x})_4O_9$ solid solutions $(0.1 < x < 1.0)$ prepared by a combined mechanochemical/thermal synthesis," *Zeitschrift fur Anorg. und Allg. Chemie*, *636(6)*, 1018-1025, 2010, doi: 10.1002/zaac.201000032.

[65]   G. Blasse, and O. B. Ho, "On the luminescence of bismuth aluminate (Bi$_2$Al$_4$O$_9$)," *J. Lumin.*, *21(2)*, 165-168, 1980, doi: 10.1016/0022-2313(80)90016-2.

[66]   H. Schneider, R. X. Fischer, T. M. Gesing, J. Schreuer, and M. Müehlberg, "Crystal chemistry and properties of mullite-type Bi$_2$M$_4$O$_9$: An overview," *Int. J. Mater. Res.*, *103(4)*, 422–429, 2012.

[67]   C. -S. Chen, W. Liu, S. Xie, G. -G. Zhang, H. Liu, G. -Y. Meng, and D. -K Peng, "A novel intermediate-temperature oxygen-permeable membrane based on the high Tc superconductor Bi$_2$Sr$_2$CaCu$_2$O$_8$," *Adv. Mater.*, *12(15)*, 1132–1134, 2000.

[68]   J. Liu W. Lu, Q. Zhong, X. Jin, L. Wei, H. Wu, X. Zhang, L. Li, and Z. Wang, "Single-crystal Bi$_2$Ga$_4$O$_9$ nanoplates with exposed {110} facets for photocatalytic degradation of Acid Red 1," *Mol. Catal.*, *433*, 354-362, 2017, doi: 10.1016/j.mcat.2017.02.033.

[69]   M. Burianek, M. Mühlberg, M. Woll, M. Schmücker, T. M. Gesing, and H. Schneider, "Single-crystal growth and characterization of mullite-type orthorhombic Bi$_2$M$_4$O$_9$ (M = Al^{3+}, Ga^{3+}, Fe^{3+})," *Cryst. Res. Technol.*, *44(10)*, 1156-1162, 2009, doi: 10.1002/crat.200900465.

[70]   L. H. Brixner, "Fluorescence and X-ray data of Bi$_2$Al$_4$O$_9$ and Bi$_2$Ga$_4$O$_9$," *Mater. Res. Bull.*, *13(3)*, 563-570, 1978, doi: 10.1016/0025-5408(78)90179-4.

[71]   C. W. M. Timmermans, and G. Blasse, "The luminescence of some oxidic bismuth and lead compounds," *J. Solid State Chem.*, *52(3)*, 222-232, 1984, doi: 10.1016/0022-4596(84)90005-7.

[72]   V. V. Volkov, and A. V. Egorysheva, "Photoluminescence in fast-response Bi$_2$Al$_4$O$_9$ and Bi$_2$Ga$_4$O$_9$ oxide scintillators," *Opt. Mater. (Amst)*, *5(4)*, 273-277, 1996, doi:10.1016/0925-3467(96)00005-5.

[73]   A. Bhattacharya, K. Mallick, and P. Thomas, "Low temperature synthesis of a bismuth vanadium oxide isomorphous with γ-Bi$_4$V$_2$O$_{11}$," *Solid State Commun.*, *91(5)*, 357-360, 1994, doi: 10.1016/0038-1098(94)90633-5.

[74]   S. C. Abrahams, P. B. Jamieson, and J. L. Bernstein, "Crystal structure of piezoelectric bismuth germanium oxide Bi$_{12}$GeO$_{20}$," *J. Chem. Phys.*, *47(10)*, 4034-4041, 1967, doi: 10.1063/1.1701572.

[75]   N. Daneshmand, H. Shokrollahi, and S. A. N. H. Lavasani, "Enhanced magnetic and dielectric properties in bismuth ferrite ($Bi_{2-x}Sr_xFe_4O_9$) derived by the reverse chemical co-precipitation method," *J. Mater. Sci. Mater. Electron*, *29(4)*, 3201-3209, 2018, doi: 10.1007/s10854-017-8255-x.

[76]   T. M. Gesing, R. X. Fischer, M. Burianek, M. Mühlberg, T. Debnath, C. H. Rüscher, J. Ottinger, J.-C. Buhl, and H. Schneide, "Synthesis and properties of mullite-type $(Bi_{1-x}Sr_x)_2(M^1_{1-y}M^2_y)_4O_{9-x}$ (M = Al, Ga, Fe)," *J. Eur. Ceram. Soc.*, *31(16)*, 3055-3062, 2011, doi: 10.1016/j.jeurceramsoc.2011.04.004.

[77]   Y. Qiu, Z. J. Zou, R. R. Sang, H. Wang, D. Xue, Z. M. Tian, G. S. Gong, and S. L. Yuan, "Enhanced magnetic and ferroelectric properties in Cr doped $Bi_2Fe_4O_9$ ceramics," *J. Mater. Sci. Mater. Electron*, *26(3)*, 1732-1736, 2015, doi: 10.1007/s10854-014-2600-0.

[78]   N. Nizeki, and M. Wachi, "The crystal structures of $Bi_2Mn_{40}O_{10}$, $Bi_2Al_4O_9$ and $Bi_2Fe_4O_9$," *Zeitschrift fur Krist. - New Cryst. Struct.*, *127(1-6)*, 173-187, 1968, doi: 10.1524/zkri.1968.127.1-4.173.

[79]   T. Debnath, C. H. Rüscher, P. Fielitz, S. Ohmann, and G. Borchardt, "Series of compositions $Bi_2(M'_xM_{1-x})_4O_9$ (M', M = Al, Ga, Fe; $0 \leq x \leq 1$) with mullite-type crystal structure: Synthesis, characterization and 18O/16O exchange experiment," *J. Solid State Chem.*, *183(11)*, 2582-2588, 2010, doi :10.1016/j.jssc.2010.07.019.

[80]   D. M. Giaquinta, G. C. Papaefthymiou, W. M. Davis, and H. C. Zur Loye, "Synthesis, structure, and magnetic properties of the layered bismuth transition metal oxide solid solution $Bi_2Fe_{4-x}Ga_xO_9$," *J. Solid State Chem.*, *99(1)*, 120-133, 1992, doi: 10.1016/0022-4596(92)90296-8.

[81]   D. M. Giaquinta, G. C. Papaefthymiou, and H. C. Zur Loye, "Structural and magnetic studies of $Bi_2Fe_{4-x}Al_xO_9$," *J. Solid State Chem.*, *114(1)*, 199-205, 1995, doi: 10.1006/jssc.1995.1028.

[82]   H. Rager, H. Schneider, and H. Graetsch, "Chromium incorporation in mullite," *Am. Mineral.*, *75(3-4)*, 392-397, 1990.

[83]   A. Beran, E. Libowitzky, M. Burianek, M. Mühlberg, C. Pecharromán, and H. Schneidere, "Infrared and Raman spectroscopy of mullite-type $Bi_2Ga_4O_9$," *Cryst. Res. Technol.*, *43(11)*, 1230-1239, 2008, doi: 10.1002/crat.200800396.

[84]   M. Pooladi, H. Shokrollahi, S. A. N. H. Lavasani, and H. Yang, "Investigation of the structural, magnetic and dielectric properties of Mn-doped $Bi_2Fe_4O_9$ produced by reverse chemical co-precipitation," *Mater. Chem. Phys.*, *229*, 39-48, 2019, doi: 10.1016/j.matchemphys.2019.02.076.

[85]   L. Berggren, "Optical absorption and electrical conductivity in lithium intercalated amorphous tungsten oxide films," *Doctoral Dissertation*, Acta Universitatis Upsaliensis, 2004.

[86]   H. R. Shanks, "Growth of tungsten bronze crystals by fused salt electrolysis," *J. Cryst. Growth*, *13-14*, 433–437, 1972, doi: 10.1016/0022-0248(72)90199-6.

[87]   C. J. Howard, V. Luca, and K. S. Knight, "High-temperature phase transitions in tungsten trioxide-the last word?," *J. Phys. Condens. Matter*, *14(3)*, 377-387, 2002, doi: 10.1088/0953-8984/14/3/308.

[88]   A. Faudoa-Arzate, A. Arteaga-Durán, R. J. Saenz-Hernández, M. E. Botello-Zubiate, P. R. Realyvazquez-Guevara, and J. A. Matutes-Aquino, "HRTEM microstructural characterization of β-WO_3 thin films deposited by reactive RF magnetron sputtering," *Materials (Basel).*, *10(2)*, 200, 2017, doi: 10.3390/ma10020200.

[89]   E. Salje, and K. Viswanathan, "Physical properties and phase transitions in WO_3," *Acta Crystallogr. Sect. A*, *31(3)*, 356-359, 1975, doi: 10.1107/S0567739475000745.

[90]   J. Y. Kim, S. Y. Jeong, G. J. Shin, S. K. Lee, and K. H. Choi, "Near infrared cut-off characteristics of various perovskite-based composite films," *Appl. Mech. Mater.*, *229-231*, 2733–2736, doi: 10.4028/www.scientific.net/AMM.229-231.2733.

[91]   C. J. Howard, and H. T. Stokes, "Structures and phase transitions in perovskites – a group-theoretical approach," *Acta Crystallogr. Sect. A Found. Crystallogr.*, *61(1)*, 93–111, 2005, doi: 10.1107/S0108767304024493.

[92]   F. Wöhler, Ann. Chim. *Phys.*, 29, 23, 1823.

[93]   A. Hussain, "Phase analyses of potassium, rubidium and cesium tungsten bronzes," *Acta Chem. Scand.*, *32(6)*, 479, 1978, doi: 10.3891/acta.chem.scand.32a-0479.

[94]   L. A. Hallopeau, Ann. Chim. *Phys.*, 19 (7), 92, 1900.

[95]   A. Magnéli, "Studies on the hexagonal tungsten bronzes of potassium, rubidium and cesium," *Acta Chem. Scand.*, *7*, 315–324, 1953.

[96]   R. K. Stanley, R. C. Morris, and W. G. Moulton, "Conduction properties of the hexagonal tungsten bronze, Rb_xWO_3," *Phys. Rev. B*, *20(5)*, 1903-1914, 1979, doi: 10.1103/PhysRevB.20.1903.

[97]   M. J. Sienko, and S. M. Morehouse, "Electrical and magnetic properties of potassium tungsten bronze and rubidium tungsten bronze and rubidium tungsten bronze," *Inorg. Chem.*, *2(3)*, 485-489, 1963, doi: 10.1021/ic50007a014.

[98]   C. G. Granqvist, "Electrochromic tungsten oxide films: Review of progress 1993-1998," *Sol. Energy Mater. Sol. Cells*, *60(3)*, 201-262, 2000, doi: 10.1016/S0927-0248(99)00088-4.

[99]   S. Rahman, "Synthesis, characterization and structure-property relationship of alkali metal tungsten bronzes" (*Doctoral Dissertation*, Bremen, Universität Bremen), 2015.

[100]   C. J. Raub, A. R. Sweedler, M. A. Jensen, S. Broadston, and B. T. Matthias, "Superconductivity of sodium tungsten bronzes," *Phys. Rev. Lett.*, *13(25)*, 746, 1964, doi: 10.1103/PhysRevLett.13.746.

[101]   L. H. Cadwell, R. C. Morris, and W. G. Moulton, "Normal and superconducting properties of K_xWO_3," *Phys. Rev. B*, *23(5)*, 2219, 1981, doi: 10.1103/PhysRevB.23.2219.

[102]   S. Reich, G. Leitus, Y. Tssaba, Y. Levi, A. Sharoni, and O. Millo, "Localized high-Tc superconductivity on the surface of Na-Doped WO_3," *J. Supercond.*, *13(5)*, 855-861, 2000.

[103]   G. Leitus, H. Cohen, and S. Reich, "Interplay of Cs concentration, dimensionality and superconductivity in Cs_xWO_3," *Phys. C: Superconductivity*, *371(4)*, 321-329, 2002, doi: 10.1016/S0921-4534(01)01104-2.

[104] H. R. Shanks, P. H. Slides, and G. C. Danielson, "Electrical properties of the tungsten bronzes," *39*, 237, 1963, doi: 10.1021/ba-1964-0039.ch022.

[105] A. R. Sweedler, C. J. Raub, and B. T. Matthias, "Superconductivity of the alkali tungsten bronzes," *Phys. Lett.*, *15(2)*, 108, 1965, doi: 10.1016/0031-9163(65)91292-8.

[106] W. A. Kamitakahara, K. Scharnberg, and H. R. Shanks, "Special phonons and superconductivity in the hexagonal tungsten bronzes," *Phys. Rev. Lett.*, *43(21)*, 1607, 1979, doi: 10.1103/PhysRevLett.43.1607.

[107] D. R. Wanlass and M. J. Sienko, "Concentration dependence of superconductivity in rubidium tungsten bronzes," *J. Solid State Chem.*, *12(3-4)*, 362-369, 1975, doi: 10.1016/0022-4596(75)90342-4.

[108] J. D. Greiner, H. R. Shanks, and D. C. Wallace, "Magnetic susceptibility of the cubic sodium tungsten bronzes," *J. Chem. Phys.*, *36*, 772-776, 1962, doi: 10.1063/1.1732608.

[109] P. G. Dickens and M. S. Whittingham, "The tungsten bronzes and related compounds," *Q. Rev. Chem. Soc.*, *22*, 30-44, 1968, doi: 10.1039/qr9682200030.

[110] M. S. Rahman, M. M. Murshed, D. Baabe, and T. M. Gesing, "Tantalum and vanadium substitution in hexagonal $K_{0.3}WO_3$ bronze: Synthesis and characterization," *Zeitschrift fur Krist. - Cryst. Mater*, *231(1)*, 11-21, 2016, doi: 10.1515/zkri-2015-0003.

[111] G. Hägg, "The spinels and the cubic sodium-tungsten bronzes as new examples of structures with vacant lattice points ," *Nature*, *135(3421)*, 874-874, 1935, doi: 10.1038/135874b0.

[112] S. Raj, T. Sato, S. Souma, T. Takahashi, D. D. Sarma, and P. Mahadevan, "Metal-insulator transition of Na_xWO_3 studied by angle-resolved photoemission spectroscopy," *Mod. Phys. Lett. B*, *23(24)*, 2819-2846, 2009, doi: 10.1142/S0217984909021004.

[113] S. Paul, and S. Raj, "Understanding metal-insulator transition in sodium tungsten bronze," *Pramana - J. Phys.*, *84(6)*, 957-966, 2015, doi: 10.1007/s12043-015-0993-9.

[114]   G. Hägg, "Zur Kenntnis der kubischen Natrium-Wolfram-Bronzen," *Zeitschrift für Phys. Chemie*, *29(1)*, 192-204, 1935, doi: 10.1515/zpch-1935-2920.

[115]   J. F. Smith and G. C. Danielson, "Sodium diffusion in sodium tungsten bronze," *J. Chem. Phys.*, *22(2)*, 266-270, 1954, doi: 10.1063/1.1740049.

[116]   M. E. Straumanis, "The Sodium Tungsten Bronzes. I. Chemical Properties and Structure," *J. Am. Chem. Soc.*, *71(2)*, 679-683, 1949, doi: 10.1021/ja01170a085.

[117]   K. S. Park, H. G. Kim, Y. H. Kim, C. H. Park, and K. Do Kim, "The preparation and characterization of $NaWO_3$ particles for heat shielding by Taguchi optimization method," *Chem. Eng. Res. Des.*, *89(11)*, 2389-2395, 2011, doi: 10.1016/j.cherd.2011.04.008.

[118]   F. Corà, M. G. Stachiotti, C. R. A. Catlow, and C. O. Rodriguez, "Transition metal oxide chemistry: Electronic structure study of WO_3, ReO_3, and $NaWO_3$," *J. Phys. Chem. B*, *101(20)*, 3945-3952, 1997, doi: 10.1021/jp963724z.

[119]   O. Glemser, and C. Naumann, "Kristallisierte Wolframblauverbindungen; Wasserstoffanaloga der Wolframbronzen H_xWO_3," *ZAAC - J. Inorg. Gen. Chem.*, *265(4-6)*, 288-302, 1951, doi: 10.1002/zaac.19512650413.

[120]   P. G. Dickens, and R. J. Hurditch, "X-ray and neutron diffraction studies of a tetragonal hydrogen bronze H_xWO_3," *Nature*, *215(5107)*, 1266-1267, 1967, doi: 10.1038/2151266a0.

[121]   I. P. Klimova, V. I. Voronkova, and V. K. Yanovskij, "New compounds $AB_nW_{3-n}O_9$ with the structure of hexagonal tungsten bronze type," *Neorg. Mater*, *31(2)*, 262-267, 1995.

[122]   Z. Gu, M. Ying, T. Zhai, B. Gao, W. Yang, and J. Yao, "A simple hydrothermal method for the large-scale synthesis of single-crystal potassium tungsten bronze nanowires," *Chem. - A Eur. J.*, *12(29)*, 7717-7723, 2006, doi: 10.1002/chem.200600077.

[123]   P. F. Weller, B. E. Taylor, and R. L. Mohler, "Crystal preparation of doped sodium tungsten bronze," *Mater. Res. Bull.*, *5(6)*, 465-476, 1970, doi: 10.1016/0025-5408(70)90086-3.

[124]   K. R. Dey, "Synthesis and characterization of alkali metal tungsten bronzes, Li_xWO_3 and $M_xM'_yW_{1-y}O_3$ (M = Li, Na, Cs and M' = Nb, Mo) systems" (*Doctoral Dissertation*, Hannover: Universität), 2004.

[125]   Y. Miyamoto, S. Kume, J. P. Doumerc, and P. Hagenmuller, "High pressure synthesis and structural evolution of new compounds of formulation $NaNb_{1-x}W_xO_3$," *Mater. Res. Bull.*, *18(12)*, 1463-1470, 1983, doi: 10.1016/0025-5408(83)90185-X.

[126]   M. A. Dubson, and D. F. Holcomb, "Metal-insulator transition in the compensated sodium bronze, $Na_xTa_yW_{1-y}O_3$," *Phys. Rev. B*, *32(4)*, 1985, doi: 10.1103/PhysRevB.32.1955.

[127]   S. A. Lawrence, S. Stevenson, K. Mavadia, and P. A. Sermon, "Solid-state properties of some polycrystalline alkali-metal tungsten bronzes," *Proc. R. Soc. London, Ser. A Math. Phys. Sci.*, *411(1840)*, 95-121, 1987, doi: 10.1098/rspa.1987.0056.

[128]   J. Ranninger, and K. P. Sinha, "Structural phase transitions and superconductivity in hexagonal tungsten bronzes," *Proc. Indian Acad. Sci. - Chem. Sci.*, *95(1)*, 102, 1985, doi: 10.1007/BF02839720.

[129]   T. E. Gier, D. C. Pease, A. W. Sleight, and T. A. Bither, "New lithium, ammonium, and tin hexagonal tungsten bronzes prepared hydrothermally," *Inorg. Chem.*, *7(8)*, 1646-1647, 1968, doi: 10.1021/ic50066a036.

[130]   N. D. Zakharov, P. Werner, I. P. Zibrov, V. P. Filonenko, and M. Sundberg, "Structural studies of calcium tungsten bronzes, Ca_xWO_3, formed at high pressure," *Cryst. Res. Technol.*, *35(6-7)*, 713-720, 2000, doi:10.1002/1521-4079(200007)35:6/7<713::AID-RAT713>3.0.CO;2-Z.

[131]   X. L. Xu, H. W. Schmalle, and J. R. Günter, "Crystal structure of a hexagonal tin tungsten bronze prepared by a mild reaction," *Solid State Ionics*, *76(3-4)*, 221-228, 1995, doi: 10.1016/0167-2738(94)00281-V.

[132]   P. E. Bierstedt, T. A. Bither, and F. J. Darnell, "Superconductivity of some new hexagonal tungsten bronzes," *Solid State Commun.*, *4(1)*, 25-26, 1966, doi: 10.1016/0038-1098(66)90097-4.

[133] B. R. and J. C. T. A. Deschanvres, and M. Frey, "Substitution of tungsten by tantalum and niobium in potassium tungstates. Evidence for new phases $K_x (Nb_xW_{1-x})O_3$," *Bull. Soc. Chim.Fr*, 9, 3519, 1968.

[134] B. Darriet, M. Rat, J. Galy, and P. Hagenmuller, "Sur quelques nouveaux pyrochlores des systemes MTO_3 WO_3 et MTO_3 TeO_3 (M = K, Rb, Cs, Tl; T = Nb, Ta)," *Mater. Res. Bull.*, *6(12)*, 1305-1315, 1971, doi: 10.1016/0025-5408(71)90129-2.

[135] A. Hussain, and L. Kihlborg, "Intergrowth tungsten bronzes," *Acta Crystallogr. Sect. A*, *32(4)*, 551-557, 1976, doi: 10.1107/S0567739476001216.

[136] P. Zhao, "Syntheses, structures and characterizations of novel arsenotungstates: NLO, conductivity, band-gap and thermal expansion properties," *(Doctoral Dissertation, Univ. Bremen)*, 2015.

[137] A. Magnéli, A. I. Virtanen, J. Olsen, A. I. Virtanen, and N. A. Sörensen, "Studies on the hexagonal tungsten bronzes of potassium, rubidium, and cesium.," *Acta Chem. Scand.*, *7(2)*, 315-324, 1953, doi: 10.3891/acta.chem.scand.07-0315.

[138] K. Adachi, Y. Ota, H. Tanaka, M. Okada, N. Oshimura, and A. Tofuku, "Chromatic instabilities in cesium-doped tungsten bronze nanoparticles,"*J. Appl. Phys.*, *114(19)*, 194304, 2013, doi: 10.1063/1.4831950.

[139] K. Machida, K., Tofuku, and A. Adachi, *Handbook of Functional Nanomaterials, Vol. 1: Synthesis and Modifications*, Nova Science Publishers, 2013.

[140] M. Mann, G. E. Shter, G. M. Reisner, and G. S. Grader, "Synthesis of tungsten bronze powder and determination of its composition," *J. Mater. Sci.*, *42(3)*, 1010-1018, 2007, doi: 10.1007/s10853-006-1384-x.

[141] A. J. Bevolo, M. F. Weber, H. R. Shanks, and G. C. Danielson, "Electrocatalytic activity of cubic sodium tungsten bronze: II. Effects of intentional platinization," *J. Electrochem. Soc.*, *128(5)*, 1004, 1981, doi: 10.1149/1.2127540.

[142] M. F. Weber, A. J. Bevolo, H. R. Shanks, and G. C. Danielson, "Electrocatalytic activity of cubic sodium tungsten bronze: I. Effects of platinum doping, anodization, and platinum pre-electrolysis of the electrolyte," *J. Electrochem. Soc.*, *128(5)*, 996, 1981, doi: 10.1149/1.2127588.

[143]   P. B. Hahn, M. A. Wechter, D. C. Johnson, and A. F. Voigt, "Sodium Tungsten Bronze as a Potentiometric Indicating Electrode for Dissolved Oxygen in Aqueous Solution," *Anal. Chem.*, *45(7)*, A651-A658, 1973, doi: 10.1021/ac60329a004.

[144]   I. Hossain, "A new phase of hexagonal bronze, $Rb_xW_{1-x}V_yO_3$," (*M.S. Dissertation, University of Dhaka), 2013.*

[145]   T. M. Gesing, C. H. Ruscher, and A. Hussain, "Crystal structure of rubidium niobium tungsten bronzes, $Rb_xNb_yW_{1-y}O_3$ (x ≈ 0.3; y = 0.13, 0.19)," *Zeitschrift fur Krist. - New Cryst. Struct.*, *216(1-4)*, 37-38, 2001, doi: 10.1524/ncrs.2001.216. 14.37.

[146]   M. Mączka, J. Hanuza, and A. Waśkowska, "Vibrational studies of alkali metal hexatungstates," *J. Raman Spectrosc.*, *34(6)*, 432-437, 2003, doi: 10.1002/jrs.1017.

[147]   R. Brusetti, P. Bordet, and J. Marcus, "Investigation of the Rb-W-O system in connexion with the superconducting properties of the hexagonal tungsten bronzes," *J. Solid State Chem.*, *172(1)*, 148-159, 2003, doi: 10.1016/S0022-4596(03)00006-9.

[148]   M. Mczka, J. Hanuza, and A. Majchrowski, "Vibrational properties of ferroelectric hexagonal tungsten bronzes $AB_xW_{3-x}O_9$, where A = K, Rb, Cs and B = Nb, Ta, Zr, Cr," *J. Raman Spectrosc.*, *32(11)*, 929-936, 2001, doi: 10.1002/jrs.776.

[149]   H. Onoda and T. Sakumura, "Synthesis and catalytic properties of iron-cerium phosphate prepared in ethylene glycol using additives," *J. Adv. Ceram.*, *2(1)*, 49-54, 2013, doi: 10.1007/s40145-013-0041-5.

[150]   H. Onoda, H. Nariai, A. Moriwaki, H. Maki, and I. Motooka, "Formation and catalytic characterization of various rare earth phosphates," *J. Mater. Chem.*, *12(6)*, 1754-1760, 2002, doi: 10.1039/b110121h.

[151]   H. Onoda, T. Ohta, J. Tamaki, and K. Kojima, "Decomposition of trifluoromethane over nickel pyrophosphate catalysts containing metal cation," *Appl. Catal. A Gen.*, *288(1-2)*, 98-103, 2005, doi: 10.1016/j.apcata.2005.04.028.

[152] H. Onoda, K. Yokouchi, K. Kojima, and H. Nariai, "Addition of rare earth cation on formation and properties of various cobalt phosphates," *Mater. Sci. Eng. B Solid-State Mater. Adv. Technol.*, *116(2)*, 189-195, 2005, doi: 10.1016/j.mseb.2004.10.002.

[153] B. Domengès, M. Hervieu, and B. Raveau, "Monophosphate tungsten bronzes with hexagonal tunnels, $Na_x(PO_2)_4(WO_3)_{2m}$: X-ray diffraction and HREM study," *Acta Crystallogr. Sect. B*, *46(5)*, 610-619, 1990, doi: 10.1107/S010876819000475X.

[154] P. Labbé, M. Goreaud, B. Raveau, and J. C. Monier, "Etude comparative des structures M_xWO_3 de type bronze hexagonal. II. Evolution structurale dans la série des bronzes In_xWO_3 (0.12 < x < 0.33)," *Acta Crystallogr. Sect. B Struct. Crystallogr. Cryst. Chem.*, *35(5-8)*, 1557-64, 1979, doi: 10.1107/s0567740879007123.

[155] P. Roussel, O. Pérez, and P. Labbé, "Phosphate tungsten bronze series: Crystallographic and structural properties of low-dimensional conductors," *Acta Crystallogr. Sect. B Struct. Sci.*, *57*(5), 603-632, 2001, doi: 10.1107/S0108768101009685.

[156] J. P. Giroult, M. Goreaud, P. Labbé, and B. Raveau, "$Rb_xP_8W_{32}O_{112}$: a tunnel structure built up from ReO_3 -type blocks and P_2O_7 groups," *Acta Crystallogr. Sect. B Struct. Crystallogr. Cryst. Chem.*, *36(11)*, 2570-2575, 1980, doi: 10.1107/ s0567740880009466.

[157] V. V. Lisnyak, N. V. Stus, N. S. Slobodyanik, N. M. Belyavina, and V. Y. Markiv, "Crystal structure of a novel cubic pyrophosphate WP_2O_7," *J. Alloys Compd.*, *309(1-2)*, 83-87, 2000, doi: 10.1016/S0925-8388(00)00922-1.

[158] J. P. Giroult, M. Goreaud, P. Labbé, and B. Raveau, "Bronzes with a tunnel structure $Rb_xP_8W_{8n}O_{24n+16}$. III. $Rb_xP_8W_{28}O_{100}$: a member corresponding to a non-integral n value n = 3.5," *Acta Crystallogr. Sect. B Struct. Crystallogr. Cryst. Chem.*, *38(9)*, 2342-2347, 1982, doi: 10.1107/s0567740882008759.

[159]   B. Domengès, M. Hervieu, B. Raveau, and R. J. D. Tilley, "The monophosphate tungsten bronzes with pentagonal tunnels (MPTBP, $P_4O_8(WO_3)_{2m}$: A high-resolution electron microscopy study," *J. Solid State Chem.*, *54(1)*, 10-28, 1984, doi: 10.1016/0022-4596(84)90126-9.

[160]   P. Roussel, G. Mather, B. Domengès, D. Groult, and P. Labbé, "Structural Investigation of $P_4W_{24}O_{80}$: A New Monophosphate Tungsten Bronze," *Acta Crystallogr. Sect. B Struct. Sci.*, *54(4)*, 365-375, 1998, doi: 10.1107/S0108768197013785.

[161]   P. Labbe, M. Goreaud, and B. Raveau, "Monophosphate tungsten bronzes with pentagonal tunnels $(PO_2)_4(WO_3)_{2m}$: Structure of two even-m members $P_4W_{12}O_{44}$ (m = 6) and $P_4W_{16}O_{56}$ (m = 8)," *J. Solid State Chem.*, *61*, 324-331, 1986, doi: 10.1016/0022-4596(86)90038-1.

[162]   S. L. Wang, C. C. Wang, and K. H. Lii, "Crystal structure of WPO_5, the second member of the monophosphate tungsten bronze series $(WO_3)_{2m}(PO_2)_4$," *J. Solid State Chem.*, *82*, 298-302, 1989, doi: 10.1016/0022-4596(89)90295-8.

[163]   M. Greenblatt, "Phosphate tungsten bronzes-a new family of quasi-low-dimensional metallic oxides," *Int. J. Mod. Phys. B*, 3937-3971, 1993, doi: 10.1142/s0217979293003553.

[164]   O. Pérez, L. Elcoro, J. M. Pérez-Mato, and V. Petříček, "Monophosphate tungsten bronzes with pentagonal tunnels: Reinvestigation through the peephole of the superspace," *Acta Crystallogr. Sect. B Struct. Sci. Cryst. Eng. Mater.*, *69(2)*, 122-136, 2013, doi: 10.1107/S2052519213002820.

[165]   P. Roussel, D. Groult, A. Maignan, and P. Labbé, "Phase relations, crystal structure, and electron transport properties of phosphate tungsten bronzes $(K_xNa_y)(PO_2)_4(WO_3)_{2m}$ (m = 4, 6)," *Chem. Mater.*, *11(8)*, 2049-2056, 1999, doi: 10.1021/cm9807790.

[166]   B. Domengès, M. Hervieu, B. Raveau, and M. O'Keeffe, "Potassium monophosphate tungsten bronzes with hexagonal tunnels, $K_x(PO_2)_4(WO_3)_{2m}$: X-ray diffraction and HREM study," *J. Solid State Chem.*, *72(2)*, 155-172, 1988, doi: 10.1016/0022-4596(88)90019-9.

[167]   S. C. Roy, "Thermodynamically Stable and Metastable Solids. New Approaches to the Synthesis of Anhydrous Phosphates Containing Vanadium, Molybdenum, and/or Tungsten," (*Doctoral Dissertation*, Universitäts-und Landesbibliothek Bonn), 2015.

[168]   P. Kierkegaard, I. Lindqvist, T. A. Bak, S. Refn, and G. Westin, "On the crystal structure of $W_2O_3(PO_4)_2$.," *Acta Chem. Scand.*, *111*, 657-676, 1960, doi: 10.3891/acta.chem.scand.14-0657.

[169]   M. Lamire, P. Labbé, M. Goreaud, and B. Raveau, "$Ba_2P_8W_{32}O_{112}$: Structural study in comparison with the K and Rb diphosphate tungsten bronzes with hexagonal tunnels," *J. Solid State Chem.*, *71(2)*, 342-348, 1987, doi: 10.1016/0022-4596(87)90241-6.

[170]   M. Greenblatt, "Molybdenum oxide bronzes with quasi-low-dimensional properties," *Chem. Rev.*, *88(1)*, 31-53, 1988, doi: 10.1021/cr00083a002.

[171]   B. Hervieu, M., Domengès, and B. Raveau, "Intergrowths of diphosphate planes and crystallographic shear planes in the reduced diphosphate tungsten bronzes series - $K_x(P_2O_4)_2(WO_{3-Y})_{2m}$.," *Chem. Scripta*, Vol. *25(4)*, pp. 361–368, 1985.

Appendices
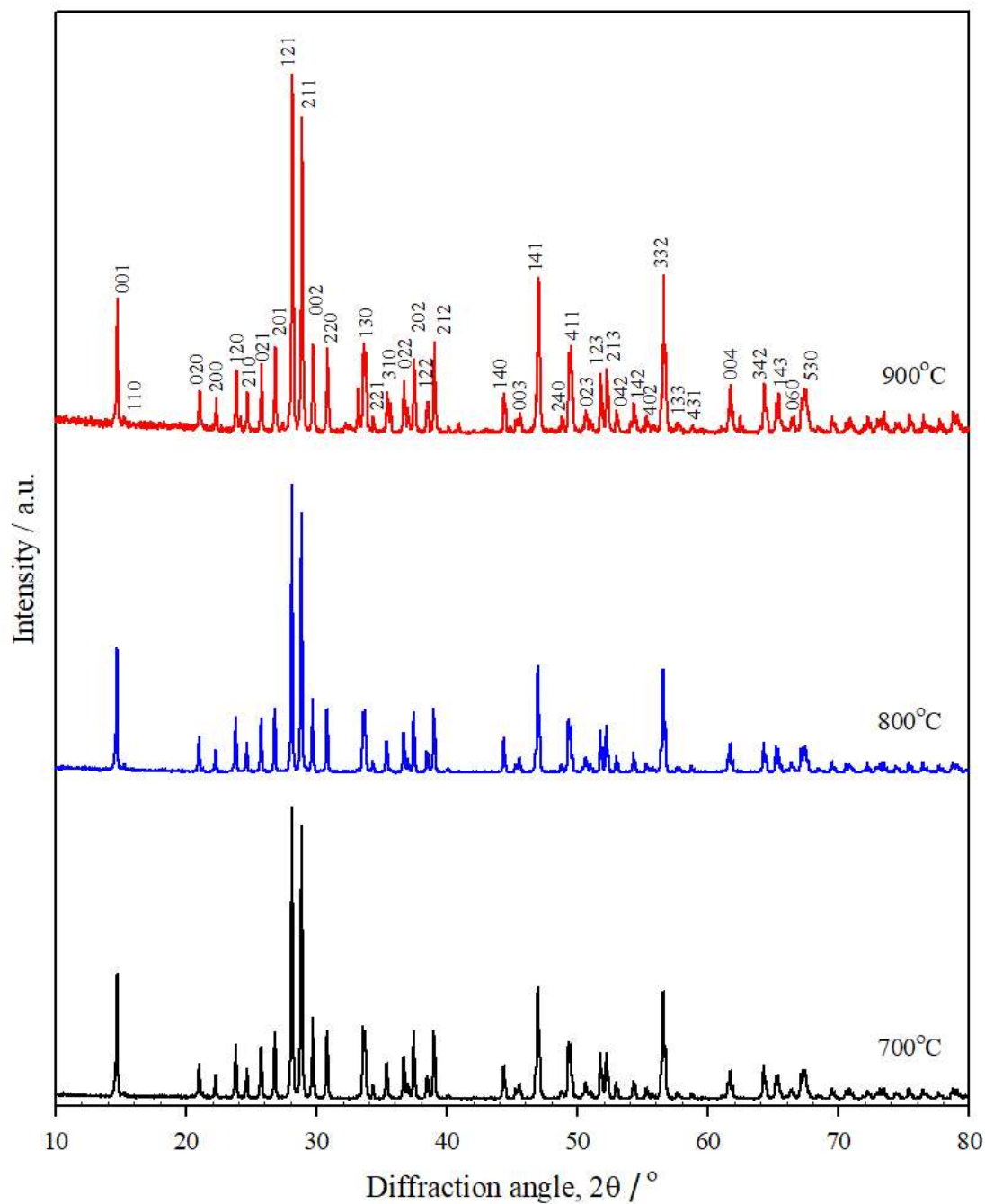
Fig. A.2.1. XRD patterns of BiFe$_4$O$_9$ at different temperatures. For clarity, the diffraction patterns are vertically shifted. The figure shows the patterns are orthorhombic phase at all temperatures.
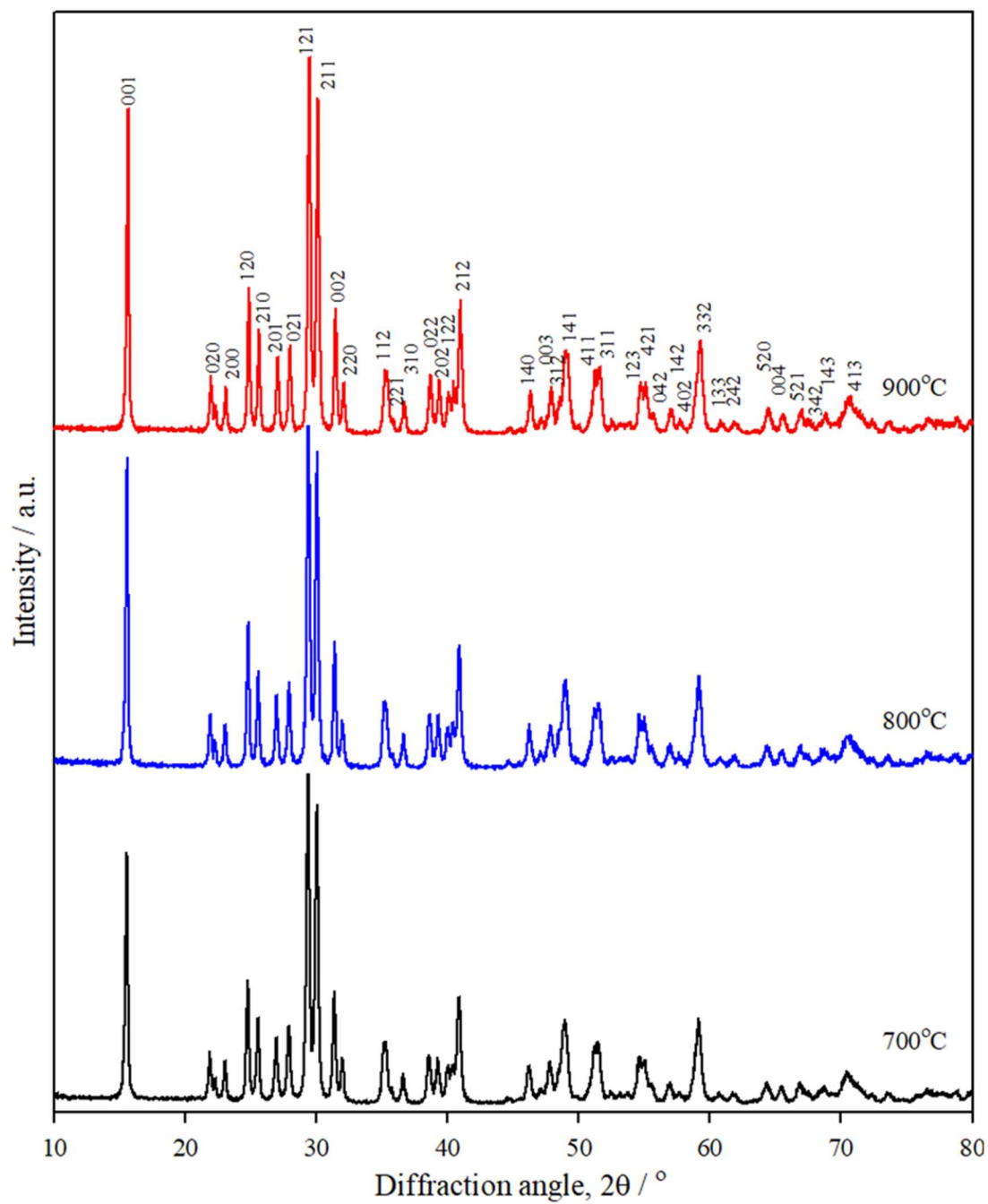
Fig. A.2.2. XRD patterns of $Bi_2Al_4O_9$ at different temperature. For clarity, the diffraction patterns are vertically shifted. The patterns show orthorhombic phase at all temperatures.
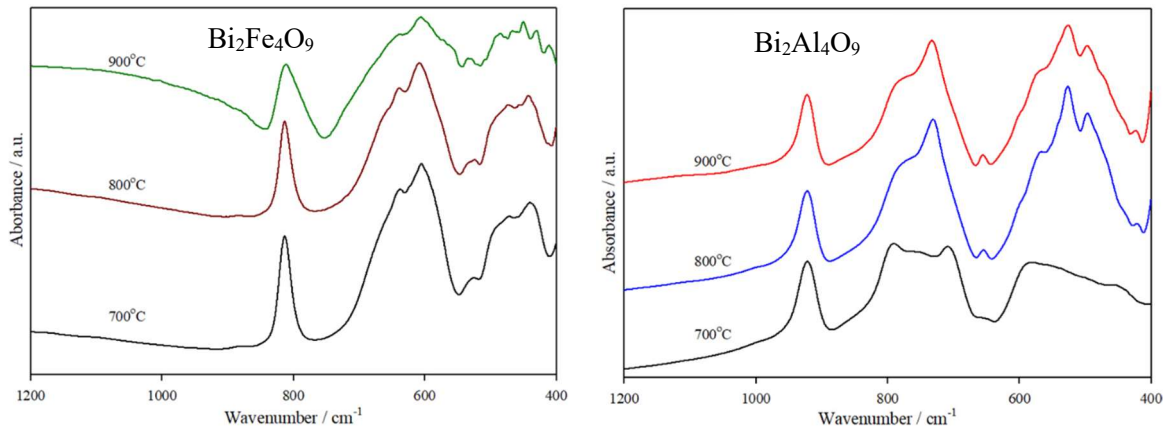
Fig. A.2.3. FT-IR spectra of $Bi_2Fe_xAl_{4-x}O_9$ (x = 4, 0) at different temperatures. For clarity, the spectra are shifted vertically. Three distinct characteristic bands for mullite are observed.
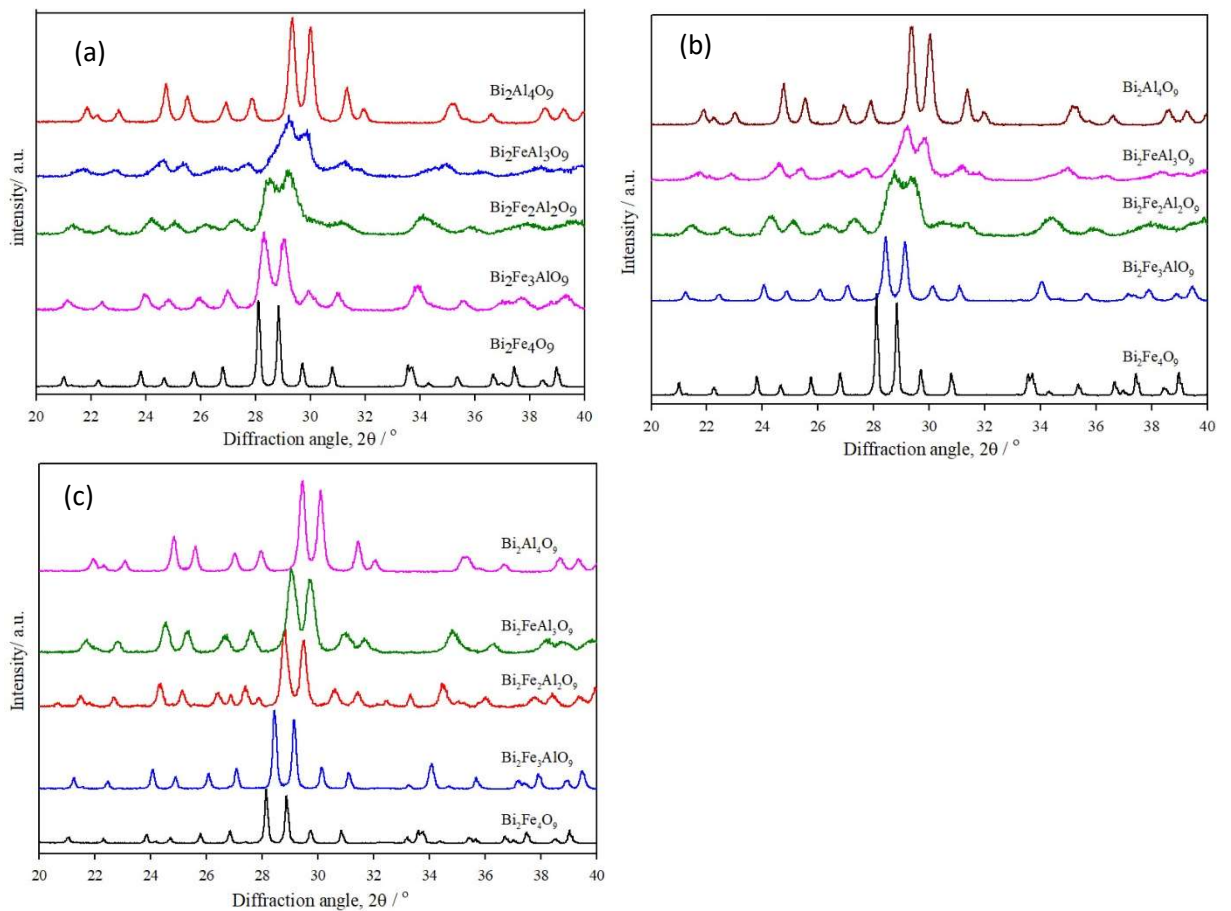
Fig. A.2.4. XRD patterns of $Bi_2Fe_xAl_{4-x}O_9$ (magnified) with different nominal compositions at (a) 700°C, (b) 800°C and (c) 900°C.

Fig. A.2.5. Optical appearances of $Bi_2M'_yM''_{4-y}O_9$ at different temperatures and compositions.
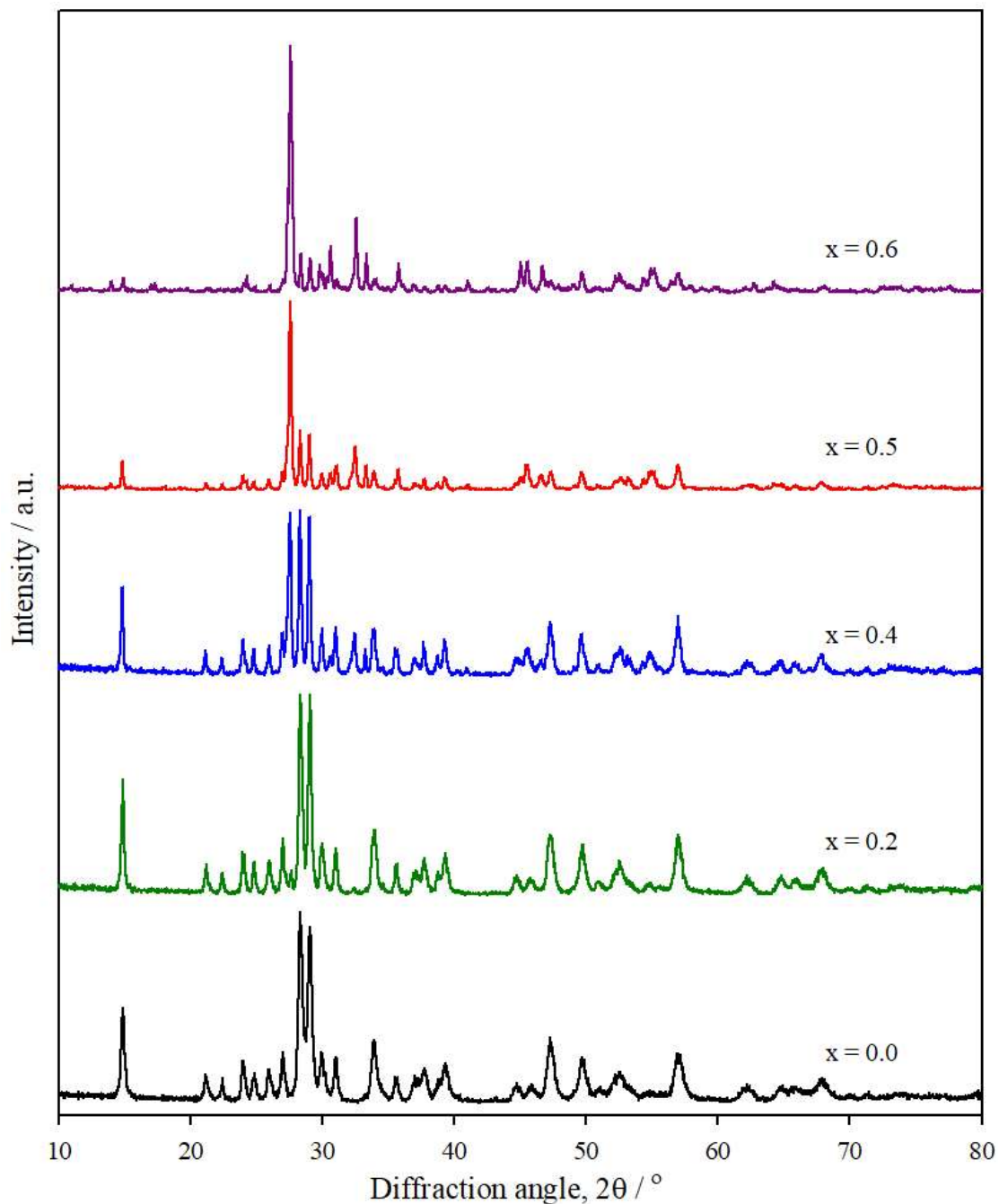
Fig. A.2.6. XRD patterns of $Bi_2Fe_3(Cr_xAl_{(1-x)})O_9$ with different nominal compositions at 700ºC. The diffraction patterns are vertically shifted, for clarity. The XRD patterns show that nominal compositions of x = 0.0 and x = 0.2 form mullite type orthorhombic phase.
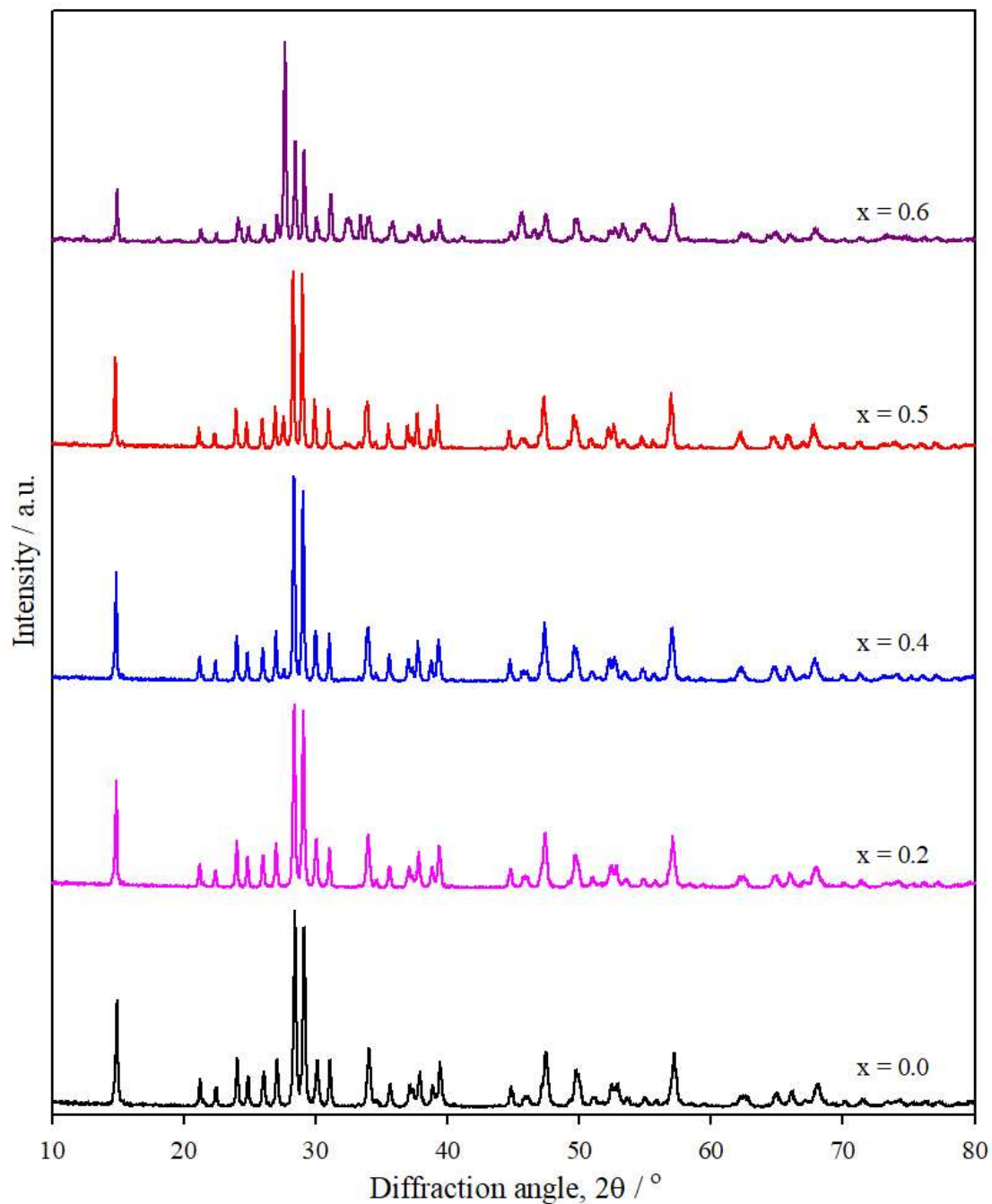
Fig. A.2.7. XRD patterns of $Bi_2Fe_3(Cr_xAl_{(1-x)})O_9$ with different nominal compositions at 800°C. The diffraction patterns are vertically shifted, for clarity. All compositions show orthorhombic mullite-type phase except x = 0.6.

Fig. A.2.8. Photographs of $Bi_2Fe_3(Cr_xAl_{1-x})O_9$ prepared at different temperatures.
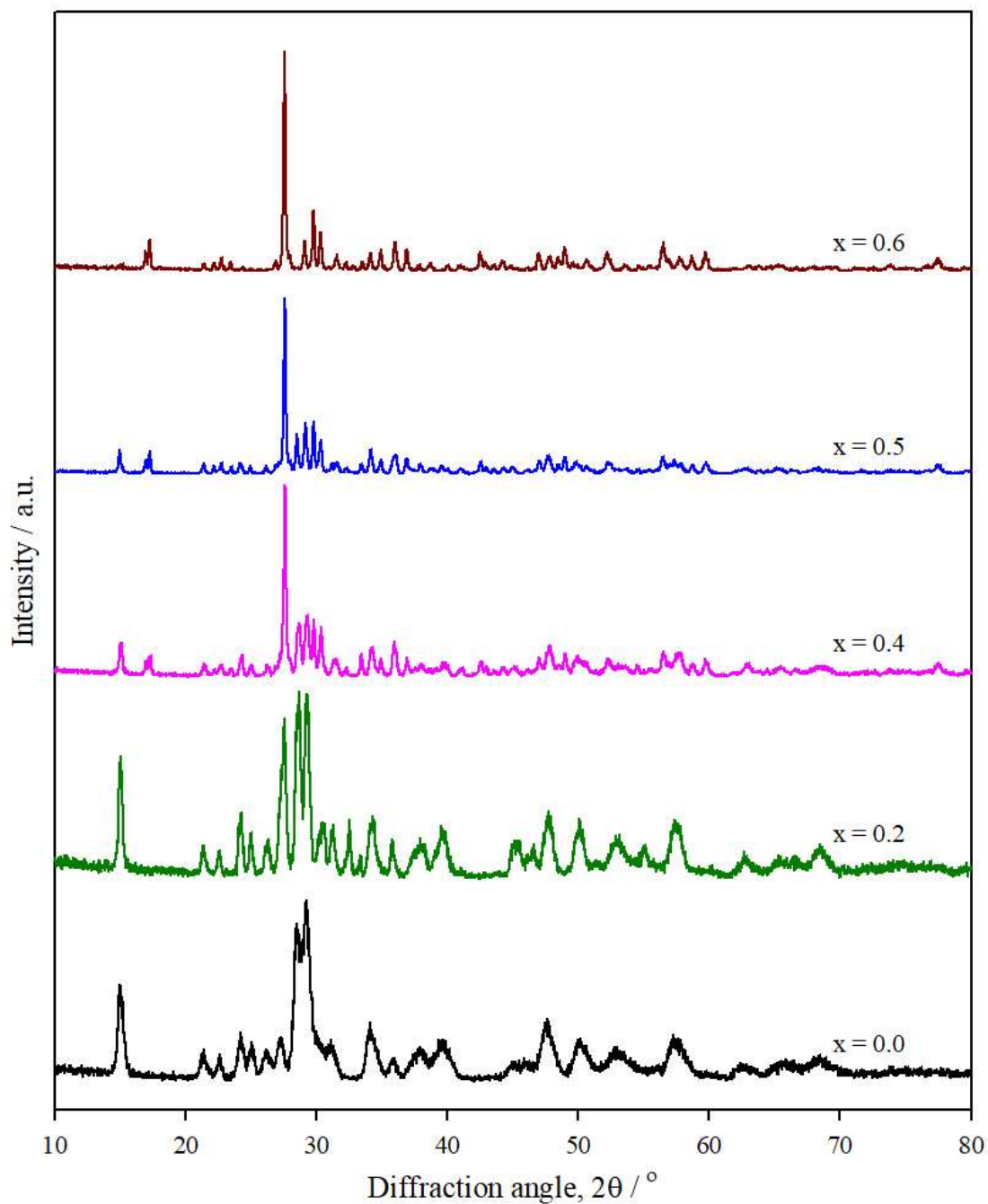
Fig. A.2.9. XRD patterns of $Bi_2Fe_2(Cr_xAl_{(1-x)})_2O_9$ with different nominal compositions at 700°C. The diffraction patterns are vertically shifted, for clarity. Only nominal composition of x = 0.0 can be indexed as mullite type orthorhombic phase at 700°C.

Fig. A.2.10. XRD patterns of $Bi_2Fe_2(Cr_xAl_{(1-x)})_2O_9$ with different nominal compositions at 800°C. The diffraction patterns are vertically shifted, for clarity. Nominal compositions of x = 0.0 and x = 0.2 form mullite type orthorhombic phase.

700ºC	800ºC	900ºC
x = 0	x = 0	x = 0
x = 0.2	x = 0.2	x = 0.2
x = 0.4	x = 0.4	x = 0.4
x = 0.5	x = 0.5	x = 0.5
x = 0.6	x = 0.6	x = 0.6
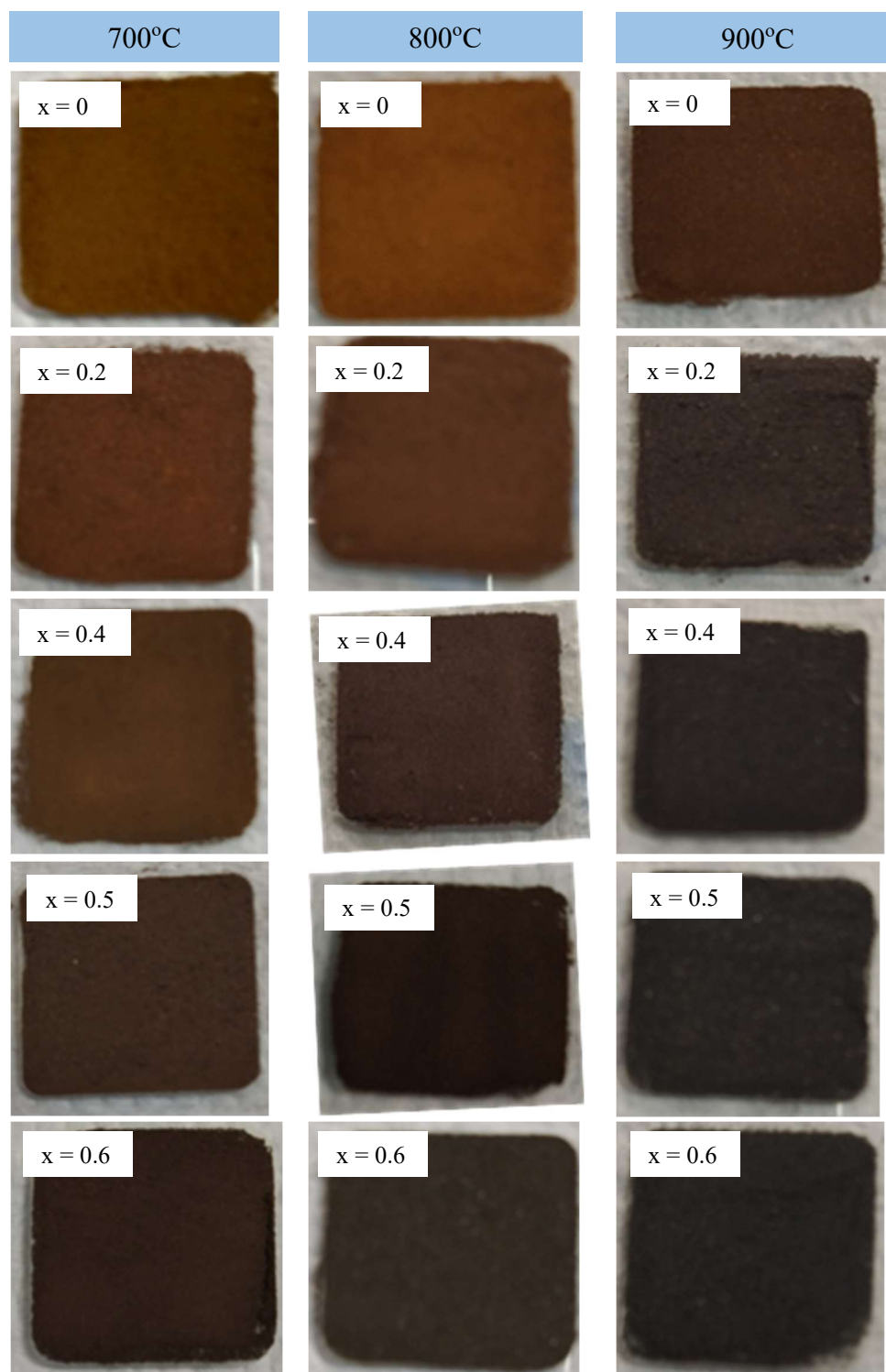
Fig. A.2.11. Optical images of $Bi_2Fe_2(Cr_xAl_{(1-x)})_2O_9$ with different compositions at different temperatures.
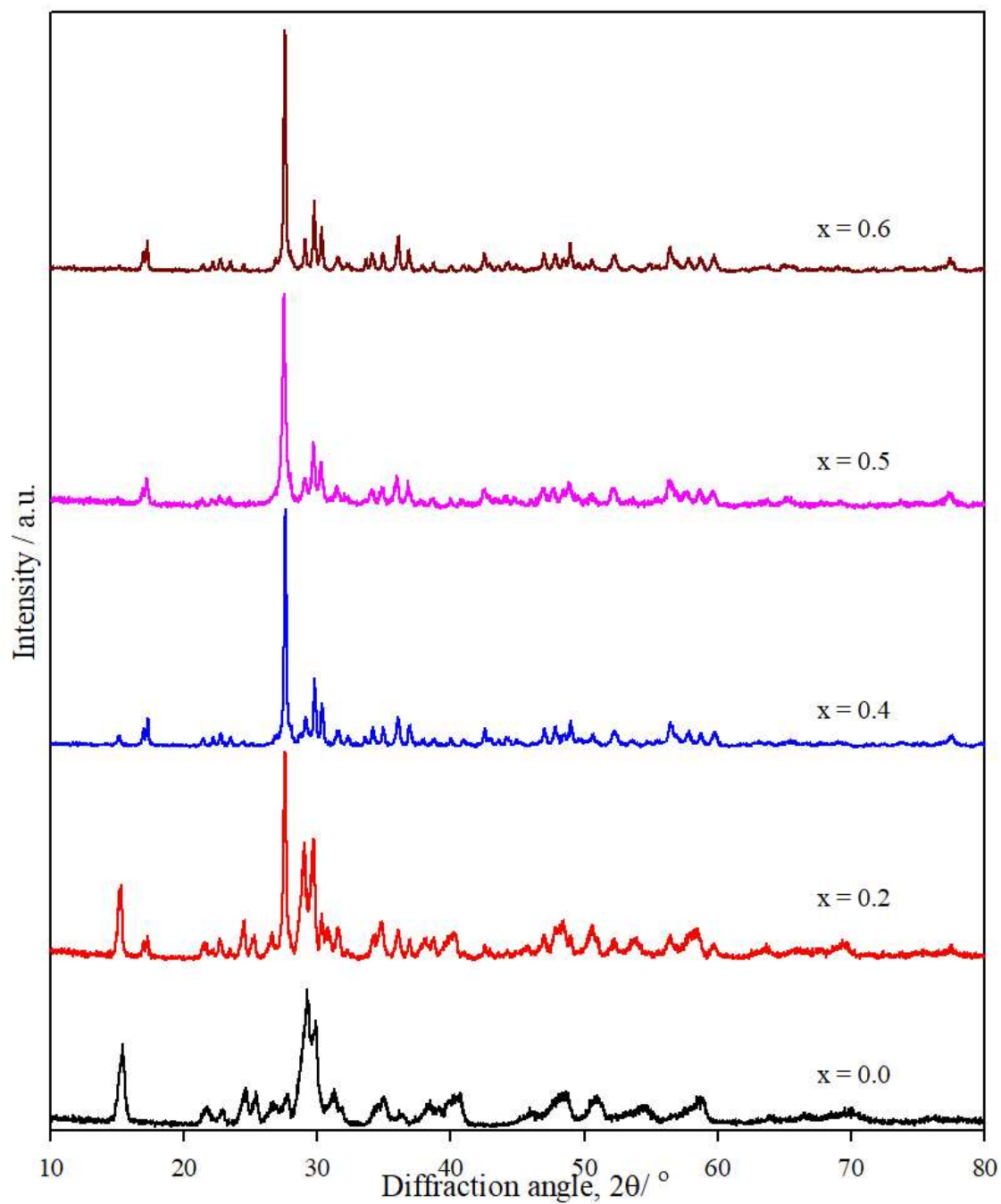
Fig. A.2.12. XRD patterns of $Bi_2Fe(Cr_xAl_{(1-x)})_3O_9$ with different nominal compositions at 700°C. The diffraction patterns are vertically shifted, for clarity. Only nominal composition of x = 0.0 can be indexed as mullite type orthorhombic phase.
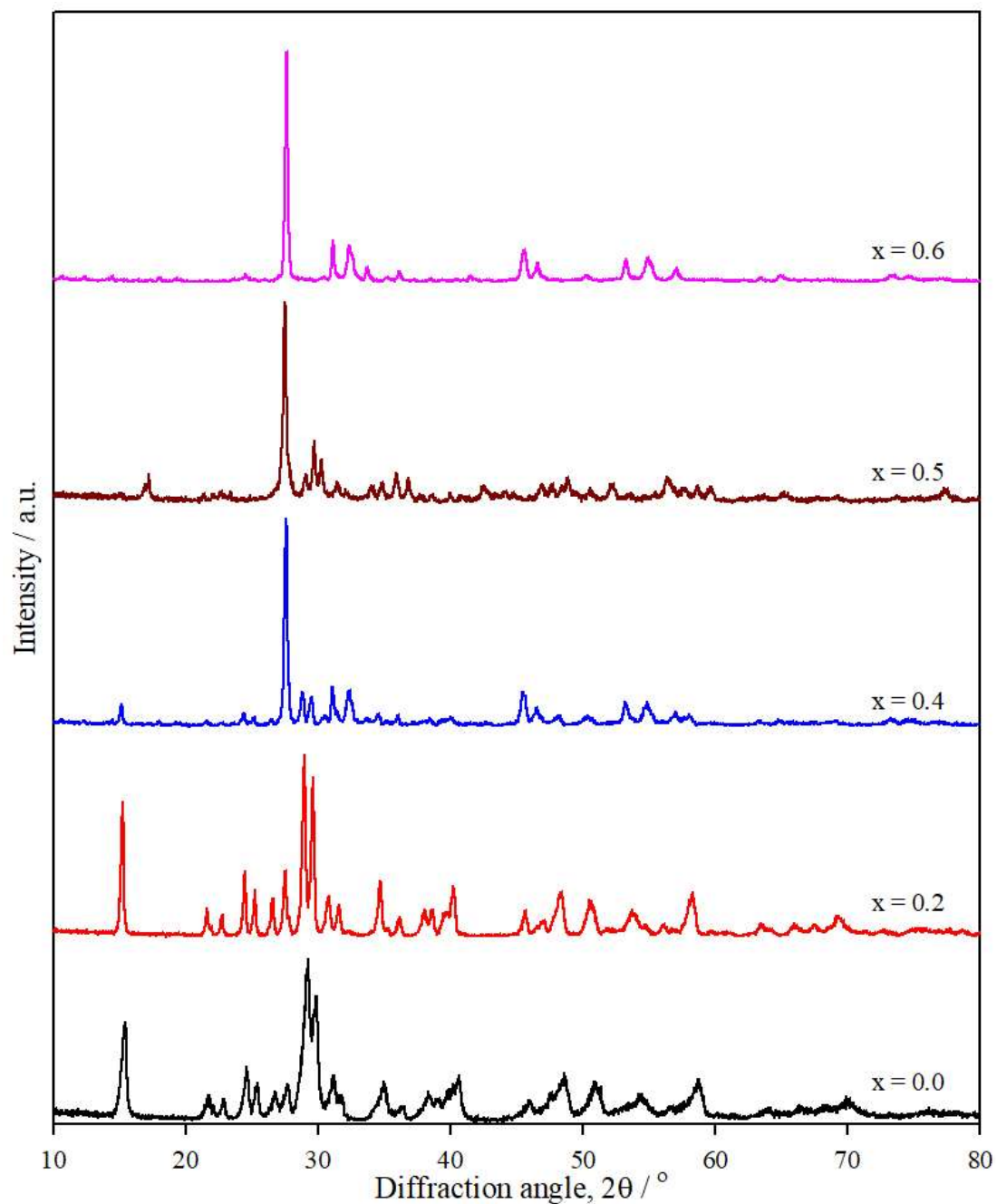
Fig. A.2.13. XRD patterns of $Bi_2Fe(Cr_xAl_{(1-x)})_3O_9$ with different nominal compositions at 800°C. The diffraction patterns are vertically shifted, for clarity. Nominal compositions of x = 0.0 and x = 0.2 form mullite type orthorhombic phase.
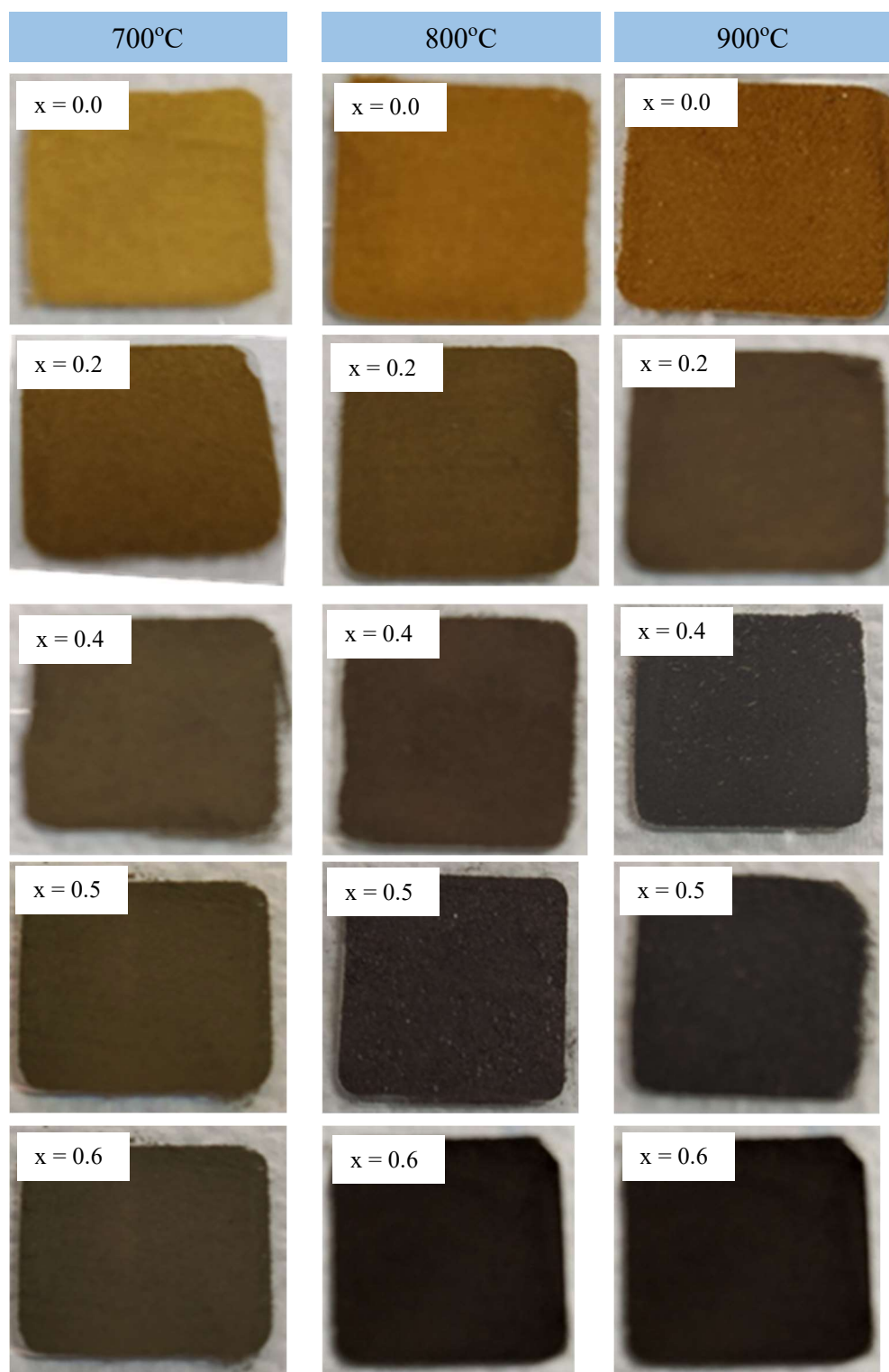
Fig. A.2.14. Optical appearances of $Bi_2Fe(Cr_xAl_{(1-x)})_3O_9$ at different temperatures and compositions.
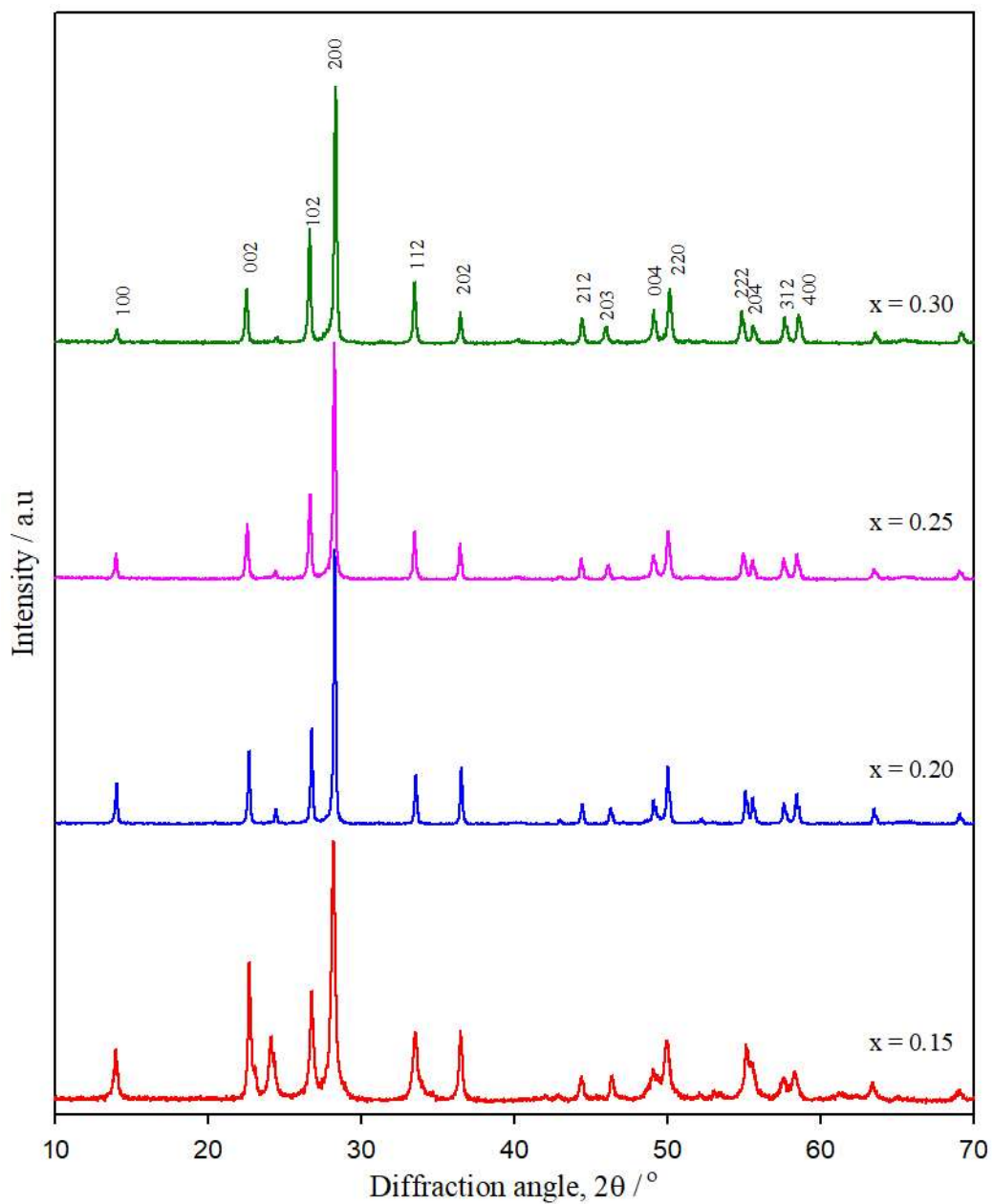
Fig. A.3.1. XRD pattern of $Cs_xV_xW_{1-x}O_3$ at 500°C. The diffraction patterns are vertically shifted, for clarity. The figure shows a pure HTB type bronze phase formed at all compositions.

Fig. A.3.2. XRD pattern of $K_xV_xW_{1-x}O_3$ at 500°C. The diffraction patterns are vertically shifted, for clarity. The figure shows a pure HTB type bronze phase formed at all compositions.
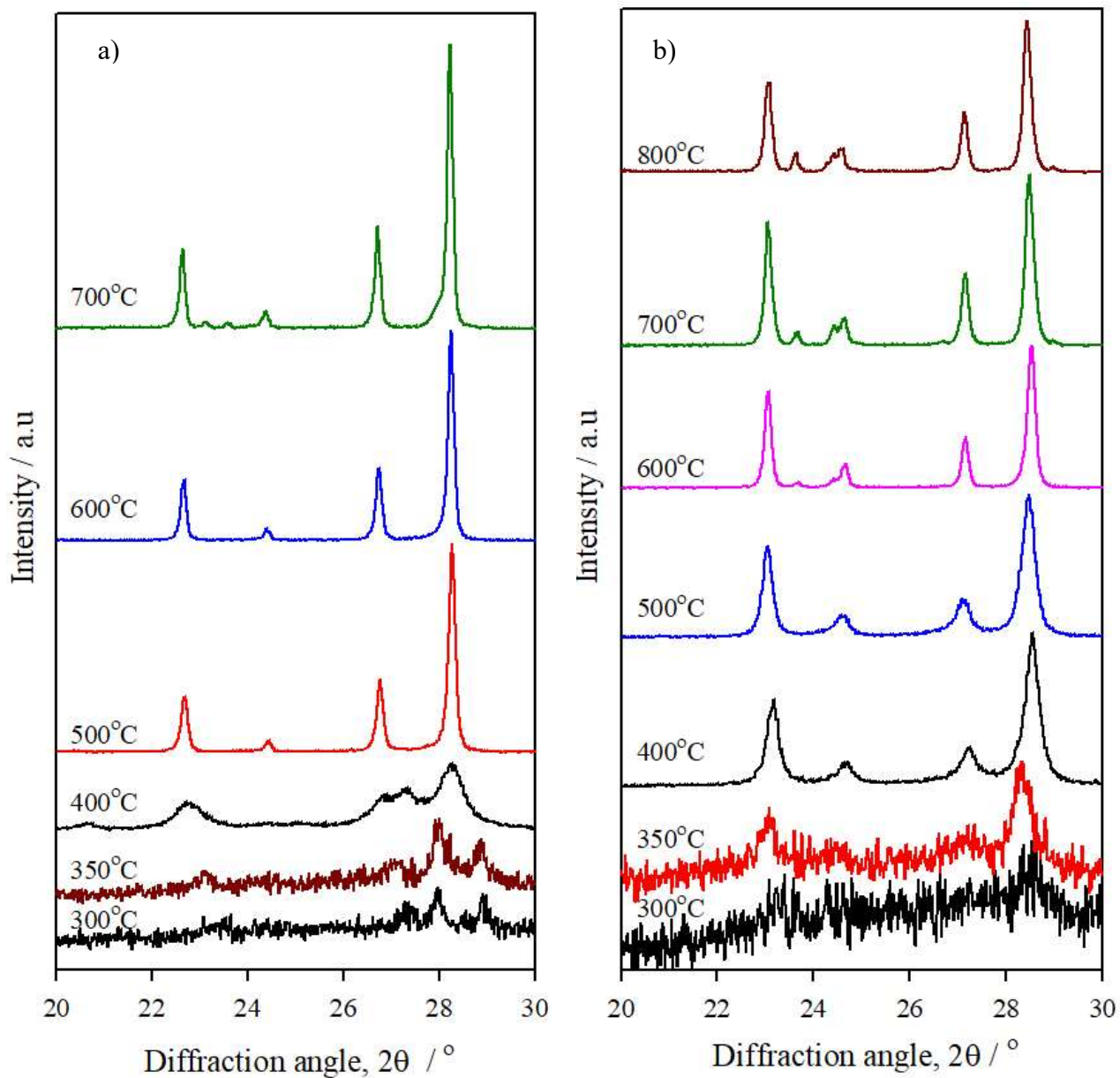
Fig. A.3.3. XRD pattern of (a) $Cs_xV_xW_{1-x}O_3$ (magnified) and (b) $Ks_xV_xW_{1-x}O_3$ (magnified) at nominal composition x = 0.20 at with djfferent temerature.The XRD patten shows the presence of an unknown second phase at higher temperature .
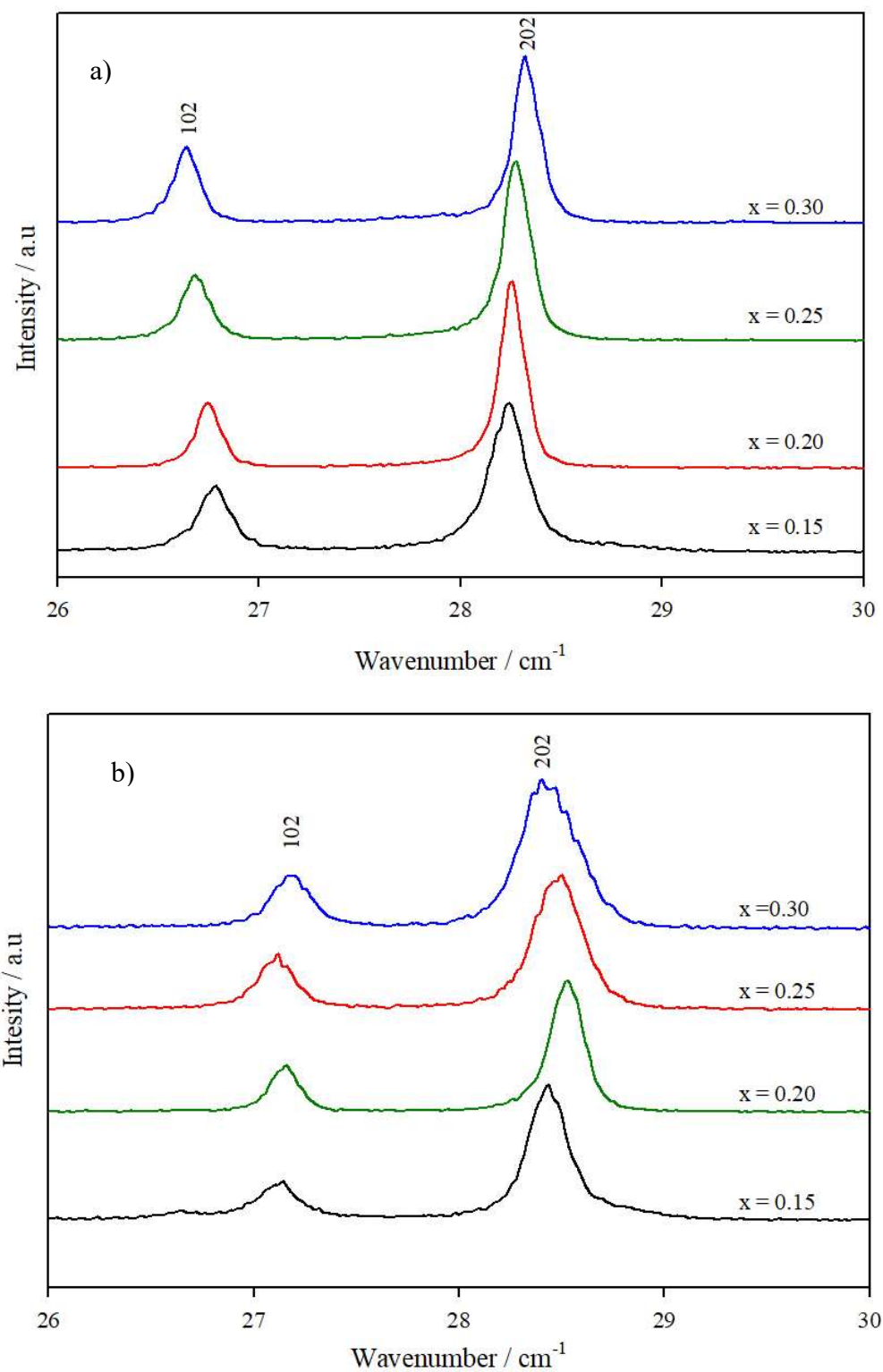
Fig. A.3.4. XRD pattern of (a) $Cs_xV_xW_{1-x}O_3$ (magnified) and (b) $Ks_xV_xW_{1-x}O_3$ (magnified) at 600°C with djfferent nominal composition. The pattern shows the systematic shifting of the peak position for 102 and 200 planes.

Table A.3.1 Crystallite sizes of $Cs_xV_xW_{1-x}O_3$ calcined at different temperatures.

Composition, x of $Cs_xV_xW_{1-x}O_3$	Temperature (°C)	Size (nm)
0.15	400	11.03
	500	45.92
	600	98.96
0.20	400	12.44
	500	147.60
	600	205.58
0.25	400	24.41
	500	92.97
	600	132.70
0.30	400	21.83
	500	100.78
	600	163.83

Table A.3.2 Crystallite sizes of $K_xV_xW_{1-x}O_3$ calcined at different temperatures.

Composition, x in $K_xV_xW_{1-x}O_3$	Temperature (°C)	Size (nm)
0.15	400	14.53
	500	44.41
	600	78.77
0.20	400	32.69
	500	38.80
	600	118.00
0.25	400	11.03
	500	39.81
	600	80.42
0.30	400	32.44
	500	33.97
	600	45.69
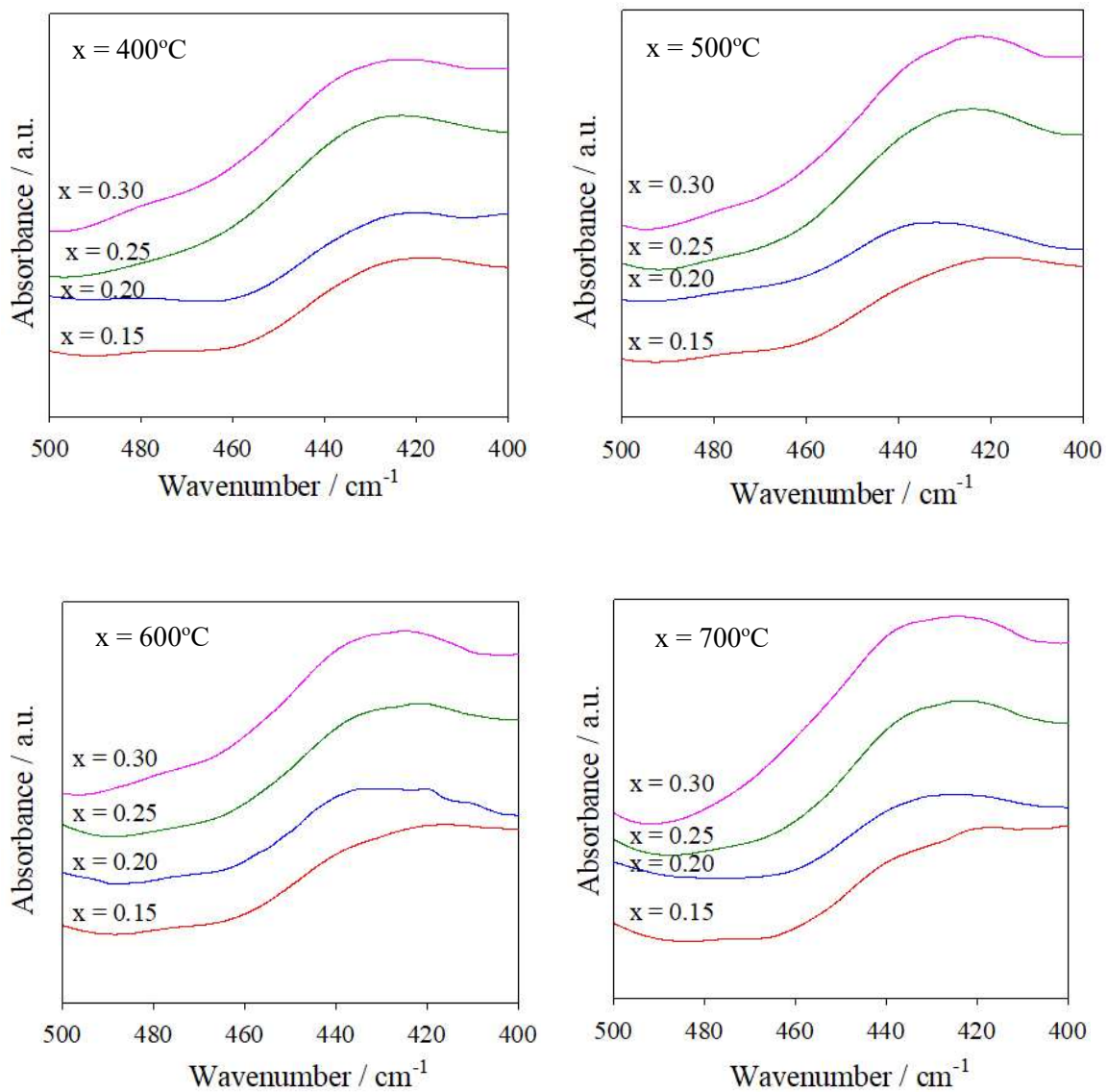
Fig. A.3.5. FT-IR spectra of $Cs_xV_xW_{1-x}O_3$ (x = 0.15 - 0.30) at different temperatures. The spectra are shifted vertically for the sake of clarity.
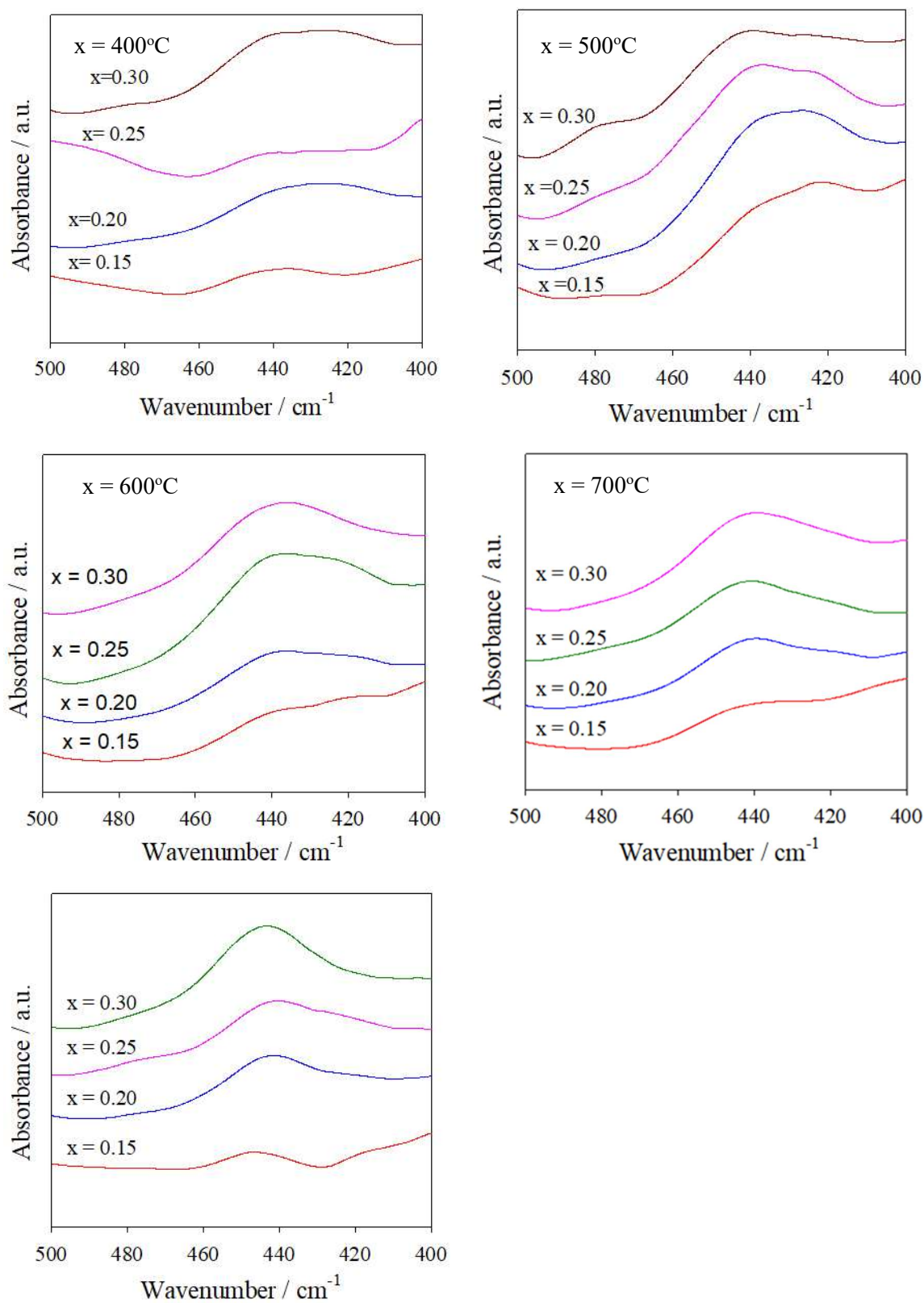
Fig. A.3.6. FT-IR spectra of $K_xV_xW_{1-x}O_3$ (x = 0.15 - 0.30) at different temperatures. The spectra are shifted vertically for the sake of clarity.
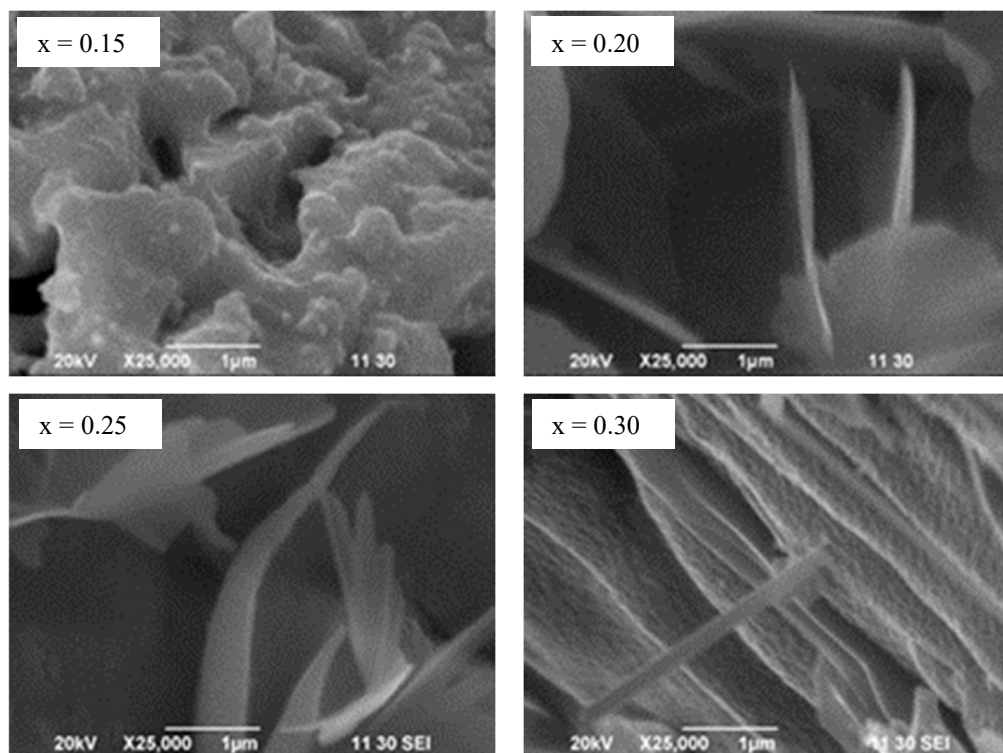
Fig. A.3.7. SEM micrographs of $Cs_xV_xW_{1-x}O_3$ at 400°C.
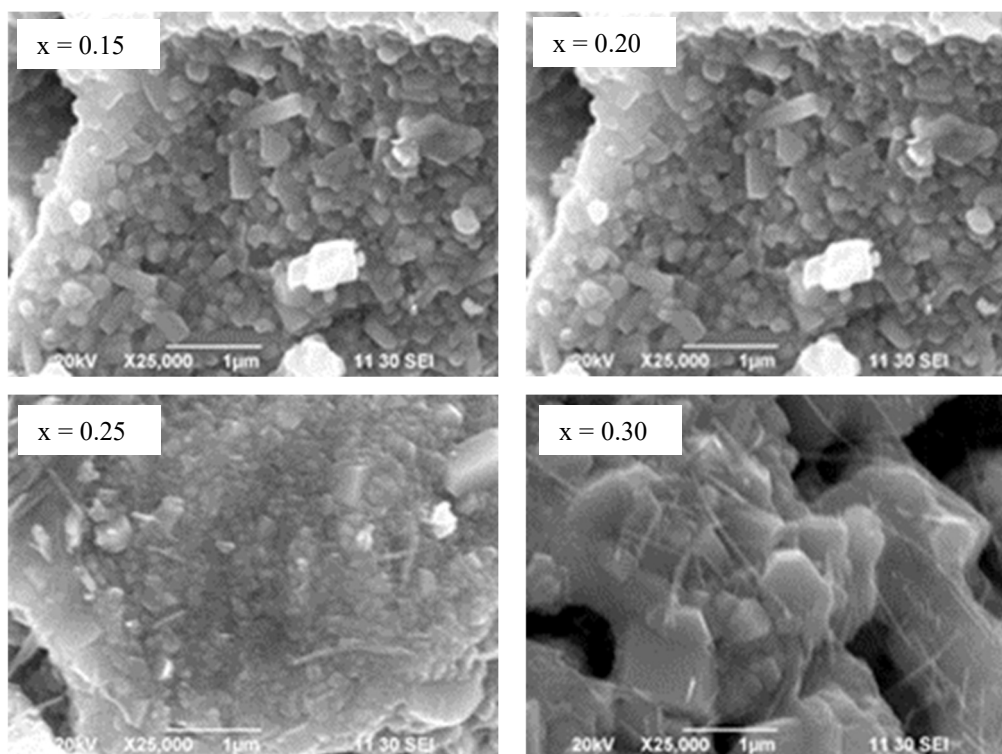
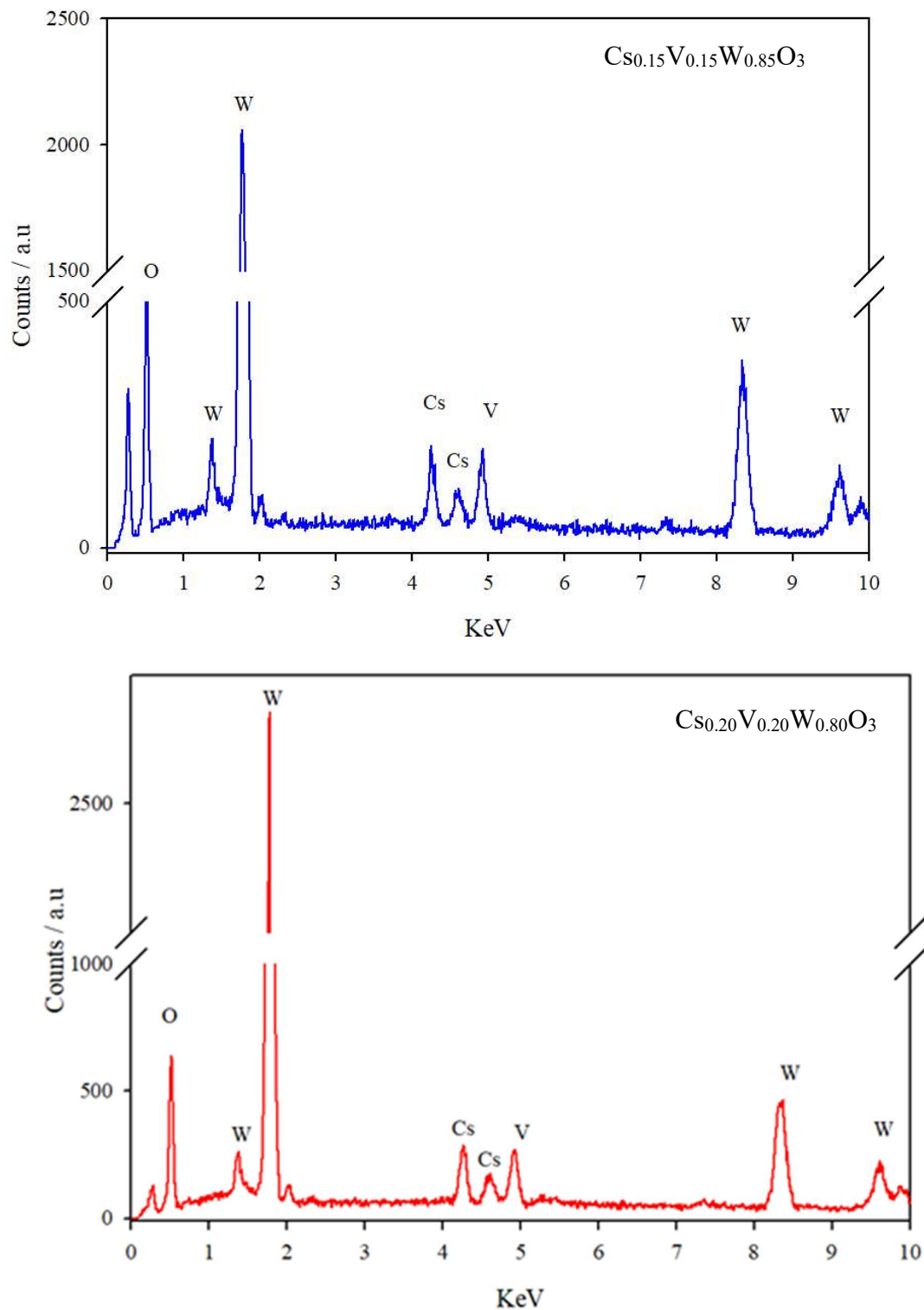Fig. A.3.8. SEM micrographs of $Cs_xV_xW_{1-x}O_3$ at 600°C.
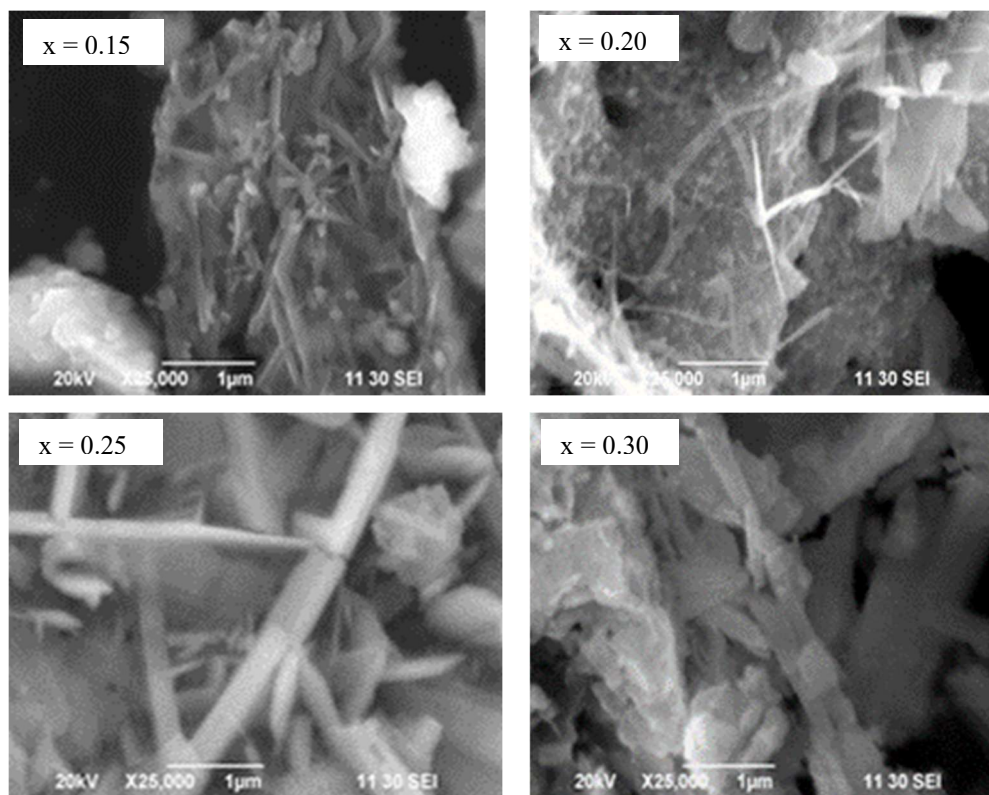
Fig. A.3.9. SEM micrographs of $K_xV_xW_{1-x}O_3$ at 400ºC.
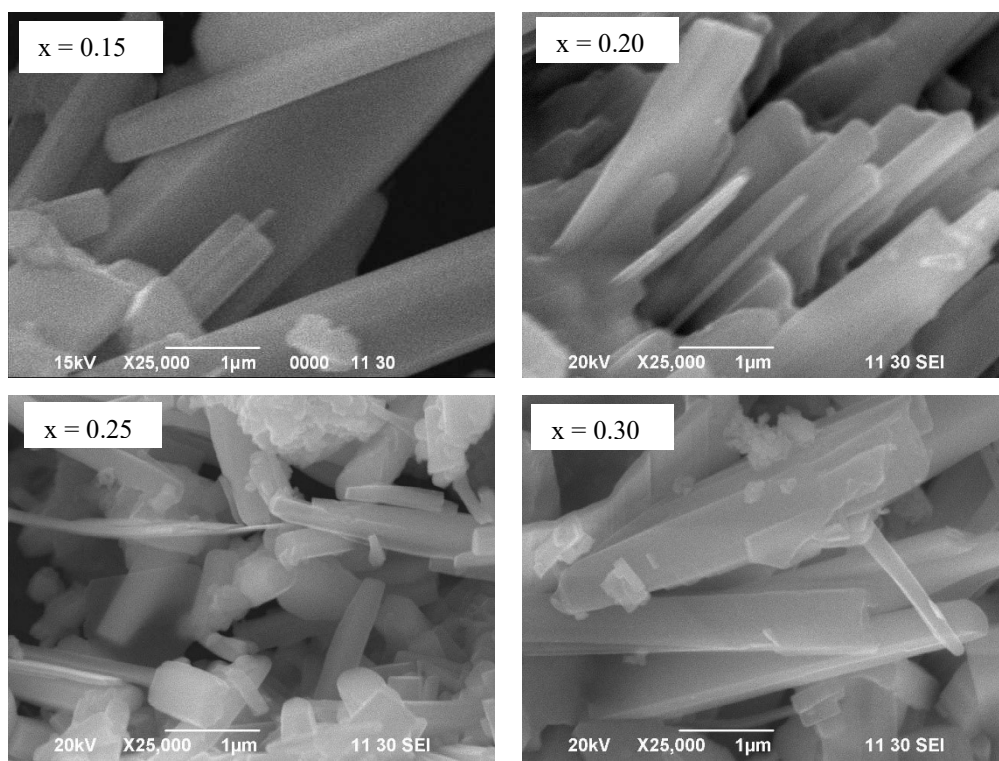
Fig. A.3.10. SEM micrographs of $K_xV_xW_{1-x}O_3$ at 600ºC.

Fig. A.3.11. EDX spectrum of $Cs_xV_xW_{1-x}O_3$ for nominal composition at 500°C. The EDX spectrum show the presence of O, Cs, V and W are present, no foreign element found.
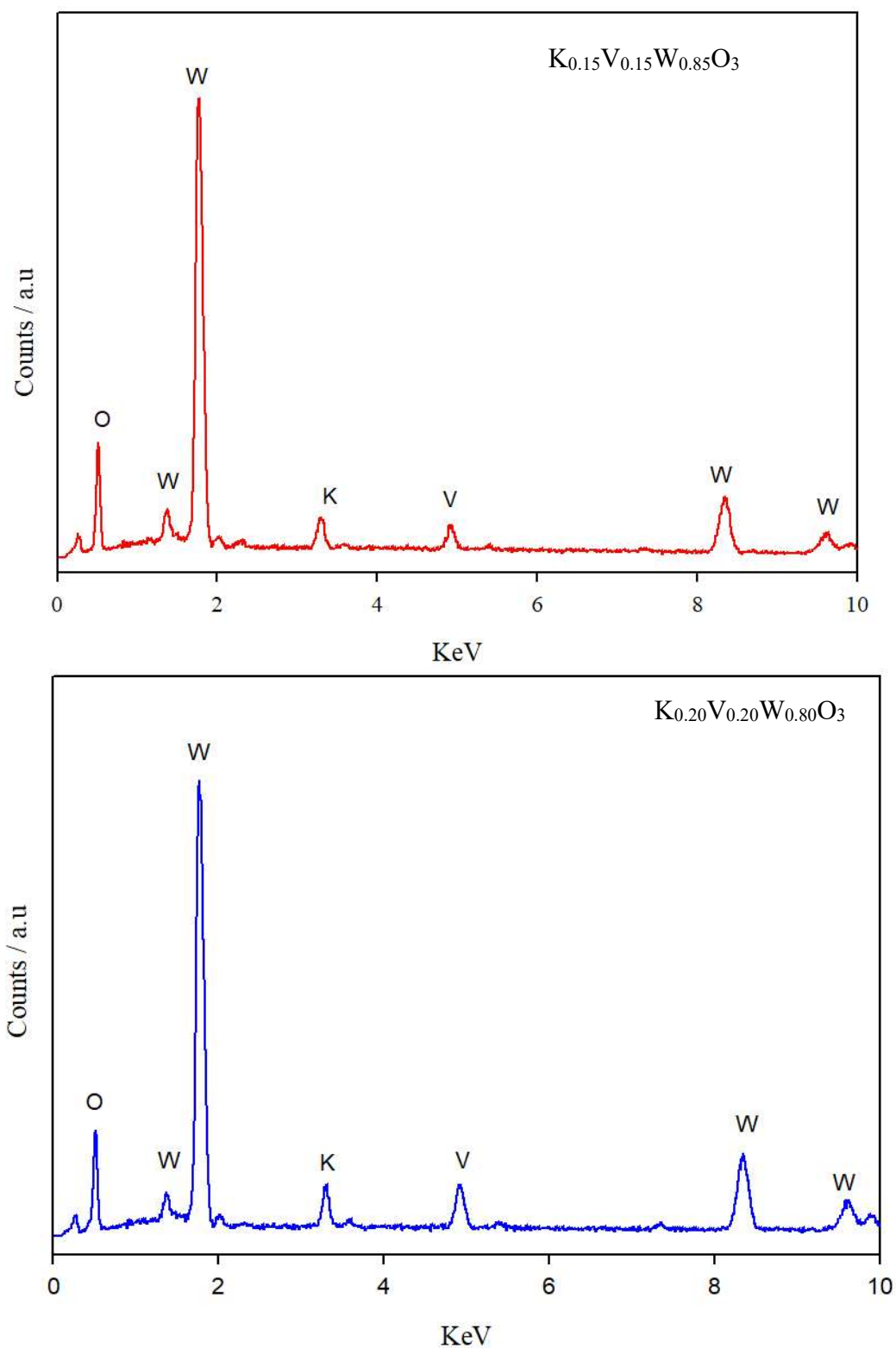
Fig. A.3.12. EDX spectrum of $K_xV_xW_{1-x}O_3$. EDX spectrum show the presence of O, K, V and W are present, no foreign element found.
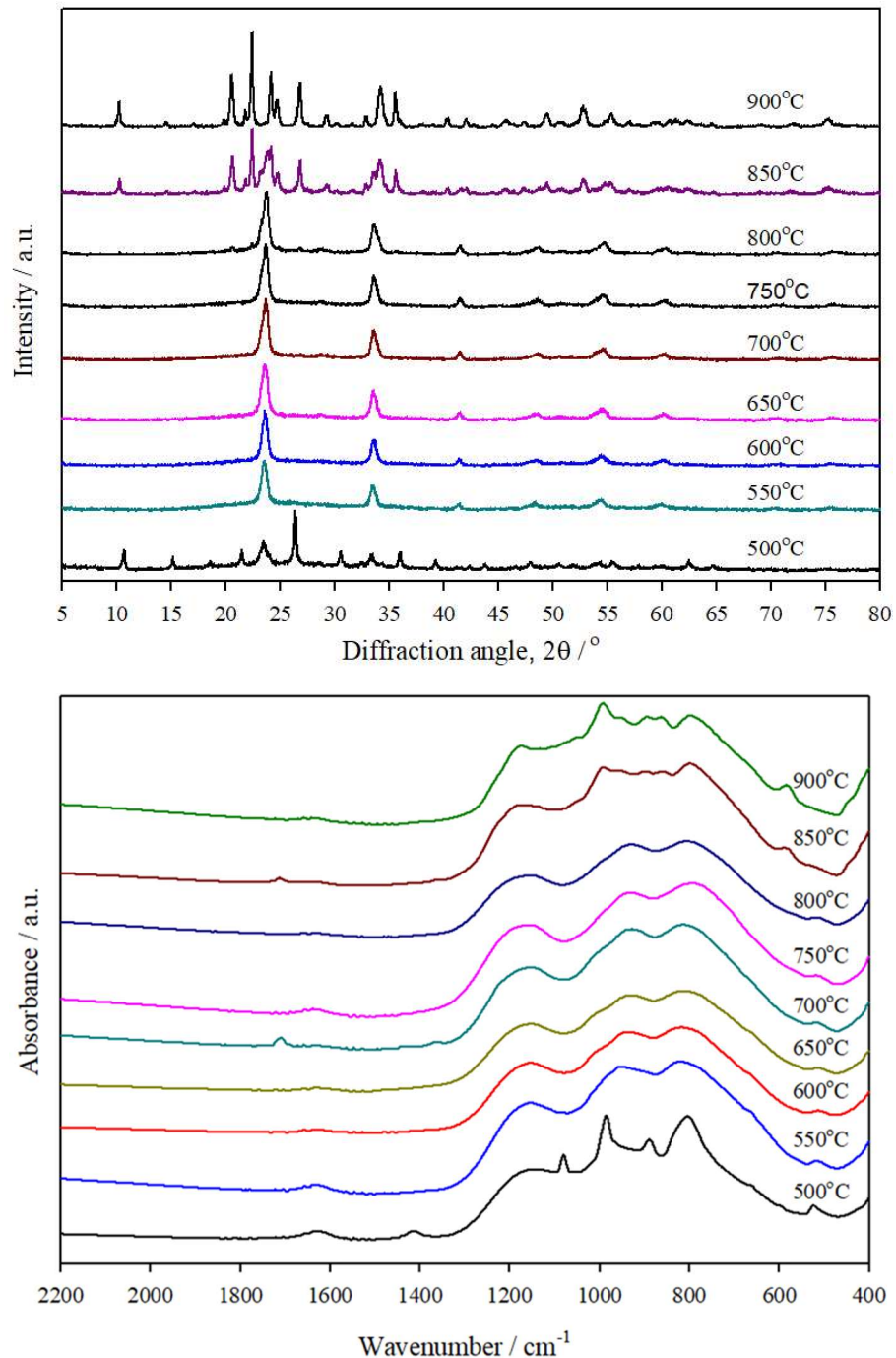
Fig. A.4.1. XRD pattern and FT-IR spectra of $Cr_{4/3-x}Fe_xW_{20/3}O_{24}(PO_2)_4$ with nominal composition x = 0, at different temperatures. The XRD pattern shows the patterns are cubic type crystalline phases up to 750°C. At 800°C, some characteristic lines related to the orthorhombic phase were observed in addition to the cubic phase, and at 850°C, the mixture completely turns to the pure orthorhombic phase of $Cr_{4/3}W_{20/3}O_{24}(PO_2)_4$. The FT-IR spectra completely agree with XRD data and other compositions follow a similar trend.
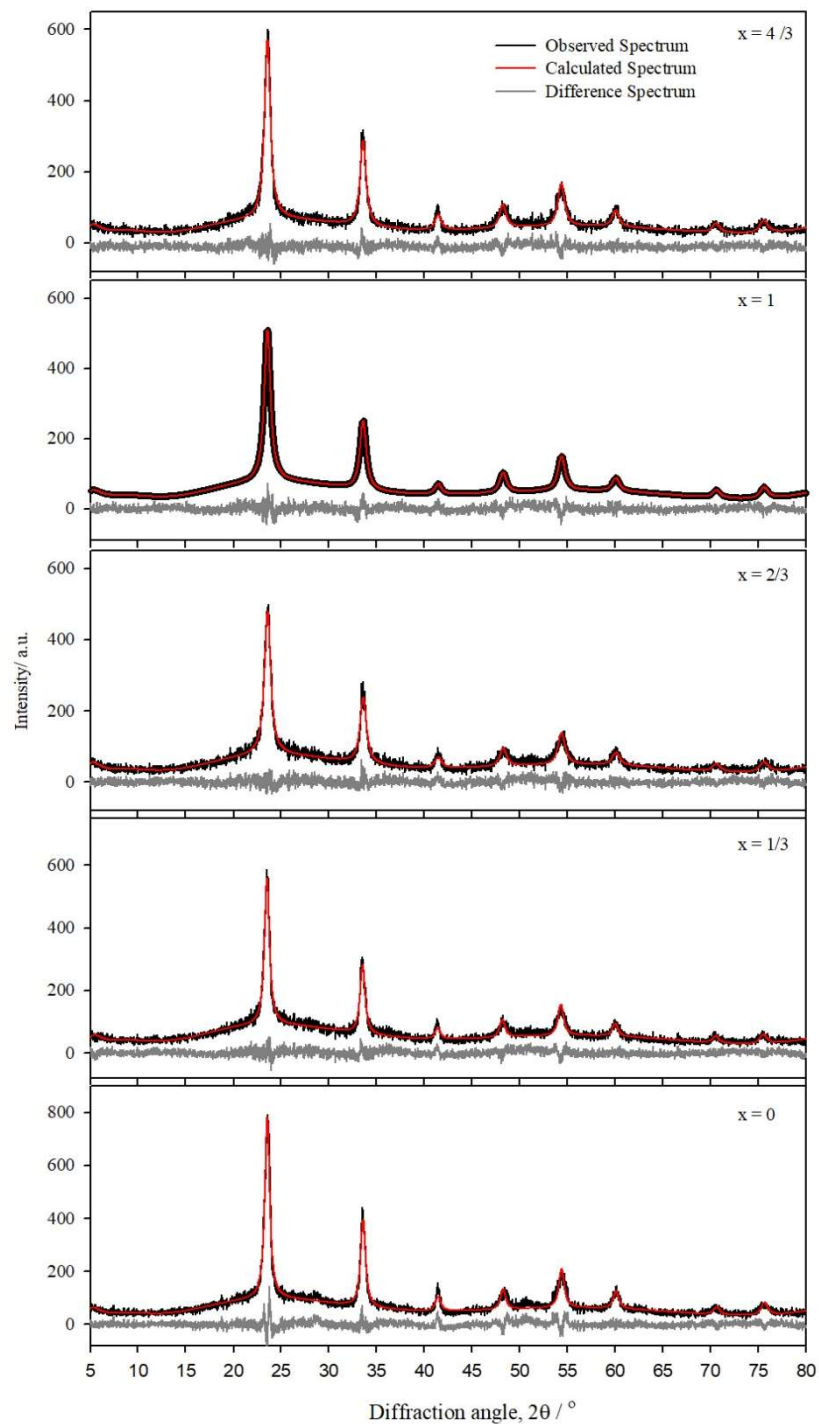
Fig. A.4.2. Rietveld refinements fit of the $Cr_{4/3-x}Fe_xW_{20/3}O_{24}(PO_2)_4$ series samples prepared at 650°C. The black spectrum represents the observed/measured spectrum, and the red spectrum represents calculated data. The curve below the spectrum represents the difference spectrum.

Table A.4.1 Crystallite sizes of $Cr_{4/3-x}Fe_xW_{20/3}O_{24}(PO_2)_4$ (x = 0, 1/3, 2/3, 1, 4/3) at different compositions and temperatures.

Composition of $Cr_{4/3-x}Fe_xW_{20/3}O_{24}(PO_2)_4$	Temperature (°C)	Size (nm)
x = 0	550	14.57
	600	15.89
	650	14.00
	700	14.67
	750	15.20
x = 1/3	550	16.06
	600	14.92
	650	14.70
	700	15.84
	750	15.20
x = 2/3	550	12.04
	600	12.46
	650	12.14
	700	11.63
	750	13.97
x = 1	550	12.05
	600	12.46
	650	12.14
	700	11.63
	750	13.97
x = 4/3	550	12.11
	600	12.11
	650	12.50
	700	14.40
	750	-

x = 0

20kV   X25,000   1µm   11 30

x = 1/3

20kV   X25,000   1µm   11 30

x = 2/3

20kV   X25,000   1µm   11 30

x = 1

20kV   X25,000   1µm   11 30

x = 4/3

20kV   X25,000   1µm   11 30
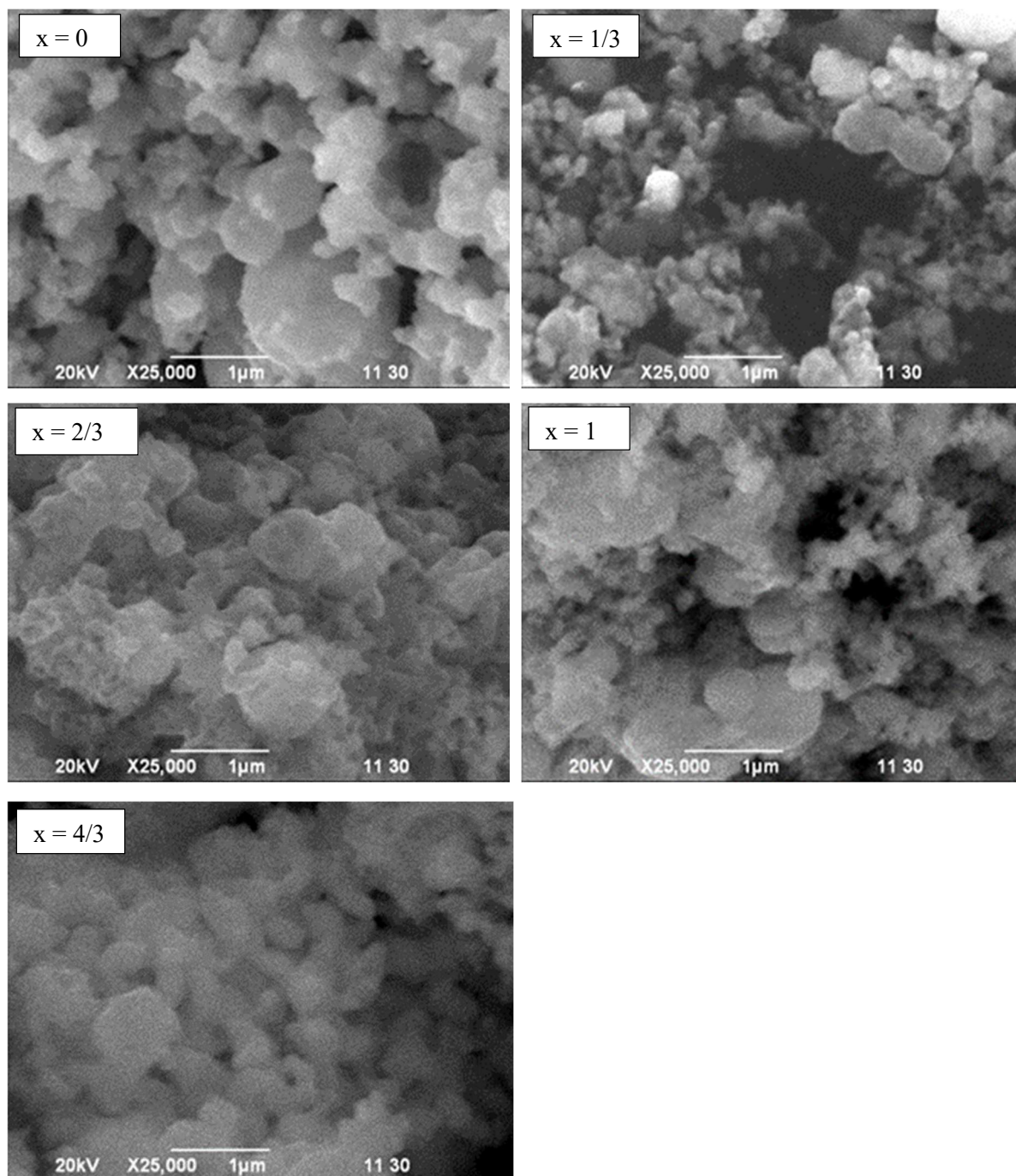
Fig. A.4.3. SEM images of $Cr_{4/3-x}Fe_xW_{20/3}O_{24}(PO_2)_4$ with different nominal compositions at 600^oC.
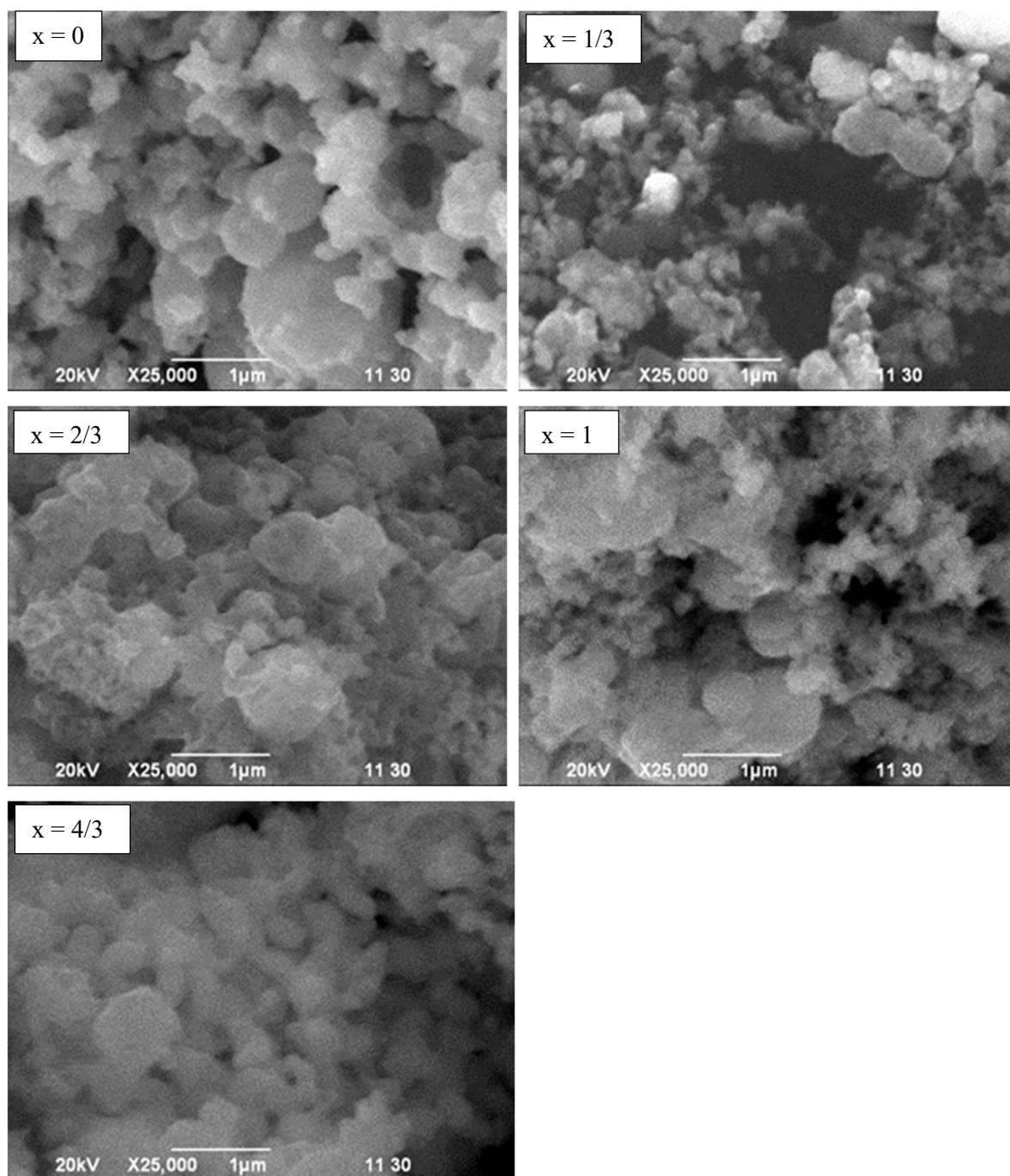
Fig. A.4.4. SEM images of $Cr_{4/3-x}Fe_xW_{20/3}O_{24}(PO_2)_4$ with different nominal compositions at 700°C.
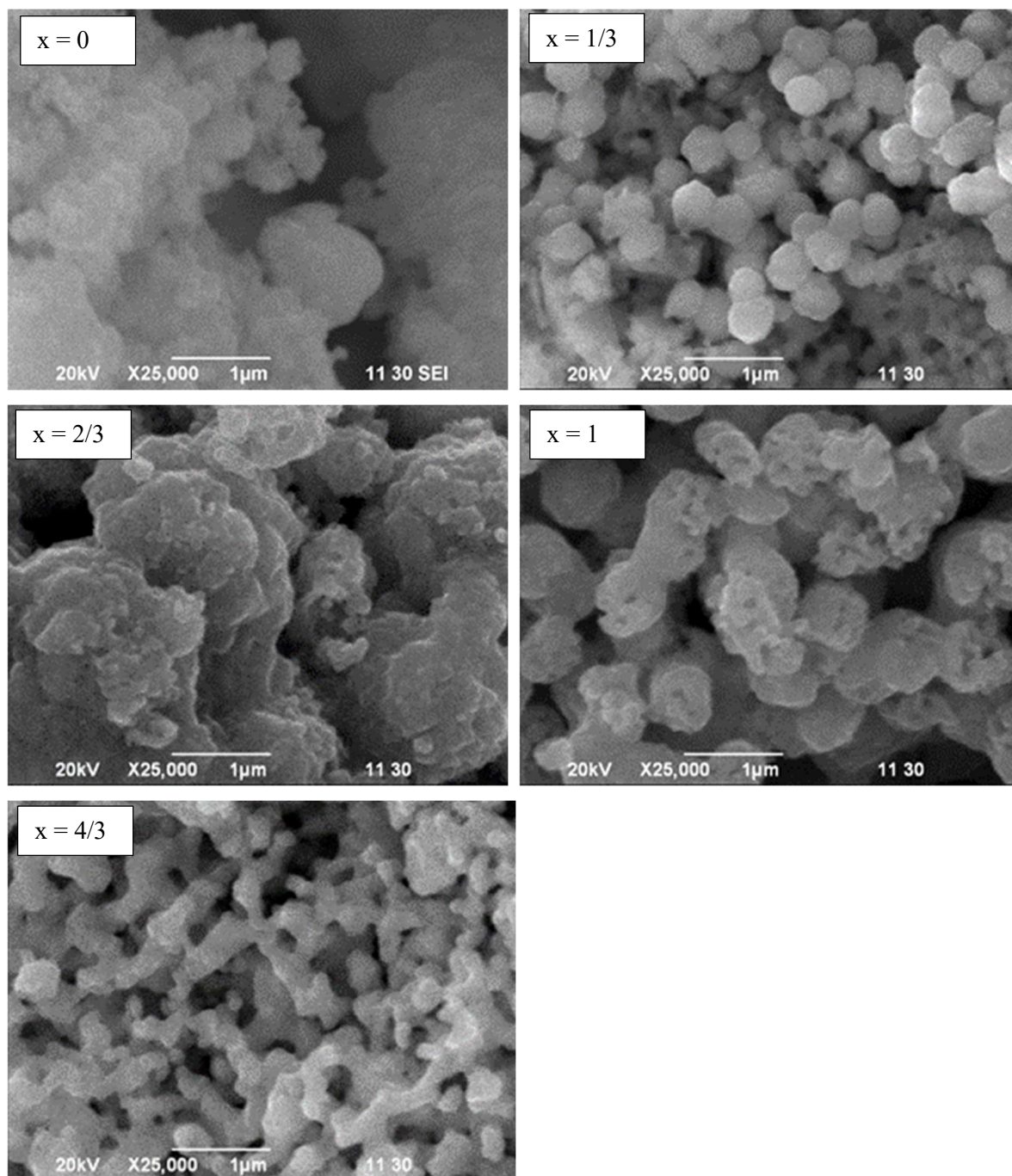
Fig. A.4.5. SEM images of $Cr_{4/3-x}Fe_xW_{20/3}O_{24}(PO_2)_4$ with different nominal compositions at 800°C.
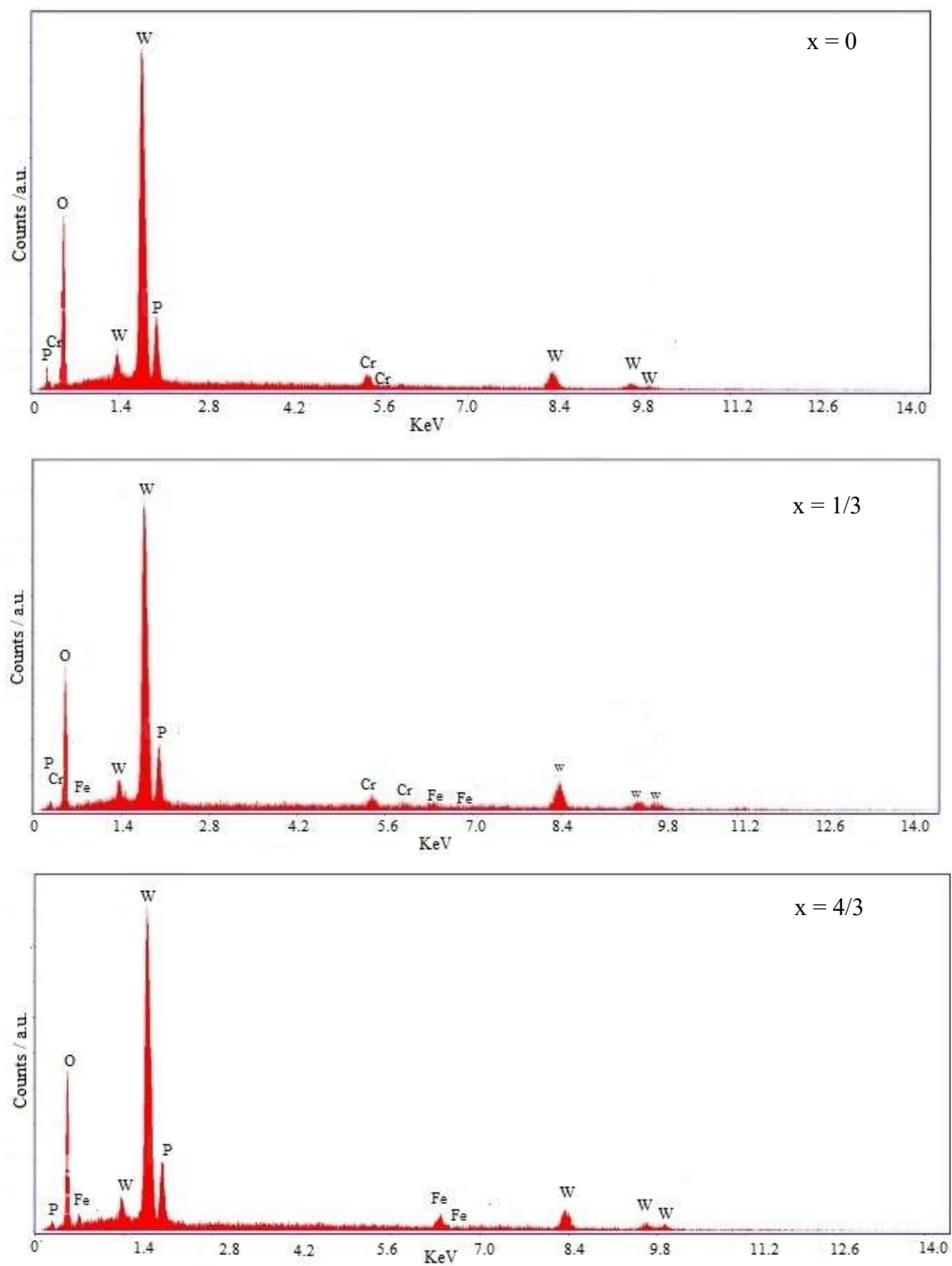
Fig. A.4.6. EDX spectrum of $Cr_{4/3-x}Fe_xW_{20/3}O_{24}(PO_2)_4$ with different nominal compositions at 900°C.

Table A.4.2 Crystallite sizes of $Cr_{4/3-x}Al_xW_{20/3}O_{24}(PO_2)_4$ at different compositions and temperatures.

Composition of $Cr_{4/3-x}Al_xW_{20/3}O_{24}(PO_2)_4$	Temperature (ºC)	Size (nm)
x = 0	550	14.57
	600	15.89
	650	14.00
	700	14.67
	750	15.20
x = 1/3	550	12.91
	600	11.22
	650	12.10
	700	12.29
	750	13.03
x = 2/3	550	16.91
	600	16.04
	650	15.28
	700	17.17
	750	16.06
x = 1	550	16.91
	600	16.04
	650	15.28
	700	17.18
	750	16.07
x = 4/3	550	9.19
	600	14.69
	650	14.30
	700	14.11
	750	13.70
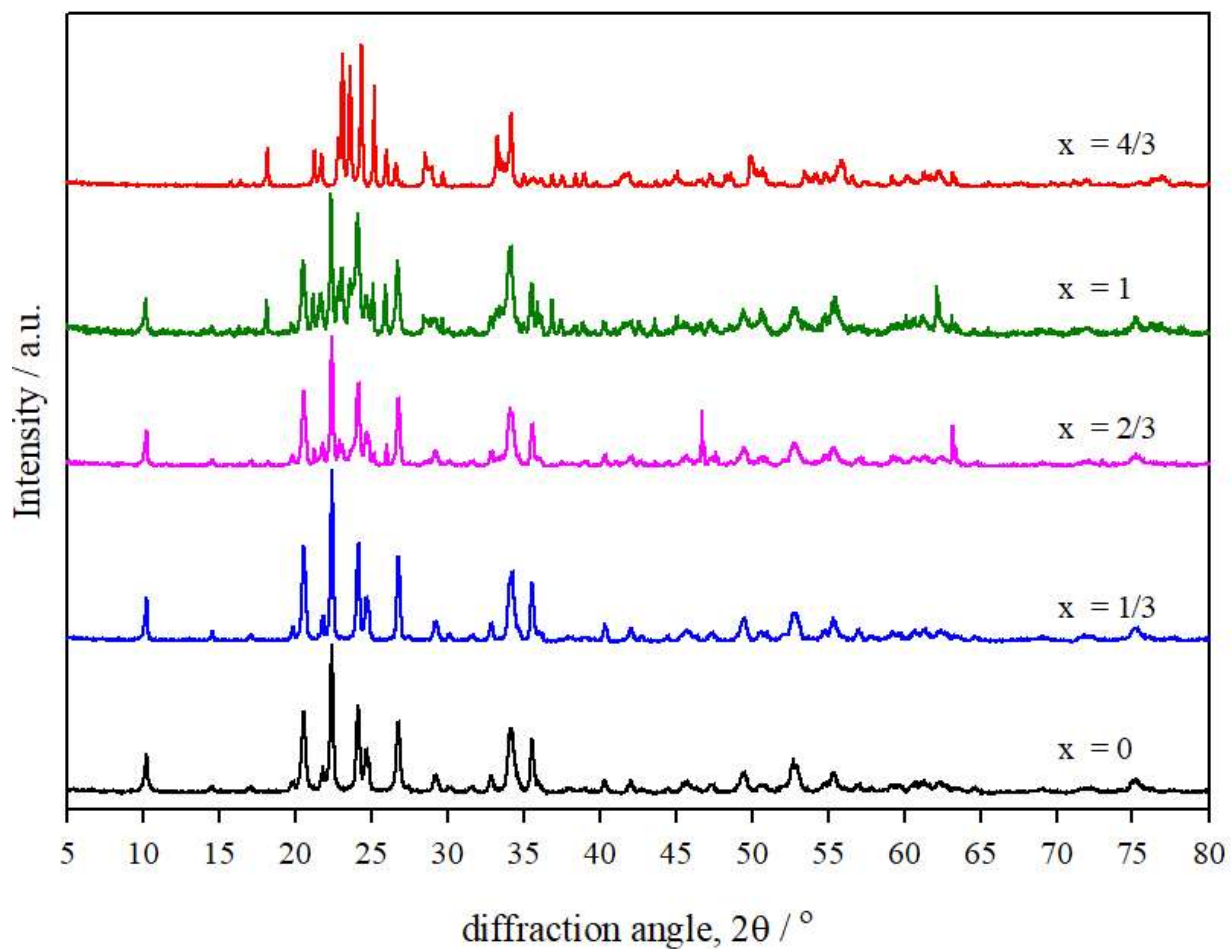
Fig. A.4.7. XRD pattern of $Cr_{4/3-x}Al_xW_{20/3}O_{24}(PO_2)_4$ with different nominal compositions at 900°C. At nominal composition x = 2/3, 1 and x = 4/3, additional phases are observed, which are not related to the orthorhombic phase.

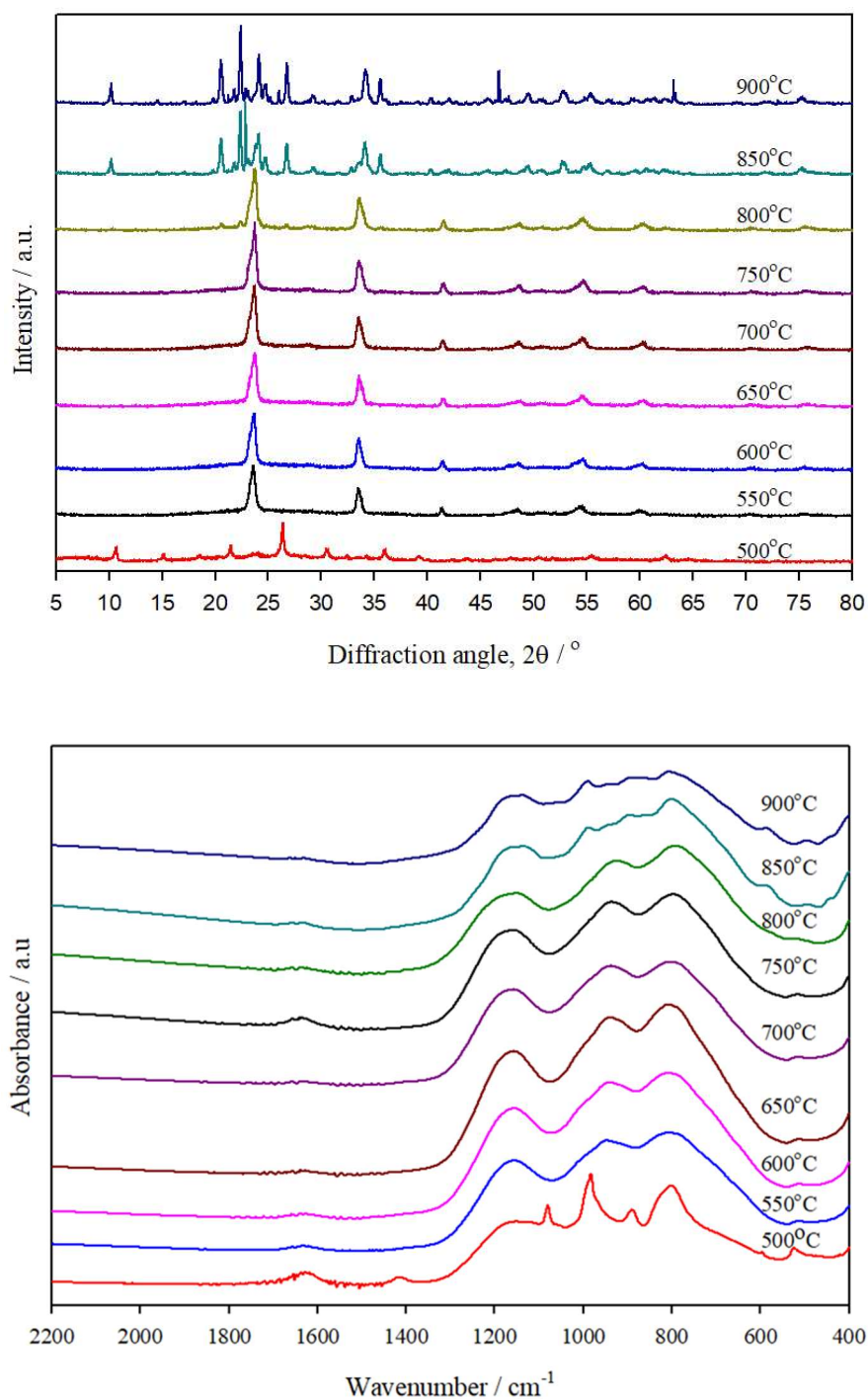Fig. A.4.8. XRD pattern and FT-IR spectra of $Cr_{4/3-x}Al_xW_{20/3}O_{24}(PO_2)_4$ with nominal composition x = 2/3, at different temperatures. The XRD pattern shows the patterns are cubic type crystalline phase up to 750°C. At 800°C, some additional phases were observed in addition to the cubic phase, i.e., $2\theta \approx 23.06$, which are not related to the orthorhombic phase. The FT-IR spectra completely agree with the XRD data.
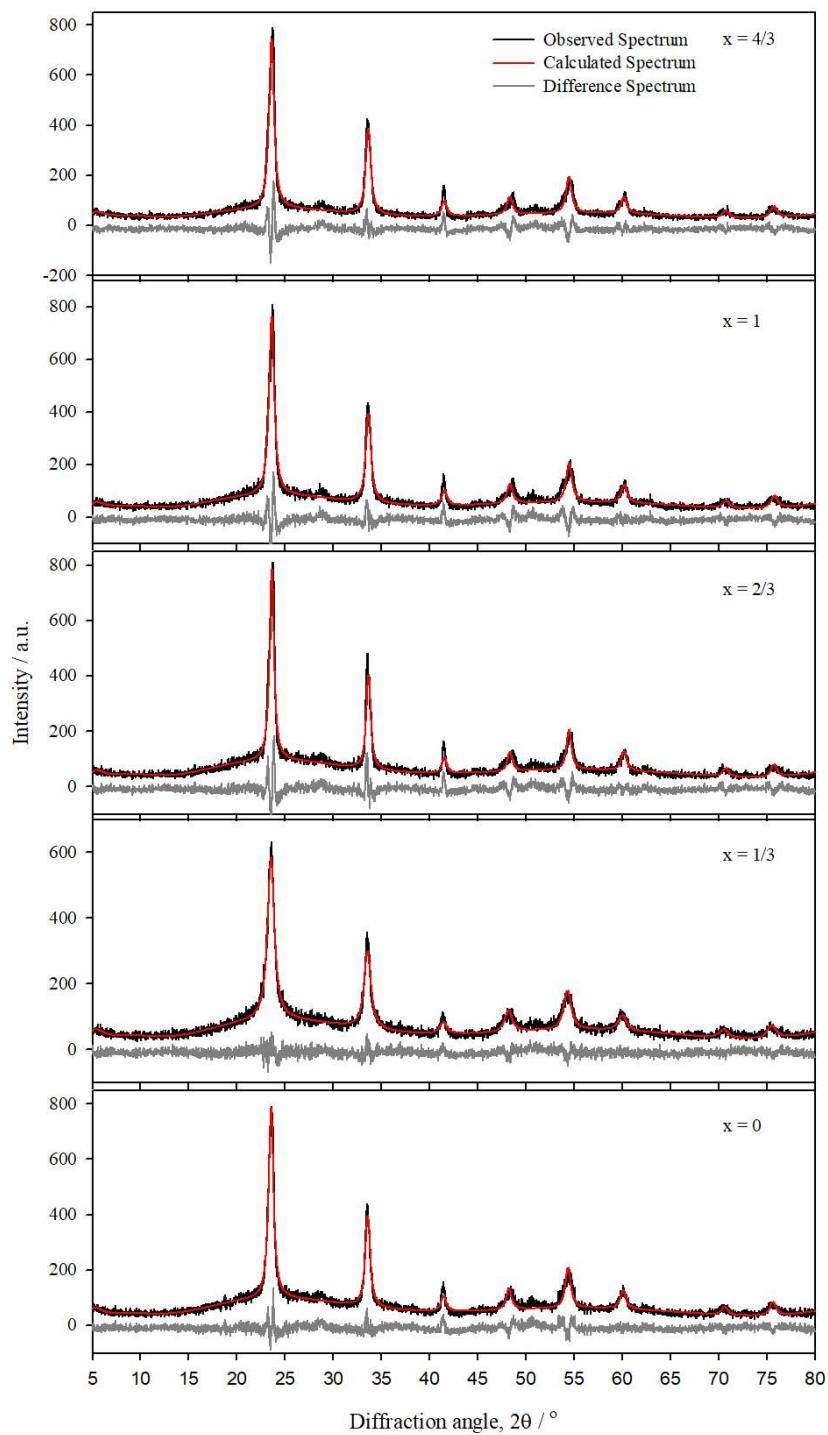
Fig. A.4.9. Rietveld refinements fit of the $Cr_{4/3-x}Al_xW_{20/3}O_{24}(PO_2)_4$ series samples prepared at 650°C. The black spectrum represents the observed/measured spectrum, and the red spectrum represents calculated data. The curve below the spectrum represents the difference spectrum.
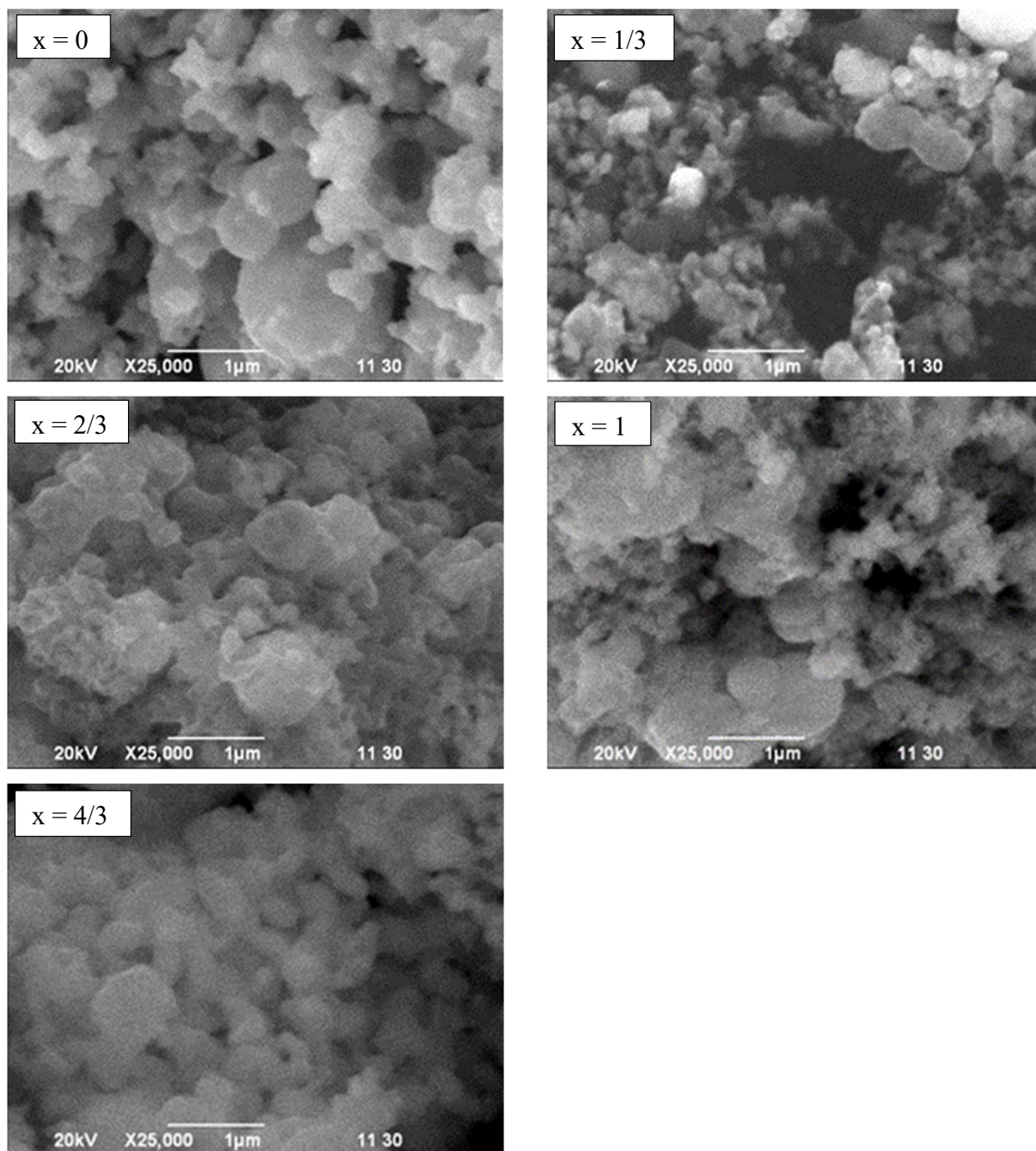
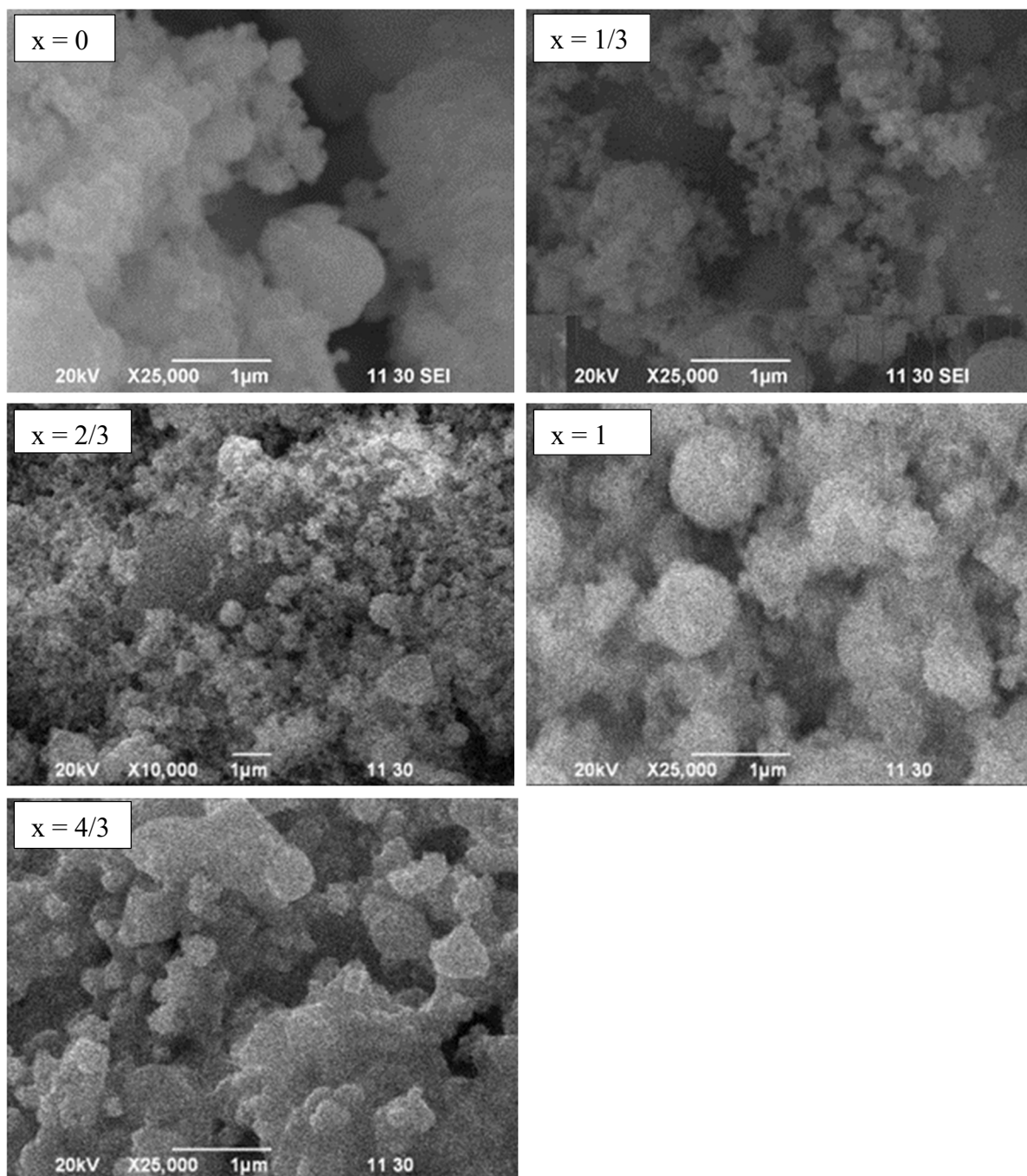Fig. A.4.10. SEM images of $Cr_{4/3-x}Al_xW_{20/3}O_{24}(PO_2)_4$ with different nominal compositions at 600ºC.

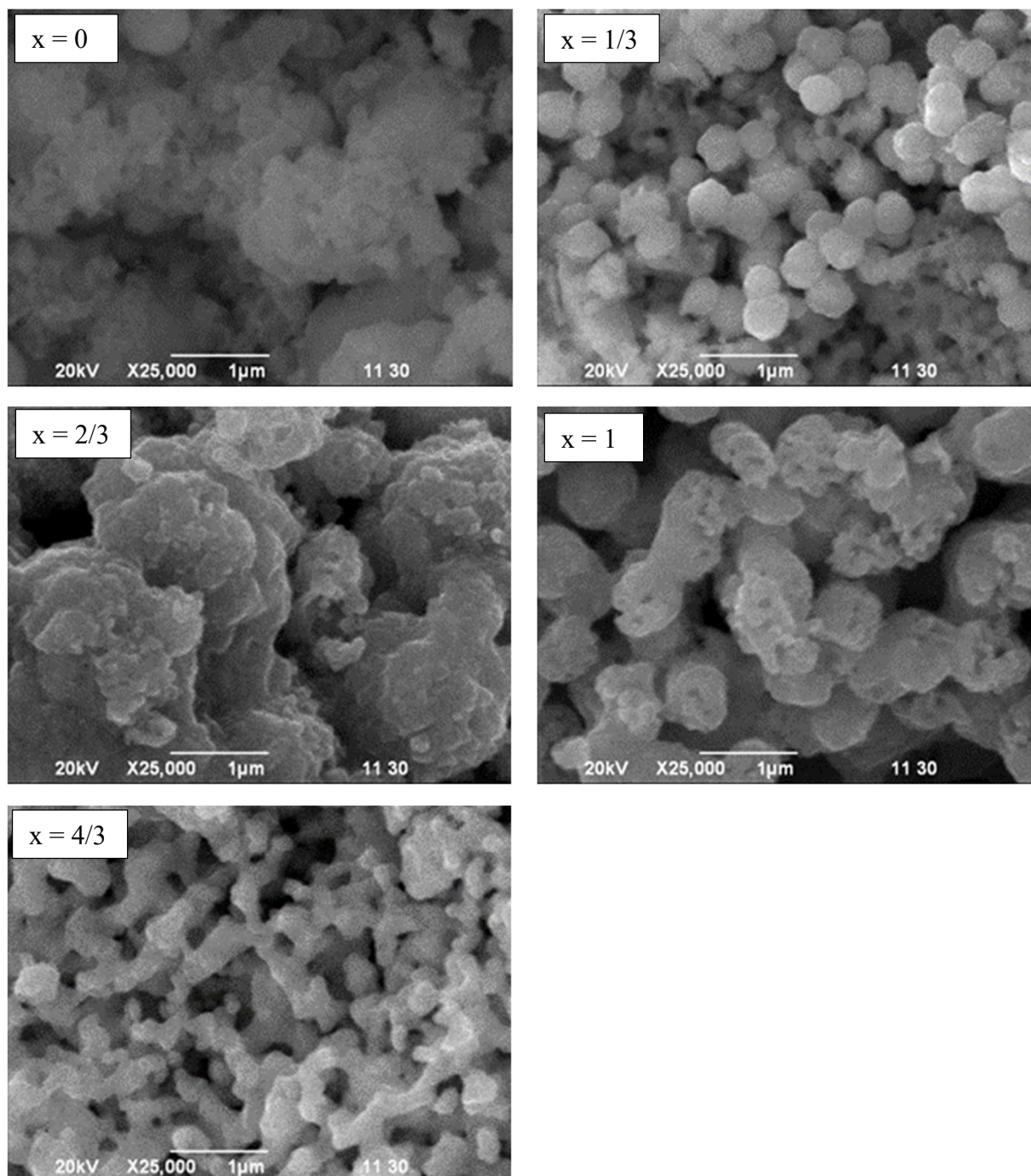Fig. A.4.11. SEM images of $Cr_{4/3-x}Al_xW_{20/3}O_{24}(PO_2)_4$ with different nominal compositions at 700ºC.

Fig. A.4.12. SEM images of $Cr_{4/3-x}Al_xW_{20/3}O_{24}(PO_2)_4$ with different nominal compositions at 800°C.

Table A.4.3 Crystallite sizes of $Al_{4/3-x}Fe_xW_{20/3}O_{24}(PO_2)_4$ at different compositions and temperatures.

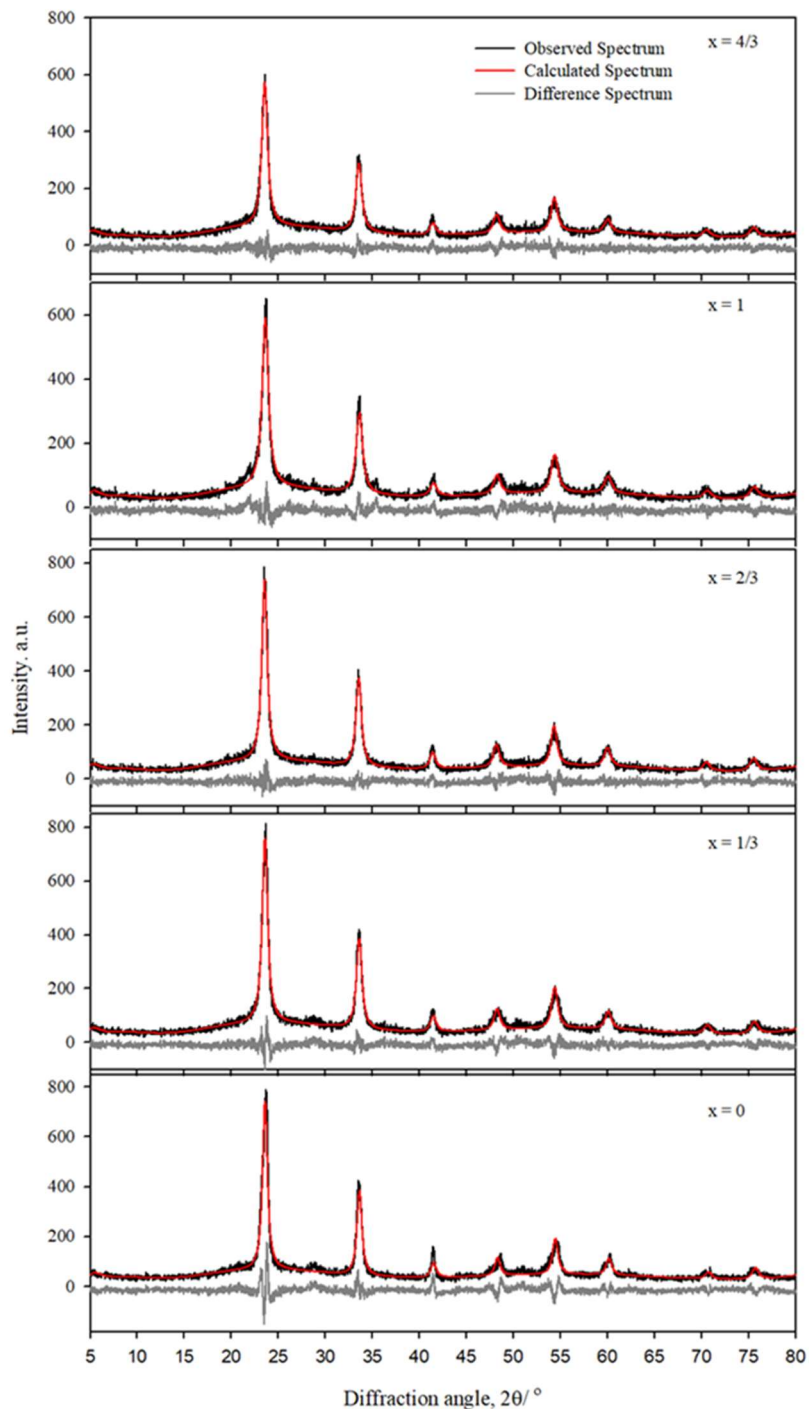| Composition x of $Al_{4/3-x}Fe_xW_{20/3}O_{24}(PO_2)_4$	Temperature (ºC)	Size (nm)
x = 0	550	9.19
	600	14.69
	650	14.30
	700	14.10
	750	13.69
x = 1/3	550	14.33
	600	14.16
	650	13.75
	700	13.74
	750	15.19
x = 2/3	550	15.41
	600	15.58
	650	13.65
	700	14.04
	750	13.97
x = 1	550	12.91
	600	11.97
	650	12.82
	700	12.46
	750	11.76
x = 4/3	550	12.11
	600	12.11
	650	12.50
	700	14.40
	750	-

Fig. A.4.12. Rietveld refinements fit of the $Al_{4/3-x}Fe_xW_{20/3}O_{24}(PO_2)_4$ series samples prepared at 650°C. The black spectrum represents the observed/measured spectrum, and the red spectrum represents calculated data. The curve below the spectrum represents the difference spectrum.
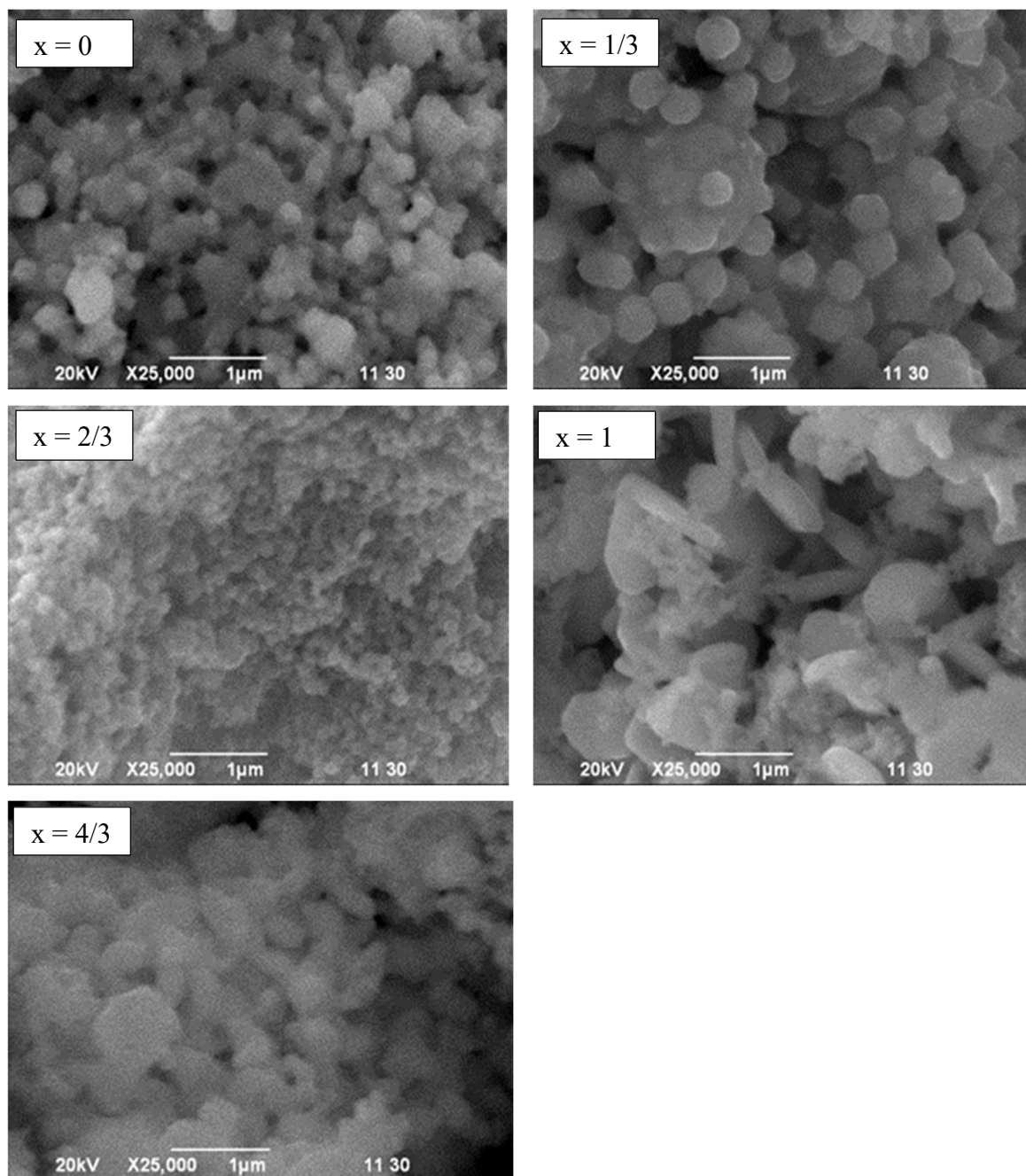
Fig. A.4.13. SEM images of $Al_{4/3-x}Fe_xW_{20/3}O_{24}(PO_2)_4$ with different nominal compositions at 600°C.

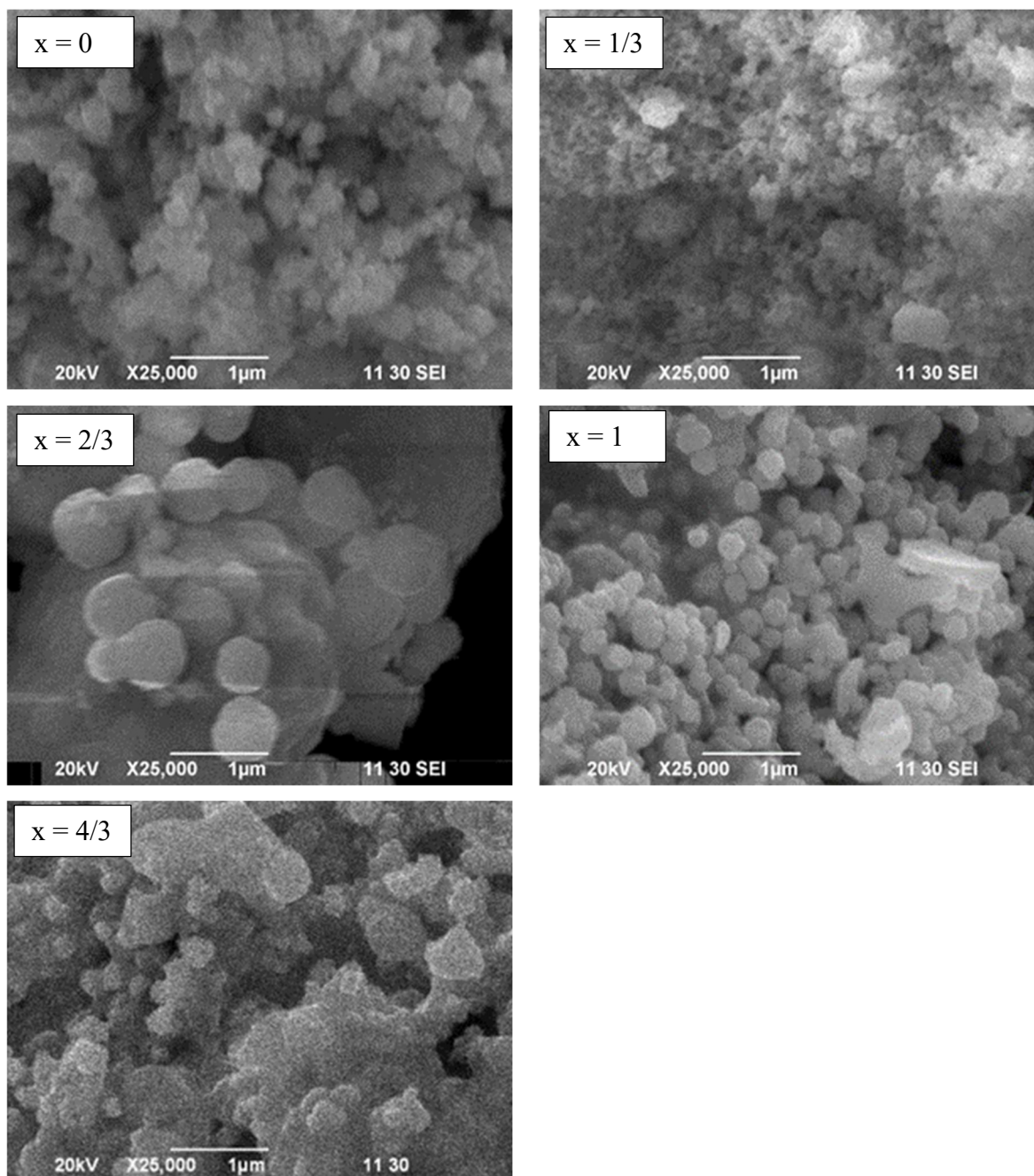Fig. A.4.14. SEM images of $Al_{4/3-x}Fe_xW_{20/3}O_{24}(PO_2)_4$ with different nominal compositions at 700°C.

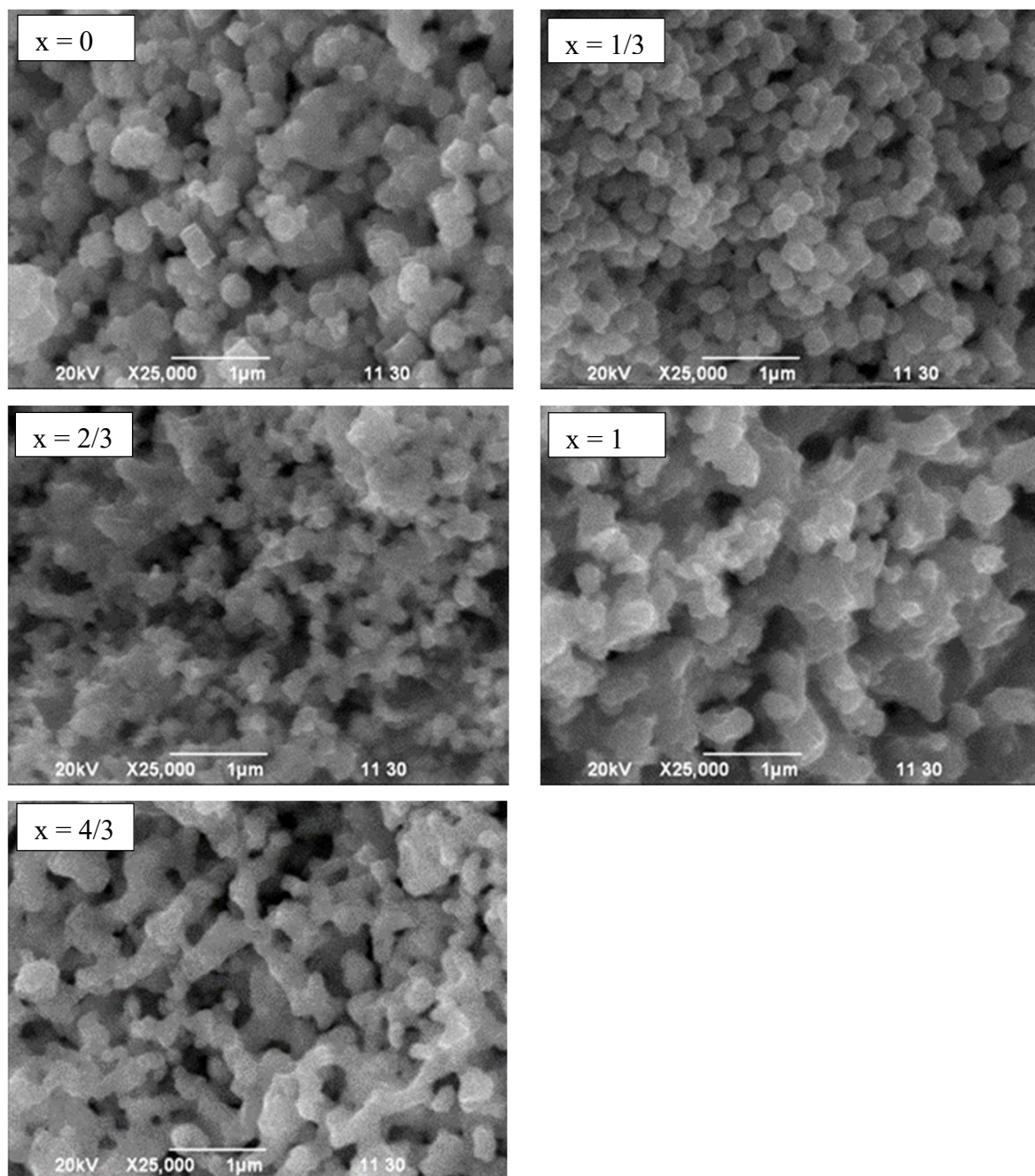Fig. A.4.15. SEM images of $Al_{4/3-x}Fe_xW_{20/3}O_{24}(PO_2)_4$ with different nominal compositions at 800°C.